
INCORPORATING CALCIUM SIGNALLING
IN VERTEX MODELS OF
NEURAL TUBE CLOSURE



Abhishek Chakraborty
School of Mathematics
Cardiff University

March 2024

A thesis submitted for the degree of
Doctor of Philosophy

Abstract

Recent experiments have shown that apical constriction (AC) during neural tube closure (NTC) is driven by cell contractions preceded by asynchronous and cell-autonomous Ca^{2+} flashes. Disruption of these Ca^{2+} signals and contractions leads to neural tube defects, such as anencephaly. However, the inherent two-way mechanochemical coupling of Ca^{2+} signaling and mechanics is poorly understood, and live-cell imaging is difficult. Thus, models can help greatly but the few available partially reproduce experimental findings. We first study a modified implementation of the mechanochemical vertex model of Suzuki et al [196]; the modified Suzuki model. We numerically implement it by developing CelluLink, a new open-source (Python), user-friendly software package for vertex modelling. CelluLink's parallel processing enables fast yet thorough parameter sweeps, guided by an analytically derived bifurcation diagram. CelluLink can be adapted to study other multicellular challenges. Subsequently, in close collaboration with experimentalists, we develop a one-way mechanochemical model to study the effect of Ca^{2+} on mechanics. This model significantly improves upon the Suzuki model, reproducing several experimental observations. We incorporate, for the first time, the surface ectoderm and the experimental Ca^{2+} flash amplitude and frequency profiles. Furthermore, guided by experiments, we model the damping coefficient of the vertices and cell-cell adhesion as functions of actomyosin concentration and cell size. The one-way model successfully reproduces the significant reduction in neural plate size during AC, within 2%-8% of the initial area. We then develop a two-way mechanochemical model which captures the two-way coupling between Ca^{2+} signals and mechanics. We incorporate stretch-sensitive Ca^{2+} channels, enabling the cell to respond to mechanical stimuli. The model reproduces the results of the one-way model, but more accurately, the Ca^{2+} frequency and amplitude arise from the interaction between the cells and are not imposed. We leverage our models to propose a series of hypotheses for future experiments.

Acknowledgements

First and foremost, I would like to thank my supervisor, Dr. Katerina Kaouri. If not for her, I would not have had the opportunity to pursue this doctorate. Be it helping with my application process, training me to present my work at conferences, or polishing up my written work, she has been with me every step of the way. I would like to thank my supervisor Prof. Tim Phillips for his continual support and guidance. I am especially grateful to him for training and testing me on numerical methods. His comments and feedback greatly helped in improving the overall quality of this thesis. I appreciate their regular reminders to eat well and take care of myself!

I am grateful to the Cardiff University Doctoral Academy for sponsoring my doctorate through the Vice Chancellor's International Scholarship for Research Excellence.

I would like to express my gratitude towards Dr. Clinton Durney, for his advice on programming vertex models in Python, and Dr. Makoto Suzuki, for providing feedback on my implementation of their vertex model.

I am especially thankful to Dr. Neophytos Christodoulou for helping me understand the underlying biology and navigate the experimental literature.

I am also thankful to Prof. Philip Maini, Prof. Ruth Baker, and Prof. Paris Skourides for their comments and suggestions.

Finally, I would like to thank my parents and grandparents for their unconditional love and support. I could not have completed my doctoral journey without their encouragement.

In the memory of S.C. Banerjee and A. Pakrashi.

Contents

Abstract	i
Acknowledgements	ii
Contents	iv
List of Tables	vii
List of Figures	ix
1 Introduction	1
1.1 Motivation	1
1.2 The cellular machinery	5
1.2.1 Ca^{2+} signalling	5
1.2.2 Cell mechanics	8
1.2.3 Coupling of Ca^{2+} signalling and mechanics	9
1.3 Mathematical models	12
1.3.1 Ca^{2+} signalling	12
1.3.2 Cell mechanics	15
1.3.2.1 Vertex models	20
1.3.3 Coupling of Ca^{2+} signalling and mechanics	27
1.4 Aims and objectives	29
1.5 Thesis overview	31
2 Experimental results on the role of Ca^{2+} in NTC	33
2.1 Christodoulou and Skourides	34
2.2 Suzuki et al	37
2.3 Summary	41

3	The Suzuki model	46
3.1	Vertex model	46
3.1.1	Modelling assumptions	47
3.1.2	The potential energy term	48
3.1.3	Cell activation	51
3.1.4	The ratchet-like mechanism	52
3.2	Computational results	54
4	CelluLink - A new software package for vertex models:	
	Algorithm and features	62
4.1	Existing computational software	62
4.2	Features of the software	64
4.3	The algorithm	66
4.4	Testing the software	74
5	The modified Suzuki model	81
5.1	Modelling assumptions	82
5.2	Comparing with the Suzuki model	84
5.3	Deriving the bifurcation diagram	88
5.4	Activating the ratchet-like mechanism	103
5.5	Parameter sweep	108
6	Comparing numerical methods for vertex models	116
6.1	Convergence of one-step methods	116
6.2	Discretising the system	120
6.3	Forward Euler method	122
6.4	Predictor-corrector method	126
7	A new mechanochemical model for NTC:	
	One-way coupling	132
7.1	Adding the surface ectoderm	133
7.1.1	Deriving the damping function	145
7.1.2	Deriving the adhesion term	148
7.2	Modelling the Ca^{2+} frequency	154
7.3	Modelling the Ca^{2+} amplitude	161
7.4	Discussion	169

8 A new mechanochemical model for NTC:	
Two-way coupling	179
8.1 Modelling the SSCCs	179
8.2 Discussion	189
9 Summary, conclusions, and future work	198
Bibliography	206

List of Tables

3.1	Parameter values for Figures 3.5, 3.7, and 3.8.	57
4.1	Comparison of software tools for cell-based modelling.	63
4.2	Parameter index table for the modified Suzuki model.	76
4.3	Parameter values for Figures 4.8 and 4.9.	77
5.1	Parameter values for Figures 5.1b and 5.2b.	85
5.2	Cell equilibria and corresponding conditions.	93
5.3	Regions of the modified Suzuki model's parameter space.	100
5.4	Parameter values for Figures 5.4 and 5.5.	103
5.5	Parameter values for Figures 5.6 and 5.7.	104
5.6	Experimentally determined material properties for the neural plate.	109
5.7	Experimentally-valid parameter ranges for the vertex model. . . .	110
5.8	Parameter values for Figures 5.8 and 5.9.	111
5.9	Effect of increasing parameters p_c , K_n^A , K_n^P , μ , T_{0n} , and ξ on the rate of tissue contraction and final tissue area.	114
6.1	Parameter values for Figures 6.1, 6.2, 6.3, and 6.4.	123
7.1	Parameter values for Figure 7.1.	135
7.2	Parameter values for Figure 7.2.	140
7.3	Parameter values for Figure 7.5.	152
7.4	Parameter values for Figures 7.6 and 7.7.	158
7.5	Parameter values for Figures 7.8, 7.9, 7.10, 7.11, 7.12, 7.13, and 7.14.	163
7.6	Comparison of the experimentally observed behaviours captured by the Suzuki and one-way models.	176
8.1	Parameter values for Figures 8.2, 8.3, 8.4, 8.5, 8.6, 8.7, and 8.8. .	184

8.2 Comparison of the experimentally observed behaviours captured
by the one-way and two-way models. 194

List of Figures

1.1	Schematic of neural tube closure.	2
1.2	Common types of neural tube defects.	3
1.3	Schematic of apical constriction.	4
1.4	The PLC pathway for Ca^{2+} signalling.	6
1.5	Schematic of the ratchet-like mechanism.	8
1.6	A schematic diagram for Ca^{2+} dynamics.	13
1.7	Schematics of the five most widely used cell-based models.	17
1.8	Ventral furrow formation in <i>Drosophila</i>	20
1.9	The 2D vertex model.	21
1.10	Schematics of the four types of vertex models.	22
2.1	Examples of single-cell, two-cell, and multi-cellular Ca^{2+} flashes during NTC.	35
2.2	Temporal profiles of Ca^{2+} flash frequency and NTC velocity	36
2.3	Time-lapse of a <i>Xenopus laevis</i> embryo undergoing NTC.	38
2.4	Ca^{2+} transients in the neural plate over the course of NTC.	39
2.5	Temporal profiles of the Ca^{2+} flash amplitude, F-actin distribution, and relative change in apical area of a single cell during NTC.	40
2.6	Ca^{2+} oscillation amplitude and apical surface area of a single cell during AC.	42
2.7	Ca^{2+} oscillation frequency and cell surface area over the duration of AC.	43
2.8	Ca^{2+} oscillation amplitude over the duration of AC.	44
3.1	The physical attributes of the cell that impact vertex dynamics.	49
3.2	Ratchet-like stabilization of cell area.	53
3.3	Ratchet-like stabilization of cell perimeter.	54

3.4	Initial configuration of the tissue modelled by Suzuki et al.	55
3.5	Effects of Ca^{2+} transients and the constrictive nature of the apical cell surface on the modelled tissue.	56
3.6	Sparse and dense distribution of Ca^{2+} transients.	58
3.7	Tissue area constriction as a function of cell-activation frequency.	59
3.8	Change in tissue size over simulation runtime for different Ca^{2+} -activation periods.	60
4.1	Two types of tissue configurations in CelluLink.	65
4.2	Indexing scheme used in CelluLink.	67
4.3	Cell arrangement in the hexagon-shaped configuration.	68
4.4	High-level process flow diagram for CelluLink.	71
4.5	Flow chart for CelluLink's main process.	72
4.6	Flow chart for CelluLink's child processes.	73
4.7	CelluLink running in a terminal window.	75
4.8	Time evolution of the tissue captured by CelluLink.	78
4.9	Time series data for the tissue visualised in Figure 4.8.	79
5.1	Comparison with the simulation results of Suzuki et al (Figure 3.5a).	86
5.2	Comparison with the simulation results of Suzuki et al (Figure 3.8).	87
5.3	Bifurcation diagram of the modified Suzuki model.	99
5.4	Equilibrium cell sizes corresponding to each region of the modified Suzuki model's parameter space.	101
5.5	Equilibrium tissue configurations corresponding to each region of the modified Suzuki model's parameter space.	102
5.6	Cell area and perimeter at equilibrium as functions of the natural area and the natural perimeter respectively.	106
5.7	Effect of the ratchet-like mechanism on the area and perimeter of the tissue.	107
5.8	Effect of p_c , K_n^A , K_n^P , μ , T_{0n} , and ξ on the time taken to complete AC.	112
5.9	Effect of p_c , K_n^A , K_n^P , μ , T_{0n} , and ξ on the final area of the tissue.	113
6.1	Convergence of the forward Euler method.	124
6.2	Convergence error vs time step for the forward Euler method.	125
6.3	Convergence of the predictor-corrector method.	129

6.4	Convergence error vs time step for the predictor-corrector method.	130
7.1	Effect of the surface ectoderm on AC in the modified Suzuki model.	136
7.2	Effect of the introduction of growth laws on AC.	141
7.3	Schematic depicting the maximum allowable range for vertex displacement.	146
7.4	Scaled adhesion force as a function of cell edge length.	151
7.5	Impact of revising the ratchet-like mechanism on AC.	153
7.6	Incorporating the Ca^{2+} frequency profile into the vertex model.	159
7.7	Effect of the continuous elevation of cytosolic Ca^{2+} on AC.	160
7.8	Effect of varying k_ξ on the final area attained by the anterior neural plate.	164
7.9	Time evolution of the neural plate and surface ectoderm in the one-way model.	166
7.10	Time series data for the neural plate visualised in Figure 7.9.	167
7.11	Descriptive statistics for the one-way model.	168
7.12	Effect of amp and fpm on the final area attained by the anterior neural plate.	173
7.13	Time series data for the anterior neural plate for $fpm = 0.25$.	174
7.14	Effect of $duty$ on the final area attained by the anterior neural plate.	175
8.1	Probability of SSCC-driven cell activation as a function of cortical actomyosin concentration.	182
8.2	Time evolution of the neural plate and surface ectoderm in the two-way model.	185
8.3	Time series data for the neural plate visualised in Figure 8.2.	186
8.4	The absence of initially activated cells in the anterior neural plate prevents AC in the two-way model.	187
8.5	Descriptive statistics for the two-way model.	188
8.6	Effect of disabling the ‘stretch activation’ mechanism on AC.	193
8.7	Multicellular Ca^{2+} transient and Ca^{2+} wave propagation in the two-way model.	195
8.8	Average number of Ca^{2+} flashes per cell in each layer of the anterior neural plate in the two-way model.	196

Chapter 1

Introduction

1.1 Motivation

Neurulation, a key developmental process, takes place in the early stages of embryogenesis, typically during the third week of gestation [141]. During neurulation, the neural plate tissue transforms into the neural tube in a process known as neural tube closure (NTC) (Figure 1.1). The neural tube is the embryonic precursor to the central nervous system, which is made up of the brain and spinal cord. The failure of NTC results in neural tube defects, like Anencephaly and Spina Bifida (Figure 1.2), which are among the most common congenital malformations, affecting over 300,000 births annually, worldwide [41].

NTC is facilitated by a process in which the cells of the anterior neural plate undergo a dramatic change in size, apical constriction (AC) [33]. During AC, the apical side of a cell contracts, causing the cell to take on a wedged shape (Figure 1.3) [120]. This shape change is coordinated across many cells of the neuroepithelial layer and generates the force required to bend or fold the cell layer.

Experiments have shown that AC during NTC is driven by Ca^{2+} -induced cell contractions and that disrupting the Ca^{2+} signals leads to malformations [33, 196]. However, this interplay of Ca^{2+} signalling and cell mechanics and its effect on NTC is poorly understood. Furthermore, live-cell imaging is difficult since NTC entails the neural plate folding in on itself. In this scenario, mathematical modelling and simulations are indispensable. However, there are very few models of Ca^{2+} signalling in AC [96, 196], and they only capture a small number of the behaviours

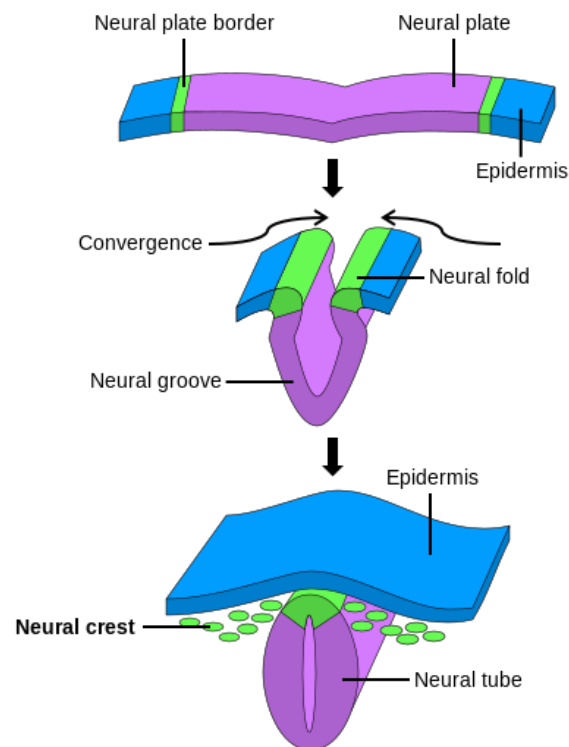


Figure 1.1: Schematic depicting a neural plate undergoing NTC. The cells of the neural plate undergo AC, causing the neural plate to fold and form the neural tube. Source: [142].



(a) Spina Bifida.



(b) Anencephaly.

Figure 1.2: Disruptions in NTC lead to neural tube defects in embryos, such as Spina Bifida and Anencephaly. Spina Bifida encompasses a spectrum of defects, including myelomeningocele, illustrated in Figure 1.2a, where the spinal cord and meninges protrude through a spinal opening. This condition often results in neurological impairments like paralysis and issues with bladder and bowel control. Figure 1.2b depicts Anencephaly, a fatal condition where the infant is born without parts of the brain and skull. Source: [22, 210].

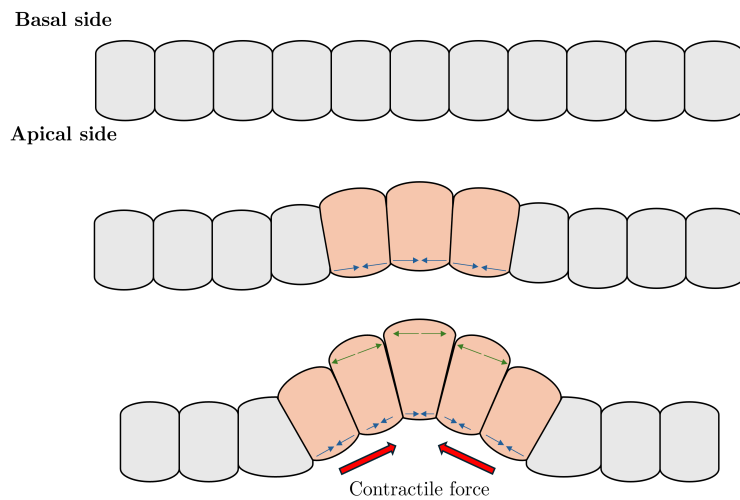


Figure 1.3: Schematic depicting a group of cells undergoing AC. Constriction of the apical side of cells in an epithelial layer generates enough force to initiate invagination. The wedge shape results when constriction of the apical side of the cell squeezes the cytoplasm, expanding the basal side.

observed experimentally.

The aim of this doctoral thesis is to develop new mathematical models of the anterior neural plate during the AC phase of NTC based on the data available from experiments. These models aim to accurately capture the mechanochemical coupling between Ca^{2+} signalling and cellular mechanics, reproducing a variety of experimentally observed behaviours *in silico*. The models can then be used to study processes at the sub-cellular, cellular, and tissue level, which would be difficult or impossible to explore experimentally, and identify future directions for *in vivo* experiments.

The research for this thesis was undertaken in collaboration with Dr. Neophytos Christodoulou and Prof. Paris Skourides, experimentalists at the University of Cyprus, and guided by frequent discussions with Prof. Philip Maini and Prof. Ruth Baker, at the University of Oxford.

1.2 The cellular machinery

Ca^{2+} signalling is an indispensable method of information transfer within the human body [17]. In this project, we focus on the role of Ca^{2+} signalling in NTC and its interplay with mechanical forces at the cell and tissue-level. Before we address the current state of research in the field, it is worth visiting the cellular machinery driving Ca^{2+} signalling and tissue morphogenesis to gain familiarity with the terminologies used and mechanisms involved.

1.2.1 Ca^{2+} signalling

In a typical cell, the resting concentration of Ca^{2+} in the cytosol is maintained at $\approx 100\text{nM}$. This is between 20,000 to 100,000 times lower than the Ca^{2+} concentration of the extracellular fluid [37], and between 1,000 to 8,000 times lower than the Ca^{2+} concentration of the endoplasmic reticulum (ER) [20], the major store of Ca^{2+} in the cell.

Due to the extremely low cytosolic Ca^{2+} concentration, the entry of minute quantities of Ca^{2+} ions from the ER or from the extracellular fluids causes rapid, distinctive, and readily reversible changes in the cytoplasmic Ca^{2+} concentration, which manifest as transients, oscillations, and waves. This enables Ca^{2+} to serve as a very fast, potent intracellular signal, a second messenger¹, for various functions e.g. muscle contraction, blood clotting, wound healing, fertilization, embryogenesis, and cancer [17].

The different types of Ca^{2+} fluctuations in cells exhibit distinct characteristics in terms of duration, amplitude, frequency, and spatial propagation. A Ca^{2+} transient (also referred to as a Ca^{2+} flash or Ca^{2+} pulse) occurs when the cytosolic Ca^{2+} concentration rises transiently, transitioning the cell from a low Ca^{2+} state (inactivated) to a high Ca^{2+} state (activated) [33, 196]. Ca^{2+} oscillations refer to repetitive, rhythmic fluctuations in cytosolic Ca^{2+} concentration [53], while Ca^{2+} waves are propagating waves of increased cytosolic Ca^{2+} concentration that spread spatially across cells or tissues [14].

The Ca^{2+} signalling process is initiated when the concentration of cytosolic Ca^{2+} rises. When Ca^{2+} acts as the primary messenger, the process is triggered when Ca^{2+} enters the cell through ion channels on the plasma membrane. When

¹**Second messenger** A molecule that relays signals received at receptors on the cell's surface to target molecules or structures inside the cell.

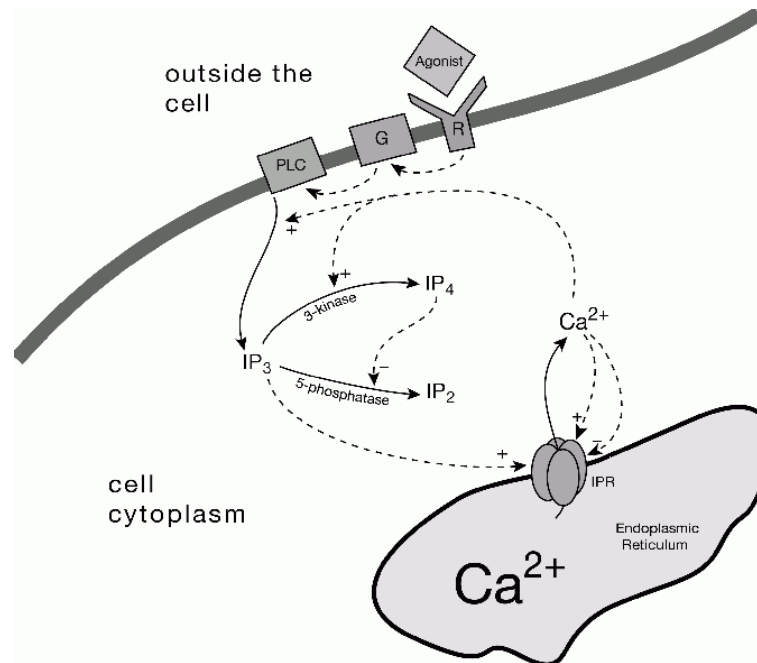


Figure 1.4: The PLC pathway for Ca^{2+} signalling (R - Receptor, G - GPCR).

Source: [185].

Ca^{2+} acts as the secondary messenger, the cell is stimulated to release Ca^{2+} ions from intracellular stores, such as the ER, when an agonist² binds to a receptor on the plasma membrane [37].

The most common signalling pathway that leads to an increase in the cytoplasmic Ca^{2+} concentration is the phospholipase-C (PLC) pathway (Figure 1.4), which is activated as follows [5]:

1. Upon stimulation, i.e., agonist-receptor binding, the receptor (located on the plasma membrane) activates the PLC enzyme via the G protein-coupled receptors (GPCR).
2. PLC hydrolyses the membrane phospholipid phosphatidylinositol 4,5-bisphosphate (PIP_2) to form the water soluble inositol 1,4,5-trisphosphate (IP_3), and lipid soluble diacylglycerol (DAG).
3. IP_3 diffuses to the ER and binds to an IP_3 receptor.

²**Agonist** A molecule that binds to a receptor on a cell, triggering a response from the cell.

4. The IP_3 receptor (IPR) then activates and begins to serve as a channel to release Ca^{2+} from the ER into the cytosol.

In all non-muscle cells that exhibit Ca^{2+} waves, the inositol 1,4,5-triphosphate receptor (IPR)/ Ca^{2+} channel governs the mechanism of Ca^{2+} release from the ER. The release of Ca^{2+} via IPR channels can stimulate the release of additional Ca^{2+} from the ER, often by binding to the IPR and increasing its open probability [70]. This leads to the autocatalytic³ release of Ca^{2+} from the ER, in a process called Ca^{2+} -induced Ca^{2+} release (CICR) [185].

Since Ca^{2+} itself is an activator of the IPR, the rate of IP_3 -induced Ca^{2+} release (IICR) was shown to be enhanced when cytosolic Ca^{2+} concentration is within a certain range [70]. However, if the Ca^{2+} concentration exceeds the upper bound of this range, the rate of IICR will be suppressed e.g. for brain cells, this value is between 100nM (inactivated state) and 1 μ M [66].

The Ca^{2+} signalling process is terminated when ATP-dependent Ca^{2+} pumps, located in the plasma membrane (plasma membrane Ca^{2+} ATPases - PMCAs) and in the membranes of organelles such as the ER (sarco/endoplasmic reticulum Ca^{2+} ATPases - SERCAs), actively transport Ca^{2+} ions against their concentration gradient out of the cytoplasm and into the extracellular space or back into intracellular calcium stores. This process thereby decreases the cytoplasmic Ca^{2+} concentration and restores Ca^{2+} homeostasis [185].

While Ca^{2+} signalling appears deterministic and tightly regulated at the cell and tissue scale, several stochastic elements contribute to variability and complexity in signalling dynamics. Essentially, Ca^{2+} flashes are emergent properties of the interaction of channel-level stochastic processes [54]. Some of these stochastic elements are:

- *Channel gating*: The opening and closing of IPR channels can exhibit stochastic behaviour, leading to variability in the timing and magnitude of Ca^{2+} fluxes [54].
- *Buffering*: The binding of Ca^{2+} ions to intracellular buffering proteins, such as calmodulin, can exhibit stochastic interactions due to the random collision of ions and proteins. This can influence Ca^{2+} dynamics by modulating the duration and amplitude of Ca^{2+} flashes [40].

³**Autocatalytic reaction** A chemical reaction is said to be autocatalytic if one of the reaction products is also a catalyst for the same or a coupled reaction.

- *Feedback regulation:* Feedback mechanisms within Ca^{2+} signalling pathways, such as the Ca^{2+} -dependent opening and closing of ion channels or activation of Ca^{2+} -regulated enzymes, can introduce stochasticity into signalling dynamics [54].

1.2.2 Cell mechanics

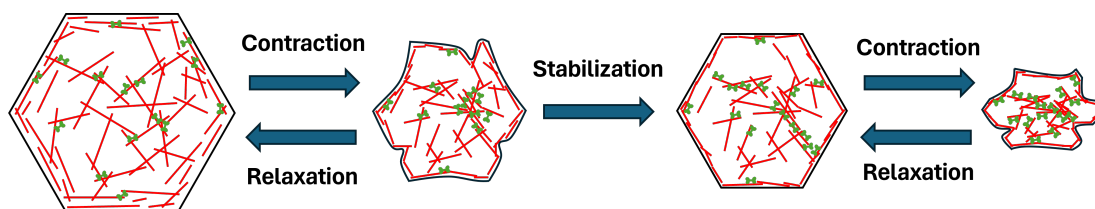


Figure 1.5: Schematic depicting the ratchet-like mechanism proposed by Martin et al [121]. Actin filaments (red) coalesce across the apical cortex, forming a network. Myosin (green) accumulates on this actin network. Myosin activity causes the actin filaments to contract, pulling on the cell boundaries, which leads to a reduction in apical surface area.

The cell cortex is a specialized region near the cell membrane in animal cells [198]. It is a dynamic and structurally complex layer primarily composed of cytoskeletal elements, such as actin filaments, and associated proteins, such as myosin. The actin filaments form a network just beneath the cell membrane. This actin cytoskeleton provides structural support and contributes to the determination of cell shape. When myosin molecules attach to the actin filaments, they function as motors and contract the actin filament, which pulls on the junctions of the cell boundary, reducing the area of the cell [46, 121]. The degree of assembly and crosslinking of the actomyosin bundles determines the mechanical properties, shape, and size of the cell [24].

During AC, actin filaments accumulate in the apical cortex, providing a substrate for the binding of myosin molecules (collectively referred to as the apical actomyosin network) [121]. The motor activity of the myosin molecules causes actin filament contraction, which results in a reduction of the cell's apical surface area. The relaxation of the apical area results from the exhaustion of the myosin motors, which detach from the actin filaments, allowing for the relaxation of the actin network back to a 'rest area' [121].

If the actin network is reassembled during contraction, the network can no longer relax to its previous rest area, and instead settles into a smaller rest area. The repeated assembly and disassembly of the actomyosin bundles results in pulsed contractions of the apical area. Thus, AC proceeds incrementally via a ratchet-like mechanism of contraction and stabilization [121]. The process is depicted in Figure 1.5. Despite the dynamic nature of the contractions in individual cells, the behaviour of the system at the tissue level is continuous i.e. the tissue area decreases monotonically [121].

1.2.3 Coupling of Ca^{2+} signalling and mechanics

Ca^{2+} can regulate the activity of the actomyosin network [136]. When a Ca^{2+} transient occurs in a cell, it changes the structure of the actomyosin bundles in the cell cortex, triggering them to generate contractile stresses [138]. The forces generated by the myosin motors (tension) and actin filaments (elastic forces) are in the piconewton range [9, 38].

At low Ca^{2+} levels ($\approx 100\text{nM}$), the actomyosin network is highly crosslinked⁴ and stable [66]. As Ca^{2+} concentration rises, the network begins to contract actively. If the Ca^{2+} level is too high (in the micromolar range), however, the network becomes so weakly crosslinked that it cannot support any more stress [136]. Thus, there is a ‘window’ of Ca^{2+} concentration which is optimal for contractile activity.

Actomyosin-based contractions have been documented in response to Ca^{2+} release in both embryonic and cultured cells [33, 82, 89, 196, 215] and it has become clear that Ca^{2+} is responsible for contractions in both muscle and non-muscle cells, albeit through different mechanisms [40].

In striated muscle cells, cell contraction is mediated by the binding of Ca^{2+} to troponin but in non-muscle cells (and in smooth muscle cells), contraction is mediated by phosphorylation of the regulatory light chain of myosin. This phosphorylation promotes the assembly of myosin into filaments, and it increases myosin activity. Myosin light-chain kinase (MLCK), the enzyme responsible for this phosphorylation, is itself regulated by calmodulin⁵ [173]. Elevated cytosolic Ca^{2+} promotes the binding of calmodulin to MLCK, resulting in its activation.

⁴**Crosslinking** The process of chemically joining two or more molecules by a covalent bond.

⁵**Calmodulin** A Ca^{2+} -binding protein found freely floating in the cytoplasm of the cell.

This activation leads to the subsequent phosphorylation of the myosin regulatory light chain, followed by myosin contraction.

In some tissues, these Ca^{2+} -induced contractions result in distinct changes in cell shape. One such example is AC [213], which is the subject of our modelling problem. AC is essential for tissue and organ development, playing a critical role not only during NTC [33, 196] but also in other processes [170] such as wound healing in *Xenopus* [47], eye patterning in *Drosophila* [172], and gastrulation in *Drosophila* [42] and *C. elegans* [165].

To date, there have been many studies exploring the role of Ca^{2+} signalling in tissue morphogenesis. Here, we look at some experimental studies that explore the relationship between Ca^{2+} and tissue mechanics in the context of fertilization and embryogenesis.

Starting from the Ca^{2+} waves manifesting in the egg during fertilization [49], Ca^{2+} plays a vital role in every stage of embryonic development. Throughout fertilization and embryogenesis, Ca^{2+} signals evoke mechanical responses in cells and tissues [4, 33, 215]. This influences morphogenesis and, ultimately, impacts organogenesis.

In fertilization, experiments have shown that an increase in Ca^{2+} concentration is sufficient to induce many of the inherent processes [23, 191, 192]. Indeed, in some cases of fertilization failure that might occur during intra-cytoplasmic sperm injection (ICSI) cycles in IVF treatment, oocyte activation can be induced manually by injecting Ca^{2+} [97].

The amplitude and frequency of the Ca^{2+} oscillations at the time of fertilization affect the processes occurring in the later stages of embryonic development. In a study involving fertilized eggs implanted in surrogate rabbit mothers, it was observed that the morphology of the developing embryos depended upon the stimulating Ca^{2+} wave patterns of the initial hours following fertilization [199].

The importance of Ca^{2+} signalling in the later stages of embryonic development is also well known and backed by empirical evidence. For instance, Ca^{2+} waves accompany convergent extension movements during gastrulation [215] and Ca^{2+} transients regulate the following processes: apical-basal cell thinning in the enveloping layer cells [228], morphological patterning in the brain [166, 218], and NTC [33, 196].

It is no surprise, therefore, that experimentally induced changes in intracellular Ca^{2+} concentration were found to perturb the following morphogenetic processes:

neural fold formation in *Xenopus* [132], cell rearrangements during somitogenesis in chicken [31] and zebrafish [109], tissue folding during sea urchin gastrulation [103], convergent extension movements during gastrulation in *Xenopus* [79, 215] and zebrafish [102], epiboly progression in zebrafish [30, 161] and newt [201], and elongation of the egg chamber in *Drosophila* [80]. Crucially, it was observed that pharmacological inhibition of Ca^{2+} led to defects in the embryo [33, 196, 215].

Conversely, the ability of cells to sense and respond to forces by elevating their cytosolic Ca^{2+} concentration is also well established. Ca^{2+} release can be triggered by straining the cytoskeleton, a phenomenon called ‘stretch activation’ [136]. Stretch sensitive Ca^{2+} channels (SSCCs) on the cell membrane allow Ca^{2+} to flow into the cytosol from the extracellular space. They are activated when exposed to mechanical stimulation and they close either by relaxation of the mechanical force or by adaptation to the mechanical force [11, 54, 78, 131].

Mechanically stimulated Ca^{2+} waves have been observed propagating through developing rat brain glial cells [25, 26, 27], developing epithelial cells in *Drosophila* wing discs [139], and many other cell types [16, 168, 169, 209, 225, 226]. These studies show that different types of mechanical stimuli, from shear stress to direct mechanical stimulation, can elicit Ca^{2+} elevation (although the sensing mechanism may differ in each case).

Therefore, it is clear that cytosolic Ca^{2+} concentration can be elevated not only due to the action of chemical signals (extrinsic to the cell), as discussed in Section 1.2.1, but also because of mechanical stresses.

Since mechanical stimulation elicits Ca^{2+} release and Ca^{2+} elicits contractions, which are sensed as mechanical stimuli by the cell, it can be inferred that there must exist a **two-way mechanochemical feedback between Ca^{2+} and cell contraction**. Furthermore, this indicates that cells communicate not only through chemical signalling but also through mechanochemical transduction⁶.

Now, we briefly review two studies [33, 196] that are of particular importance to this thesis because they focus specifically on the role played by Ca^{2+} in reshaping cells undergoing AC during NTC.

Christodoulou and Skourides’ study [33] of Ca^{2+} flashes during NTC in *Xenopus* embryos revealed that the contraction pulses in cells undergoing AC are triggered by ‘cell-autonomous’ Ca^{2+} flashes and that the contraction pulses are driven

⁶**Mechanochemical transduction** The conversion of mechanical signals into biochemical responses or vice versa.

by the contraction of a transient apical actin network. They observed that the Ca^{2+} flashes are typically restricted to single cells and that cell contraction typically followed within a minute of the occurrence of a Ca^{2+} flash. Additionally, they provided evidence that the cell autonomy and asynchrony of contractions are required for the correct spatial distribution of constriction and, as a result, are critical for tissue morphogenesis.

Suzuki et al [196] examined the role of intracellular Ca^{2+} signalling during NTC in *Xenopus* by live-recording the dynamics of the actin complex in neuroepithelial cells during AC in the vertebrate neural plate. They show that intracellular Ca^{2+} signalling is essential for *Xenopus* neural tube formation and that there are two types of Ca^{2+} fluctuations, a single-cell and a multicellular wave-like transient, in the developing neural plate. They observed that transient increases in Ca^{2+} concentration induced cortical F-actin (filamentous actin) remodelling, leading to AC and accelerating NTC.

Because of their importance to this doctoral work, the studies above will be covered in detail in Chapter 2, where we will describe the full range of characteristic behaviours observed in the anterior neural plate during NTC.

Based on observations in [33, 196], we understand that cells are chemically isolated from one another, meaning that Ca^{2+} transients from one cell cannot propagate to another. Therefore, any model aiming to simulate the constricting anterior neural plate during the AC phase of NTC must be able to resolve individual cells. Essentially, we are interested in studying how changes in the shape and size of individual cells impact the rate and extent of tissue morphogenesis.

In the following section, we will review some key Ca^{2+} signalling models and mechanical models to determine the most suitable modelling approach for our specific problem.

1.3 Mathematical models

1.3.1 Ca^{2+} signalling

Ca^{2+} oscillations and waves appear over diverse timescales and lengthscales and pose many interesting mathematical questions. A multitude of deterministic and stochastic Ca^{2+} signalling models have been presented in the literature for various cell types and at various scales [54, 60, 98].

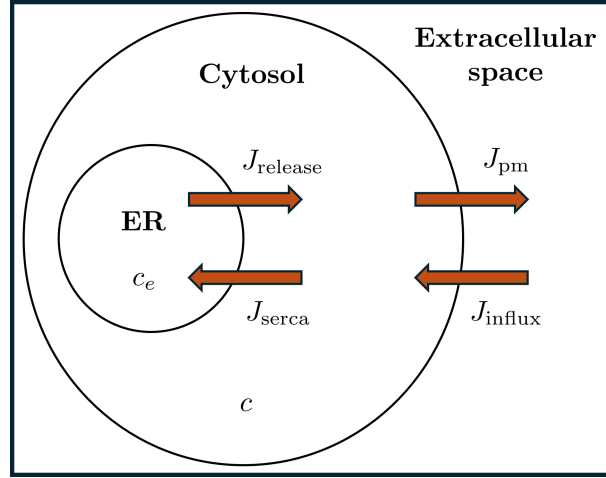


Figure 1.6: A schematic diagram for Ca^{2+} dynamics, depicting Ca^{2+} fluxes into and out of the cytosol. J_{release} and J_{serca} denote Ca^{2+} flux from the ER into the cytosol and Ca^{2+} flux from the cytosol to the ER, respectively. J_{pm} and J_{influx} denote Ca^{2+} efflux from and influx to the cytosol across the plasma membrane, respectively. c_e and c denote the Ca^{2+} concentration in the ER and cytosol, respectively.

A typical Ca^{2+} dynamics schematic (Figure 1.6) describes the various Ca^{2+} fluxes into and from the cytoplasm. Using the conservation of Ca^{2+} , a simple model could be constructed as follows [185]:

$$\frac{dc}{dt} = J_{\text{release}} - J_{\text{serca}} + J_{\text{influx}} - J_{\text{pm}}, \quad (1.1)$$

$$\frac{dc_e}{dt} = \gamma(J_{\text{serca}} - J_{\text{release}}), \quad (1.2)$$

where c denotes the cytosolic Ca^{2+} concentration, c_e denotes the Ca^{2+} concentration in the ER, J_{release} and J_{serca} denote Ca^{2+} flux from the ER to the cytosol and Ca^{2+} flux from the cytosol to the ER, respectively, J_{pm} and J_{influx} denote Ca^{2+} efflux from and influx to the cytosol across the plasma membrane, respectively, and γ denotes the ratio of the cytoplasmic volume to the ER volume.

Equations (1.1) and (1.2) equate the temporal rates of change of c and c_e to the influx and efflux of cytosolic Ca^{2+} and Ca^{2+} in the ER, respectively. Additional Ca^{2+} fluxes such as mitochondrial and buffer fluxes can be added in the same manner. Also, the conservation equations for c and c_e can be coupled to other

equations that describe, for instance, the cytosolic IP_3 concentration, the fraction of active IPRs on the ER, and the states of the ATPase pumps or Ca^{2+} buffers [12, 48, 52, 75, 111].

In some cell types, Ca^{2+} oscillations occur practically uniformly across the cell, meaning that at any time, the measurement of the Ca^{2+} concentration at any point of the cell would yield the same value [185]. More often, however, the Ca^{2+} signal takes the form of a wave moving across the cell. To account for Ca^{2+} diffusion, the model must include a diffusion term. It is frequently assumed that Ca^{2+} diffuses with constant diffusion coefficient, D_c , and that the cellular cytoplasm is isotropic and homogeneous. Adding the diffusion term to Equation (1.1), the resulting reaction-diffusion equation for Ca^{2+} is

$$\frac{\partial c}{\partial t} = D_c \nabla^2 c + J_{\text{release}} - J_{\text{serca}} + J_{\text{influx}} - J_{\text{pm}}. \quad (1.3)$$

Below, we briefly review some seminal models of Ca^{2+} signalling. The Goldbeter model [75] is based on CICR from intracellular stores and shows how sustained oscillations of cytosolic Ca^{2+} may arise as a result of a rise in IP_3 , triggered by external stimulation. The model contains only two variables (concentrations of free Ca^{2+} in the cytosol and in the ER) and predicts the occurrence of periodic Ca^{2+} spikes in the absence of IP_3 oscillations, indicating that repetitive Ca^{2+} spikes do not necessarily require the concomitant, periodic variation of IP_3 and can be induced by external stimulation.

The De Young-Keizer model [48] was developed to investigate the properties of the IPR/ Ca^{2+} channel. The rate constants in the equations were tuned to fit kinetic and equilibrium data and it was found that the model successfully reproduced a variety of *in vivo* and *in vitro* experiments [74, 133, 184, 204]. The model incorporates a positive-feedback mechanism of Ca^{2+} on IP_3 production by the PLC pathway. This was noted to enrich the properties of the oscillations and led to Ca^{2+} oscillations accompanied by IP_3 oscillations.

Atri et al [12] constructed two models: an ODE model for Ca^{2+} oscillations and a PDE model for Ca^{2+} waves. The two-variable ODE model expresses oscillations of cytosolic Ca^{2+} and is based on Ca^{2+} release via the IPR/ Ca^{2+} channel. The variables represent cytosolic Ca^{2+} concentration and the percentage of IPRs that have not been inactivated, respectively. The PDE model incorporates IP_3 dynamics by introducing a third variable, cytosolic IP_3 concentration, and adding

diffusion terms for Ca^{2+} and IP_3 . The ODE model exhibits Ca^{2+} oscillations for a constant value of IP_3 concentration and the PDE model produces circular, planar, and spiral waves of Ca^{2+} which annihilate upon collision. Both models reproduce a number of crucial experiments [66, 72, 90, 104, 156].

The Li-Rinzel model [111] reduces the nine-variable De Young-Keizer model to a two-variable system. Similar to the Atri ODE model, the variables represent cytosolic Ca^{2+} concentration and the percentage of IPRs that have not been inactivated. This was achieved by using the method of multiple scales to solve the equations of the De Young-Keizer model on a succession of faster time scales to reduce it to a 2D system. The reduced system is analogous in form to the Hodgkin-Huxley equations for plasma membrane electrical excitability [84].

1.3.2 Cell mechanics

Tissue morphogenesis is an area of great fascination for many applied mathematicians and mathematical biologists. Often involving a large number of cells, this phenomenon poses a significant modelling challenge that requires an interdisciplinary effort from both experimental biologists and mathematical modellers. The models used to study tissue-level deformations can be broadly grouped into two classes:

- Discrete or cell-based models
- Continuum models

Cell-based models are used to capture cell shapes and the interplay of intracellular and intercellular forces within a tissue. They allow for a more detailed description of the cellular and sub-cellular dynamics that influence tissue scale behaviour and can be broadly categorized as on-lattice or off-lattice models. Continuum models coarse-grain such detail to derive a system of PDEs that describe the tissue as a continuum, prioritizing global properties and behaviours.

Cell-based models

- *On-lattice models*: On-lattice models such as cellular automata or cellular Potts restrict the spatial arrangement of the cells to a fixed grid. The mechanical interactions are carried out according to deterministic or stochastic

rules (cellular automata) or by minimizing the total energy of the system (cellular Potts), resulting in cells being displaced from one grid box to another.

- *Off-lattice models:* Off-lattice models allow for the continuous movement of cells in space and evolve the system in time according to force laws governing the mechanical interactions between the individual cells. Examples of off-lattice models are vertex models and centre-based models e.g. node-based models, which can be modelled as overlapping spheres, or mesh-based models, where the cell centres are denoted by mesh points and the polygonal cell area is determined by Voronoi tessellations with respect to the centres of the neighbouring cells.

These models treat cells, or sub-cellular components, as discrete entities and are the natural candidates for studying the regulation of cell-level processes in tissue dynamics. However, they are less amenable to mathematical analysis than continuum models. The precise rules and methods of implementation differ between modelling approaches and must be adapted to suit the requirements of the biological system under study. Five of the most widely used approaches are listed below:

1. *Cellular automata:* Each lattice site (or grid box) can contain at most a single cell (Figure 1.7a). The system is evolved discretely, using a fixed time-stepping or event-driven approach, with the new state of each cell determined using deterministic or stochastic rules and the state of the system at the previous timestep. The computational simplicity of this approach makes it the method of choice for simulating large numbers of cells [107].
2. *Cellular Potts:* Each cell can be represented by several lattice sites, allowing for more realistic cell shapes (Figure 1.7b). The shape of each cell is evolved via some form of energy minimization. Unlike cellular automata, the cellular Potts model can incorporate mechanical processes such as cell membrane tension, cell-cell and cell-substrate adhesion, and cell volume conservation. The cellular Potts model has been used to study biological processes ranging from cell sorting [73] and morphogenesis [93] to tumour growth [180].
3. *Overlapping spheres:* Cells are treated as particles which are free to move in space (Figure 1.7c). The centre of each cell is tracked over time. The

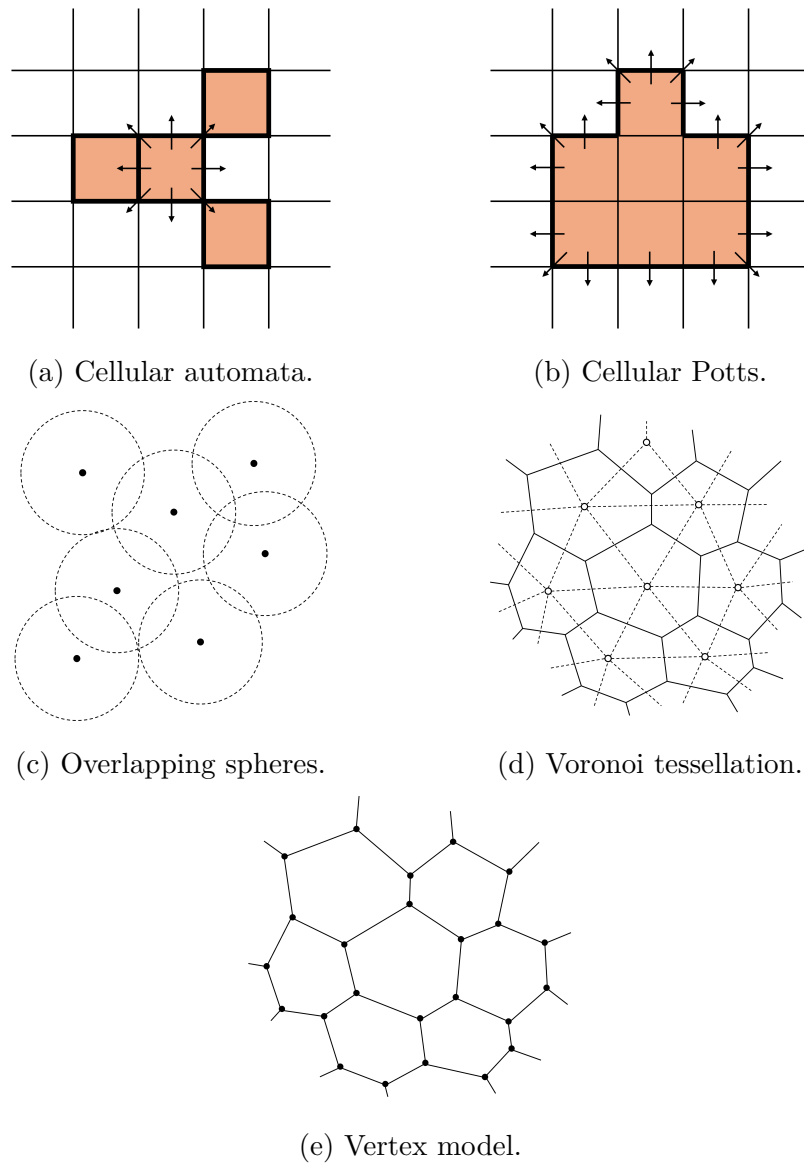


Figure 1.7: Schematics of the five most widely used cell-based models: (a) Cellular automata (on-lattice), (b) Cellular Potts (on-lattice), (c) Overlapping spheres (off-lattice), (d) Voronoi tessellation (off-lattice), and (e) Vertex model (off-lattice).

overlapping spheres approach views cells as spherical in the absence of any interactions but which deform upon cell-cell or cell-substrate contact [50].

4. *Voronoi tessellation*: The shape of each cell is defined to be the set of points in space that are nearer to the centre of the cell than the centres of any other cell (Figure 1.7d); a Delaunay triangulation [15] is performed to connect those cell centres that share a common face, thus determining the neighbours of each cell. In both, overlapping spheres and Voronoi tessellations, Monte Carlo methods [51] or Langevin equations [227] may be used to simulate cell dynamics.
5. *Vertex models*: Each cell is modelled as a polygon, with the edges representing the cell's membrane (Figure 1.7e). Vertex models track the vertices of the polygon and update the position of each vertex according to tensions in the cell membrane, resulting from cell-cell adhesion forces, cell elasticity, compressibility, and cytoskeletal contractility. Additional rules can be implemented to govern cell neighbour rearrangements, growth, mitosis, and cell death. These models are commonly used to describe tightly packed epithelial cell sheets [62].

Continuum models

The continuum description of a tissue can either be conceptualized from first principles or derived from an existing vertex model by coarse-graining. The former method assumes the tissue *ad hoc* as a material of a certain type e.g. porous [100], elastic [63], poroelastic [181], hyperelastic [143], viscoelastic [135], etc. In the latter approach, local dynamics are averaged over the lengths of several cell diameters, disregarding features such as cellular junctions and the density of cellular adhesions and instead treating the tissue as a continuous material, however, many technical challenges lie in deriving a continuum model from a discrete cell model. In both cases, the resulting PDE model of the tissue can be computationally solved using the Finite Element Method [96] or, in some cases, treated by rigorous mathematical analysis [55].

Both cell-based and continuum models have been successfully employed in modelling a broad range of morphogenetic events, such as angiogenesis [135, 207], neurulation [28, 29], tissue invagination [91], dorsal closure [57], and salivary gland

tubulogenesis [56].

The simulations conducted in these studies demonstrate that tissue motions are highly sensitive to the mechanical properties of the constituent cells. These findings suggest that Spina Bifida and other neural tube defects may result from abnormalities in the mechanical processes underlying morphogenesis [29]. It also suggests that modest interventions might be sufficient to prevent neural tube defects [28]. These interventions might involve introducing compounds that regulate gene expression, signalling pathways, or cellular behaviours involved in neural tube formation, aiming to correct any aberrations or deficiencies that could lead to defects.

A key advantage of cell-based models is the ease with which they can be coupled to continuum models [214], as they can be easily modified to incorporate chemical signalling. Vertex and cellular Potts models frequently couple descriptions of morphogen (or nutrient) transport and signalling to cell behaviour [2, 83, 148, 167, 171]. For example, Aegerter-Wilmsen et al. [2] coupled a vertex model of cell proliferation and rearrangement with a differential algebraic equation model for a protein regulatory network to describe the interplay between mechanics and signalling in regulating tissue size in the *Drosophila* wing imaginal disk.

The coupling of the vertex model with chemical signalling is of particular interest to us as it directly links to our aim of developing a mechanochemical model that captures the coupling between cytosolic Ca^{2+} and cellular mechanics during NTC.

After comparing the modelling approaches described above, we decided to develop and explore vertex models as they were deemed best suited to address the modelling requirements outlined in Section 1.2.3.

Since we are interested in studying how changes in cell shape and size impact tissue morphogenesis, our model must be able to resolve individual cells. A continuum model is naturally ill-suited for studying such a problem. Given our focus on dynamic changes in cell shape, both the cellular automata and overlapping spheres modelling approaches would be unsuitable for us. The epithelial cells of the anterior neural plate are tightly packed and resemble polygons (similar to the epithelial cells depicted in Figure 1.8); these shapes are best captured by a Voronoi tessellation or vertex model. A cellular Potts model is more suited to loosely packed cells with unpredictable shapes and would also be more computationally expensive than a Voronoi tessellation or vertex model. Ultimately, we

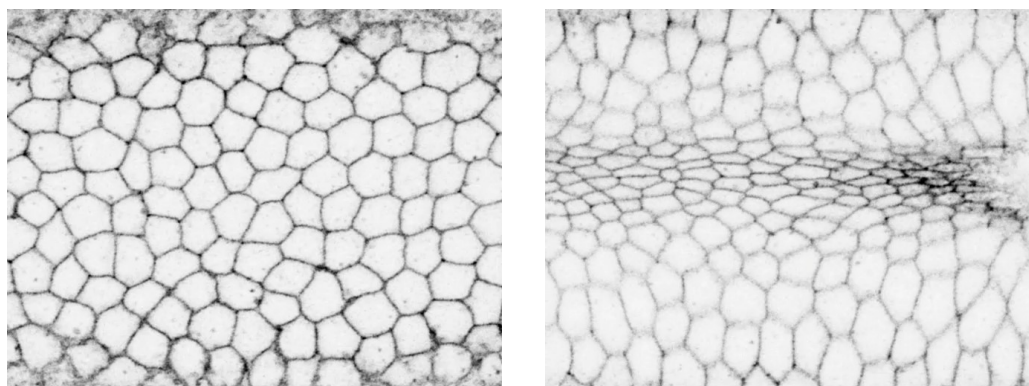
(a) $t = 0s$.(b) $t = 600s$.

Figure 1.8: Snapshots of the ventral epithelium of a *Drosophila* embryo undergoing ventral furrow formation. Source: [186].

decided to choose the vertex model over the Voronoi tessellation model because it is better suited to tightly packed cells and due to its lower computational cost.

1.3.2.1 Vertex models

Originally used to study the physics of foams [108, 203, 216, 217], vertex models have been adapted to model and study epithelial tissues as well. They have been used to great effect in modelling tissue morphogenetic events in a number of biological systems such as: growth regulation in the *Drosophila* wing disc [1], ventral furrow formation in the *Drosophila* embryo [186], amphibian neurulation [29], and notochord morphogenesis in *Xenopus* [220] to name a few.

In a vertex model, a tissue is represented by a collection of non-overlapping connected polygons whose vertices are free to move and each polygon corresponds to a cell, i.e., the tissue is represented as a convex polygonal partitioning of the plane (Figure 1.9). The main simplification, compared to models of foams, is that most implementations of the vertex model of tissues assume that contacts between neighbouring cells are straight lines, whereas in foam modelling, the interfaces between foam cells are curved. However, there have also been several studies where this assumption has been removed and cell-cell junctions were allowed to be curved [92, 157].

Another modelling assumption is that neighbouring cells share a single edge, whereas in real tissues, junctions between two neighbouring cells consist of two

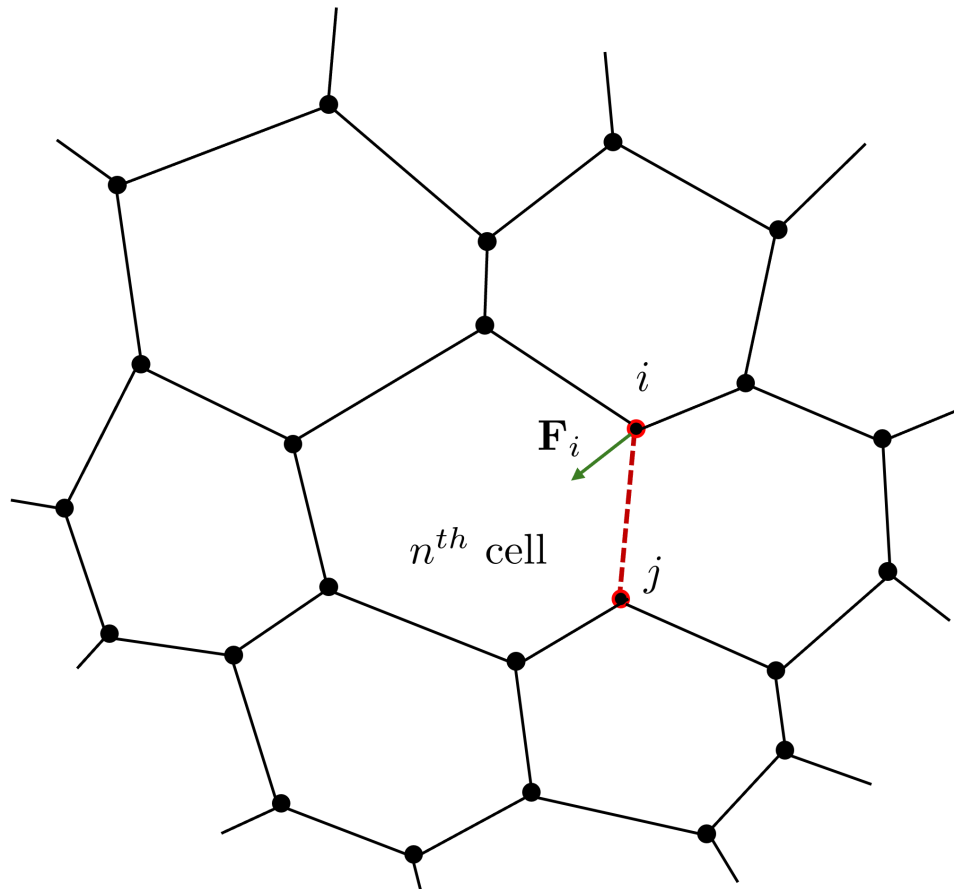


Figure 1.9: The 2D vertex model. The epithelial sheet is represented as a polygonal tiling of the plane with no holes or overlaps. The dots represent nodes, or vertices, and the lines connecting them represent edges. The shape of the n^{th} cell changes when its vertices are displaced as a consequence of the forces acting on them.

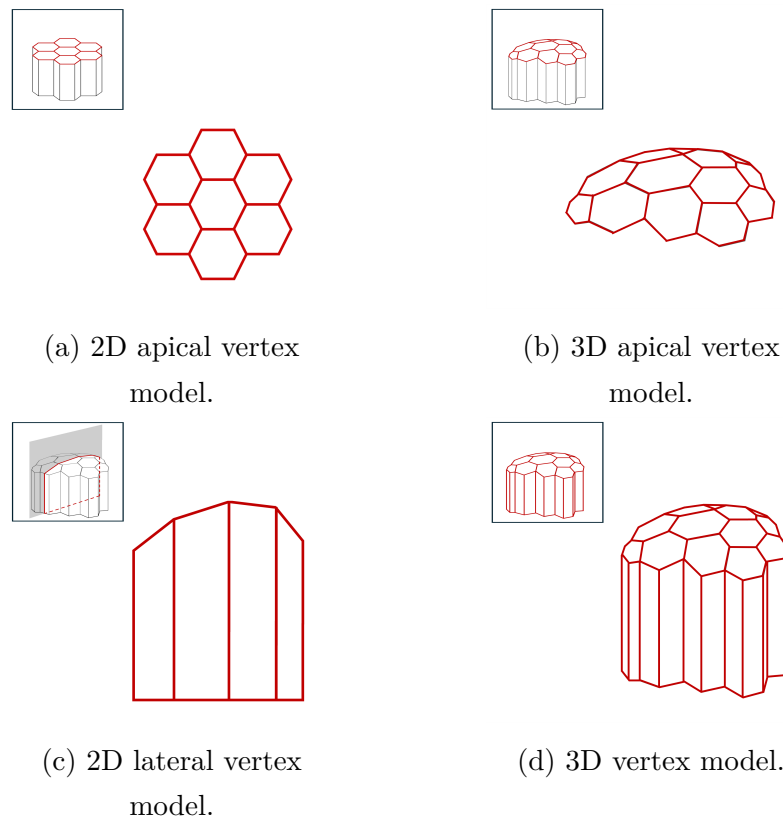


Figure 1.10: Vertex models can be classified into four types, depending on their geometrical representation of tissues: (a) 2D apical vertex model, (b) 3D apical vertex model, (c) 2D lateral vertex model, (d) 3D vertex model.

separate cell membranes that can be independently regulated [187]. In the vertex model, typically, three junction lines meet at a vertex. However, vertices with a higher number of contacts are also possible, e.g., multicellular rosettes, where four or more cells share a common vertex [18]. The model tissue is, therefore, a mesh consisting of polygons (cells), edges (cell junctions), and vertices (meeting points of three or more cells).

Four types of vertex models have been used to study epithelial morphogenesis. They are listed as follows:

1. 2D apical vertex model (Figure 1.10a) - Represents only the apical surface of a cell in a 2D space [3, 62, 138, 167, 189],
2. 3D apical vertex model (Figure 1.10b) - Represents only the apical surface of a cell in a 3D space, allowing for out-of-plane configurations [134, 153, 208],

3. 2D lateral vertex model (Figure 1.10c) - Represents only a cross-section of a tissue [59, 145, 160, 164],
4. 3D vertex model (Figure 1.10d) - Represents the full 3D description of a cell, by modelling the apical surface, basal surface, and lateral faces of the cell [128, 147].

It should be noted that during NTC, the apical surface of the anterior neural plate bends out of the 2D plane. However, based on discussions with our experimental collaborators, Neophytos Christodoulou and Paris Skourides, we decided to describe it using a 2D apical vertex model. We found this approach sufficient to capture the experimentally observed behaviours we were interested in. For the purposes of this work, we aim to develop models that capture: (i) the effect of the deformation of the surface ectoderm on the constricting neural plate [34], and (ii) the two-way coupling between Ca^{2+} signalling and cellular mechanics, along with its impact on NTC.

Moreover, a prior study [196] has already employed a 2D apical vertex model to successfully reproduce key experimental behaviours and offer insights into the effect of Ca^{2+} fluctuations on the rate of NTC. This study will be discussed further in Section 1.3.3 and Chapter 3.

The extension to a 3D apical vertex model or a full 3D vertex model can be explored in future works (Chapter 9). For brevity, we will use the term ‘vertex model’ to refer to the 2D apical vertex model throughout this thesis.

In the vertex model, the vertices are represented by a set of points $\{\mathbf{r}_1, \dots, \mathbf{r}_{N_V}\}$. It is straightforward to express the cell area and the cell perimeter in terms of the vertex coordinates. The vertex positions together with their connectivities uniquely determine the energy of the epithelial sheet, E_{VM} , which can be expressed as:

$$E_{VM}(t) = \sum_{n=1}^{N_{cells}(t)} \left(\alpha_n (A_n - A_n^{(0)})^2 + \beta_n (P_n - P_n^{(0)})^2 \right) + \sum_{\langle i,j \rangle} \Gamma_{\langle i,j \rangle} l_{\langle i,j \rangle}, \quad (1.4)$$

where $N_{cells}(t)$ is the total number of cells at time t , A_n and P_n are the area and perimeter of the n^{th} cell, respectively, and $A_n^{(0)}$ and $P_n^{(0)}$ are the target area and perimeter values of the n^{th} cell. α_n and β_n are the area modulus and perimeter modulus, respectively, with units of energy per area squared and energy per length squared.

The index $\langle i, j \rangle$ in the last term denotes that the sum is over all pairs of vertices that are connected. $\Gamma_{\langle i, j \rangle}$ denotes the interaction energies between two cells through the cell-cell interface, and can take on different values for homotypic and heterotypic interfaces and for ‘boundary’ interfaces between cells and the surrounding medium. $l_{\langle i, j \rangle}$ denotes the length of the cell-cell interface.

In the model, different cells can have different area and perimeter moduli, as well as different target areas and perimeters. This allows for the modelling of tissues consisting of different types of cells.

The first and second terms in the first sum, i.e., the area energy and the perimeter energy, represent the compressibility of the cell and contractility of the cell boundary, respectively. These energy terms depend on factors that determine the cell’s compressibility and contractility, for instance, they could be determined by the cytosolic pressure [115] or the contractile properties of the actomyosin bundles in the cell cortex [58, 62, 154]. It should be noted that the moduli α_n and β_n need not be constant; they may change due to the remodelling of actomyosin bundles [34, 119].

The second sum represents the adhesive forces between neighbouring cells that share a given edge. $\Gamma_{\langle i, j \rangle}$ can take positive and negative values depending on whether the dominating term is surface tension or the adhesive forces at the cell boundary, respectively [69]. The surface tension could be dependent on the force generated by cortical actin contraction (triggered by myosin activity) [119, 196].

If the tissue features cell growth and/or contraction, these could be captured by regulating $A_n^{(0)}$ and $P_n^{(0)}$. For example, during AC, the actin cytoskeleton is reconfigured by the rearrangement of the cortical actin filaments. This causes the cell to contract irreversibly [32, 119, 121], which can be modelled by decreasing $A_n^{(0)}$ and $P_n^{(0)}$ [196].

The main assumption of the vertex model is that the tissue will always be in a configuration which minimises the total energy (Equation (1.4)). Determining the minimum energy configuration is a non-trivial multidimensional optimisation problem and, with the exception of a few very simple cases, it can only be solved

numerically. A basic implementation of the vertex model, therefore, needs to use advanced multidimensional numerical minimisation algorithms to determine the positions of vertices that minimise the total energy for a given set of parameters α_n , β_n , and $\Gamma_{\langle i,j \rangle}$. This approach assumes that the tissue evolves quasistatically, so that the minimum energy of the system is obtained instantaneously between cell rearrangement events [62].

In the quasistatic approach, the tissue is assumed to relax instantly to the closest mechanical equilibrium state after each perturbation of the tissue (which could be caused by cell division, cell death, or cell-cell intercalation [62]). The relaxation to the closest mechanical equilibrium state can be implemented using high-dimensional minimization methods, such as the conjugate gradient method [8]. The system evolves through a sequence of equilibrium configurations, which always results in a net zero force on the vertices at each iteration. While this approach is suitable for studying some problems, it is unable to fully describe effects that are inherently related to being out of equilibrium, such as dorsal closure, convergent extension, and AC.

During AC, actin filaments and myosin motors undergo constant assembly and disassembly in response to signalling pathways, leading to continuous remodelling of the cytoskeleton and dynamic changes in cellular morphology [121]. This dynamic remodelling is essential for processes such as NTC, where cells undergo coordinated contraction to alter tissue shape and structure.

Since we aim to capture the temporal evolution of the shape of the tissue and the constituent cells during AC, the quasistatic approach is clearly unsuitable for us. To introduce dynamics into the vertex model [68, 86, 219], force balance is applied on each vertex to derive its equation of motion, making the standard assumption that inertial terms are small compared to dissipative terms (as cells move in dissipative environments with very small Reynolds number [162]).

Since the cells are tightly packed, the stochastic motion of individual vertices is dominated by strong cell-cell coupling forces and cytoskeletal forces alike. Within the cell, there can be multiple mechanisms for dampening vertex motion, including viscous forces, actomyosin stiffness, and cell-cell or cell-ECM adhesions. For simplicity, these effects are commonly combined into a single ‘viscosity’ parameter, i.e., the damping coefficient η . We assume that the damping force is proportional to the vertex velocity, with coefficient η .

The force on the i^{th} vertex is derived from the energy function (Equation (1.4)),

which is balanced with a viscous drag term, leading to a first-order equation of motion

$$\eta \frac{d\mathbf{r}_i}{dt} = -\frac{\partial E_{VM}(t)}{\partial \mathbf{r}_i} = \mathbf{F}_i(t), \quad (1.5)$$

where η is a damping coefficient, \mathbf{r}_i is the position vector of the i^{th} vertex, and $\mathbf{F}_i(t)$ is the total force acting on vertex i at time t which is assumed to equal the sum of all forces coming from the cell area and perimeter elasticities and from the connections with all neighbouring vertices $j \in \mathcal{N}_i(t)$ adjacent to i at that time.

From the above, it is clear that the expression for the force is local, i.e., computing the force does not require including cells and vertices beyond the immediate neighbourhood of a given vertex. This is extremely beneficial from a computational standpoint as one can readily utilise standard force cut-off techniques, such as cell and neighbour lists [6], in order to speed up force computations.

Numerical methods should be selected to ensure convergence and accuracy. In many studies, the forward Euler method is preferred due to its low computational cost, high speed, and because it satisfies the convergence and accuracy requirements of the implemented model [68, 69, 150]. Equation (1.5) can be solved numerically using a simple forward Euler method with sufficiently small timestep, δt , to ensure numerical stability:

$$\mathbf{r}_i(t + \delta t) = \mathbf{r}_i(t) + \frac{\delta t}{\eta} \mathbf{F}_i(t). \quad (1.6)$$

Higher-order explicit (or implicit) methods are more computationally intensive, and require modifications to account for cell death and division changing the size of the dynamical system over each time step, but could allow larger time steps to be used while maintaining stability [13]. In Chapter 6, we compare the forward Euler method with a second-order predictor-corrector method in terms of convergence and computational speed.

In addition to incorporating dynamics, a number of implementations of the vertex model [44, 68, 187] introduce topology (connectivity) changing moves to manage events such as cell edge rearrangement (T1 swap), cell removal (T2 swap),

vertex-edge intersection (T3 swap), cell concavity (node switch), mitosis, and cell death. However, as these events do not occur concomitantly with AC during NTC [32, 34], we do not incorporate them into our models.

1.3.3 Coupling of Ca^{2+} signalling and mechanics

In Section 1.3.1, we reviewed some seminal models of Ca^{2+} signalling. In Section 1.3.2, we presented the most frequently used mechanical modelling frameworks for cell and tissue modelling. Since we are interested in the interplay of Ca^{2+} signalling and mechanics, in this section, we will review a few mechanochemical models that combine Ca^{2+} signalling and cell and tissue mechanics.

Narciso et al [140] studied the relationship between the spatiotemporal properties of Ca^{2+} transients and the mechanical characteristics of the *Drosophila* wing disc by adapting the Atri model [12] for Ca^{2+} waves. The Atri model was originally developed for intracellular Ca^{2+} dynamics. To study intercellular Ca^{2+} dynamics, Narciso et al [140] incorporated the passage of Ca^{2+} and IP_3 into neighbouring cells via gap junctions [222] into the model. Their model demonstrated that intercellular Ca^{2+} transients follow lines of mechanical tension and, in doing so, reflect the mechanical state of the underlying tissue.

The ODE model developed by Kaouri et al [95] builds on early continuum models that couple Ca^{2+} dynamics to the cell mechanics and replaces the hypothetical bistable Ca^{2+} release [135, 136, 137, 152] with the modern, experimentally validated IP_3 -mediated Ca^{2+} dynamics of the Atri model [12]. In this model, embryonic cells and tissue are assumed to behave as a linear, viscoelastic material. A novel contribution of this work is that it expresses the ‘stretch-activation’ Ca^{2+} flux in the early mechanochemical models as a bottom-up contribution from SSCs [11, 54, 78, 131] on the cell membrane (Section 1.2.3). The Ca^{2+} -induced contraction stress is modelled with a Hill function, assuming that the mechanical responsiveness of the cytosol to Ca^{2+} saturates for high Ca^{2+} levels. This model demonstrates that mechanical effects can cause Ca^{2+} oscillations to vanish (implying information loss), resulting in the failure of key processes during embryogenesis, like AC.

In a later study, Kaouri et al [96] extended their previous model [95] to two spatial dimensions to study anterior neural plate morphogenesis during the AC phase of NTC. The governing equations consist of an advection-diffusion-reaction

system for Ca^{2+} concentration which is coupled to a force balance equation for the tissue. The experimentally observed asynchronous Ca^{2+} flashes [33, 196] are implemented as a random distribution of Ca^{2+} ‘sparks’ in the model. Their simulations reproduce important experimental features, such as the spatiotemporal correlation between Ca^{2+} transients and tissue deformation and the monotonic reduction of the apical surface area of the anterior neural plate.

Since it is a continuum model, however, it is unable to resolve individual cells and capture crucial cell-level behaviours. As the model cannot implement cell boundaries, Ca^{2+} waves freely diffuse over multiple cells. However, experiments have established that Ca^{2+} transients from one cell cannot propagate to another [33]. Additionally, the model fails to capture the ‘pulsed’ cell contractions, which are a characteristic feature of AC [121].

Suzuki et al [196] developed a mechanochemical vertex model to investigate the impact of different types of Ca^{2+} transients on AC during NTC in the *Xenopus* neural plate. The behaviour of their model was found to be in agreement with their experimental observations [196]. For instance, in their model, a considerable relaxation event follows the Ca^{2+} -induced contractions of apical cell surface area and perimeter, and the simulated Ca^{2+} transients accelerate AC. Furthermore, their model suggests that spatially and temporally random Ca^{2+} transients at the single-cell level are able to reduce the overall tissue size more effectively than multicellular Ca^{2+} transients.

Despite its successes, however, their model has some significant limitations. For instance, in the model, a Ca^{2+} transient triggers cell contraction immediately, whereas in reality, a Ca^{2+} transient *precedes* cell contraction [33, 95, 196], i.e., there is a latency between the occurrence of a Ca^{2+} transient and the onset of cell contraction. Moreover, the model fails to incorporate the increasing frequency and amplitude of Ca^{2+} transients, which have been observed in experiments [32, 95]. The model also does not account for the two-way feedback between Ca^{2+} and cell mechanics since cell contractions do not have any effect on Ca^{2+} flashes in the model. Lastly, the model does not consider the surface ectoderm, a crucial structure in the developing embryo. During AC, the contraction of the apical surface of the anterior neural plate exerts a force on the cells of the surface ectoderm, deforming and displacing them. Consequently, the cells of the surface ectoderm exert a resistive force on the anterior neural plate, influencing morphogenesis during NTC [34].

The AC phase of NTC takes approximately 40 to 60 minutes. To ensure the successful completion of NTC, the apical surface of the anterior neural plate must contract to within 2% to 8% of its initial area within this timeframe [32, 34]. However, to date, no model of NTC [96, 196] has demonstrated this key behaviour.

In this work, therefore, we aim to develop new mechanochemical vertex models that will address these limitations.

As far as we are aware, the Suzuki et al [196] model is the only mechanochemical vertex model that incorporates Ca^{2+} signalling, making it an excellent foundation from which to start developing our models. Therefore, we will review their experimental results in Chapter 2 and conduct a detailed review and critical analysis of their model and simulation results in Chapter 3.

1.4 Aims and objectives

As live-cell imaging of the apical surface of the anterior neural plate is challenging due to AC occurring in the final stages of NTC, when the neural plate is highly folded, it is essential to develop an accurate mathematical model. This model can enable the computational study of phenomena that cannot be investigated *in vivo*.

The primary aim of this doctoral thesis is to develop mechanochemical vertex models of the anterior neural plate based on the data available from experiments. These models aim to capture the coupling between Ca^{2+} signalling and cellular mechanics, reproducing a variety of experimentally observed behaviours *in silico*.

As it is difficult to study vertex models analytically, except for very simple cases, we must explore their behaviour computationally. Currently, there are limited software packages designed for vertex models. Additionally, implementing new model features in the existing software packages can be challenging, making them less conducive to the development of new models. So, we opted to develop our own software package, providing us with greater convenience for testing and modifying our models by incorporating desired features.

In line with the motivations outlined above, we set the following objectives for this doctoral study:

1. Develop a software package, optimised to carry out parameter sweeps, for vertex models.

2. Revise the modelling assumptions of Suzuki et al [196] to create a model that better reflects the biology and has a simpler structure. We refer to this model as the modified Suzuki model.
3. Implement the modified Suzuki model using the created software and validate the simulation results by comparing them with the results of Suzuki et al [196]. This serves as a form of validation for both our software package and the modified Suzuki model.
4. Derive a bifurcation diagram for the modified Suzuki model by performing single-cell analysis for a structurally simple tissue - a hexagonal lattice.
5. Conduct a parameter sweep for the modified Suzuki model to investigate the effects of various parameters on both the final tissue area and the time taken to reach the final area.
6. Develop a new mechanochemical vertex model drawing on insights from the bifurcation diagram and the results obtained through the parameter sweep. The model should address the limitations of the Suzuki et al [196] model, highlighted in Section 1.3.3. Since this model only captures the effect of Ca^{2+} on cellular mechanics and not vice versa, we refer to it as the one-way coupling model or the one-way model.
7. Develop a new mechanochemical vertex model that incorporates the two-way coupling between Ca^{2+} and cellular mechanics and reproduces all the behaviours captured by the one-way coupling model. We refer to this model as the two-way coupling model or the two-way model.
8. Propose new hypotheses and potential directions for future experiments on the basis of the simulation results from both the one-way and two-way models.

Our model-building approach in this thesis involves building up complexity sequentially. We first construct the one-way model as an important intermediate step towards building the two-way model, to study the effect of Ca^{2+} on cell mechanics and tissue behaviour; this offers valuable insights for the development of the two-way model.

In the two-way model, the effect of Ca^{2+} on cell mechanics is modelled in the same manner as the one-way model. Additionally, we incorporate the effect of

cell mechanics on Ca^{2+} signalling. To capture this feedback, we assume that stretching a cell induces a Ca^{2+} flash through stretch-sensitive Ca^{2+} channels that sense the mechanical deformation.

Although the two-way model supersedes the one-way model, the latter is very useful for studying the effect of Ca^{2+} on cell mechanics in the absence of the two-way coupling. For example, a future study aiming to incorporate more sophisticated Ca^{2+} dynamics, such as IP_3 -mediated Ca^{2+} dynamics, into the two-way model could begin by first integrating these dynamics into the one-way model. Insights gained from this preliminary step could then be used to inform modifications to the one-way model, which could subsequently be implemented in the two-way model.

1.5 Thesis overview

In the initial chapters (Chapters 1, 2, 3), we conduct an extensive literature review. Subsequent chapters (Chapter 4 onwards) are devoted to fulfilling the objectives outlined in Section 1.4 sequentially.

In Chapter 1, we introduce the biological challenge that motivates the work undertaken in this doctoral thesis, summarises key developments in Ca^{2+} signalling with emphasis on the interplay of Ca^{2+} signalling and mechanics in embryogenesis, and review a few key mathematical models which have been used to simulate these processes *in silico*.

In Chapter 2, we present the experimental findings of Christodoulou and Skourides [33] as well as Suzuki et al [196]. We summarize the behaviours exhibited by the constricting anterior neural plate during the AC phase of NTC since the primary aim of this doctoral work is to develop mathematical models capable of reproducing these observed behaviours *in silico*.

In Chapter 3, we provide a detailed description of the 2D mechanochemical vertex model developed by Suzuki et al [196], which we refer to as the Suzuki model. We conclude this chapter with a critical analysis of their simulation results, highlighting the necessity of developing new mechanochemical vertex models of AC during NTC. We use the Suzuki model as a foundation to develop new models in Chapters 7 and 8.

In Chapter 4, we compare some of the available computational tools for cell-based modelling and introduce CelluLink, a new software package for vertex mod-

els. We first explore the algorithm underlying CelluLink and then provide an overview of its key features and functions.

In Chapter 5, we revise the modelling assumptions of the Suzuki model to create the modified Suzuki model. We then simulate the modified Suzuki model in CelluLink and compare its behaviour to the Suzuki model. Additionally, we analytically derive a bifurcation diagram for the modified Suzuki model and conduct a systematic parameter sweep to numerically investigate the parameter sensitivity of the modified Suzuki model.

In Chapter 6, we compare the performance of the two numerical schemes currently available in CelluLink: the forward Euler method and a predictor-corrector method based on an Euler/trapezoidal pair. Based on the results of this comparison, we adopt the forward Euler method for the simulations in subsequent chapters due to its higher speed and lower computational cost.

In Chapter 7, we develop a new 2D mechanochemical vertex model for the constriction of the apical surface of the anterior neural plate during the AC phase of NTC. Starting with the modified Suzuki model as a foundation, we incorporate the surface ectoderm and make progressive modifications to facilitate the contraction of the anterior neural plate despite the resistive force exerted by the surface ectoderm. We then incorporate frequency and amplitude profiles for Ca^{2+} flashes into the model, based on the experimental data provided in Chapter 2. Since this model only captures the effect of Ca^{2+} on cellular mechanics and not vice versa, we refer to it as the one-way model.

In Chapter 8, we extend the one-way model by incorporating the experimentally validated ‘stretch activation’ mechanism into the behaviour of the neural plate cells, creating a new model. Since this model captures the bilateral feedback or two-way mechanochemical coupling between Ca^{2+} flashes and cellular mechanics, we refer to it as the two-way model.

In Chapter 9, we summarize the outcomes of this doctoral work, present our conclusions, and suggest potential avenues for future work.

Chapter 2

Experimental results on the role of Ca^{2+} in NTC

Under basal conditions, intracellular Ca^{2+} concentration in the neuroepithelial cells is maintained at a low level and increased transiently (i.e., a Ca^{2+} ‘flash’) by Ca^{2+} influx through membrane-localized Ca^{2+} channels or by a release of Ca^{2+} from the endoplasmic reticulum (ER) via IP_3 -receptor channels [37]. Inhibiting Ca^{2+} influx causes neural tube closure (NTC) to fail due to insufficient folding of the neural plate [106, 182], whereas inducing an increase in intracellular Ca^{2+} promotes the folding of the neural plate [65, 132]. However, prolonged elevation of intracellular Ca^{2+} causes improper folding, resulting in the failure of NTC [33]. Since these morphological changes at the tissue level are accompanied by changes in the shapes of the constituent cells, it has long been proposed that intracellular Ca^{2+} signalling and its coupling with mechanics regulates apical constriction (AC).

The papers by Christodoulou and Skourides [33, 34] and Suzuki et al [196] investigate this relationship between Ca^{2+} and changes in cell shape in the context of embryogenesis. These works are of particular importance to us because they study the role played by Ca^{2+} in reshaping the cells undergoing AC during NTC.

This chapter summarizes the findings of the aforementioned papers and highlights key aspects of the behaviour of intracellular Ca^{2+} , along with the corresponding changes in cell and tissue shape, observed during NTC. The new mathematical models developed in this doctoral work (Chapters 7 and 8) aim to reproduce these behaviours *in silico*.

2.1 Christodoulou and Skourides

Christodoulou and Skourides' study [33] of Ca^{2+} flashes during NTC is of vital importance for this doctoral work because that is precisely the phenomenon we are trying to model. In this work, they allow *Xenopus laevis* embryos to develop to Stage 14 and then image the neural plate (via confocal microscopy and fluorescence microscopy) during NTC. They use live imaging data combined with gain- and loss-of-function approaches to study AC during neurulation. Their findings are described below.

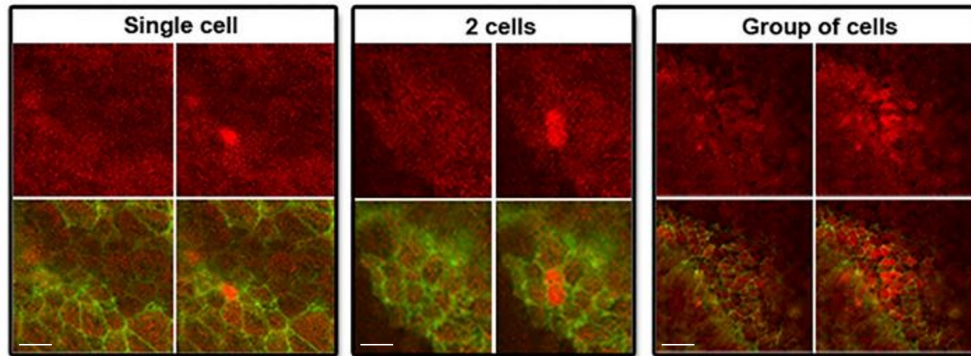
Over the course of AC during NTC, a subset of cells in the neural plate experience cell-autonomous and asynchronous contraction pulses, which are driven by transient apical actin polymerization events. Ca^{2+} flashes are seen to occur just before the narrowing of the apical cell surface and accumulation of apical actin¹, suggesting that they trigger the contraction pulses probably by inducing apical actin polymerization and/or contraction. AC during NTC occurs in a stepwise fashion, where the surface area of individual cells is initially reduced (contraction pulse), followed by a slight increase and stabilization (stabilization step).

They observe that the surface areas of small regions within the neural plate that do not display contraction pulses also decrease over time. Based on the results of their analysis, they suggest that surface area reduction in the absence of apical actin-driven AC stems from mediolateral junction shrinkage.

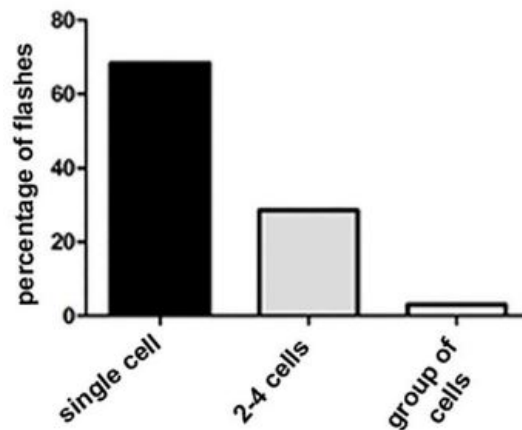
So, both mediolateral cell junction shrinkage and cell-autonomous and asynchronous contraction pulses occur simultaneously during NTC and contribute to the overall reduction of apical cell surface area in the neural plate.

The majority of the Ca^{2+} flashes during NTC are cell autonomous and asynchronous, similar to the contraction pulses and apical actin enrichment events described above. However, synchronized Ca^{2+} flashes are also present but they occur with lower frequency, either in small groups of two to five neighbouring cells or in larger groups of cells (Figure 2.1). The Ca^{2+} flashes are restricted to the neuroepithelium and their frequency is higher in regions like the neural folds, where cells display the highest apical cell surface area reduction. The typical Ca^{2+} flash is short lived ($\approx 40\text{s}$) and the frequency of Ca^{2+} flashes increases gradually as NTC progresses faster, becoming extremely frequent during the late stages

¹Apical actin enrichment was found to occur within one minute after a Ca^{2+} flash and never before or during a Ca^{2+} flash [33].



(a) Types of Ca^{2+} signalling patterns seen during NTC.



(b) Quantification of the different types of Ca^{2+} signalling patterns.

Figure 2.1: Figure 2.1a visualises the different types of Ca^{2+} signalling patterns seen during NTC: (i) single-cell Ca^{2+} transients (scale bar: $50\mu\text{m}$), (ii) Ca^{2+} transients over 2-4 cells (scale bar: $50\mu\text{m}$), and (iii) Ca^{2+} transients over a group of cells (scale bar: $100\mu\text{m}$). Cell cortices are tracked using mem-GFP (green) and Ca^{2+} levels are tracked using GECO-RED (red). For each case, the images in the top and bottom rows show the tissue without and with mem-GFP expression, respectively. The left and right columns show the tissue before and after the occurrence of Ca^{2+} flashes, respectively. The data for Figure 2.1b was recorded using 150 Ca^{2+} events taken from 3 embryos undergoing NTC. Source: [33].

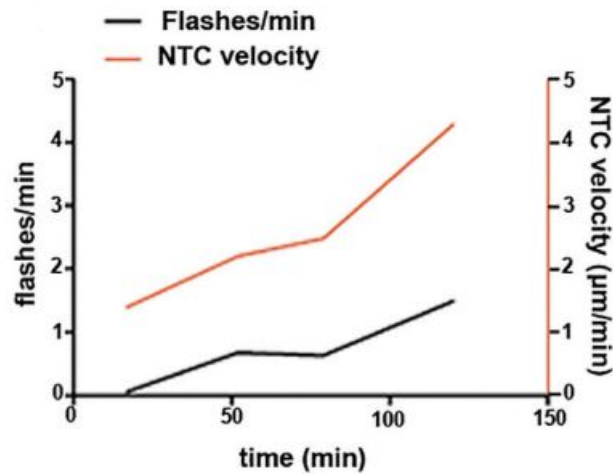


Figure 2.2: Frequency of Ca^{2+} flashes and NTC velocity over time during NTC. NTC velocity is measured as the speed at which the periphery of the tissue, i.e. the neural plate, moves towards the centre of the tissue. Source: [33].

(Figure 2.2 & 2.7) i.e. the frequency of the Ca^{2+} flashes generated during NTC correlates with the rate at which NTC occurs.

The constricting cells are not only able to contain Ca^{2+} transients without depolarizing neighbouring cells but they also do not respond to the Ca^{2+} elevation of their neighbours. Christodoulou and Skourides suggest that this is because the gap junctions² close transiently upon detecting an elevated level of intracellular Ca^{2+} [151] and prevent the propagation of Ca^{2+} to neighbouring cells, enabling cell-autonomous intracellular Ca^{2+} flashes. Thus, cell autonomy is achieved through the isolation of constricting cells from the surrounding tissue.

Cytosolic Ca^{2+} levels are linked with the rate of constriction and the pulsed asynchrony displayed by cells undergoing AC stems from the asynchronous and cell-autonomous Ca^{2+} transients. It was found that the pharmacological elevation of cytosolic Ca^{2+} levels led to higher rates of AC due to synchronous and continuous cellular contractions. However, the elevated rate of AC causes the failure of NTC, suggesting that asynchronous and cell-autonomous pulsed contractions are essential for the correct spatial and temporal distribution of the constriction and, consequently, the correct morphogenesis of the neural tube.

²**Gap junctions** Specialized low-resistance intercellular channels that are responsible for the propagation of tissue-level Ca^{2+} waves [110].

To summarize, their data suggests that the contraction events are triggered by cell-autonomous Ca^{2+} flashes and the imaging of actin dynamics reveals that the contraction pulses are driven by the contraction of a transient apical actin network. Additionally, they provide evidence that the cell autonomy and asynchrony of contraction are required for the correct spatial distribution of constriction and, as a result, are critical for tissue morphogenesis.

2.2 Suzuki et al

Most works on AC are either experimental studies [33, 120] or explorations of mathematical models [68, 95, 134, 186]. The 2017 article by Suzuki et al [196] sets itself apart by presenting experiments and a mathematical model. The objective of their study was to investigate the role of intracellular Ca^{2+} signalling during NTC in the *Xenopus* embryo (Figure 2.3).

Changes in intracellular Ca^{2+} concentration have been observed during development in several organisms, including *Xenopus* [89, 105, 118, 179, 215]. Therefore, Suzuki et al hypothesised that Ca^{2+} signalling correlates to cellular morphogenesis, spatially and temporally. To test this hypothesis, they investigated intracellular Ca^{2+} patterns during NTC using live cell-imaging analysis via spinning-disc confocal microscopy and fluorescence microscopy.

The Ca^{2+} signals were observed to occur in the neural plate rather than in the non-neural surface ectoderm³. It should be noted that, although the surface ectoderm does not experience any Ca^{2+} activity, it significantly impacts neural plate morphogenesis. The surface ectoderm cells are stretched and displaced due to neural plate contraction, and in turn, exert a resistive force on the neural plate, influencing morphogenesis during NTC [34].

Spatially, two types of Ca^{2+} signals were observed in the neural plate; the first signal was at the single-cell level and lasted less than 40s and the other originated from one or a few cells and propagated radially, in a wavelike manner, over the neighbouring cells. The range of propagation of these multicellular waves could vary from a few cells to hundreds of cells, and they could last up to 100s. Also, waves having a larger range of propagation were noted to spread at higher speeds.

³**Surface ectoderm** A structure consisting of layers of cells that lies lateral to the neural plate. It plays a key role in the development of the skin and certain parts of the nervous system in the early embryo.

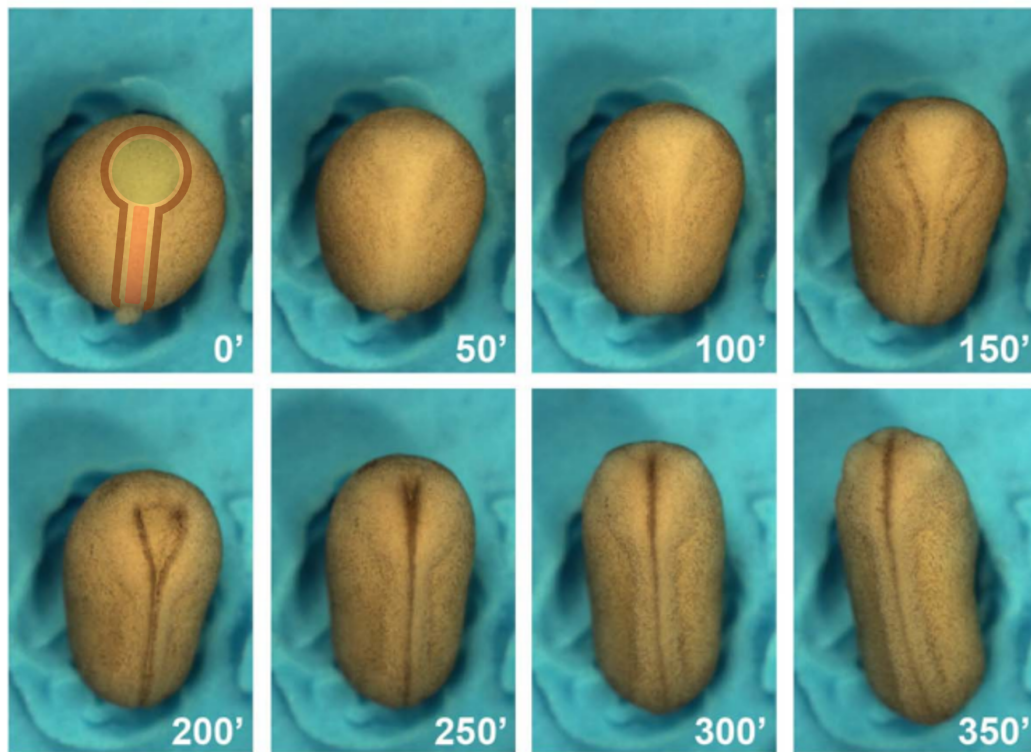
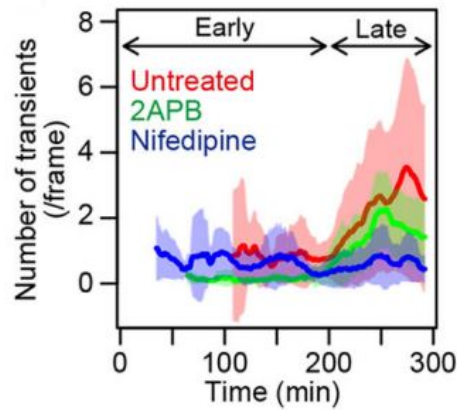


Figure 2.3: Time-lapse imaging data of a *Xenopus laevis* embryo undergoing NTC (dorsal view). The elapsed time (minutes) is shown at the bottom right of each panel. The shaded regions in the top left image demarcate the anterior neural plate (green), posterior neural plate (red), and the surface ectoderm (brown). Source: [196].

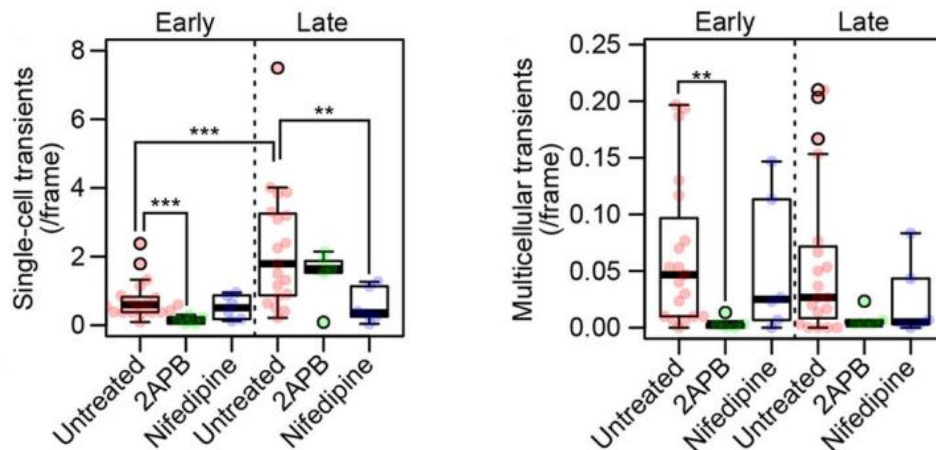
This result validates the observation made in Christodoulou and Skourides [33].

Upon quantifying the number of Ca^{2+} transients, it was found that the number of single-cell transients increased significantly in the last 100 minutes before NTC was completed, such that the number of multicellular transients was an order of magnitude smaller than that of single-cell transients throughout NTC. Based on this, the NTC process was divided into an early and a late phase (Figure 2.4).

The pharmacological agents 2APB and nifedipine block IP_3 -mediated and voltage dependent Ca^{2+} channels, respectively. Examination of their effects on Ca^{2+} fluctuations revealed that the IP_3R pathway regulates both types of Ca^{2+} transients, whereas voltage-dependent Ca^{2+} channels primarily regulate single-cell transients (Figure 2.4).



(a) Number of Ca^{2+} transients during NTC (data points averaged over 20s intervals).



(b) Number of single-cell Ca^{2+} transients in the early and late phases of NTC.

(c) Number of multicellular Ca^{2+} transients in the early and late phases of NTC.

Figure 2.4: Number of Ca^{2+} transients in the neural plate over the course of NTC: (a) the mean number of Ca^{2+} transients during NTC (the smoothed curves represent the mean values taken over 20s intervals, the shaded area indicates the standard deviation), (b) the number of single-cell Ca^{2+} transients in the early and late phases of NTC, (c) the number of multicellular Ca^{2+} transients in the early and late phases of NTC. Source: [196].

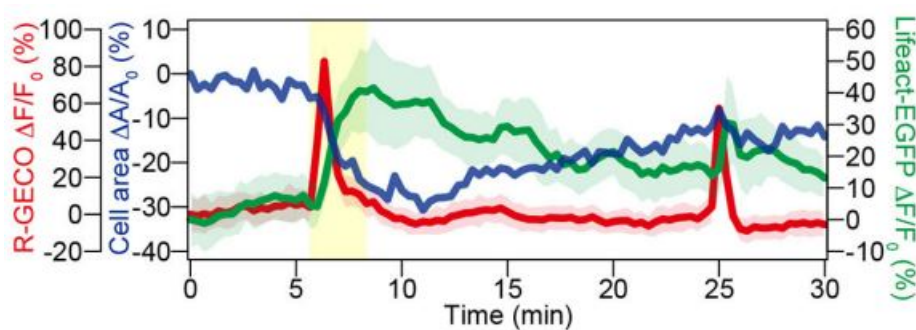


Figure 2.5: Temporal profiles of the mean fluorescent intensities of R-GECO (red), Lifeact-EGFP (green), and relative change in apical area (blue) of a single cell during NTC. The intensities of R-GECO and Lifeact-EGFP measure cytosolic Ca^{2+} concentration and F-actin distribution, respectively. In response to an increase in the Ca^{2+} level, the apical surface area of the cell decreases rapidly. Simultaneously, the F-actin level in the cell cortex increases. Even after Ca^{2+} drops to basal levels, F-actin levels remain high, preventing the cell from relaxing to its original area. Source: [196].

Overall, they showed that single-cell Ca^{2+} transients were more frequent in the late phase than in the early phase of NTC, whereas the spatial scale (range of propagation) of the Ca^{2+} transients was larger in the early phase than in the late phase. These results suggest that the effect of Ca^{2+} fluctuations on NTC was derived from both single-cell and multicellular transients in the early phase, but mostly from single-cell transients in the late phase.

Similar to Christodoulou and Skourides [33], Suzuki et al observed that mesh-like F-actin structures developed in the center of the cell immediately following a Ca^{2+} transient. The actin structures were maintained for several minutes, even after Ca^{2+} concentration had dropped back to basal levels within a few tens of seconds. Furthermore, the surface area of the cell decreased rapidly (contraction pulse) and then stabilized within a minute (stabilization step) after the occurrence of a Ca^{2+} transient (Figure 2.5), which was also observed in [33].

Based on this, Suzuki et al suggest that the rapid activation and prolonged F-actin remodelling induced by Ca^{2+} may be the mechanism of AC and NTC by which relaxation to the original state (i.e. before Ca^{2+} transients occurred) is suppressed [196]. This behaviour is captured by the ratchet-like mechanism,

which will be explored in Section 3.1.4. These experimental results indicate that the Ca^{2+} fluctuations effectuate a decrease in the total apical area of the neural plate by regulating the localization of F-actin which, in turn, is involved in regulating both cell properties and mechanical processes.

To sum up, Suzuki et al showed that: (i) the occurrence of a Ca^{2+} transient is followed by cell contraction and; (ii) two types of active Ca^{2+} signalling patterns - single-cell transients and multicellular waves, modulate AC via cortical F-actin remodelling, thereby contributing differently to NTC. Their experimental results were in line with the findings of Christodoulou and Skourides [33].

2.3 Summary

Based on the findings of Christodoulou and Skourides [33, 34] and Suzuki et al [196], the characteristic behaviours observed in the neural plate during the AC phase of NTC have been summarized below. The mathematical models in the following chapters shall attempt to capture these behaviours and reproduce them *in silico*.

- The cells of the anterior neural plate experience cell-autonomous and asynchronous Ca^{2+} flashes that drive AC during NTC.
- In addition to the single-cell Ca^{2+} flashes, Ca^{2+} waves that propagate over groups of cells are also observed during NTC, but they occur more infrequently compared to the single-cell flashes.
- The amplitude and frequency of Ca^{2+} flashes increases gradually over the course of NTC.
- The occurrence of a Ca^{2+} flash is followed by cellular contraction.
- Each individual cell contracts in a pulsed manner, whereas the tissue contracts monotonically without any recovery phases.
- Cell-autonomy and the asynchrony of Ca^{2+} flashes are necessary for successful NTC; conversely, continuous and synchronized contractions lead to the failure of NTC.
- The contraction of the anterior neural plate stretches the surface ectoderm, which, in turn, exerts a force opposing the contraction of the neural plate.

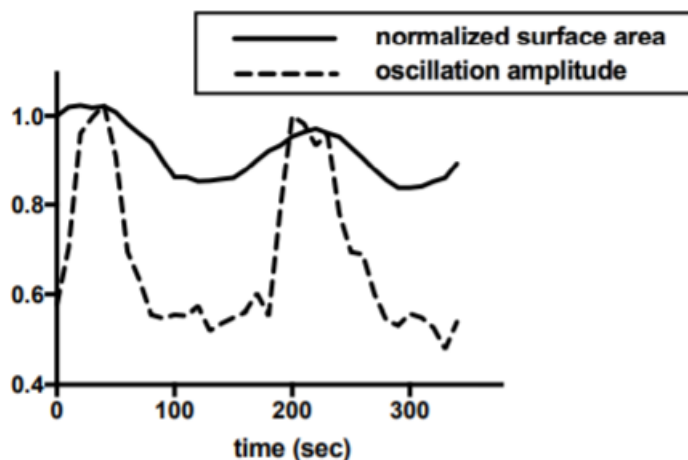


Figure 2.6: Normalised Ca^{2+} oscillation amplitude (measured in a.u. or arbitrary units) and normalised apical surface area (measured in a.u.) of a single cell during AC. The Ca^{2+} oscillation amplitude, representing cytosolic Ca^{2+} concentration, was measured using the fluorescence intensity of the non-ratiometric Ca^{2+} sensor (GECO-RED). For normalization, all values were divided by the highest intensity value. To normalise the surface area, all the area values (measured in μm^2) were divided by the largest area value. Source: [95].

- The AC phase of NTC takes approximately 40 to 60 minutes, during which the apical surface of the anterior neural plate contracts to within 2% to 8% of its initial area.

Figure 2.6 shows the effect of a Ca^{2+} transient on the area of a single cell on the apical side of the neural plate. Ca^{2+} elevation always precedes the initiation of a contraction pulse. At $t = 0\text{s}$, Ca^{2+} begins to rise and, at $t \approx 50\text{s}$, the area starts decreasing. The area reduction is followed by relaxation and stabilization of the cell at a smaller surface area i.e. the cell can not recover its original size. This pulsed contraction is only observed for individual cells, the tissue on the whole contracts monotonically without any recovery phases [32, 33, 196]. The image is from Kaouri et al [95], based on the experiments of Christodoulou and Skourides [33], and validates the observations of Suzuki et al [196].

Figure 2.7 shows that the reduction in cell surface area corresponds to an increase in Ca^{2+} oscillation frequency. The data was taken from 10 cells on the apical surface of the neural plate. The surface area of each cell and average

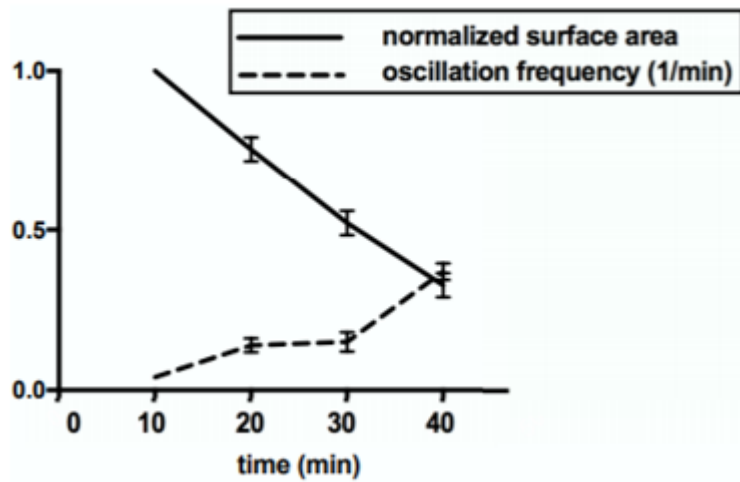


Figure 2.7: Mean Ca^{2+} oscillation frequency (measured in min^{-1}) and mean normalised apical surface area (measured in a.u.) measured over 10 cells on the apical surface of the neural plate. Ca^{2+} oscillation frequency increases over time during AC and this increasing frequency correlates to a reduction in apical surface area. The average surface area of each cell was evaluated for four time intervals; 0-10, 10-20, 20-30, and 30-40 minutes. For normalization, for each cell, the average surface area in each time period was divided by the average surface area of the first period (0-10 minutes). The Ca^{2+} oscillation frequency in each cell was calculated by counting the number of Ca^{2+} oscillations in each time interval. This value was then divided by 10 since there are 10 minutes in each time interval. Source: [95].

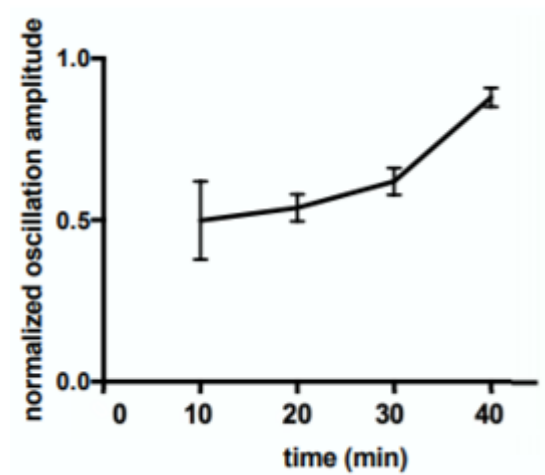


Figure 2.8: Mean Ca^{2+} oscillation amplitude (measured in a.u.) increases over time during AC (measured over the same 10 cells as in Figure 2.7). The Ca^{2+} oscillation amplitude, representing cytosolic Ca^{2+} concentration, was measured using the fluorescence intensity of the non-ratiometric Ca^{2+} sensor (GECO-RED). The fluorescence intensity of GECO-RED was measured per Ca^{2+} oscillation in each of the cells over time. For normalization, the values were then divided by the highest intensity value. Source: [95].

Ca^{2+} oscillation frequency were calculated in 10-minute intervals over a 40-minute window in the late stage of NTC. This image is also from Kaouri et al [95], based on the experiments of Christodoulou and Skourides [33], and is in agreement with the observations of Suzuki et al [196].

Figure 2.8 shows that Ca^{2+} oscillation amplitude, representing cytosolic Ca^{2+} concentration, increases over time in the late stage of NTC. Suzuki et al [196] did not investigate changes in the Ca^{2+} oscillation amplitude or its impact on cell and tissue area. However, any mathematical model aiming to capture the two-way coupling between Ca^{2+} and mechanics must take into account the amplitude of the Ca^{2+} transients.

The studies discussed in this chapter [33, 196] propose a new role of active Ca^{2+} fluctuations in accelerating AC. They reveal that AC during neurulation involves cell-autonomous and asynchronous pulsed contractions that are preceded by flashes of Ca^{2+} . These Ca^{2+} pulses also correlate with the accumulation of F-actin in the medial region of the neuroepithelial cells, suggesting that Ca^{2+} regulates AC by influencing actin dynamics and/or myosin contractility. Pharmacologically elevating the level of intracellular Ca^{2+} disrupts the dynamics and spatial distribution of constriction events, ultimately blocking NTC [33]. This evidence indicates that neuroepithelial cells must cycle through periods of high and low Ca^{2+} to enable pulsating contractions, which leads to the successful completion of NTC.

To further investigate how distinct Ca^{2+} fluctuation patterns affect AC and persistent epithelial remodelling, Suzuki et al [196] constructed a mathematical model of the apical surface of the anterior neural plate based on the well-established vertex modelling framework. We shall explore the features of this model and their simulation results in Chapter 3.

Chapter 3

The Suzuki model

Embryonic epithelial tissues undergo complex morphogenetic movements like in-plane reshaping, bending, and folding through the coordinated action of the individual epithelial cells. Computational modelling techniques are used, in conjunction with experimental approaches, to investigate these morphologies *in silico* and explore experimentally intractable questions.

To this end, a variety of modelling approaches have been used to simulate cell–cell mechanical interactions, ranging from FEM-based continuum models to cell-based models (Section 1.3.2). In combination with their experiments, Suzuki et al [196] use a vertex model to study the effect of distinct Ca^{2+} fluctuation patterns on epithelial remodelling during apical constriction (AC).

To our knowledge, the Suzuki et al [196] model is the only mechanochemical vertex model that incorporates Ca^{2+} signalling, making it an excellent foundation for developing our models. In this chapter, we first review their mathematical model in detail, then discuss the key experimental behaviours reproduced by their simulations and highlight the model’s limitations.

3.1 Vertex model

In order to evaluate the differences in the effect and function of the two different types of Ca^{2+} transients on tissue deformation, Suzuki et al [196] constructed a cell-based mechanochemical neural tube closure (NTC) model (which will be referred to as the Suzuki model hereafter). The model is based on the vertex model, a well-known framework used to describe multicellular tissue dynamics [62, 138, 146, 163].

The Suzuki model employs a simple implementation of the Ca^{2+} fluctuations - at any given time, a cell having a baseline value of Ca^{2+} concentration has a probability of experiencing a spike in its Ca^{2+} level. The effect of this Ca^{2+} transient on the cell mechanics is simulated by increasing the line tension of the cell edges.

Additionally, to regulate the cells' natural surface area and perimeter, the model introduces a ratchet-like mechanism, which is a novel feature of this mathematical model. This mechanism is essential for capturing the experimentally-observed ratcheting behaviour of cells [120], where cells contract progressively in a stepwise manner. The ratchet-like mechanism ensures that once a cell contracts past a certain point, it cannot expand back to its original size, thereby stabilizing the contraction.

3.1.1 Modelling assumptions

The tissue under study - the anterior neural plate, is modelled as a two-dimensional, viscoelastic cell sheet comprising 256 cells, in line with observations that the anterior neural plate typically consists of ≈ 250 epithelial cells [33]. Tissue polarities are not defined for simplicity.

It should be noted that, in reality, NTC involves three-dimensional morphological changes in the tissue and cells that have planar anterior-posterior and dorso-ventral cell polarities [87, 88, 146, 196]. The model assumes no cell proliferation or cell death but models a topology altering operation - the T1 process i.e. cell edge rearrangement, which finds frequent use in vertex models [62, 68, 138].

Another simplification of the model is the binary nature of the intracellular Ca^{2+} concentration - a cell is either in a low Ca^{2+} (inactivated) state or a high Ca^{2+} (activated) state. This is in-line with older models where Ca^{2+} evolution is modelled with a hypothetical *bistable* reaction-diffusion process in which chemical signals (extrinsic to the cell) or the application of stress can switch the Ca^{2+} state from low to high stable concentration [135, 136, 137, 152]. However, in the Suzuki model, the Ca^{2+} concentration affects cellular contraction unilaterally i.e. Ca^{2+} triggers cell contraction but not vice versa, so the impact of stress on the Ca^{2+} level of the cell is neglected.

Since the Suzuki model is only concerned with the unilateral effect of Ca^{2+} on cellular contractions, it is acceptable to work with the simplified Ca^{2+} signals

described above. However, it should be noted that more recent models of Ca^{2+} signalling incorporate more sophisticated Ca^{2+} dynamics e.g. IP_3 -mediated CICR, that have been verified experimentally [12]. Future mechanochemical models, with a two-way feedback between Ca^{2+} signalling and mechanics, should incorporate more sophisticated Ca^{2+} dynamics into the model (Chapter 9).

3.1.2 The potential energy term

The Suzuki model considers the following mechanical components: the elasticity of the cell apical surface area (U_A), the elasticity of the cell apical perimeter (U_P), and the line tension generated on each edge of the cell (U_L), all of which are often employed in other vertex models [62, 138, 146, 163]. The mechanical potential energies derived from these three components are modelled as follows. The potential energy for the cell area is given by:

$$U_A = \sum_n^{N_{\text{cells}}} \frac{K_n^A}{2} \left(\frac{A_n}{A_n^0} - 1 \right)^2 A_n^0, \quad (3.1)$$

where A_n and A_n^0 are the cell apical surface area and its natural/preferred apical surface area, respectively, and K_n^A is the coefficient of elasticity for the area.

The potential energy for the cell perimeter is given by:

$$U_P = \sum_n^{N_{\text{cells}}} \frac{K_n^P}{2} \left(\frac{P_n}{P_n^0} - 1 \right)^2 P_n^0, \quad (3.2)$$

where P_n and P_n^0 are the cell apical perimeter and its natural/preferred apical perimeter, respectively, and K_n^P is the coefficient of elasticity for the perimeter.

The quadratic terms in the energy expressions U_A and U_P represent the quadratic components in the Taylor series expansion of the energy function around the equilibrium state. These terms give rise to linear restoring forces upon perturbation of the system, which is a reasonable assumption when modelling the elasticity of epithelia for small deformations [62, 81, 196].

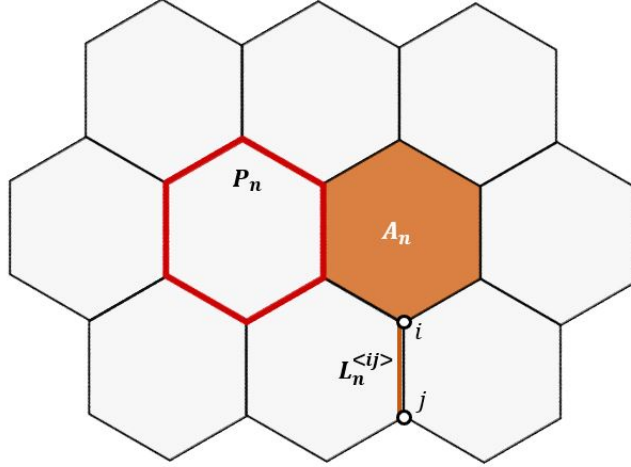


Figure 3.1: Schematic of part of the neural plate (10 cells), as represented in a vertex model. The three physical attributes: cell perimeter (P_n), cell area (A_n), and edge length ($L_n^{<ij>}$) determine the mechanical potential energies: U_P , U_A , and U_L , respectively, in the Suzuki model. The edge $L_n^{<ij>}$ is bound by vertices i and j .

Generally, formulations of the vertex model use deformations of the cell area ($A_n - A_n^0$) and perimeter ($P_n - P_n^0$) to define the potential energies [62, 115, 138]. In comparison, Equations (3.1) and (3.2) describe the potential energies using the strains of the cell area ($\frac{A_n}{A_n^0} - 1$) and perimeter ($\frac{P_n}{P_n^0} - 1$), similar to [146].

In the studies that define the energy terms using deformation, the values of natural area and natural perimeter do not change much over the simulation runtime [68]. Whereas, tissue contraction in the Suzuki model is driven by the ratchet-like mechanism (which will be described in detail in Section 3.1.4) which greatly reduces the natural area and natural perimeter over the course of the simulation.

When the energy terms are modelled using deformation, the restorative elastic forces depend on changes in area and perimeter. For small cell sizes, these changes are correspondingly small, leading to weaker elastic forces relative to the line tension as natural area and natural perimeter approach zero. This imbalance can cause excessive contraction of the cell edges, resulting in numerical instability.

In contrast, using strain in the energy terms makes the elastic forces dependent on changes in area and perimeter relative to their natural values. Consequently, the strength of the elastic forces remains consistent across different length scales

and the model maintains stability for large changes in the values of natural area and natural perimeter.

The potential energy due to the line tension generated at the cell-cell junctions is given by:

$$U_L = \sum_n^{N_{cells}} \sum_{\langle ij \rangle}^{edge} T_n^{\langle ij \rangle} L_n^{\langle ij \rangle}, \quad (3.3)$$

where $T_n^{\langle ij \rangle}$ and $L_n^{\langle ij \rangle}$ are the line tension and the length of each cellular edge connecting the i^{th} and j^{th} vertices, respectively. A cell-cell junction is formed by the adhesion of two cells, and is, thus, composed of two cellular edges derived from the two associating cells. Therefore, the line tension on a cell-cell junction is determined by the sum of the two line tensions derived from the two cellular edges.

Thus, the total potential energy, U , is

$$U = U_A + U_P + U_L. \quad (3.4)$$

U represents the potential energy $U(\mathbf{r}(t))$ of the apical surface of the tissue at some time instant t . As is typical of vertex models, the apical surface of the tissue comprises a collection of non-overlapping connected polygons i.e. the cells (see Figure 3.1). The vertices of these polygons are represented by a set of positions $\mathbf{r} = (\mathbf{r}_1 \ \mathbf{r}_2 \ \dots \ \mathbf{r}_{N_V})$. The force on the i^{th} vertex \mathbf{F}_i is derived from the phenomenological energy function (Equation (3.4)):

$$\mathbf{F}_i = -\frac{\partial U}{\partial \mathbf{r}_i}, \quad (3.5)$$

where $\mathbf{r}_i = (x_i \ y_i)$ is the position vector of the i^{th} vertex, and

$$\frac{\partial U}{\partial \mathbf{r}_i} = \left(\frac{\partial U}{\partial x_i} \quad \frac{\partial U}{\partial y_i} \right). \quad (3.6)$$

The force \mathbf{F}_i is balanced with a viscous drag term, leading to a first-order equation of motion

$$\mu \frac{d\mathbf{r}_i}{dt} = -\frac{\partial U}{\partial \mathbf{r}_i}, \quad (3.7)$$

where μ is the damping coefficient.

Like most vertex models to date, the Suzuki model assumes that all effects of friction (i.e. between neighbouring cells as well as between the cells and the substrate and the extracellular matrix) can be modelled by a single constant. While this may appear to be a major simplification, the resulting model is capable of capturing many key features of real epithelial tissues.

Equation (3.7) is a first order equation since the mass terms have been omitted. This *overdamped limit* is commonly applied to biological systems, since the inertial effects (acceleration) are typically several orders of magnitude smaller than the effects arising from the cell-cell interactions [15]. The force on vertex i depends on the position of its neighbouring vertices, resulting in a set of coupled non-linear ordinary differential equations. Since the system (Equation (3.7)) lacks an analytical solution (as far as we are aware), it has to be solved numerically.

3.1.3 Cell activation

In the Suzuki model, a Ca^{2+} transient (or Ca^{2+} flash) occurs when the intracellular Ca^{2+} concentration in a cell rises from a low level to a high level. Based on their experiments, Suzuki et al [196] conclude that a Ca^{2+} flash temporally regulates certain mechanical parameters in the cell. In their model, they assume that the Ca^{2+} flash modifies the line tension of the cellular edges.

After every unit time interval, each cell has a finite probability of experiencing a Ca^{2+} flash. This probability is determined by a predefined parameter p_c , where p_c is the probability of cell activation per unit time. Each cellular edge in the activated cell then has a finite probability of being activated, according to a

predefined probability p_e . Finally, the line tension of the activated cell edge is elevated by some constant amount ξ (edge activation).

The activation period is determined by the constant τ , which is predefined for every simulation. When an inactivated cell experiences a Ca^{2+} flash, it becomes activated for the duration τ . When an activated cell experiences a Ca^{2+} flash, its remaining activation period is prolonged by τ .

Prior to activation, the cell edges experience a non-zero baseline value of line tension. The expression for line tension on the activated cell edge is

$$T_n^{<ij>} = T_{0n}^{<ij>} + \xi, \quad (3.8)$$

where $T_{0n}^{<ij>}$ is the line tension of an inactivated cell edge, i.e., the baseline value of line tension, and ξ is determined at the start of each edge activation and held constant for the duration of the activation period. After the activation period elapses, the line tension of the activated cell edge relaxes to its baseline value.

3.1.4 The ratchet-like mechanism

For a cell operating under the mechanisms established in Sections 3.1.2 and 3.1.3, a temporary increase in line tension would decrease the apical surface area and perimeter of the cell. However, after the line tension returns to its baseline value, the apical surface area and perimeter of the cell would recover. In contrast, during NTC, the apical surface area of a cell gradually decreases and does not recover. Thus, the apical cell surface has a constrictive nature.

A possible mechanism for maintaining the decrease in the apical surface area, despite the effect of a restoring force, is a ratchet-like mechanism that stabilizes the apical cell membrane, as reported in [120, 123, 170], such that once the cell apical surface contracts, the surface area (and perimeter) does not recover. To model the ratchet-like stabilization mechanism, Suzuki et al [196] took into consideration both the cell natural surface area (A_n^0) and the cell natural perimeter (P_n^0). The natural area and natural perimeter are the values of area and perimeter that the cell would attain in the absence of line tension.

The assumption they made was that A_n^0 could be decreased but not increased, as observed in the experiments. The decrease in A_n^0 was assumed to be determined

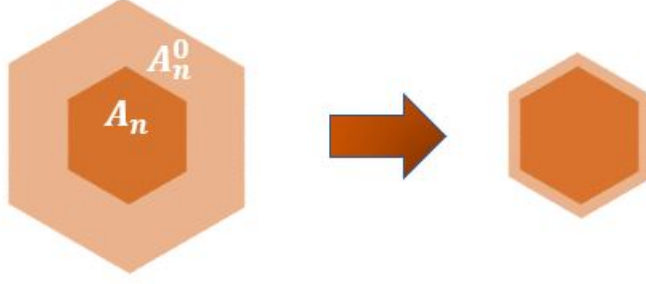


Figure 3.2: Regulation of the natural cell area by the ratchet-like stabilization mechanism in the Suzuki model. The lighter region represents the cell natural area, A_n^0 , and the darker region represents the cell area, A_n . When the area drops below the threshold specified in Equation (3.9), the cell natural area is reduced accordingly.

relative to the cell surface area (A_n); when A_n^0 is sufficiently large in comparison with A_n , A_n^0 tends to decrease according to the following differential equation:

$$\frac{dA_n^0}{dt} = \begin{cases} \kappa_A(A_n - \omega_A A_n^0), & \text{if } (A_n - \omega_A A_n^0) < 0, \\ 0, & \text{if } (A_n - \omega_A A_n^0) \geq 0, \end{cases} \quad (3.9)$$

where κ_A is a constant, and ω_A is a threshold parameter that determines whether or not A_n^0 should be decreased. Under normal simulation conditions, A_n^0 is larger than A_n . For A_n^0 to decrease, $\frac{dA_n^0}{dt} < 0$. Thus, when $\omega_A \geq 1$, A_n^0 will always decrease.

Similarly, for the cell's natural perimeter, we have the following differential equation:

$$\frac{dP_n^0}{dt} = \begin{cases} \kappa_P(P_n - \omega_P P_n^0), & \text{if } (P_n - \omega_P P_n^0) < 0, \\ 0, & \text{if } (P_n - \omega_P P_n^0) \geq 0, \end{cases} \quad (3.10)$$

where κ_P is a constant, and ω_P is a threshold parameter that determines whether or not P_n^0 should be decreased.

To prevent the cell surface area and perimeter from becoming negative, Suzuki et al [196] limited the minimum values of A_n^0 and P_n^0 to 0.3 and 2.0, respectively. It should be noted, however, that this approach only sets a strict lower bound on

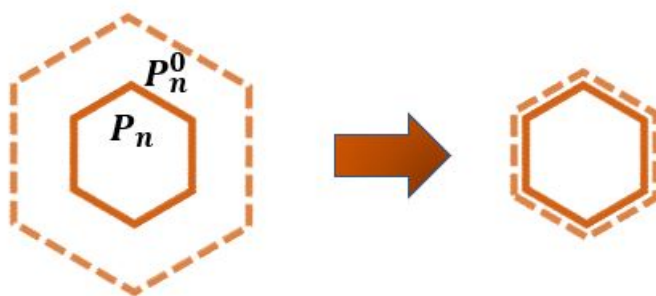


Figure 3.3: Regulation of the natural cell perimeter by the ratchet-like stabilization mechanism in the Suzuki model. The dashed line represents the cell natural perimeter, P_n^0 , and the solid line represents the cell perimeter, P_n . When the perimeter drops below the threshold specified in Equation (3.10), the cell natural perimeter is reduced accordingly.

the cell natural area (A_n^0) and perimeter (P_n^0), the cell area (A_n) and perimeter (P_n) are free to contract below zero, which is unrealistic and risks making the simulation unstable.

The model behaviour can, thus, be summarised as follows. Under equilibrium conditions, the elastic force on any vertex, arising from the adjacent cells' area and perimeter elasticity, is cancelled out by the line tensions of the connecting edges. When a cell experiences a Ca^{2+} transient, the tension of its activated edges, $T_{0_n}^{<ij>}$, is elevated by a constant value, ξ , for a finite time duration, τ (the activation period), disrupting this equilibrium. As a result, the cells associated with the activated edges contract their perimeters and areas to restore equilibrium. In the absence of the ratchet-like mechanism, the deformed cells would revert to their original shape and size upon the relaxation of the line tension, at the end of the activation period. However, if the conditions for activating the ratchet-like mechanism are met within the activation period (Equations (3.9) and (3.10)), the deformed cells' natural area and natural perimeter are assigned smaller values and the tissue then tends to a new equilibrium state.

3.2 Computational results

To simulate the vertex model, Suzuki et al [196] program their simulation in C. They generate the initial cell configurations using Voronoi diagrams - 256 cells

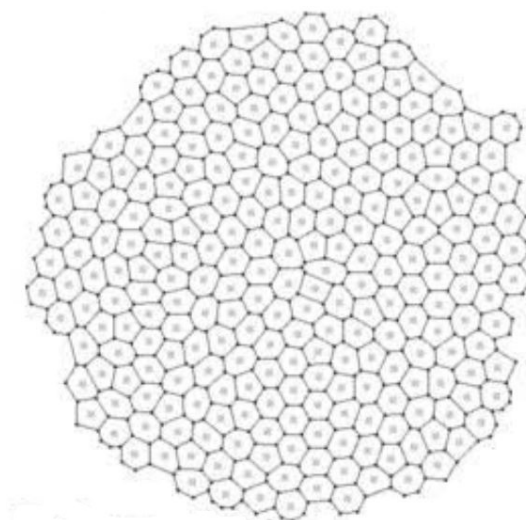


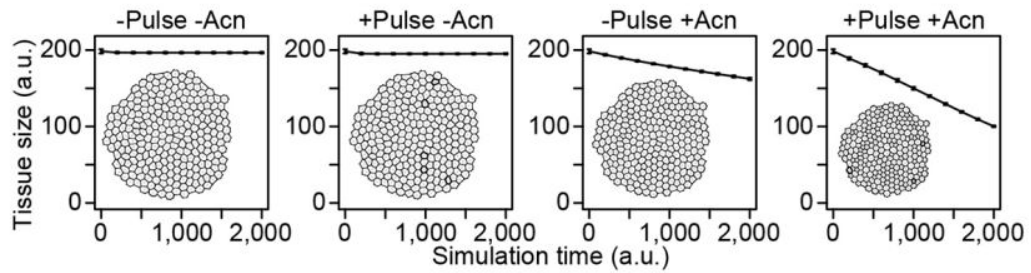
Figure 3.4: The initial configuration of the tissue modelled by Suzuki et al using Voronoi diagrams. The cells are modelled as irregular polygons having 5, 6, 7 or 8 sides. Source: [196].

are positioned in an almost circular region (Figure 3.4). This circular region approximates the apical surface of the anterior neural plate, which later develops into the brain [32]. The model simulates the temporal evolution of the batch of cells by solving Equation (3.7) for every vertex using the forward Euler method.

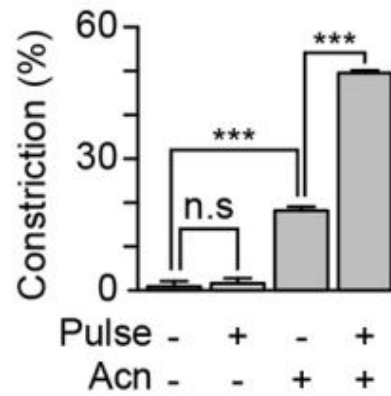
Using their vertex model, Suzuki et al [196] examined the combined effect of the Ca^{2+} transient (*Pulse*) and the constrictive nature of the apical cell surface (*Acn*), i.e., the ratchet-like mechanism, on the modelled epithelial tissue (Figure 3.5). The activation of the ratchet-like mechanism (*+ Acn*) prevents recovery of cell size and allows the tissue to contract. The presence of Ca^{2+} flashes (*+ Pulse*) expedites the contraction. Without the *Acn* component, the tissue does not change size regardless of the presence of the Ca^{2+} signal. Adding the *Acn* component causes the tissue to gradually decrease in size, and the combined effect of Ca^{2+} and *Acn* components accelerates the size decrease (Figure 3.5a).

Figure 3.5a depicts the effects of Ca^{2+} transients and the constrictive nature of the apical cell surface on tissue constriction. The subfigures also have snapshots of the modelled tissue at the end of the simulation in each case. Figure 3.5b displays the reduction in tissue area (as a percentage of the initial area) for each case.

At the single-cell level, it was found that after the contractions of area and



(a) Tissue sizes over simulation runtime.



(b) Tissue constriction at the end of the runtime.

Figure 3.5: The effects of Ca^{2+} transients (Pulse) and the constrictive nature of the apical cell surface (Acn) on the modelled epithelial tissue. -/+ Pulse indicates the absence/presence of Ca^{2+} flashes, +/- Acn indicates the whether the ratchet-like mechanism was active/inactive in the model. *** indicates a statistically significant difference (by the two-sided Student's t-test) and n.s. indicates a non-significant difference. Model parameters: Table 3.1. Source: [196].

Parameter	Value
Cells	256
p_c	0.025
δt	0.2
K_n^A	0.3
K_n^P	0.2
μ	1
κ_A	1
κ_P	0.001
ω_A	0.6
ω_P	0.8
A_n^0 (initial)	1
P_n^0 (initial)	5
A_n^0 (minimum)	0.3
P_n^0 (minimum)	2
T_{0n}	0.1
ξ	0.05
τ	5

Table 3.1: Parameter values for Figures 3.5, 3.7, and 3.8.

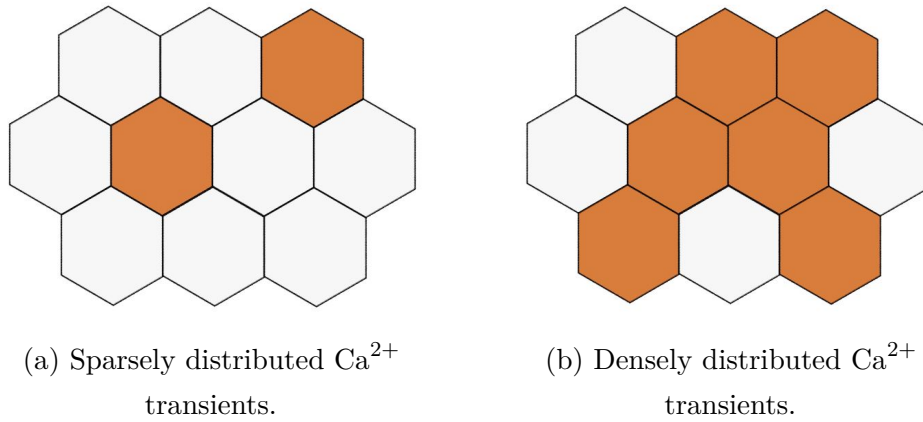


Figure 3.6: Examples of sparse and dense spatial distributions of Ca^{2+} transients. Activated cells are coloured. The density of the distributions can be regulated with the parameter p_c , the frequency of cell activation per unit time.

perimeter were induced by Ca^{2+} , a considerable relaxation event also occurred, in which the area and perimeter recover to new values, slightly lower than their original values. This was indeed observed during an AC event after a single Ca^{2+} transient *in vivo* [196]. A key point to note is that this relaxation event is only observed at the level of a single-cell while the tissue experiences only a monotonic decrease in size without any noticeable relaxation phase [121]. The model captures this accurately.

These results suggest that the Suzuki model reproduces the *in vivo* experiments qualitatively, in which Ca^{2+} transients accelerate AC and, hence, decrease the tissue size when the stabilization mechanisms are present.

In comparing dense (pulses having higher spatial and temporal frequency, this corresponds to a high p_c value in the model) versus sparse pulses (Figure 3.6), Suzuki et al [196] found that dense pulses induced tissue deformation more rapidly within the activation period. They performed this comparison by gradually increasing p_c and found that the area reduction was larger for higher values of p_c , regardless of the value of p_e (Figure 3.7). However, over the entire course of the simulation, dense pulses were found to be less effective than sparse pulses when the same number of total pulses were used in both cases (Figure 3.8).

Figure 3.8 depicts the change in tissue size over simulation runtime for different Ca^{2+} -activation windows. The simulated tissue is subjected to the same number

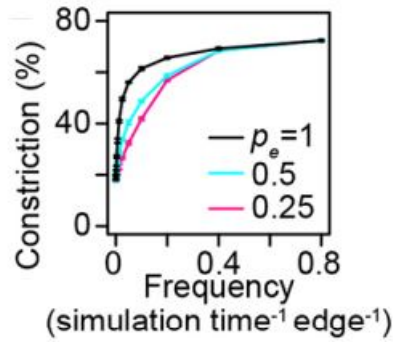


Figure 3.7: The constriction of tissue area (%) at the end of simulation runtime plotted as a function of the frequency of cell activation (p_c) for different values of the frequency of edge activation (p_e). At low values of p_c , increasing p_e greatly decreases the final tissue area. At higher values of p_c (> 0.1), the drop in final area is not as sharp. Model parameters: Table 3.1. Source: [196].

of Ca^{2+} flashes (pulses) over different ‘activation windows’. Outside the activation windows, the tissue is inactive, i.e., it does not experience any Ca^{2+} flashes. Since the total number of Ca^{2+} flashes experienced by the tissue within the activation window is the same for each case, each case uses a different value of p_c (0 - 2000: 0.025, 400 - 1600: 0.0417, 600 - 1400: 0.0625, 800 - 1200: 0.125, 900 - 1100: 0.25). Comparing the different activation windows, it can be seen that while denser pulses produce a sharp drop in tissue area over a small period of time, sparser pulses yield a greater reduction in tissue area over the entire runtime.

These results suggest that random Ca^{2+} fluctuations at the single-cell level decrease the tissue size more effectively than multicellular Ca^{2+} fluctuations. This is in agreement with the well-established experimental results of Christodoulou and Skourides [33].

We note here that the term ‘multicellular Ca^{2+} fluctuations’ used in the paragraph above may be misleading. Suzuki et al [196] refer to a dense spatial distribution of Ca^{2+} pulses as a multicellular fluctuation. However, this is not entirely accurate. As described in Chapter 2, a multicellular Ca^{2+} transient originates from one or a few cells and propagates over the neighbouring cells. So, a mathematical model attempting to emulate a multicellular transient needs to, at the very least, provide a mechanism for and demonstrate the propagation of Ca^{2+} across cell boundaries. Thus, in any prospective model, adjacent cells must

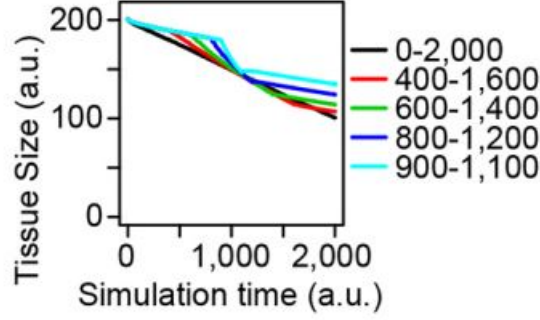


Figure 3.8: Change in tissue size over the simulation runtime for different Ca^{2+} -activation windows, i.e., in the cases depicted, the modelled tissue experiences Ca^{2+} flashes over activation windows of 2000, 1200, 800, 400, and 200 a.u. (arbitrary units or non-dimensional units). The total number of Ca^{2+} flashes experienced by the tissue over the runtime is the same in each case.

Model parameters: Table 3.1. Source: [196].

demonstrate some form of intercellular communication via Ca^{2+} signalling.

Overall, the study done by Suzuki et al [196] provides insight regarding the effect of Ca^{2+} fluctuations on the rate of tissue constriction, but it does not investigate the time taken by the tissue to achieve maximum constriction and its final size (Figure 3.7 plots tissue area at the end of simulation runtime but it should be noted that the model allows for further constriction). However, both the factors are vital for successful NTC and investigating them by means of a parameter sweep is a key objective of this doctoral work and will be performed in Chapter 5.

In spite of the success of the model, it has its limitations. As seen in Figure 2.6, Ca^{2+} flashes *precede* cellular contractions *in vivo*. In the model, however, a Ca^{2+} flash immediately triggers cellular contraction by elevating the line tension without any latency. Also, in Figure 2.7, it can be seen that the frequency of occurrence of Ca^{2+} flashes increases over time. Whereas, in all of their simulations, Suzuki et al [196] assign p_c a constant value during the period in which Ca^{2+} flashes are active. Additionally, Suzuki et al [196] model the neural plate in isolation, without considering the effects of any surrounding tissue. However, in reality, the neural plate is attached to and bounded by a layer of cells that

exerts a force on it during NTC. These cells form a part of the surface ectoderm, a crucial structure in the developing embryo [32]. In the following chapters, we will use the Suzuki model as a foundation and sequentially build up complexity to develop new mechanochemical models for NTC that address these limitations.

Chapter 4

CelluLink:

Algorithm and features

From a modelling viewpoint, tissue morphogenesis is a problem of collective cell behaviour, in which the tissue evolves based on the deterministic and/or stochastic rules that the individual cells follow. Cell-based modelling is a useful computational tool for studying collective cell behaviour [10, 125] but because most cell-based simulations cannot be solved analytically, insight into their behaviour must be obtained via simulations. Individual simulations with visual output, in the form of animations and time-series plots for instance, can give some initial intuition about the behaviour and parameter sensitivity of the model. However, to obtain a more systematic overview of the range of behaviours the model can exhibit, along with its parameter sensitivity, it becomes necessary to rerun the simulation many times for different parameters, and, in case of stochastic models, to obtain statistical measures of the model results by rerunning many random instantiations of the model.

In this chapter, we introduce CelluLink, a new software package for vertex models. We first explore the algorithm underlying CelluLink and then provide an overview of its key features and functions.

4.1 Existing computational software

Compared to the plethora of software applications available for continuum-based models, software tools for cell-based modelling have more limited availabil-

Software	Open Source	GUI	CA	CP	PM	VT	VM	Source
CompuCell3D	✓	✓		✓				[200]
Morpheus	✓	✓		✓				[190]
EPISIM		✓			✓			[195]
CellSys		✓			✓			[85]
PhysiCell	✓				✓			[71]
Biocellion					✓			[94]
EmbryoMaker	✓	✓			✓			[117]
VirtualLeaf	✓	✓					✓	[127]
LAMMPS	✓				✓			[206]
TissueForge	✓	✓			✓		✓	[175, 176]
SAMoS	✓				✓	✓	✓	[15]
cellGPU	✓					✓	✓	[193]
Chaste	✓		✓	✓	✓	✓	✓	[39]
Tyssue	✓						✓	[205]
CelluLink	✓						✓	

Table 4.1: A comparison of software tools for cell-based modelling. GUI: graphical user interface. CA: cellular automata. CP: cellular Potts. PM: particle model. VT: Voronoi tessellation. VM: vertex model.

ity. Table 4.1 compares some of the commonly used software tools for cell-based modelling.

The computational tools listed in Table 4.1 have been used to successfully model and investigate a variety of phenomena like the dynamics of intestinal homeostasis and carcinogenesis [7], the biomechanical characterization of epithelial tissue development and wound healing [202], and in studies of epithelia morphogenesis in *Drosophila melanogaster* [76, 122, 129]. However, most of the time, models are developed independently by research groups for a specific biological question and are either difficult to adapt to other systems or not made available for public use.

Of particular interest to us were Chaste and Tyssue. Chaste (Cancer, Heart And Soft Tissue Environment) is an open source simulation package for the numerical solution of mathematical models arising in physiology and biology, with

a particular focus on the continuum modelling of cardiac electrophysiology (‘Cardiac Chaste’), discrete cell-based modelling of soft tissues (‘Cell-based Chaste’), and modelling of ventilation in lungs (‘Lung Chaste’). Simulations are written as ‘tests’ in C++, and can be run on all major operating systems via a Docker image. Chaste provides libraries for common scientific computing infrastructure such as linear algebra operations, finite element meshes, and ordinary and partial differential equation solvers.

Tyssue is a library written in Python 3 that provides a unified interface to implement bio-mechanical models of living tissues. Its main focus is on vertex based epithelium models, allowing users to model the mechanical behaviour of 2D, apical 3D or full 3D epithelia. As far as we are aware, it is the only publicly available software for the simulation of 3D vertex models. Tyssue implements common cellular processes such as cell elimination, division, or rearrangements based on the methodologies used in Brodland and Veldhuis [19], Okuda et al [149], and Finegan et al [67]. The dynamical behaviour of the epithelium is described either by solving the equations of motion for the cell vertices or by finding the quasi-static equilibrium of the tissue as the solution of a gradient descent problem.

However, while running test suites in Chaste is straightforward enough, making modifications to the existing models in the Chaste library requires extensive experience with C++ development. Tyssue provides detailed documentation for running the vertex models, but lacks a feature for implementing intercellular signalling. Considering these factors, we decided to create our own computational tool, CelluLink, as it would afford us more convenience in modifying our model and adding desired features.

4.2 Features of the software

In the initial plan for this doctoral work, we envisioned constructing a 3D vertex model with two-way coupling between Ca^{2+} and cellular mechanics. However, owing to the complexity of such an undertaking and the time constraints of the doctoral program, we decided to restrict our scope to the two-dimensional vertex model. Accordingly, we focussed on only implementing the features essential to our modelling problem in the current version of CelluLink. Additional features (Voronoi diagram generator, topology changing events, and ray tracing for three-dimensional cells, for instance) can be implemented in future releases. Moreover,

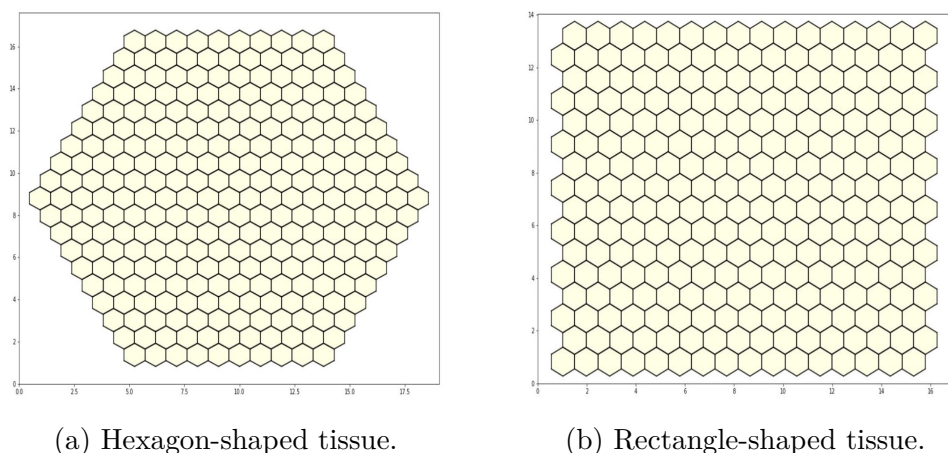


Figure 4.1: Examples of the two types of tissue configurations available in CelluLink.

users are welcome to contribute to the development of CelluLink.

Current version

- *Tissue generator (2D)*: Hexagonal honeycomb lattice of cells arranged in a: (i) hexagon-shaped tissue, or (ii) rectangle-shaped tissue.
- *Solvers*: (i) Forward Euler, (ii) Backward Euler, and (iii) Predictor-corrector schemes.
- *Parallel processing*: Simulations for different parameter sets run in parallel.
- *Data visualisation*: (i) Time series plots for tissue area, tissue perimeter, average cell area, average cell perimeter, and tissue energy, (ii) Animation folder contains frames depicting tissue evolution. Additional plots and figures can be generated easily from the simulation data saved in the output directories.

In the case of vertex models, it is non-trivial to determine model parameters experimentally. So, we test the model for a range of experimentally plausible parameter values [45, 126]. These systematic parameter studies allow us to predict the response of the system to pharmaceutical treatments [99, 174], or to evaluate the behaviour of the tissue. Thus, systematic parameter studies are a critical tool for analysing vertex models. However, as vertex models grow in size and

complexity, performing such parameter studies poses a challenge both in terms of computational power and data storage.

Bearing this in mind, CelluLink has been designed to utilize the multiprocessing libraries in Python to run large parameter sweeps for vertex models on desktop machines or computational clusters. In case the model incorporates stochastic effects, statistical measures can be obtained by running many random instantiations of the model for the same parameter value. Each simulation is run as a separate process. In this manner, a predefined number of processes can be run in parallel. The parallel processing feature will be explained in greater detail in Section 4.3, along with the algorithm flowchart.

4.3 The algorithm

A computational tool that lacks a GUI will always pose a challenge for new users, especially those lacking programming experience [61]. This is why, out of all the available software options for vertex models, there is no single software whose usage is predominant compared to the others. Modellers generally favour the software that either offers the desired features or one that uses a programming/scripting language they are familiar with. And even then, there is a learning curve to be overcome. It is no surprise then, that in a large number of studies involving vertex models, the research team just develops their own code in-house [62, 196].

Taking cognizance of this fact, the CelluLink source code takes a procedural programming approach rather than an object-oriented one. While object-oriented programming is indisputably powerful, it can be difficult to: (i) follow the flow of control and, (ii) modify the existing code to implement new functionality. Procedural programming is based on the concept of the procedure call. Procedures (a type of routine or subroutine) simply contain a series of computational steps to be carried out. Any given procedure might be called at any point during a program's execution, including by other procedures or itself. Examples of these procedures will be provided when we discuss the algorithm flowcharts in Figures 4.5 & 4.6.

The development of CelluLink draws inspiration from Durney et al [55, 56, 57]. In their work, they develop a two-dimensional vertex model for *Drosophila* dorsal closure and a three-dimensional vertex model for *Drosophila* salivary gland tubulogenesis. Both models are developed in Python and utilise the `NetworkX`

package. The `NetworkX` package was designed for the study of complex networks and contains functions and commands for the creation and manipulation of graphs.

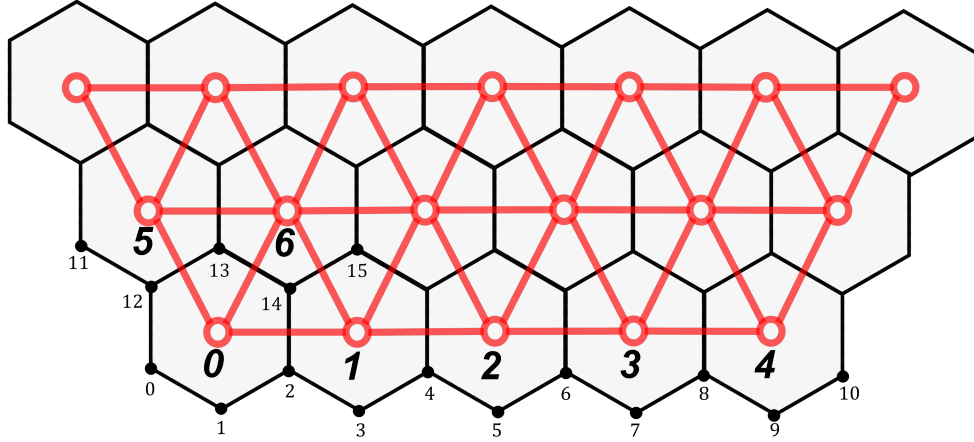


Figure 4.2: Indexing scheme used in `CelluLink` to assign numeric values to the cells and vertices of the vertex model. The vertex at the bottom left corner of the tissue is assigned 0. As we move to the right along the cell edge, the index goes up by one for the next vertex. On reaching the end of that row, we move to the leftmost vertex on the row above it and resume assigning indices. The cells are assigned indices in a similar manner. The black and red lines depict the connectivities of the vertex and cell graphs respectively.

Similarly, `CelluLink` is written in Python 3 and utilises the `NetworkX` package to store the data associated with the cells and vertices of the vertex model in graph-like data structures. The vertex of each polygon i.e. a cell, is imagined as a node and the connection between a pair of vertices i.e. a cell edge, is imagined as an edge in the vertex graph $\mathcal{V} = (V_{\mathcal{V}}, E_{\mathcal{V}})$, where $V_{\mathcal{V}}$ and $E_{\mathcal{V}}$ are the sets of nodes and edges of the vertex graph, respectively.

Also, each cell is imagined as a node and the connection between two cells that share an edge, is imagined as an edge in the cell graph $\mathcal{C} = (V_{\mathcal{C}}, E_{\mathcal{C}})$, where $V_{\mathcal{C}}$ and $E_{\mathcal{C}}$ are the sets of nodes and edges of the cell graph, respectively. The nodes of the graphs \mathcal{V} and \mathcal{C} are assigned indices according to the numbering scheme visualised in Figure 4.2.

The nodes and edges of the `NetworkX` graphs can each hold a number of data structures. This proves very useful in storing, accessing, and manipulating the

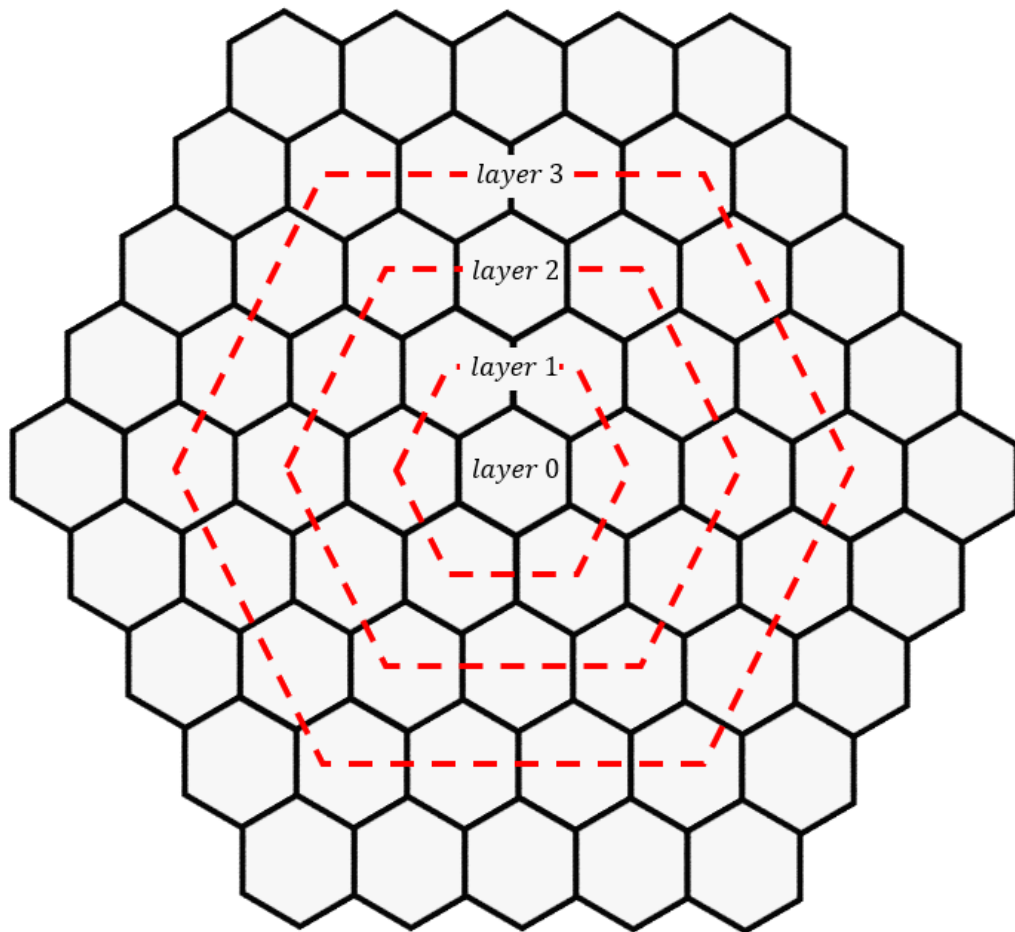


Figure 4.3: Arrangement of cells in the hexagon-shaped tissue configuration. The cells are arranged in concentric layers, where layer 0 has only one cell - the cell at the centre of the modelled tissue.

data associated with the vertices and cells. For instance, each node of \mathcal{V} holds a 2-tuple describing the position of the corresponding vertex, and a list of integers representing the indices of the cells which share that vertex.

The impact of the initial shape of the tissue on tissue evolution and final shape varies across vertex models. However, in our modelling challenge, due to the absence of topological transitions [34] and low adhesion [196], the final shape is simply a smaller version of the initial shape. Therefore, the choice of initial shape directly affects the final shape.

So, all the simulations in this doctoral work model the tissue in the hexagonal

rather than the rectangular configuration because they more closely resemble the circular shape of the tissue under study i.e. the apical surface of the anterior neural plate. To model this tissue, we imagine the constituent cells to be arranged in concentric layers (Figure 4.3) such that the relationship between the number of layers and the number of cells in the tissue is

$$cells = 1 + 6 \sum_{n=0}^{layers} n = 1 + 3(layers)(layers + 1), \quad (4.1)$$

and the total number of vertices in the tissue is given by

$$vertices = 6 \sum_{n=0}^{layers} (2n + 1) = 6(layers + 1)^2. \quad (4.2)$$

Figure 4.4 provides an overview of CelluLink’s algorithm. The ability to parallelize large parameter sweeps is CelluLink’s most important feature and its implementation greatly influenced the software design process. The parallel processing feature utilises the `multiprocessing` package to spawn child processes and manage communication between them.

To elucidate the working of the parallelization feature, let us consider a typical parameter sweep for the Suzuki model. The model has 16 free parameters: p_c , δt , K_n^A , K_n^P , μ , κ_A , κ_P , ω_A , ω_P , A_n^0 (initial), P_n^0 (initial), A_n^0 (minimum), P_n^0 (minimum), T_{0n} , ξ , τ . First, we set the default values for each parameter. Then, we define a list of values for each parameter that we’d like to sweep over:

$$\begin{aligned} p_c &= [value\ 1, value\ 2, \dots], \\ \delta t &= [value\ 1, value\ 2, \dots], \\ &\vdots \\ \tau &= [value\ 1, value\ 2, \dots]. \end{aligned}$$

Then, the simulation runs for an instance of the model with $p_c = value\ 1$ and all other parameters set to their default values. In this manner, a single instance of the model is run in a child process. A separate child process runs for an instance of the model with $p_c = value\ 2$ and all other parameters set to their

default values, and so on. These child processes run in parallel and the main process only allows a predefined number of parallel child processes at a time so as to not overburden the CPU.

If we are interested in examining stochastic effects, it becomes necessary to run many instances of the model for the same parameter value. For example, to examine the stochastic effects for $p_c = \text{value 1}$, we'd have to repeatedly run the model with $p_c = \text{value 1}$ and all other parameters set to their default values. In this case as well, each run would be performed by a distinct child process.

Figure 4.5 depicts the flow chart of the algorithm for CelluLink's main process. The main process is written within the `main()` function. The process starts by initialising the following variables: *layers* (number of concentric cell layers), *hs* (cell edge length), *simtime* (duration of time for which the model is simulated), *samples* (number of runs for the same parameter value), and *num_proc* (number of child processes allowed to run in parallel). All units are non-dimensional.

Since CelluLink uses procedural programming, the main process then calls a sequence of functions to execute the next steps of the algorithm. The top-level results directory is created by the `create_results_dir()` function, the tissue is generated by calling the `generate_tissue()` function which defines the cell and vertex graphs, and the `set_sim_params()` function is called to assign the model parameters their default values and to create a list containing the values over which the parameter sweep will run. The total number of child processes that will be required is given by $\text{samples} \times \text{num_par}$, where *num_par* is the number of values over which the parameter sweep will run.

Figure 4.6 depicts the flow chart of the algorithm for a child process (*solver*). This algorithm also calls a sequence of functions to execute the tasks associated with each step. For the sake of brevity, they will not be listed here. The CelluLink source code along with all the function definitions can be found on GitHub¹. Modifications or additions can be made to the model by changing an existing function and/or by writing new ones.

The *solver* process starts by creating an output directory (within the top-level results directory) to store the simulation data for the associated parameter value. Then, it iterates the following sequence of actions over the full range of timesteps:

¹GitHub repository: <https://github.com/Yudhajit-95/CelluLink>

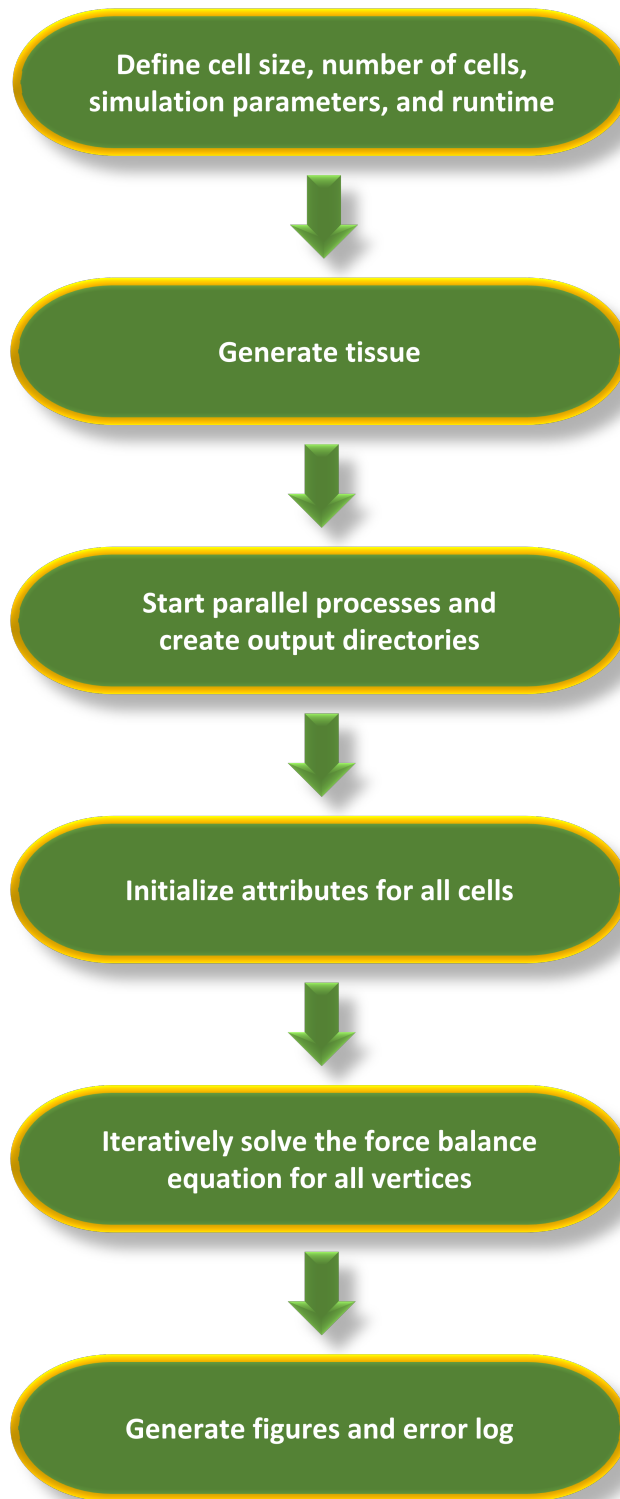


Figure 4.4: A high-level process flow diagram of CelluLink's algorithm.

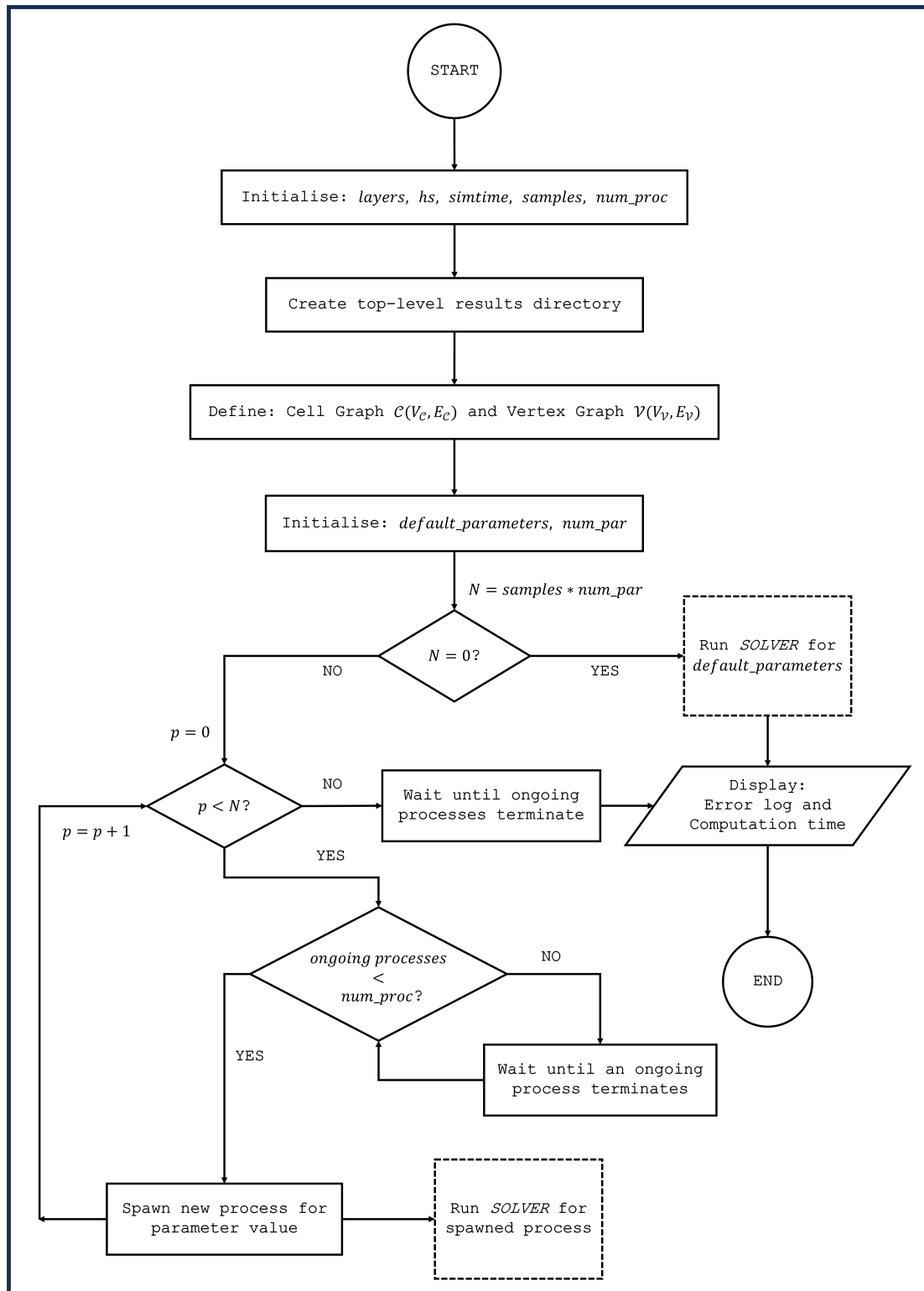


Figure 4.5: Flow chart of the algorithm for CelluLink's main process. The boxes with the dashed borders depict child processes spawned by the main process.

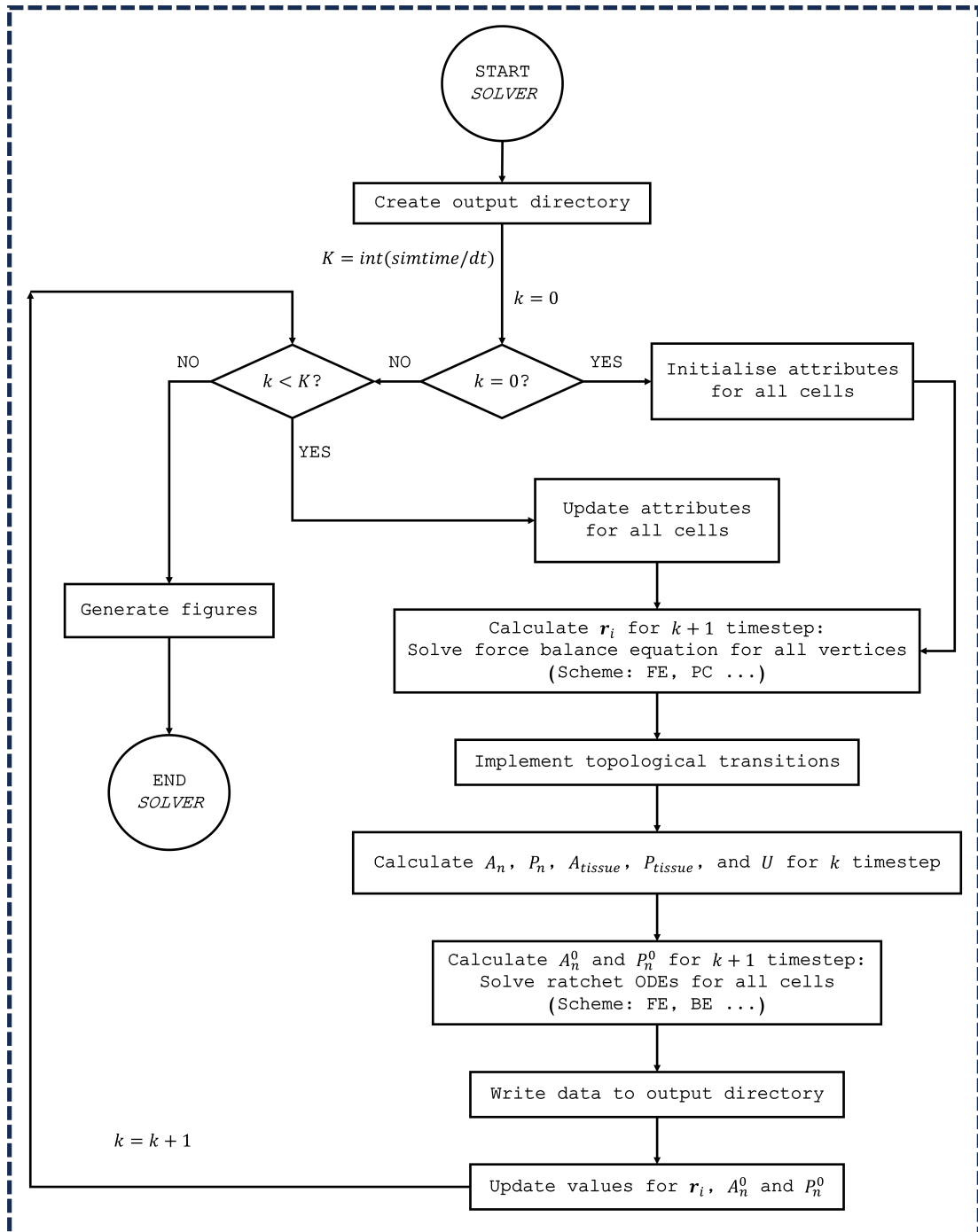


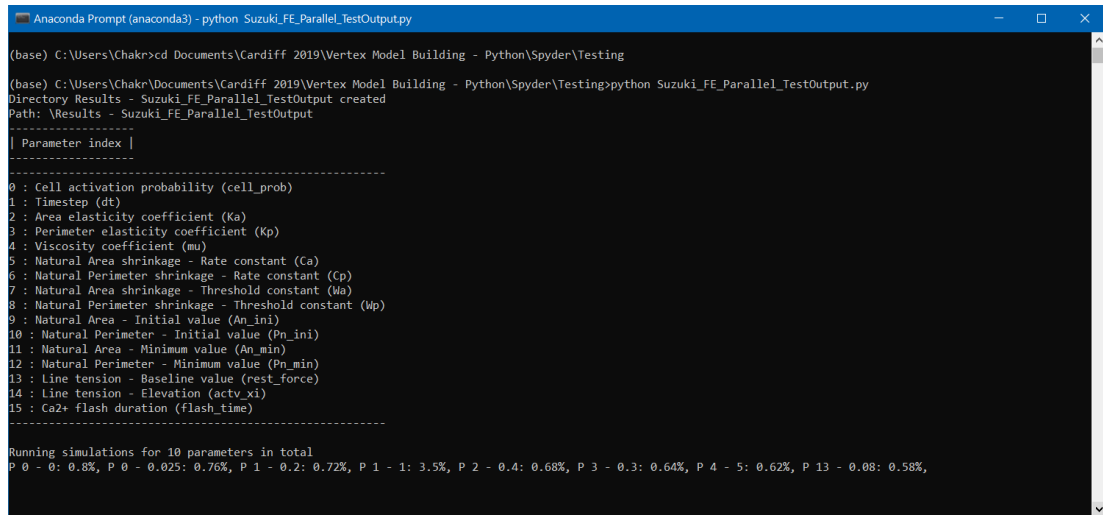
Figure 4.6: Flow chart of the algorithm for CelluLink's child processes. Each child process runs a different instance of the vertex model simulation.

- (i) Initialise or update the attributes that define cell state e.g. Ca^{2+} concentration level,
- (ii) Calculate position vector \mathbf{r}_i for all vertices for the *next timestep* by solving the force balance equation (Equation (3.7)) using the numerical scheme of choice e.g. forward Euler or predictor-corrector,
- (iii) Implement any changes in topology (It is to be noted that this feature is not currently available in CelluLink. However, it is listed here for the sake of completeness - to demonstrate where it can be implemented in the algorithm.),
- (iv) Calculate area A_n and perimeter P_n for all cells, and net area A_{tissue} , perimeter P_{tissue} , and total energy of the tissue U ,
- (v) Calculate the natural area A_n^0 and natural perimeter P_n^0 for all cells for the *next timestep* by solving the ODEs of the ratchet-like mechanism (Equations (3.9) & (3.10)) using the numerical scheme of choice e.g. Forward Euler or Backward Euler,
- (vi) Write the data from the previous steps to the output directory,
- (vii) Update the position vector \mathbf{r}_i for all vertices, and update the natural area A_n^0 and natural perimeter P_n^0 for all cells.

After completing this sequence for the final timestep, the data in the output directory is read to generate snapshots of the tissue at different timesteps and time series plots of interest e.g. tissue area versus time, tissue perimeter versus time. Upon completing these actions, the *solver* process terminates.

4.4 Testing the software

A Python script containing the CelluLink `main()` function can be run from any command line interface. Figure 4.7 shows an instance where the script is being executed via an Anaconda Prompt terminal to simulate one of the models developed in this thesis - the modified Suzuki model, which will be studied in detail in Chapter 5.



```

Anaconda Prompt (anaconda3) - python_Suzuki_FE_Parallel_TestOutput.py
(base) C:\Users\Chakr>cd Documents\Cardiff 2019\Vertex Model Building - Python\Spyder\Testing
(base) C:\Users\Chakr\Documents\Cardiff 2019\Vertex Model Building - Python\Spyder\Testing>python Suzuki_FE_Parallel_TestOutput.py
Directory Results - Suzuki_FE_Parallel_TestOutput created
Path: \Results - Suzuki_FE_Parallel_TestOutput
-----
| Parameter index |
-----
0 : Cell activation probability (cell_prob)
1 : Timestep (dt)
2 : Area elasticity coefficient (Ka)
3 : Perimeter elasticity coefficient (Kp)
4 : Viscosity coefficient (mu)
5 : Natural Area shrinkage - Rate constant (Ca)
6 : Natural Perimeter shrinkage - Rate constant (Cp)
7 : Natural Area shrinkage - Threshold constant (Mb)
8 : Natural Perimeter shrinkage - Threshold constant (Mp)
9 : Natural Area - Initial value (An_ini)
10 : Natural Perimeter - Initial value (Pn_ini)
11 : Natural Area - Minimum value (An_min)
12 : Natural Perimeter - Minimum value (Pn_min)
13 : Line tension - Baseline value (rest_force)
14 : Line tension - Elevation (actv_xi)
15 : Ca2+ flash duration (flash_time)
-----
Running simulations for 10 parameters in total
P 0 - 0: 0.8%, P 0 - 0.025: 0.76%, P 1 - 0.2: 0.72%, P 1 - 1: 3.5%, P 2 - 0.4: 0.68%, P 3 - 0.3: 0.64%, P 4 - 5: 0.62%, P 13 - 0.08: 0.58%,

```

Figure 4.7: CelluLink running in a terminal window. In this instance, CelluLink is being run via Anaconda Prompt on Windows 10.

Suzuki_FE_Parallel_TestOutput.py, the Python script being executed, contains the `main()` function. Each parameter in the model is assigned a numeric value, as displayed in the parameter index table (Table 4.2). This visual aid helps the user monitor the progress of the simulations being run for the corresponding parameter values e.g. ‘P 0 - 0: 0.8%’ indicates that the simulation for $p_c = 0$ is 0.8% complete.

Parameter	Index number	Variable name
p_c	0	<i>cell_prob</i>
δt	1	<i>dt</i>
K_n^A	2	<i>Ka</i>
K_n^P	3	<i>Kp</i>
μ	4	<i>mu</i>
κ_A	5	<i>Ca</i>
κ_P	6	<i>Cp</i>
ω_A	7	<i>Wa</i>
ω_P	8	<i>Wp</i>
A_n^0 (initial)	9	<i>An_ini</i>
P_n^0 (initial)	10	<i>Pn_ini</i>
A_n^0 (minimum)	11	<i>An_min</i>
P_n^0 (minimum)	12	<i>Pn_min</i>
T_{0n}	13	<i>rest_force</i>
ξ	14	<i>actv_xi</i>
τ	15	<i>flash_time</i>

Table 4.2: The parameter index table for the modified Suzuki model. The numerical index and variable name assigned to each parameter is listed above.

Parameter	Value
Cells	271
p_c	0.025
δt	0.2
K_n^A	0.3
K_n^P	0.2
μ	1
κ_A	1
κ_P	0.001
ω_A	0.6
ω_P	0.8
A_n^0 (initial)	1
P_n^0 (initial)	5
A_n^0 (minimum)	0.3
P_n^0 (minimum)	2
T_{0n}	0.1
ξ	0.05
τ	5

Table 4.3: Parameter values for Figures 4.8 and 4.9.

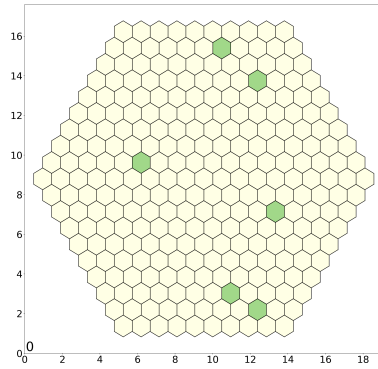
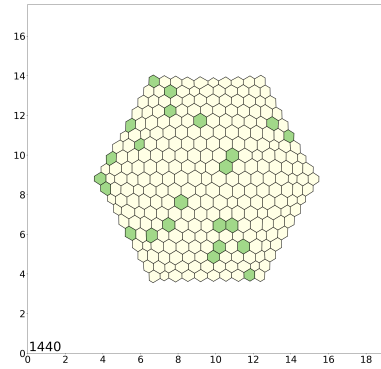
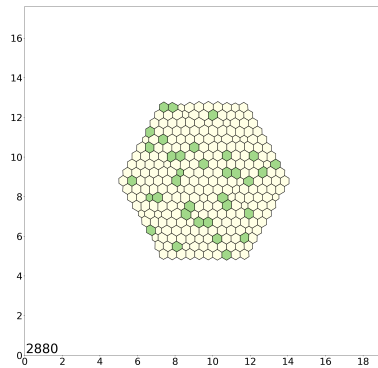
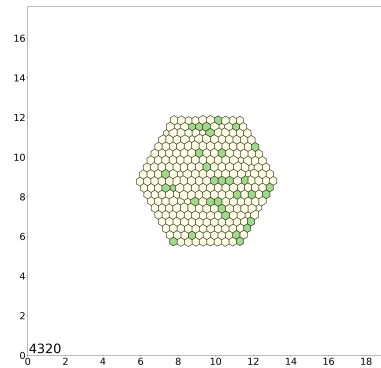
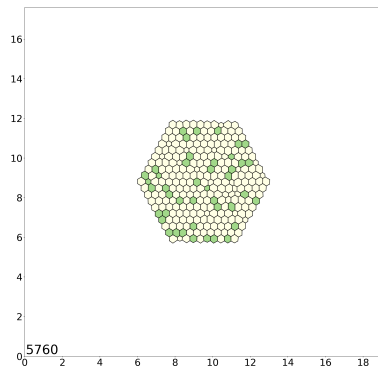
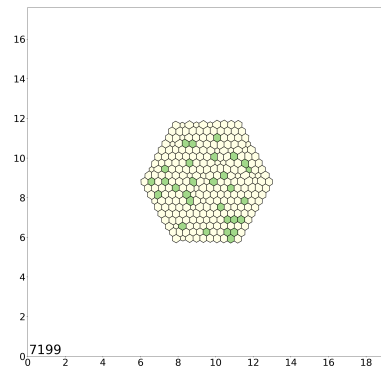
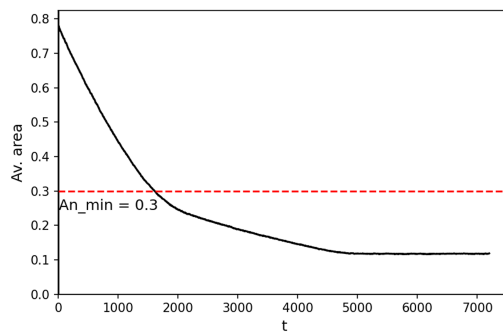
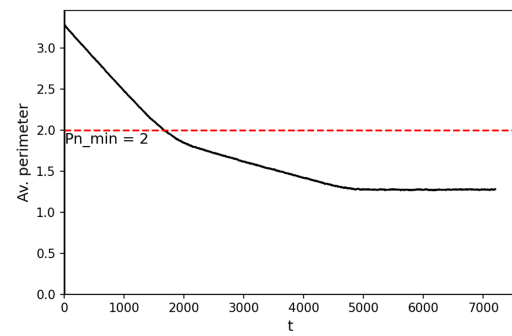
(a) $t = 0$.(b) $t = 1440$.(c) $t = 2880$.(d) $t = 4320$.(e) $t = 5760$.(f) $t = 7199$.

Figure 4.8: The time evolution of the tissue in the modified Suzuki model is visualized through images captured at the end of five equally spaced time intervals. The green-coloured cells have been activated by Ca^{2+} whereas the yellow-coloured cells are in an inactivated state. The images have been generated by CelluLink, using the `Matplotlib` package. Model parameters:

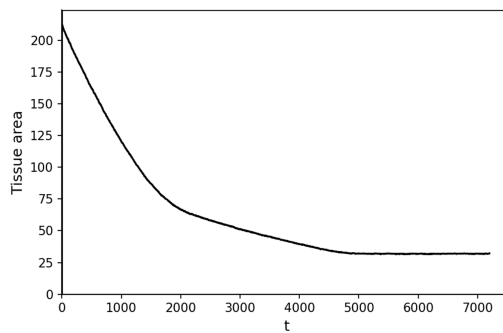
Table 4.3.



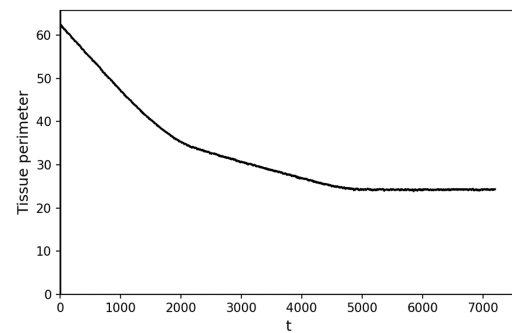
(a) Average cell area versus time.



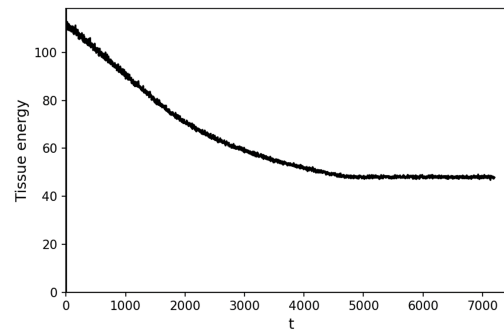
(b) Average cell perimeter versus time.



(c) Tissue area versus time.



(d) Tissue perimeter versus time.



(e) Tissue energy versus time.

Figure 4.9: The average cell area, average cell perimeter, tissue area, tissue perimeter, and total energy of the tissue visualised in Figure 4.8. Model parameters: Table 4.3.

The terminal displays the progress of every *solver* process that is currently running. Each process writes the data from the cell and vertex graphs as well as the time series data for the average cell area, average cell perimeter, tissue area, tissue perimeter, and total energy of the tissue to text files in the corresponding output directory.

At the end of each *solver* process, CelluLink reads the data files produced over the course of the simulation and generates the following figures using the `Matplotlib` package: Snapshots of the tissue at $t = 0$ and at the end of five equally-spaced time intervals between $t = 0$ and the final timestep (Figure 4.8), and time series plots of average cell area, average cell perimeter, tissue area, tissue perimeter, and tissue energy (Figure 4.9). These figures are saved to the output directory corresponding to the *solver* process. The images in Figures 4.8 and 4.9 were generated by simulating the modified Suzuki model using the forward Euler method.

In this chapter, we compared some of the available computational tools for cell-based modelling and developed CelluLink, a new software package for vertex models, and tailored it to meet the requirements of the models explored in this doctoral work. The CelluLink source code employs procedural programming rather than the object-oriented programming paradigm. This makes it easier to modify the code and affords users more convenience in implementing new features and models. CelluLink's most powerful feature is that it has been designed to leverage parallel processing to make parameter sweeps more convenient. All of the models in the following chapters will be simulated using CelluLink.

Chapter 5

The modified Suzuki model

In Chapter 3, we reviewed the Suzuki model in detail and highlighted its limitations. In this chapter, we begin addressing these limitations by revising some of the assumptions of the Suzuki model to better reflect the biology and simplify its structure, creating a model we refer to as the modified Suzuki model. We then simulate the modified Suzuki model in CelluLink and compare its behaviour to the Suzuki model.

The simplified structure of the modified Suzuki model allows us to study it analytically. So, we derive a bifurcation diagram to explore the behaviour of the model at equilibrium. For the sake of simplicity, we do not consider the effects of the ratchet-like mechanism and Ca^{2+} in this analysis. Since there is no straightforward methodology that directly relates experimentally measurable quantities e.g. Young's modulus, traction stress etc. to the vertex model parameters, the bifurcation diagram becomes a useful aid in identifying parameter regimes for which the modified Suzuki model yields a stable hexagonal network - which corresponds to a biologically realistic tissue.

We then use the results obtained from the analytical work to investigate the conditions required to activate the ratchet-like mechanism and ensure that the tissue contracts to its target size. Finally, we conduct a systematic parameter sweep of the modified Suzuki model to numerically investigate how the parameters impact the rate of tissue contraction and the final size attained by the tissue in the presence of both the ratchet-like mechanism and Ca^{2+} activity. This study informs our understanding of the parameter sensitivity of the modified Suzuki model and helps us identify the parameter ranges over which the modified Suzuki model is stable.

5.1 Modelling assumptions

Based on our discussions with our experimental collaborators, Neophytos Christodoulou and Paris Skourides (University of Cyprus), and bearing in mind the ease of implementation of certain features, we revised some of the assumptions of the Suzuki model (Chapter 3) in order to make the model more biologically accurate. Our modelling assumptions are as follows:

- *Shape of the modelled tissue*

Suzuki et al [196] modelled the initial configuration of their tissue using Voronoi diagrams. The constituent cells were modelled as irregular polygons having 5, 6, 7, or 8 sides, and positioned in an approximately circular region. In contrast, we model the cells as regular hexagons arranged in a honeycomb lattice such that the modelled tissue is hexagon-shaped because:

- (i) The symmetry of a regular polygon allows us to study the steady-state behaviour of the cells analytically and identify bifurcations (Section 5.3).
- (ii) It is more straightforward to implement a hexagonal honeycomb lattice than a Voronoi diagram generator in CelluLink.
- (iii) It is sufficient to approximate the circular shape of the anterior neural plate we are modelling.

- *Number of cells*

Based on experimental observations, it is reasonable to assume that the anterior neural plate consists of ≈ 250 cells [33]. Suzuki et al [196] modelled their tissue as a sheet comprised of 256 cells. However, our choice of tissue shape imposes a constraint on the number of cells that can make up our hexagon-shaped tissue (Equation (4.1)) i.e. the closest we can get to 250 cells is 271 cells, which is still a reasonably good approximation.

- *Cell size*

The tissue modelled in Suzuki et al [196] has an initial area of 200 a.u. (arbitrary units or non-dimensional units) and comprises 256 cells of different sizes. So, the initial average cell area can be taken as $\frac{200}{256} \approx 0.78$ a.u. Therefore, we assign each cell, modelled as a regular hexagon in our model, an initial area = 0.78, resulting in an edge length ≈ 0.55 for the hexagon.

In *Xenopus*, the average apical surface area of anterior neural plate cells at the onset of apical constriction (AC) is $250 \mu m^2$ [33, 34].

- *Neighbour exchanges*

The Suzuki model takes into account the effect of neighbour exchanges, implemented via the T1 process. However, neighbour exchanges are characteristic of cell intercalation¹ events, which drive convergent extension on the posterior neural plate [34]. In contrast, we are interested in modelling AC, which occurs on the anterior neural plate. Since, cell intercalation and AC do not occur concomitantly, we choose to ignore the effect of neighbour exchanges.

- *Probability of edge activation*

Imaging data from the *Xenopus* embryo reveals that almost all segments of the cell membrane contract *in vivo* simultaneously during cell contraction [32, 33]. Therefore, we decided to neglect the parameter p_e , probability of cell edge activation, used by Suzuki et al [196] for the sake of simplicity. In effect, we considered a special case of that parameter ($p_e = 1$), where all cell edges would experience elevated line tension in an activated cell.

- *Cell activation period*

In Suzuki et al [196], if an activated cell experienced a Ca^{2+} transient before its current activation period elapsed, its remaining activation time would be extended by τ . In reality, very high levels of cytosolic Ca^{2+} for extended periods of time can trigger apoptosis², so cells have innate mechanisms to remove the excess Ca^{2+} . A cell would thus dissipate previously accumulated Ca^{2+} prior to experiencing another elevation in Ca^{2+} level. In our model, therefore, an activated cell is not allowed to experience a Ca^{2+} transient until its activation period expires.

Since our implementation of the Suzuki model uses the same equations for vertex dynamics and the ratchet-like mechanism (Equations (3.7)-(3.10)) but differs with regards to our implementation of cell activation and the cell and tissue shape, we refer to it as **the modified Suzuki model**. As is typical of vertex models, all quantities are expressed in arbitrary or non-dimensional units.

¹**Cell intercalation** A process that occurs throughout animal development and in which neighbouring cells exchange places.

²**Apoptosis** A form of programmed cell death occurring in multicellular organisms.

5.2 Comparing with the Suzuki model

To compare with the Suzuki model, we simulate the modified Suzuki model in CelluLink to reproduce some of the key results of Suzuki et al [196] (Figures 5.1a & 5.2a). This also serves as the most straightforward way to test whether CelluLink is functioning as intended. All of the simulations in this chapter were performed using the forward Euler method. Figures 5.1b & 5.2b capture the results depicted in Figures 5.1a & 5.2a, respectively.

Figure 5.1b depicts a successful reproduction of the effect of the Ca^{2+} transients (*Pulse*) and ratchet-like mechanism (*Acn*) on the simulated tissue. As seen in 5.1a, without the *Acn* component, i.e., in the absence of the ratchet-like mechanism, the tissue does not contract regardless of the presence of the *Pulse* component. The *Acn* component is essential for tissue contraction in the model and the *Pulse* component expedites the rate of contraction.

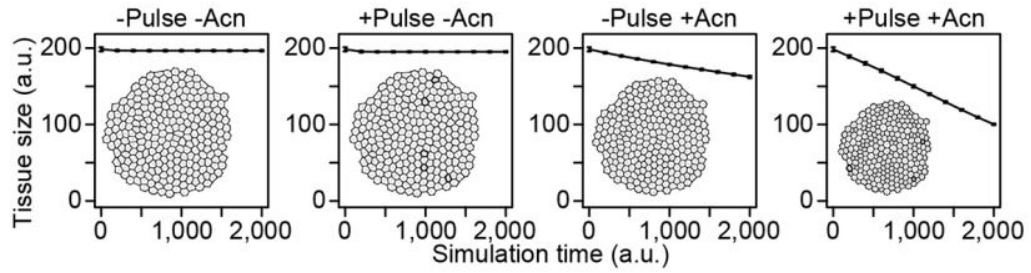
The plots for $(-Pulse, -Acn)$, $(+Pulse, -Acn)$, and $(-Pulse, +Acn)$ in Figure 5.1b show good agreement with the corresponding cases in Figure 5.1a. In the plot for $(+Pulse, +Acn)$ in Figure 5.1b, we note that the reduction in tissue area is steeper compared to the corresponding case in Figure 5.1a. This discrepancy most likely arises as a result of the differences in our respective implementations of the vertex model.

Upon close inspection of the results of Suzuki et al [196], it can be observed that cells do not exchange neighbours during tissue contraction over the course of their simulation i.e. the T1 process is not utilized. Therefore, it is unlikely that the difference in the rate of tissue contraction is an outcome of not including T1 transitions. Additionally, Suzuki et al [196] had also set $p_e = 1$ for their simulation. So, it is possible that the discrepancy stems from our choice of tissue shape, the number of cells, our assumption regarding the cell activation period, or some combination of these factors.

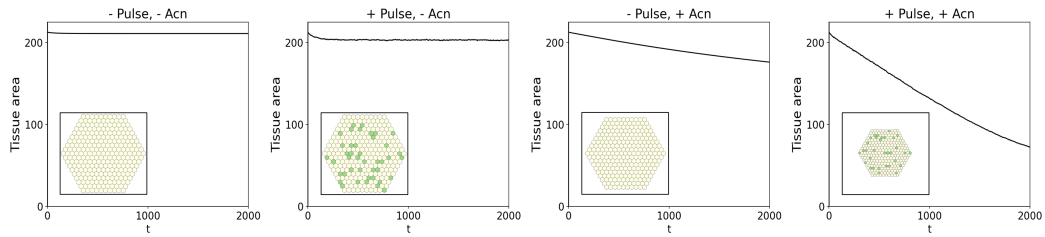
Figure 5.2b shows the successful reproduction of another key result of the Suzuki model and shows that while denser pulses produce a sharp drop in tissue area over a small period of time, sparser pulses yield a greater reduction in tissue area over the entire runtime. On comparing Figures 5.2a & 5.2b, it can be seen that there is greater spacing between the line plots in the case of the latter. This difference too stems from the steeper reduction in tissue area observed in our implementation of the vertex model.

Parameter	Value
Cells	271
p_c	0.025
δt	0.2
K_n^A	0.3
K_n^P	0.2
μ	1
κ_A	1
κ_P	0.001
ω_A	0.6
ω_P	0.8
A_n^0 (initial)	1
P_n^0 (initial)	5
A_n^0 (minimum)	0.3
P_n^0 (minimum)	2
T_{0n}	0.1
ξ	0.05
τ	5

Table 5.1: Parameter values for Figures 5.1b and 5.2b.

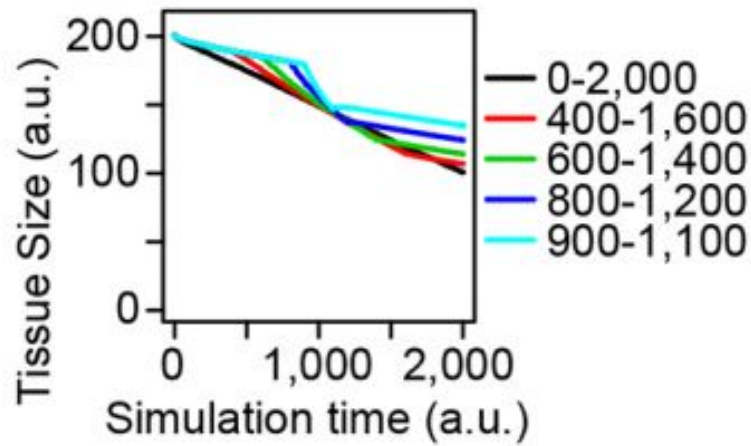


(a) The effect of the Ca^{2+} transients and ratchet-like mechanism on tissue contraction in the Suzuki model [196].

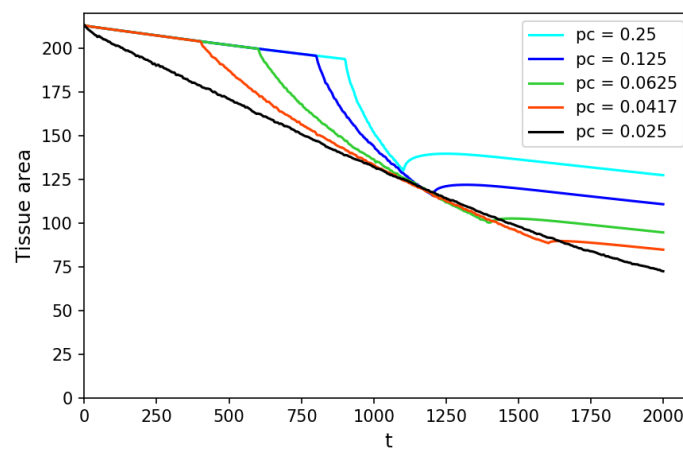


(b) The effect of the Ca^{2+} transients and ratchet-like mechanism on tissue contraction in the modified Suzuki model.

Figure 5.1: The effect of the Ca^{2+} transients (Pulse) and ratchet-like mechanism (Acn) on tissue contraction in the Suzuki and modified Suzuki models. -/+ Pulse indicates the absence/presence of Ca^{2+} flashes, +/- Acn indicates the whether the ratchet-like mechanism was active/inactive in the model. Model parameters: Table 5.1.



(a) Time evolution of the simulated tissue for different activation windows in the Suzuki model [196].



(b) Time evolution of the simulated tissue for different activation windows in the modified Suzuki model.

Figure 5.2: Tissue contraction over the simulation runtime for different Ca^{2+} -activation windows in the Suzuki and modified Suzuki models. Since the total number of Ca^{2+} flashes experienced by the tissue within the activation window is the same for each case, each case uses a different value of p_c (0 - 2000: 0.025, 400 - 1600: 0.0417, 600 - 1400: 0.0625, 800 - 1200: 0.125, 900 - 1100: 0.25). Model parameters: Table 5.1.

5.3 Deriving the bifurcation diagram

To explore the full range of equilibrium behaviours displayed by the modified Suzuki model, we derive its bifurcation diagram using the results of Magno et al [115]. Their analytical study revealed the complete spectrum of single-cell behaviour and tissue packing for their 2D vertex model. We follow the derivation for their bifurcation diagram and then apply their results to the modified Suzuki model.

The derivation in Magno et al [115]

In their analysis, Magno et al [115] start with the phenomenological energy function used to model cell surface mechanics, which takes the general form

$$E = \lambda_a(a - A)^2 + \lambda_p(p - P)^2 + Jp, \quad (5.1)$$

where p and a are the perimeter and area of the cell. The function uses five parameters for the cellular properties: J , an energy per contact length due to adhesion to other cells or the surrounding medium; P , the membrane target length (resting length); and A , the target cell area (resting area); and the constants λ_p and λ_a (comparable to elastic constants), which weigh the relative tension contributions of actin-myosin contraction and cell deformations, respectively.

The term $\lambda_a(a - A)^2$ is associated with the cell's compressibility or pressure - the energy possessed by the cell by virtue of its area deviation relative to the target area, the term $\lambda_p(p - P)^2$ is associated with the contractility of the cell cortex i.e. the cortical tension, and the term Jp is associated with the adhesion between two interfaces, such as cell-cell or cell-extracellular contacts i.e. the adhesion-driven tension.

To derive the equations for a hexagonal cell shape, we start by writing the equations for a general family of shapes, for which the perimeter and area can be parametrised as $p = k_p l$ and $a = k_a l^2$, respectively, where l is an arbitrary length factor for any cell shape (l could be the radius, for a circular cell shape, or the edge length, for a polygonal cell shape). Substituting $a = k_a l^2$, $p = k_p l$, $A = k_a L_a^2$ and $P = k_p L_p$ into Equation (5.1) yields

$$E = \lambda_a (k_a l^2 - k_a L_a^2)^2 + \lambda_p (k_p l - k_p L_p)^2 + J k_p l, \quad (5.2)$$

where L_p and L_a are the reciprocal target lengths of the target perimeter P and area A . From the energy function (Equation (5.2)), we will derive two important quantities that will aid us in understanding the cell behaviour at equilibrium - the interfacial tension and pressure.

The cell's interfacial tension (γ), the work required to extend the membrane by a unit area, is expressed in 2D as the change in energy per unit perimeter length and depends on both the cortical and the adhesion-driven tension:

$$\begin{aligned} \gamma &= \frac{\partial E}{\partial p} \\ &= J + 2k_p \lambda_p (l - L_p). \end{aligned} \quad (5.3)$$

The interfacial tension can be split up into a length-independent component, $J - 2k_p \lambda_p L_p$, and a component which depends linearly on the perimeter length, $2k_p \lambda_p l$. We can thus write

$$\gamma = \tau + 2k_p \lambda_p l, \quad (5.4)$$

where τ is defined as the length-independent component of the interfacial tension. The sign of τ is undetermined, while the length-dependent component is always non-negative.

Under positive interfacial tension, energy reduction leads to reduction in the length of the interfaces resulting in perimeter minimization. When the interfacial tension is negative, the tendency of reducing the perimeter for a determined area is lost, as there is no additional energy cost in increasing the length of the interfaces - in fact, the tendency is to increase the length of the interfaces, causing cells which are constrained in area irregular and unpredictable shapes. From Equation (5.4), it follows that for the interfacial tension to be positive at the equilibrium length l^* , the following condition needs to be satisfied:

$$\begin{aligned}
\tau + 2k_p\lambda_p l^* &> 0 \\
\implies l^* &> -\frac{\tau}{2k_p\lambda_p}.
\end{aligned} \tag{5.5}$$

The pressure (Π) within the cell that contributes to a force per unit membrane area can be represented as the work required (from an external agent) per unit area decrease or, equivalently, the decrease in energy per unit area increase:

$$\begin{aligned}
\Pi &= -\frac{\partial E}{\partial a} \\
&= -2k_a\lambda_a (l^2 - L_a^2).
\end{aligned} \tag{5.6}$$

So, to predict the qualitative behaviour of the cell, with regard to its shape, it is important to determine the sign of the interfacial tension at the equilibrium length l^* . To determine the equilibrium length, we first take the derivative of E (Equation (5.2)) with respect to l and substitute the expressions from Equations (5.3) and (5.6) which gives us

$$\begin{aligned}
\frac{\partial E}{\partial l} &= 2\lambda_a k_a^2 (l^2 - L_a^2) 2l + 2\lambda_p k_p^2 (l - L_p) + Jk_p \\
&= 2k_a l (2k_a\lambda_a (l^2 - L_a^2)) + k_p (J + 2\lambda_p k_p (l - L_p)) \\
&= -2k_a l \Pi + k_p \gamma.
\end{aligned} \tag{5.7}$$

The equilibrium length (l^*) can then be found by solving for $\frac{\partial E}{\partial l} = 0$ as follows,

$$\left. \frac{\partial E}{\partial l} \right|_{l=l^*} = -2k_a l^* \Pi(l^*) + k_p \gamma(l^*) = 0. \tag{5.8}$$

From Equation (5.8), it is clear that at equilibrium $k_p \gamma(l^*) = 2k_a l^* \Pi(l^*)$. The requirement $\gamma(l^*) > 0$ therefore also implies that $l^* \Pi(l^*) > 0$, and thus

$$\begin{aligned}
-2k_a\lambda_a l^* (l^{*2} - L_a^2) &> 0 \\
\implies l^* &< L_a,
\end{aligned} \tag{5.9}$$

since we are only considering cases where $l^* > 0$ as it is nonsensical to consider $l^* < 0$. By combining the inequalities (Equations (5.5) and (5.9)), we obtain the requirement for an equilibrium length l^* to have a positive interfacial tension, which is

$$-\frac{\tau}{2k_p\lambda_p} < l^* < L_a. \quad (5.10)$$

Two conclusions can be drawn from this inequality. First, a solution is only possible when

$$\begin{aligned} -\frac{\tau}{2k_p\lambda_p} &< L_a \\ \implies \tau &> -2k_p\lambda_p L_a. \end{aligned} \quad (5.11)$$

Consequently, the interfacial tension at $l^* > 0$ is going to be negative for any $\tau < -2k_p\lambda_p L_a$, independently of the specific value of l^* . Secondly, when $\tau > -2k_p\lambda_p L_a$, Equation (5.10) is always fulfilled, and hence it follows that the interfacial tension at l^* has to be positive. This gives us our **first bifurcation line** at

$$\tau = -2k_p\lambda_p L_a. \quad (5.12)$$

The condition $\tau > -2k_p\lambda_p L_a$ thus determines an important parameter range in which the cell is stable and its shape is predictable. When the cell becomes unstable, its shape is hard to predict and will critically depend on the specific implementation of the cell surface and surface dynamics within the diverse model formalisms. It should be noted that even if the cell shape becomes unpredictable, there is no inherent conflict between fulfilling the area constraint (equivalent to solving $\Pi(a^*) = 0$) and fulfilling the effective perimeter constraint (equivalent to solving $\gamma(p^*) = 0$). When the cell shape is stable, the equilibria can be analysed as follows next.

The number of roots of the cubic equation $\frac{\partial E}{\partial l} = 0$ (i.e. the equilibria) can be determined by analysing the properties of the cubic function $\frac{\partial E}{\partial l}$. To aid our analysis, we can rearrange the terms of Equation (5.7) as follows,

$$\begin{aligned}
\frac{\partial E}{\partial l} &= k_p (J + 2\lambda_p k_p (l - L_p)) + 2k_a l (2k_a \lambda_a (l^2 - L_a^2)) \\
&= k_p \left(\tau + 2\lambda_p k_p l - 2\frac{k_a}{k_p} l (-2\lambda_a k_a (l^2 - L_a^2)) \right) \\
&= k_p (\tau + 2\lambda_p k_p l + \beta l (l^2 - L_a^2)) \\
&= k_p \left(\tau + \beta l \left(l^2 - \left(L_a^2 - \frac{k_p^2 \lambda_p}{2k_a^2 \lambda_a} \right) \right) \right) \\
&= k_p (\tau + \beta l (l^2 - 3\epsilon)), \tag{5.13}
\end{aligned}$$

where $\beta = \frac{4k_a^2 \lambda_a}{k_p}$ and $\epsilon = \frac{L_a^2}{3} - \frac{k_p^2 \lambda_p}{6k_a^2 \lambda_a}$. Since, Equation (5.13) lacks a second degree term, it is a special form of cubic equation - the depressed cubic equation.

With Equation (5.13), we can assess how the number of equilibria depends on the two composite parameters, τ and ϵ . If $\epsilon < 0$, the right-hand side term $\beta l (l^2 - 3\epsilon)$ cannot become negative (since it is nonsensical to consider $l < 0$), so by itself this term does not give rise to non-trivial equilibria. A non-trivial equilibrium can only occur when τ balances the monotonically increasing right-hand side term. In this case, the equilibrium length l^* is positive if $\tau < 0$. This solution is unique and stable (since $\frac{\partial^2 E}{\partial l^2} > 0$ for $l = l^*$ results in a local minima). If $\tau > 0$, the only solution to Equation (5.13) is negative. Consequently, for $\epsilon < 0$ and $\tau > 0$, the only equilibrium is the trivial solution $l^* = 0$ which is stable, whereas when $\epsilon < 0$ and $\tau < 0$, the trivial solution $l^* = 0$ is unstable.

If $\epsilon > 0$, the right-hand side term $\beta l (l^2 - 3\epsilon)$ does not increase monotonically and, hence, there can be three real roots. Conveniently, the possible equilibria and their stability can be understood by visualising the value τ as a vertical shift of the cubic function $\frac{\partial E}{\partial l}$. By starting with $\tau = 0$ (for which $\frac{\partial E}{\partial l}$ is an anti-symmetric function) and then shifting the curve vertically, all possible equilibria combinations occur successively.

As the curve transitions from $\tau < 0$ to $\tau > 0$, the number of equilibria changes from two to three. Magno et al [115] note that this transition is a non-standard bifurcation that bears resemblance to a transcritical bifurcation but does not formally correspond to it. So, they refer to it as a ‘pseudo-transcritical’ bifurcation. Consequently, the **second bifurcation line** is defined by the condition

$$\tau = 0, \tag{5.14}$$

Condition	Equilibria	
$\tau < -2k_p\lambda_p L_a$	-	
$-2k_p\lambda_p L_a < \tau < 0$	1 stable, 1 unstable (trivial)	
$0 < \tau < 2\beta\epsilon^{\frac{3}{2}}$	$\epsilon > 0$	1 stable, 1 unstable, 1 stable (trivial)
	$\epsilon < 0$	1 stable (trivial)
$2\beta\epsilon^{\frac{3}{2}} < \tau$	1 stable (trivial)	

Table 5.2: The possible equilibria for a cell whose energy function is described by Equation (5.2), and the conditions that must be satisfied to obtain them.

with $\tau < 0$ resulting in an unstable trivial equilibrium, and $\tau > 0$ resulting in a stable one.

Upon increasing the value of τ further, we will encounter a transition from three equilibria to one equilibrium. This transition corresponds to a fold bifurcation, which takes place when the minimum of the $\frac{\partial E}{\partial l}$ function equals zero. The value of l at which $\frac{\partial E}{\partial l}$ has a minimum can be determined by setting $\frac{\partial^2 E}{\partial l^2} = 0$. In other words, the third bifurcation line can be found when the inflection point of the energy function coincides with the equilibrium length l^* . Taking the derivative of Equation (5.13) with respect to l , we get

$$\frac{\partial^2 E}{\partial l^2} = 3k_p\beta (l^2 - \epsilon). \quad (5.15)$$

Setting $\frac{\partial^2 E}{\partial l^2} = 0$, we find that $l = \sqrt{\epsilon}$ at the inflection point. Thus, the aggregate parameter ϵ can be interpreted as the inflection point of the energy function squared, with negative values of ϵ implying that there is no inflection point (as described previously). The **third bifurcation line** is then given by:

$$\begin{aligned} \frac{\partial E}{\partial l} \Big|_{l=\sqrt{\epsilon}} &= 0 \\ \implies k_p \left(\tau - 2\beta\epsilon^{\frac{3}{2}} \right) &= 0 \\ \implies \tau &= 2\beta\epsilon^{\frac{3}{2}}. \end{aligned} \quad (5.16)$$

Thus, we obtain all the possible equilibrium states for a cell whose energy function is described by Equation (5.2). The equilibria and the corresponding

conditions that must be satisfied to obtain them have been summarised in Table 5.2. Note that in the case where $\tau < -2k_p\lambda_p L_a$, the shape of the cell is hard to predict, and the parametrisations $p = k_p l$ and $a = k_a l^2$ may no longer necessarily apply. Therefore, we can no longer use Equation (5.13) to derive the equilibria. Note that because we model the cells as hexagons, we can parametrise the perimeter p and area a as $P = 6l$ and $a = \frac{3\sqrt{3}}{2}l^2$. Thus, we will take $k_p = 6$ and $k_a = \frac{3\sqrt{3}}{2}$ moving forward.

Deriving the bifurcation diagram for the modified Suzuki model

To apply these results to the modified Suzuki model, we start by introducing a mapping between the notation used by Magno et al [115] and the one used in the Suzuki model. Recall the energy function used in the Suzuki model:

$$U = \sum_n^{N_{cells}} \frac{K_n^A}{2} \left(\frac{A_n}{A_n^0} - 1 \right)^2 A_n^0 + \sum_n^{N_{cells}} \frac{K_n^P}{2} \left(\frac{P_n}{P_n^0} - 1 \right)^2 P_n^0 + \sum_n^{N_{cells}} \sum_{\langle ij \rangle}^{edge} T_n^{\langle ij \rangle} L_n^{\langle ij \rangle}. \quad (3.4 \text{ expanded})$$

Equation (3.4) describes the energy of the entire tissue being modelled. Magno et al [115] found that tissue properties are a manifestation of the mechanical properties of individual cells and not of collective cell behaviour. So, knowledge of the expected cell shape combined with single cell analysis is sufficient to account for the whole range of observed tissue behaviour. Following that line of thought, we perform single cell analysis for the modified Suzuki model where the energy function for a single cell is given by

$$\begin{aligned} U_{cell} &= \frac{K^A A^0}{2} \left(\frac{A}{A^0} - 1 \right)^2 + \frac{K^P P^0}{2} \left(\frac{P}{P^0} - 1 \right)^2 + TP \\ &= \frac{K^A}{2A^0} (A - A^0)^2 + \frac{K^P}{2P^0} (P - P^0)^2 + TP. \end{aligned} \quad (5.17)$$

where we drop the subscript n since we are analysing a single cell. Drawing a correspondence with the notation of Magno et al [115], we get

$$\lambda_a \rightarrow \frac{K^A}{2A^0}, \quad (5.18a)$$

$$\lambda_p \rightarrow \frac{K^P}{2P^0}, \quad (5.18b)$$

$$J \rightarrow T, \quad (5.18c)$$

$$A (= k_a L_a^2) \rightarrow A^0, \quad (5.18d)$$

$$P (= k_p L_p) \rightarrow P^0. \quad (5.18e)$$

To derive the bifurcation diagram for the modified Suzuki model, we must define meaningful aggregate parameters. So, we nondimensionalise the energy function (Equation (5.17)) and obtain the expression for nondimensional energy

$$\begin{aligned} \bar{U} &= \frac{U_{cell}}{K^P P^0} \\ &= \frac{1}{2} \frac{K^A A^0}{K^P P^0} \left(\frac{A}{A^0} - 1 \right)^2 + \frac{1}{2} \left(\frac{P}{P^0} - 1 \right)^2 + \frac{TP}{K^P P^0} \\ &= \frac{1}{2} \bar{K} (a - 1)^2 + \frac{1}{2} (p - 1)^2 + \bar{T} p, \end{aligned} \quad (5.19)$$

where $a = \frac{A}{A^0}$, $p = \frac{P}{P^0}$, $\bar{K} = \frac{K^A A^0}{K^P P^0}$ and $\bar{T} = \frac{T}{K^P P^0}$ are the normalised area, normalised perimeter, normalised area elasticity and normalised line tension, respectively. We shall derive the bifurcation diagram for the modified Suzuki model using the aggregate parameters \bar{K} and \bar{T} . In the notation of Magno et al [115], \bar{K} and \bar{T} correspond to

$$\bar{K} \rightarrow \frac{\lambda_a}{\lambda_p} \left(\frac{k_a L_a^2}{k_p L_p} \right)^2, \quad (5.20)$$

$$\bar{T} \rightarrow \frac{J}{2\lambda_p k_p L_p}. \quad (5.21)$$

The relationship between \bar{K} and \bar{T} is given by

$$\bar{K} = \frac{K^A A^0}{T P^0} \bar{T}. \quad (5.22)$$

Recall that the *first bifurcation line*, that determines negative or positive interfacial tension, is given by

$$\tau = -2k_p\lambda_p L_a. \quad (5.12 \text{ revisited})$$

The length-independent component of interfacial tension is defined as $\tau = J - 2k_p\lambda_p L_p$. Substituting this expression into Equation (5.12) gives us

$$J = 2k_p\lambda_p(L_p - L_a). \quad (5.23)$$

Substituting Equation (5.23) into Equation (5.21), we get

$$\begin{aligned} \bar{T} &= \frac{2k_p\lambda_p(L_p - L_a)}{2k_p\lambda_p L_p} \\ &= 1 - \frac{L_a}{L_p} \\ &= 1 - \frac{k_p}{\sqrt{k_a}} \frac{\sqrt{A^0}}{P^0} && \text{(substituting 5.18d and 5.18e)} \\ &= 1 - 3.722 \frac{\sqrt{A^0}}{P^0}, \end{aligned} \quad (5.24)$$

which is the **first bifurcation line (B1)** for the modified Suzuki model.

Similarly, we use the condition

$$\tau = 0 \quad (5.14 \text{ revisited})$$

to obtain the corresponding expression for J :

$$J = 2k_p\lambda_p L_p. \quad (5.25)$$

Substituting Equation (5.25) into Equation (5.21) then gives us the **second bifurcation line (B2)** for the modified Suzuki model:

$$\bar{T} = 1. \quad (5.26)$$

For the *third bifurcation line*, we use the condition

$$\tau = 2\beta\epsilon^{\frac{3}{2}}, \quad (5.16 \text{ revisited})$$

where $\beta = \frac{4k_a^2\lambda_a}{k_p}$ and $\epsilon = \frac{L_a^2}{3} - \frac{k_p^2\lambda_p}{6k_a^2\lambda_a}$, to obtain the corresponding expression for J :

$$J = 2k_p\lambda_p L_p + \frac{8k_a^2\lambda_a}{k_p}\epsilon^{\frac{3}{2}}. \quad (5.27)$$

After rewriting Equation (5.22) in the notation of Magno et al [115] and rearranging the terms, we substitute Equation (5.27) to get

$$\begin{aligned} \bar{T} &= \left(\left(2k_p\lambda_p L_p + \frac{8k_a^2\lambda_a}{k_p}\epsilon^{\frac{3}{2}} \right) \frac{k_p L_p}{2\lambda_a(k_a L_a^2)^2} \right) \bar{K} \\ &= \left(\frac{\lambda_p}{\lambda_a} \left(\frac{k_p L_p}{k_a L_a^2} \right)^2 + \frac{4L_p}{L_a^4}\epsilon^{\frac{3}{2}} \right) \bar{K}. \end{aligned} \quad (5.28)$$

Rearranging the terms of Equation (5.28), we obtain an expression for ϵ :

$$\epsilon = \left(\frac{L_a^4}{4L_p} \frac{\bar{T} - 1}{\bar{K}} \right)^{\frac{2}{3}}. \quad (5.29)$$

Recalling the original definition of ϵ , the terms can be rearranged as follows,

$$\begin{aligned} \epsilon &= \frac{L_a^2}{3} - \frac{k_p^2\lambda_p}{6k_a^2\lambda_a} \\ &= \frac{L_a^2}{3} \left(1 - \frac{\lambda_p k_p^2}{2\lambda_a k_a^2 L_a^2} \right) \\ &= \frac{L_a^2}{3} \left(1 - \frac{1}{2} \frac{L_a^2}{L_p^2} \frac{\lambda_p}{\lambda_a} \left(\frac{k_p L_p}{k_a L_a^2} \right)^2 \right) \\ &= \frac{L_a^2}{3} \left(1 - \frac{1}{2} \left(\frac{L_a}{L_p} \right)^2 \frac{1}{\bar{K}} \right). \end{aligned} \quad (5.30)$$

By equating the right-hand sides of Equations (5.30) and Equation (5.29) and rearranging the terms, we get the **third bifurcation line (B3)** for the modified

Suzuki model:

$$\begin{aligned}
\bar{T} &= 1 + \frac{4}{27} \frac{L_p}{L_a} \left(1 - \frac{1}{2\bar{K}} \left(\frac{L_a}{L_p} \right)^2 \right)^{\frac{3}{2}} \bar{K} \\
&= 1 + \frac{4}{27} \frac{\sqrt{k_a}}{k_p} \frac{P^0}{\sqrt{A^0}} \left(1 - \frac{k_p^2 A^0}{2k_a P^{0^2}} \frac{1}{\bar{K}} \right)^{\frac{3}{2}} \bar{K} \\
&= 1 + 0.0398 \frac{P^0}{\sqrt{A^0}} \left(1 - 6.9284 \frac{A^0}{P^{0^2}} \frac{1}{\bar{K}} \right)^{\frac{3}{2}} \bar{K}. \tag{5.31}
\end{aligned}$$

The three bifurcation lines: B1, B2, and B3 divide the \bar{T} - \bar{K} parameter space into four regions as visualised in Figure 5.3. The intersection of B2 and B3 can be found by setting $\bar{T} = 1$ in Equation (5.31), which gives us $\bar{K} = 6.9284 \frac{A^0}{P^{0^2}}$.

It is interesting to note that, unlike the bifurcation lines derived in [62] and [115], the bifurcation lines for the modified Suzuki model depend upon the target area A^0 and target perimeter P^0 . Most likely, this is because the potential energy terms in the Suzuki model and, by extension, the modified Suzuki model are modulated by additional target area and target perimeter terms, respectively (Section 3.1.2).

The conditions corresponding to the regions are summarised in Table 5.3. When (\bar{T}, \bar{K}) lies in Region I, the cell shape is unpredictable at equilibrium. In the multicellular case, Region I would yield a *soft network* because the system is ‘soft’ with vanishing shear modulus and behaves more like a liquid in which a cell’s shape can change without any change in the value of the cell’s energy function and cells can move past one another easily [62]. In Region II, the cell shape is a regular hexagon at equilibrium, which results in a *hexagonal network* in the multicellular case. In Region IV, the cell contracts until it vanishes. Region III can yield either a stable *hexagonal network* like Region II or a *vanishing cell* like Region IV, depending upon the initial condition.

To validate our analytical results, we simulate the modified Suzuki model for different values of T , corresponding to the different regions of the parameter space, leaving all the other parameters unchanged. Note that we do not consider the effects of Ca^{2+} and the ratchet-like mechanism for this analysis. The parameter values used in the simulation are listed in Table 5.4.

However, the equilibrium state is determined not only by the mechanical parameter but also by the initial condition. In this case, the initial condition is

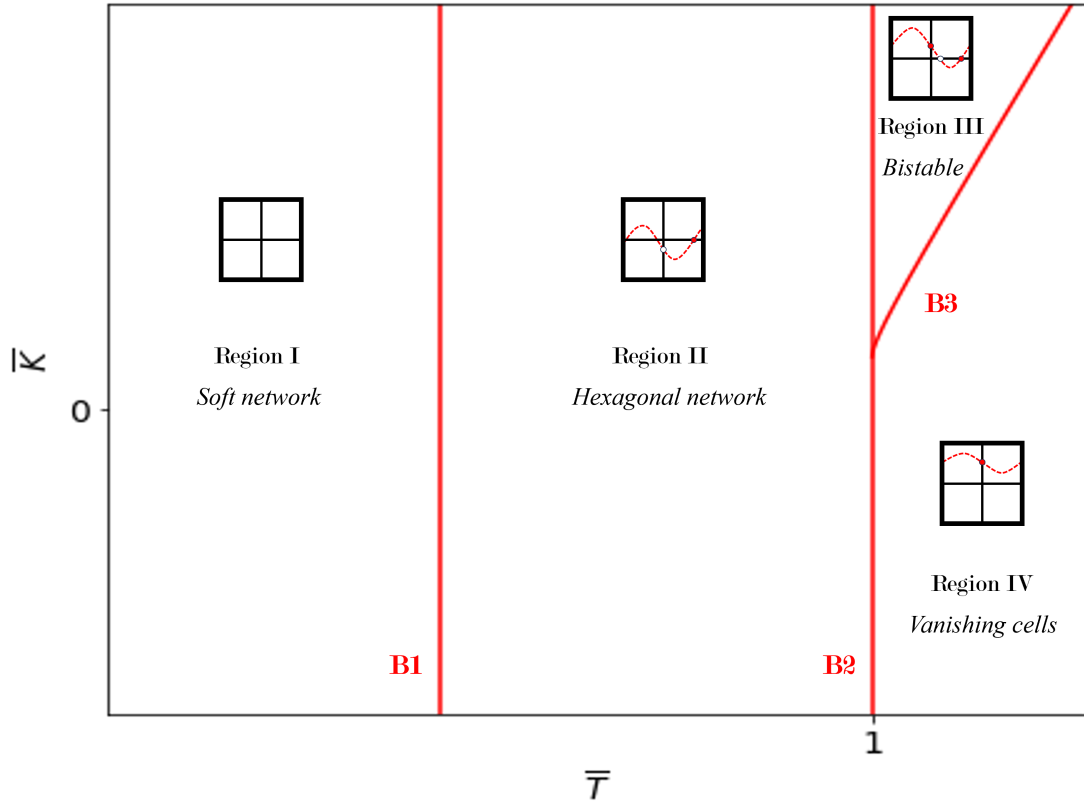


Figure 5.3: The parameter space for the modified Suzuki model in terms of the aggregate parameters \bar{T} and \bar{K} . The bifurcation lines B1, B2, and B3 divide the parameter space into four regions. The small windows depict the number and the nature of the equilibria corresponding to each region i.e. the roots of the cubic equation $\frac{\partial U_{cell}}{\partial L} = 0$, where L is the edge length of the hexagonal cell. Stable and unstable equilibria are indicated by the solid and hollow circles, respectively. In Region I, the cell shape is unpredictable so it is meaningless to solve the cubic equation for equilibria. Cell behaviour under equilibrium conditions will depend on both, the region of the parameter space the model is operating in and, the initial condition of the cell.

Region	Condition
Region I	$\bar{T} < 1 - 3.722 \frac{\sqrt{A^0}}{P^0}$
Region II	$1 - 3.722 \frac{\sqrt{A^0}}{P^0} < \bar{T} < 1$
Region III	$1 < \bar{T} < 1 + 0.0398 \frac{P^0}{\sqrt{A^0}} \left(1 - 6.9284 \frac{A^0}{P^{0^2}} \frac{1}{\bar{K}}\right)^{\frac{3}{2}} \bar{K}$
Region IV	$\bar{K} > 6.9284 \frac{A^0}{P^{0^2}}$ $1 + 0.0398 \frac{P^0}{\sqrt{A^0}} \left(1 - 6.9284 \frac{A^0}{P^{0^2}} \frac{1}{\bar{K}}\right)^{\frac{3}{2}} \bar{K} < \bar{T}$
	$\bar{K} < 6.9284 \frac{A^0}{P^{0^2}}$ $1 < \bar{T}$

Table 5.3: The four regions of the parameter space of the modified Suzuki model, as visualised in Figure 5.3, and the conditions that correspond to them.

the initial edge length of the regular hexagonal cell l_{in} . To estimate the required value of l_{in} , we must calculate the equilibria of the system by solving for the roots of $\frac{\partial U_{cell}}{\partial l} = 0$. By taking the partial derivative of Equation (5.17) (considering $P = 6l$ and $A = \frac{3\sqrt{3}}{2}l^2$) with respect to l and equating it to zero, we obtain the cubic equation

$$\left(\frac{9}{4} \frac{K^A}{A^0}\right) l^3 + \left(6 \frac{K^P}{P^0} - \frac{\sqrt{3}}{2} K^A\right) l + (T - K^P) = 0. \quad (5.32)$$

Using the parameter values in Table 5.4, we know that $\bar{K} = 0.3$. For this value of \bar{K} , the bifurcation points are at $\bar{T} = 0.2556$, $\bar{T} = 1$, and $\bar{T} = 1.0012$. So, we arbitrarily choose four values of \bar{T} that lie in distinct regions of the parameter space: 0.1, 0.5, 1.0005, and 1.1. These values of \bar{T} correspond to $T = 0.02$, $T = 0.1$, $T = 0.2001$, and $T = 0.22$. In each of the cases, other than $T = 0.2001$, we can take the initial condition $l_{in} = 0.55$. In the case of $T = 0.2001$, Equation (5.32) has the following roots: -0.1738 , 0.005053 , and 0.1687 , indicating that the system has a stable equilibrium at 0, an unstable equilibrium at 0.005053 , and a stable equilibrium at 0.1687 . So, we must run the simulation for two initial conditions, $l_{in} = 0.005$ and $l_{in} = 0.55$, to observe the different cell behaviours.

Figure 5.4 depicts the equilibrium cell sizes corresponding to each region of the parameter space of the modified Suzuki model. Figure 5.4a shows that the cell expands from its initial size due to the negative interfacial tension but is a regular hexagon at equilibrium despite the fact that the associated parameter combination lies in Region I, where the cell shape should be unpredictable. This regularity in shape arises as a result of the symmetry of the single cell. Since the

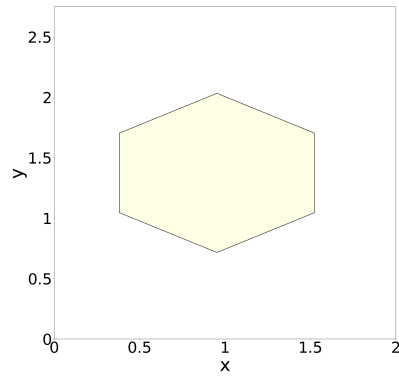
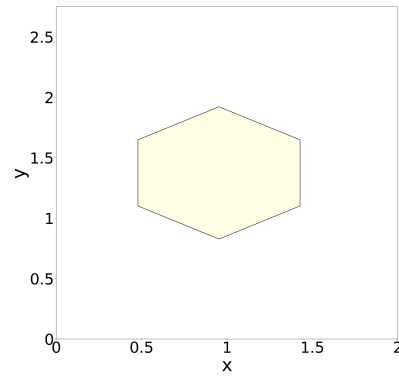
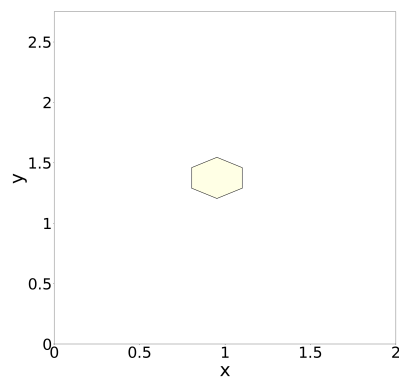
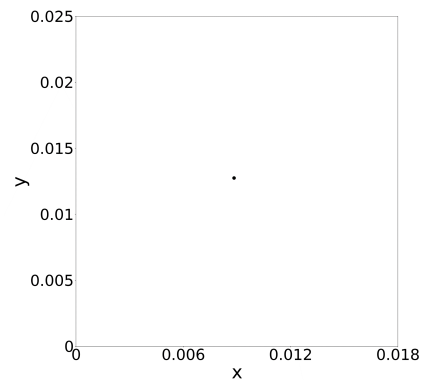
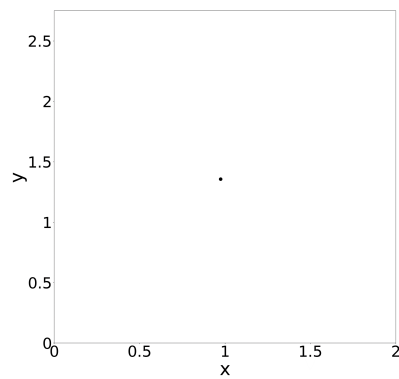
(a) $T = 0.02$, $l_{in} = 0.55$ (Region I)(b) $T = 0.1$, $l_{in} = 0.55$ (Region II)(c) $T = 0.2001$, $l_{in} = 0.55$ (Region III)(d) $T = 0.2001$, $l_{in} = 0.005$ (Region III)(e) $T = 0.22$, $l_{in} = 0.55$ (Region IV)

Figure 5.4: Cell sizes at equilibrium for different values of line tension T , corresponding to the different regions of the parameter space of the modified Suzuki model depicted in Figure 5.3. Model parameters: Table 5.4.

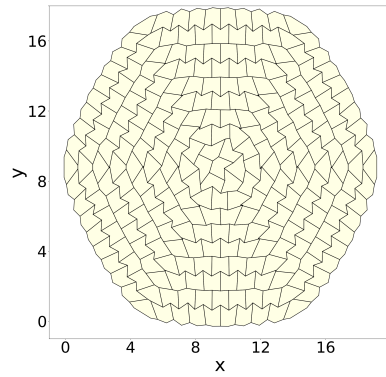
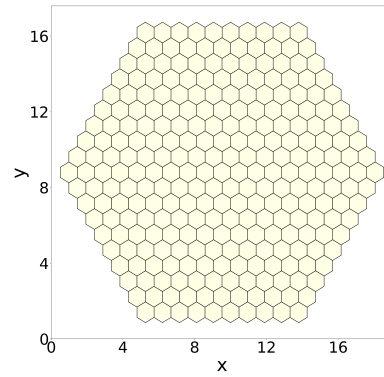
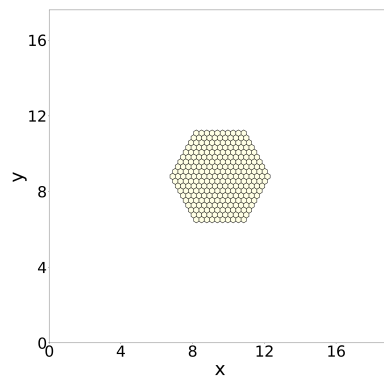
(a) $T = 0.02$, $l_{in} = 0.55$ (Region I)(b) $T = 0.1$, $l_{in} = 0.55$ (Region II)(c) $T = 0.2001$, $l_{in} = 0.55$ (Region III)

Figure 5.5: Tissue configurations at equilibrium for different values of line tension T , corresponding to the different regions of the parameter space of the modified Suzuki model depicted in Figure 5.3. The tissue is comprised of 271 cells. Model parameters: Table 5.4.

cell is a regular hexagon at equilibrium, its edge length can be calculated using Equation (5.32).

Parameter	Value
δt	0.2
K^A	0.3
K^P	0.2
μ	1
A^0	1
P^0	5

Table 5.4: Parameter values for Figures 5.4 and 5.5.

Figure 5.4b shows that the cell is a regular hexagon at equilibrium, as expected. In Figure 5.4c, we see that the cell contracts from its initial size and becomes a smaller regular hexagon at equilibrium. In Figures 5.4d and 5.4e, we see that the cell contracts from its initial size until it vanishes. All of the observations are in line with our predictions.

Figure 5.5 depicts the equilibrium tissue configurations corresponding to each region of the parameter space of the modified Suzuki model. The tissue is comprised of 271 cells. Figure 5.5a shows a soft network, and Figures 5.5b and 5.5c show hexagonal networks. Upon running the simulations for $T = 0.2001$, $l_{in} = 0.005$ and $T = 0.22$, $l_{in} = 0.55$, the tissue was observed to contract but the simulation became unstable before the tissue could vanish. Most likely, this instability arises because the vertex displacements become too large relative to the cell edge lengths, for small cell sizes.

5.4 Activating the ratchet-like mechanism

In Section 5.3, we studied the equilibrium behaviour of the tissue in the modified Suzuki model. For a given set of values of K_n^A , K_n^P , T_{0n} , A_n^0 , and P_n^0 , we can determine the equilibrium edge length of a cell and, therefore, its equilibrium area and equilibrium perimeter.

The analysis in Section 5.3 did not consider the ratchet-like mechanism (Section 3.1.4), for simplicity. However, the ratchet-like mechanism drives tissue contraction in the modified Suzuki model by decreasing A_n^0 and P_n^0 upon activation.

Parameter	Value
Cells	271
p_c	0
δt	0.2
K_n^A	0.3
K_n^P	0.2
T_{0n}	0.1
μ	1
κ_A	1
κ_P	0.001
ω_A	0.6
ω_P	0.8
A_n^0 (initial)	1
P_n^0 (initial)	5
A_n^0 (minimum)	0.3
P_n^0 (minimum)	2

Table 5.5: Parameter values for Figures 5.6 and 5.7.

Essentially, the ratchet-like mechanism must activate if the equilibrium area and perimeter fall below the mechanism's predetermined thresholds. This section visualizes the conditions required to activate the ratchet-like mechanism, driving A_n^0 and P_n^0 from their initial values to their final values.

The ratchet-like mechanism dictates that, when a cell's area A_n falls below a predetermined threshold value, the cell's natural area A_n^0 is reduced according to Equation (3.9):

$$\frac{dA_n^0}{dt} = \begin{cases} \kappa_A(A_n - \omega_A A_n^0), & \text{if } (A_n - \omega_A A_n^0) < 0, \\ 0, & \text{if } (A_n - \omega_A A_n^0) \geq 0, \end{cases} \quad (3.9 \text{ revisited})$$

where κ_A is a constant, and ω_A is a threshold parameter that determines whether or not A_n^0 should be decreased.

Similarly, when a cell's perimeter P_n falls below a predetermined threshold value, the cell's natural perimeter P_n^0 is reduced according to Equation (3.10):

$$\frac{dP_n^0}{dt} = \begin{cases} \kappa_P(P_n - \omega_P P_n^0), & \text{if } (P_n - \omega_P P_n^0) < 0, \\ 0, & \text{if } (P_n - \omega_P P_n^0) \geq 0, \end{cases} \quad (3.10 \text{ revisited})$$

where κ_P is a constant, and ω_P is a threshold parameter that determines whether or not P_n^0 should be decreased.

This reduction of A_n^0 and P_n^0 causes a cell to contract irreversibly. It should be noted that a permanent increase in line tension T_{0n} would also cause the cell to contract irreversibly but Suzuki et al [196] decide to maintain the coefficients of elasticity for the cell area K_n^A and the cell perimeter K_n^P , along with T_{0n} , as constants over the course of the simulation. Instead, they reduce A_n^0 and P_n^0 to facilitate tissue contraction. This reduction of A_n^0 and P_n^0 corresponds to the Ca^{2+} -induced F-actin remodelling observed in experiments (Section 2.2).

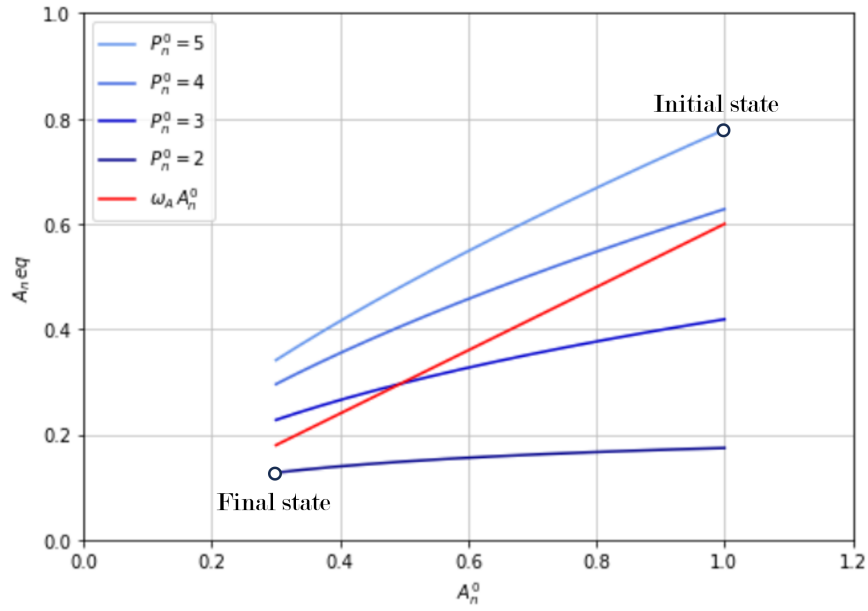
For A_n^0 to decrease, $A_n - \omega_A A_n^0 < 0$ and, similarly, for P_n^0 to decrease, $P_n - \omega_P P_n^0 < 0$. However, over the course of tissue contraction, it may happen that these criteria are no longer satisfied and, consequently, the cells stop contracting before reaching their target area and perimeter values. To ensure that the cells attain their target sizes, we need to choose appropriate values for the threshold constants ω_A and ω_P .

To understand how the ratchet-like mechanism drives tissue contraction in the Suzuki model and the modified Suzuki model, we consider the case of a tissue evolving over time from $t = 0$ to $t = 7200$ in the modified Suzuki model, for the parameters listed in Table 5.5. At $t = 0$, each cell in the tissue has $A_n^0 = 1$ and $P_n^0 = 5$. The activation of the ratchet-like mechanism causes the A_n^0 and P_n^0 of each cell to reduce over time until every cell has $A_n^0 = 0.3$ and $P_n^0 = 2$. This reduction of the A_n^0 and P_n^0 of every cell results in the monotonic contraction of the entire tissue.

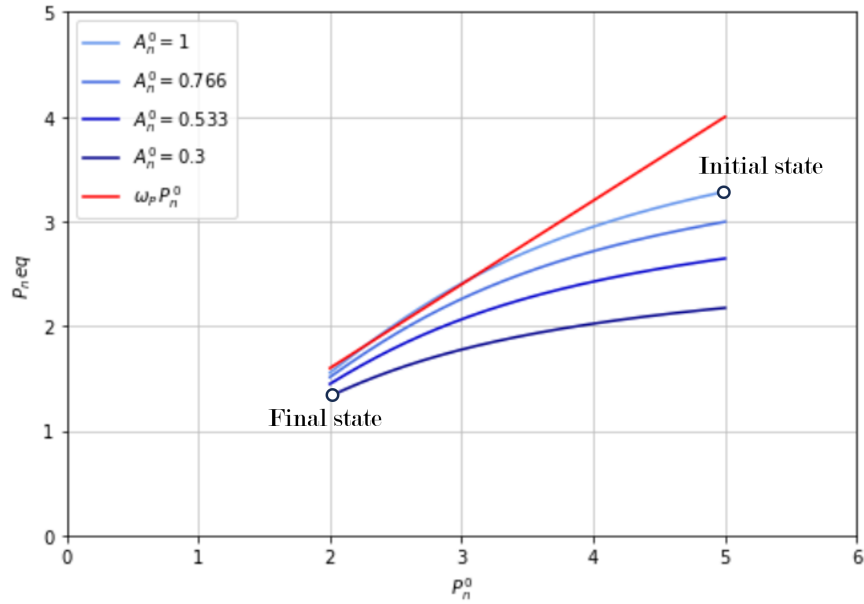
The plots in Figure 5.6 let us visualise the activation condition for the ratchet-like mechanism. The plot lines were generated by solving Equation (5.32) for the equilibrium length l , which allows us to express the equilibrium cell area and equilibrium cell perimeter as $A_n eq = \frac{3\sqrt{3}}{2}l^2$ and $P_n eq = 6l$, respectively.

Figure 5.6a depicts the equilibrium cell area $A_n eq$ as a function of A_n^0 for different values of P_n^0 . While a cell is contracting from initial state ($A_n^0 = 1$, $P_n^0 = 5$) to final state ($A_n^0 = 0.3$, $P_n^0 = 2$), the value of $A_n eq$ must lie in the region between the curves $P_n^0 = 5$ and $P_n^0 = 2$. However, the reduction in A_n^0 will only be triggered when $A_n eq$ lies below the red line i.e. $A_n eq < \omega_A A_n^0$. Clearly, towards the beginning of the simulation, $A_n eq > \omega_A A_n^0$. Therefore, initially, A_n^0 is not reduced.

Figure 5.6b depicts the equilibrium cell area $P_n eq$ as a function of P_n^0 for

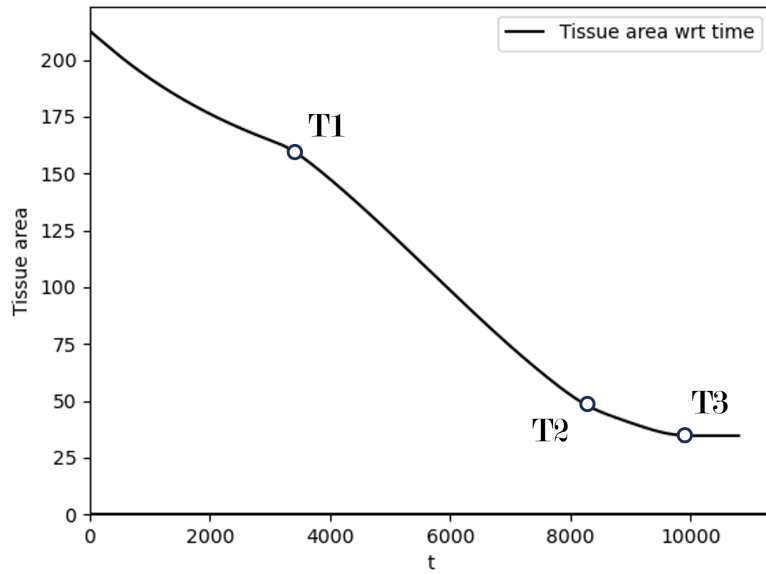


(a) Equilibrium cell area as a function of the natural area.

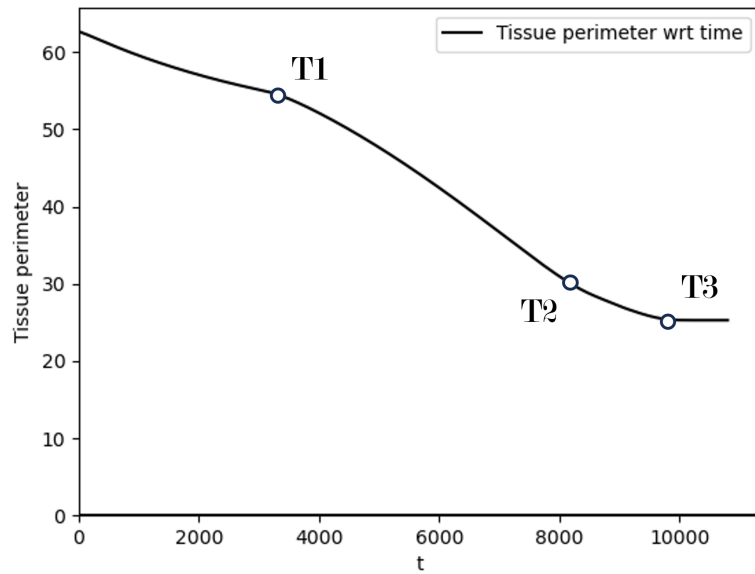


(b) Equilibrium cell perimeter as a function of the natural perimeter.

Figure 5.6: Equilibrium cell area $A_{n,eq}$ as a function of the natural area A_n^0 , plotted for different values of the natural perimeter P_n^0 , and equilibrium cell perimeter $P_{n,eq}$ as a function of the natural perimeter P_n^0 , plotted for different values of the natural perimeter A_n^0 . If $A_{n,eq}$ lies below the red line in Figure 5.6a, it triggers the reduction of A_n^0 . Similarly, if $P_{n,eq}$ lies below the red line in Figure 5.6b, it triggers the reduction of P_n^0 . The plot lines were obtained for the values of K_n^A , K_n^P , T_{0n} , ω_A , ω_P , A_n^0 (initial), P_n^0 (initial), A_n^0 (minimum), P_n^0 (minimum) as listed in Table 5.5.



(a) Tissue area versus time.



(b) Tissue perimeter versus time.

Figure 5.7: The effect of the ratchet-like mechanism on the time evolution of the total area and perimeter of the simulated tissue. T1 marks the time at which the cells' natural area begins reducing, T2 marks the time at which all the cells attain the minimum value of natural area, and T3 marks the time at which all the cells attain the minimum value of natural perimeter. Model parameters:

Table 5.5.

different values of A_n^0 . While a cell is contracting from initial state ($A_n^0 = 1$, $P_n^0 = 5$) to final state ($A_n^0 = 0.3$, $P_n^0 = 2$), the value of $P_n eq$ must lie in the region between the curves $A_n^0 = 1$ and $A_n^0 = 0.3$. Since $P_n eq$ will always lie below the red line, $P_n eq < \omega_P P_n^0$ is satisfied at all times. Therefore, P_n^0 decreases continuously until it reaches the minimum value $P_n^0 = 2$.

Since the equilibrium area and equilibrium perimeter are not independent of one another, the reduction in P_n^0 will cause both $A_n eq$ and $P_n eq$ to decrease until $A_n eq$ drops below the red line in Figure 5.6a. This causes A_n^0 to start decreasing as well. The reduction in A_n^0 and P_n^0 of each cell affects the overall rate of contraction of the tissue, as depicted in Figure 5.7.

T1 marks the time t_{T1} at which the cells' area $A_n eq$ begins dropping below their respective $\omega_A A_n^0$ values. As a result, their A_n^0 values start decreasing. T2 marks the time t_{T2} at which all the cells attain the minimum value of A_n^0 , and T3 marks the time t_{T3} at which all the cells attain the minimum value of P_n^0 .

From $t = 0$ to $t = t_{T1}$, tissue contraction is driven only by the reduction in P_n^0 . From $t = t_{T1}$ to $t = t_{T2}$, tissue contraction is driven by the reduction in both A_n^0 and P_n^0 . From $t = t_{T2}$ to $t = t_{T3}$, tissue contraction is again driven only by the reduction in P_n^0 . After $t = t_{T3}$, the tissue does not contract because every cell has attained the minimum value for A_n^0 and P_n^0 .

5.5 Parameter sweep

In Section 5.3, we derived the relationship between the cell's mechanical parameters and its equilibrium length. However, with the introduction of the ratchet-like mechanism and Ca^{2+} activity, an analytical treatment of the model becomes much more difficult. Instead, we must rely on numerical methods to observe the effect of a mechanical parameter on tissue behaviour. Therefore, we conduct a systematic parameter sweep - we perform simulations of the model for a range of values of a certain parameter while maintaining all other parameters at their default values, and observe the effect of varying that parameter on the final area attained by the tissue and the time taken to attain that area.

Table 5.6 lists the experimentally determined material properties for the neural plate. E_{NP} is the Young's modulus, \hat{T}_0 is the traction stress, and α is the viscosity. It would be reasonable to perform the parameter sweep for the range of experimentally valid values however, at present, there is no straightforward

Parameter	Mean	Range	Source
E_{NP}	44.23 Pa	32.61 – 55.85 Pa	[229]
\hat{T}_0	-	50 – 450 Pa	[144, 224]
α	0.0044 Pa.s	0.0016 – 0.0072 Pa.s	[229]

Table 5.6: Experimentally determined material properties for the neural plate.

methodology that relates the Young’s modulus and traction stress to the vertex model parameters.

While prior studies using vertex models have analytically derived expressions for the shear and bulk moduli of the tissue [81, 124, 194] and parametrised their simulations to match experimental results [81], the parametrisation process in those studies is non-trivial and beyond the scope of this work. Nevertheless, they highlight potential methods by which the vertex models developed in this thesis could be similarly parametrised in future studies.

For simplicity, we decided to relate the measured quantities to analogous parameters in the vertex model. For instance, the Young’s modulus is analogous to the elastic constants K_n^A and K_n^P since they determine the extent to which the material deforms in response to the application of a stress. Similarly, the traction stress is analogous to the line tension T_{0n} since they are associated with the deforming force.

Because we lack reference values to relate the experimentally measured quantities and vertex model parameters, we consider the parameter values used by Suzuki et al [196] (Table 5.8) to correspond to the mean values in Table 5.6. We then determine the range of experimentally-valid values using the ranges presented in Table 5.6. For example, if we consider that $K_n^A = 0.3$ corresponds to the mean value $E_{NP} = 44.23$ Pa, we determine the range of K_n^A values to sweep over as follows: the lowest value of K_n^A is given by $\frac{32.61}{44.23}0.3 = 0.2212$ and the highest value of K_n^A is given by $\frac{55.85}{44.23}0.3 = 0.3788$. Similarly, we determine the ranges for the other parameters K_n^P , T_{0n} , and μ (Table 5.7).

We conduct the parameter sweep by varying the parameter of interest while maintaining all the other parameters at their default values, as listed in Table 5.8. The parameters of interest are p_c : the frequency of cell activation per unit time, K_n^A : the coefficient of area elasticity, K_n^P : the coefficient of perimeter elasticity, μ : the damping coefficient of the tissue, T_{0n} : the line tension, and ξ : the Ca^{2+} -

Parameter	Analogous to	Mean	Range
K_n^A	E_{NP}	0.3	0.2212 – 0.3788
K_n^P	E_{NP}	0.2	0.1474 – 0.2526
T_{0n}	\hat{T}_0	0.1	–
μ	α	1	0.3672 – 1.6328

Table 5.7: Experimentally-valid parameter ranges for the vertex model.

induced elevation in the line tension. The results of the parameter sweep have been summarised in Table 5.9.

In Figures 5.8a and 5.9a, p_c is varied from 0 to 1. For low values of p_c i.e. $p_c < 0.1$, increasing p_c sharply speeds up the tissue contraction and decreases the final area attained by the tissue. For higher values of p_c i.e. $p_c > 0.1$, increasing p_c does not produce any significant increase in the rate of tissue contraction and decreases the final area attained by the tissue, but to a lesser extent than the smaller values of p_c .

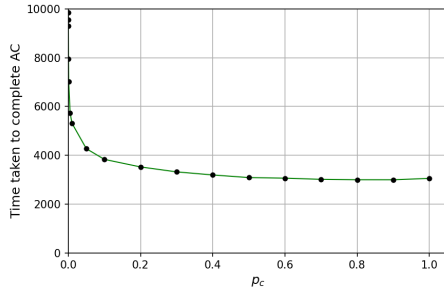
Suzuki et al [196] also measure the effect of p_c on tissue contraction (Figure 3.7). Compared to Figure 5.9a, they observe a much steeper decrease in the final area attained by the tissue, for small values of p_c . This discrepancy could result from the fact that they record their values of tissue area at $t = 2000$ whereas Figure 5.8a clearly indicates that the tissue attains its final area much later than that for the lower values of p_c .

In Figures 5.8b and 5.9b, K_n^A is varied from 0.2 to 0.4 to cover the range listed in Table 5.7. We observe that increasing K_n^A slows down the tissue contraction and increases the final area attained by the tissue. In Figures 5.8c and 5.9c, K_n^P is varied from 0.16 to 0.26 to stay as close as possible to the range listed in Table 5.7. It was found that the model became unstable and caused the simulation to fail for $K_n^P \leq 0.15$. We observe that increasing K_n^P slows down the tissue contraction and increases the final area attained by the tissue similar to K_n^A but to a greater extent. Since the elastic forces within the neural plate oppose the line tension and try to restore the cell areas, these behaviours are in line with our expectations.

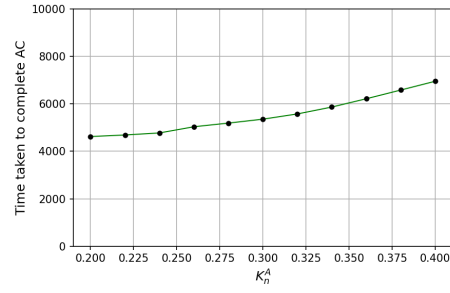
In Figures 5.8d and 5.9d, μ is varied from 0.8 to 3.6. It was found that the simulation failed for $\mu < 0.8$. This is because lowering the damping coefficient results in large vertex displacements. These displacements then grow unchecked, rendering the model unstable. This instability could be fixed by using a smaller

Parameter	Value
Cells	271
p_c	0.025
δt	0.2
K_n^A	0.3
K_n^P	0.2
T_{0n}	0.1
μ	1
κ_A	1
κ_P	0.001
ω_A	0.6
ω_P	0.8
A_n^0 (initial)	1
P_n^0 (initial)	5
A_n^0 (minimum)	0.3
P_n^0 (minimum)	2
ξ	0.05
τ	5

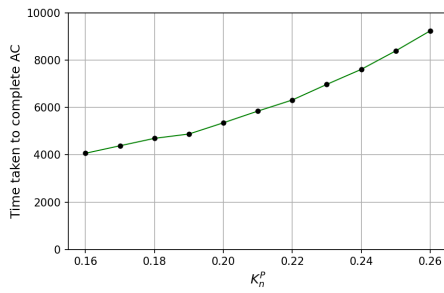
Table 5.8: Parameter values for Figures 5.8 and 5.9.



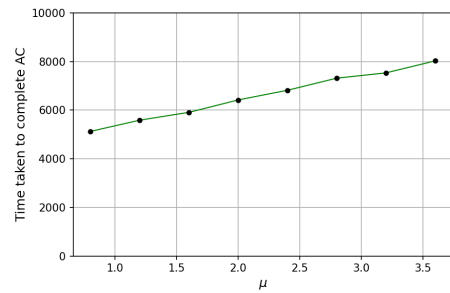
(a) AC completion time versus p_c .



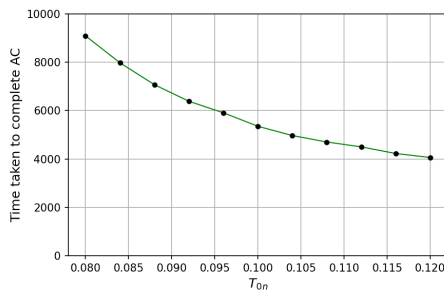
(b) AC completion time versus K_n^A .



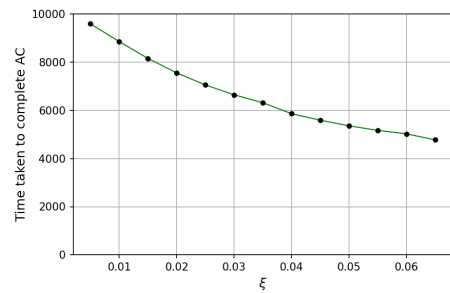
(c) AC completion time versus K_n^P .



(d) AC completion time versus μ .

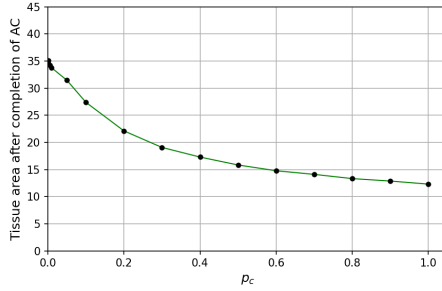


(e) AC completion time versus T_{0n} .

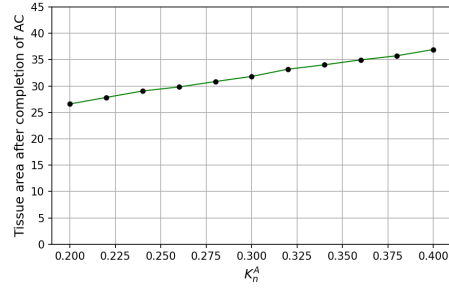


(f) AC completion time versus ξ .

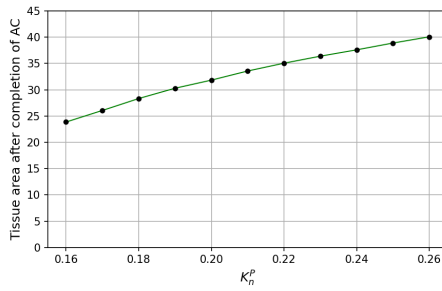
Figure 5.8: The effect of varying the parameters p_c , K_n^A , K_n^P , μ , T_{0n} , and ξ on the time taken by the tissue to complete apical constriction (AC) and attain its final area. Model parameters: Table 5.8.



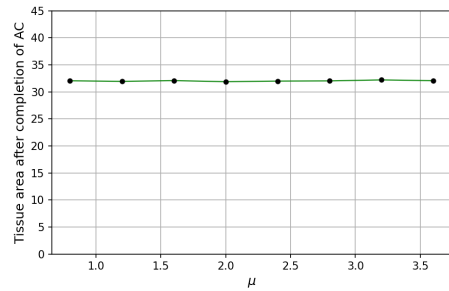
(a) Final area versus p_c .



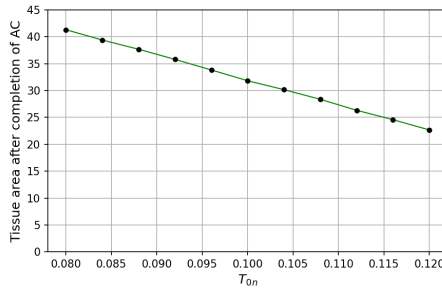
(b) Final area versus K_n^A .



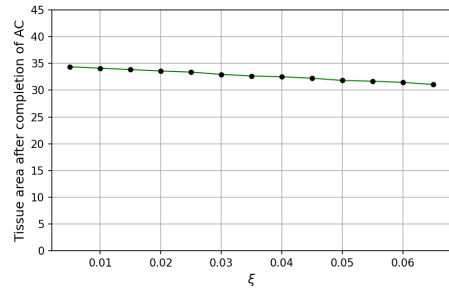
(c) Final area versus K_n^P .



(d) Final area versus μ .



(e) Final area versus T_{0n} .



(f) Final area versus ξ .

Figure 5.9: The effect of varying the parameters p_c , K_n^A , K_n^P , μ , T_{0n} , and ξ on the final area attained by the tissue upon the completion of apical constriction (AC). Model parameters: Table 5.8.

Parameter sweep - summary		
Increasing parameter	Rate of contraction	Final area
p_c	Increases	Decreases
K_n^A	Decreases	Increases
K_n^P	Decreases	Increases
μ	Decreases	No change
T_{0n}	Increases	Decreases
ξ	Increases	No change

Table 5.9: The effect of increasing the parameters p_c , K_n^A , K_n^P , μ , T_{0n} , and ξ on the rate of tissue contraction and final tissue area.

time step-size δt however, it would increase the computation time. So we decide to limit ourselves to the same δt value used by Suzuki et al [196] and instead explore the behaviour of the model for higher values of μ . We observe that increasing μ slows down the tissue contraction in a linear manner and has no effect on the final area attained by the tissue.

In Figures 5.8e and 5.9e, T_{0n} is varied from 0.08 to 0.12. Ideally, we would have varied T_{0n} over a range in which the value of the upper limit is nine times larger than the value of the lower limit, in accordance with the range of \hat{T}_0 in Table 5.6, but T_{0n} was found to be an extremely sensitive parameter and taking a value outside the range $0.08 \leq T_{0n} \leq 0.12$ destabilises the model. We observe that increasing T_{0n} in the stable range speeds up the tissue contraction and decreases the final area attained by the tissue.

In Figures 5.8f and 5.9f, ξ is varied as a fraction of T_{0n} , from $0.05T_{0n}$ to $0.65T_{0n}$. We found that the model becomes unstable for $\xi > 0.65T_{0n}$. We observe that increasing ξ speeds up the tissue contraction but does not have much effect on the final area attained by the tissue.

In this chapter, we revised the modelling assumptions of the Suzuki model to better reflect the biology, and developed a new model, the modified Suzuki model. We then simulated the modified Suzuki model in our open-source software, CelluLink, and compared it to the Suzuki model. Despite the revised modelling assumptions, the modified Suzuki model behaves very similarly to the Suzuki model and reproduces its key behaviours. The modified Suzuki model still exhibits the same limitations as the Suzuki model and thus necessitates the development of

a new mechanochemical model of NTC, which we will undertake in Chapter 7. To inform the development of the new model, we studied how varying the parameters impacted tissue contraction in the modified Suzuki model.

We derived a new bifurcation diagram for the modified Suzuki model by performing single-cell analysis in the absence of the ratchet-like mechanism and Ca^{2+} activity. This helped to understand how the relative strengths of parameters K_n^A , K_n^P , and T_{0n} impact the final area of the tissue. Thereafter, we studied the effect of the ratchet-like mechanism on the model, visualized the conditions required to activate it, and observed its impact on the rate of tissue contraction. This visualization helps us choose the threshold constants ω_A and ω_P that enable a cell to contract by driving A_n^0 and P_n^0 from their initial to final values. Finally, we incorporated Ca^{2+} activity and conducted a systematic parameter sweep to test the parameter sensitivity of the modified Suzuki model. The insights from these studies will guide parameter selection for the new mechanochemical model in Chapter 7.

Chapter 6

Comparing numerical methods for vertex models

In Chapter 4, we developed CelluLink, the computational tool that will allow us to simulate the vertex models under study. In this chapter, we elaborate upon the numerical schemes currently available in CelluLink - the forward Euler method and a predictor-corrector method based on an Euler/trapezoidal pair.

In Chapters 4 and 5, all of the simulations were performed using the forward Euler method due to its higher speed and ease of implementation. Before proceeding to the development of a new mechanochemical model for NTC in Chapter 7, we compare the forward Euler method, an explicit method, with an implicit method to determine the better choice for simulating vertex models.

We start by reviewing some fundamental concepts relating to one-step numerical methods. Then, we discretise the equations of the modified Suzuki model (Equations (3.7), (3.9), and (3.10)). Finally, we apply the two numerical schemes to simulate Equations (3.7), (3.9), and (3.10) and compare their performance.

6.1 Convergence of one-step methods

Before investigating the properties of the numerical schemes available in CelluLink, it would be prudent to review some important concepts relating to one-step numerical methods.

Numerical methods are designed to approximate the solutions of locally well-posed initial value problems. These problems are of the form

$$\mathbf{y}' = \mathbf{f}(t, \mathbf{y}), \quad \mathbf{y}(t_0) = \mathbf{y}_0, \quad \mathbf{y} \in \mathbf{R}^d. \quad (6.1)$$

Well-posedness means that there exists a unique solution $\mathbf{y}(t; t_0, \mathbf{y}_0)$ that satisfies Equation (6.1) on a maximal interval of existence $[t_0, t_0 + T_*)$, for $0 < T_* \leq +\infty$, that depends continuously on $(t_0, \mathbf{y}_0) \in \mathbf{R}^{d+1}$. To guarantee local well-posedness [155], we will assume that $\mathbf{f}(t, \mathbf{y})$ is continuous in its first argument, t , and locally uniformly Lipschitz continuous in its second argument, \mathbf{y} , i.e.,

$$\|\mathbf{f}(t, \mathbf{y}_1) - \mathbf{f}(t, \mathbf{y}_2)\| \leq L \|\mathbf{y}_1 - \mathbf{y}_2\|, \quad (6.2)$$

for some $L > 0$ and any $\mathbf{y}_1, \mathbf{y}_2$ in the neighbourhood of \mathbf{y}_0 .

If the function $\mathbf{f}(t, \mathbf{y})$ is not explicitly dependent on t , then the Lipschitz condition would typically still be interpreted in the same manner, but the dependency on t would be ignored. In this case, the Lipschitz condition,

$$\|\mathbf{f}(\mathbf{y}_1) - \mathbf{f}(\mathbf{y}_2)\| \leq L \|\mathbf{y}_1 - \mathbf{y}_2\|, \quad (6.3)$$

would be sufficient to guarantee local well-posedness.

In Equation (3.7) of the modified Suzuki model, the Lipschitz condition holds because the potential energy of the apical surface of the tissue, U , is twice continuously differentiable with respect to \mathbf{r}_i . Therefore, \mathbf{F}_i is Lipschitz continuous in \mathbf{r}_i .

Discretisation methods employ approximations of Equation (6.1) to construct a discrete set of \mathbf{y} -values ($\mathbf{y}_{(k)}$, $k = 0, 1, \dots$) in such a manner that $\mathbf{y}_{(k)}$ should approximate $\mathbf{y}(t_k)$, at a corresponding set of t -values t_k , as the separation of the timesteps $\delta t_k = t_{k+1} - t_k$ tends uniformly to zero. For the purpose of this review, we will restrict ourselves to the case where δt_k does not vary with k . In this case, δt is called the discretisation parameter or step-size.

Discretisation methods are broadly categorized as explicit or implicit. Concisely put, an explicit method obtains the successive values of $\mathbf{y}_{(k+1)}$ parametrically in terms of given or previously computed quantities and is represented symbolically in the form

$$\mathbf{y}_{(k+1)} = \mathbf{H}(\mathbf{f}, t_k, \dots, t_{k+1-l}, \mathbf{y}_k, \dots, \mathbf{y}_{k+1-l}). \quad (6.4)$$

In contrast, an implicit method defines $\mathbf{y}_{(k+1)}$ as the solution of the equation

$$\mathbf{G}(\mathbf{f}, t_{k+1}, \dots, t_{k+1-l}, \mathbf{y}_{k+1}, \dots, \mathbf{y}_{k+1-l}) = 0 \quad (6.5)$$

that cannot in general be recast in the explicit form above.

Discretisation methods are also characterized by the number m of previously computed quantities, or steps, that the method uses to compute each subsequent approximate value of the solution and by the number of evaluations r of the vector field \mathbf{f} , or stages, that are used per time-step.

Generally, r -stage one-step methods can be written in the form that characterizes methods known as Runge-Kutta methods [155]. Given numerical initial values \mathbf{y}_0 , these methods take the specific form

$$\mathbf{y}_{(k+1)} = \mathbf{y}_{(k)} + \delta t \sum_{i=1}^r \gamma_i \mathbf{y}'_{(k,i)}, \quad k = 0, 1, \dots \quad (6.6)$$

where

$$\mathbf{y}'_{(k,i)} = \mathbf{f} \left(t_k + \alpha_i \delta t, \mathbf{y}_{(k)} + \delta t \sum_{j=1}^r \beta_{ij} \mathbf{y}'_{(k,j)} \right) \quad \text{and} \quad \alpha_i = \sum_{j=1}^r \beta_{ij}.$$

If $\beta_{ij} = 0$ for $j \geq i$, the method is explicit; otherwise it is implicit. The strategy behind these methods is to obtain better approximations of $\mathbf{y}(t_{k+1})$ by sampling the vector field $\mathbf{f}(t, \mathbf{y})$ at r points in the vicinity of the solution curve emanating from (t_k, \mathbf{y}_k) . Each additional sample provides cumulatively better estimates of the solution curve. The analytical initial value is sufficient to initialize a one-step method, and no storage of previously computed values is required.

Having established the general form of r -stage one-step methods, we can now address the theoretical question of whether the values obtained by applying a method converge to the analytical solution $\mathbf{y}(t_0 + T)$, as the step-size δt tends to zero and the number of steps increases in such a way that the time interval they represent remains fixed. We call a method *convergent* if and only if, for any initial value problem (6.1) satisfying condition (6.2) and any $T > 0$ such that $t_0 + T \in [t_0, t_0 + T_*)$, the values $\mathbf{y}_{(k)}$ obtained from the method satisfy

$$\|\mathbf{y}(t_0 + T) - \mathbf{y}_{(k)}\| \rightarrow 0 \quad (6.7)$$

as $k \rightarrow \infty$ and $\delta t = T/k$. Note that condition (6.7) implies that $\mathbf{y}_{(k)}$ exists for sufficiently large k . This is only an issue for implicit methods. If a method is explicit, $\mathbf{y}_{(k)}$ is defined for any $\delta t > 0$ and $k > 0$.

The order of accuracy of a convergent method refers to how rapidly errors decrease in the limit as the step-size tends to zero. We say that such a method converges with *order of accuracy* P , and the method is called a P^{th} -order accurate method, if and only if there exists a $C > 0$ depending only on \mathbf{y} , its derivatives, and T , such that

$$\|\mathbf{y}(t_0 + T) - \mathbf{y}_{(k)}\| \leq C\delta t^P = C\left(\frac{T}{k}\right)^P \quad (6.8)$$

as $k \rightarrow \infty$ and no such estimate holds for any greater value of P . The dependence of C on T can be removed by considering only closed subintervals of the maximal interval of existence. The potential significance of accuracy is immediate: if the increase in computational effort per step required to achieve higher-order accuracy is outweighed by reducing the number of steps required to obtain an approximation within a desired tolerance, the overall computation can be performed more efficiently.

To solve the force balance equation in a vertex model, at every timestep, the force on each vertex is computed and then the vertex positions are updated synchronously. This synchronous update can cause vertices to cross cell edges, leading to overlapping edges and unrealistic cell shapes. So, while this approach works

well enough for small forces and displacements, it becomes problematic with larger forces, as vertex displacements can be so large as to cause instability. These instabilities can be resolved by adjusting the parameters to ensure the model operates in a stable regime or by performing appropriate topological transitions (T1, T2, or T3 swaps) [62, 115, 188].

The theoretical convergence and practical efficiency of a numerical method are usually analysed in terms of accuracy and absolute stability. However, the instability issues mentioned above result from parameter choices and/or the implementation of the vertex model. Consequently, investigating the stability of the numerical scheme would not provide much practical insight into the stability of the vertex model. Therefore, in Sections 6.3 and 6.4, we will only explore the rate of convergence of the numerical schemes in CelluLink.

6.2 Discretising the system

To simulate the modified Suzuki model, CelluLink needs to solve Equations (3.7)-(3.10). Since Equations (3.9) & (3.10) are first order linear ordinary differential equations, it is straightforward to solve them using an explicit or implicit numerical scheme of choice. The challenge lies in solving Equation (3.7), the force balance equation for the vertices, which drives the evolution of the tissue:

$$\mu \frac{d\mathbf{r}_i}{dt} = -\frac{\partial U}{\partial \mathbf{r}_i} = \mathbf{F}_i. \quad (3.7 \text{ revisited})$$

Equation (3.7) represents a system of coupled non-linear ordinary differential equations. Since it lacks an analytical solution (as far as we are aware), it must be solved numerically. We consider two numerical schemes for this purpose - the forward Euler method, an explicit scheme, and a predictor-corrector method, an r -stage explicit scheme that is approximate to an implicit scheme for sufficiently large r .

Prior to implementing a numerical scheme, we must discretise the equations to be solved. Equations (3.9) & (3.10) are discretised using forward differences for time-stepping, resulting in the following set of equations for the natural area and natural perimeter of the n^{th} cell, respectively:

$$\frac{A_{n(k+1)}^0 - A_{n(k)}^0}{\delta t} = \begin{cases} \kappa_A(A_{n(k)} - \omega_A A_{n(k)}^0), & \text{if } (A_{n(k)} - \omega_A A_{n(k)}^0) < 0, \\ 0, & \text{if } (A_{n(k)} - \omega_A A_{n(k)}^0) \geq 0, \end{cases} \quad (6.9)$$

$$\frac{P_{n(k+1)}^0 - P_{n(k)}^0}{\delta t} = \begin{cases} \kappa_P(P_{n(k)} - \omega_P P_{n(k)}^0), & \text{if } (P_{n(k)} - \omega_P P_{n(k)}^0) < 0, \\ 0, & \text{if } (P_{n(k)} - \omega_P P_{n(k)}^0) \geq 0, \end{cases} \quad (6.10)$$

where $A_{n(k)}^0$ and $P_{n(k)}^0$ are the discrete approximations of the natural area $A_n^0(t_k)$ and natural perimeter $P_n^0(t_k)$, from the continuous equations, at $t_k = t_0 + k\delta t$, where δt is the size of the timestep. Taking $t_0 = 0$, we have $t_k = k\delta t$. We will use this formalism to denote the discrete approximations of continuous variables.

To discretise Equation (3.7), we use a forward differences scheme for time-stepping and centred differences for the first spatial derivative, which gives us the discrete equations of motion, along the x and y directions, for the i^{th} vertex:

$$\mu \frac{x_{i(k+1)} - x_{i(k)}}{\delta t} = - \frac{U(x_{i(k)} + \frac{\delta x}{2}) - U(x_{i(k)} - \frac{\delta x}{2})}{\delta x}, \quad (6.11)$$

$$\mu \frac{y_{i(k+1)} - y_{i(k)}}{\delta t} = - \frac{U(y_{i(k)} + \frac{\delta y}{2}) - U(y_{i(k)} - \frac{\delta y}{2})}{\delta y}, \quad (6.12)$$

where $x_{i(k)}$ and $y_{i(k)}$ are the discrete approximations of $x_i(t_k)$ and $y_i(t_k)$, the components of the displacement vector \mathbf{r}_i of the i^{th} vertex, and δx and δy are the spatial step-sizes.

Since the vertex model is an off-lattice model, the movement of the vertices is not confined to a grid. Unlike in the case of partial differential equations, our choice of spatial step-size does not have much bearing on the properties of our numerical scheme so long as the step-sizes are sufficiently small. Therefore, we use the same values of δx and δy for all the simulations in this doctoral work. Taking into account the size of the tissue we are modelling, we choose sufficiently small spatial step-sizes $\delta x = \delta y = 0.01$.

Ideally, calculating the exact gradient of the potential energy U is preferable to approximating spatial derivatives with finite differences. This is especially important during topological transitions, as it yields more accurate force calculations. However, since cell-cell intercalation, cell death, and cell division do not occur during apical constriction (AC), the corresponding topological transitions (T1, T2, and T3 swaps) are not implemented in our model.

So, for ease of implementation and to reduce computational cost, we use a finite difference approximation for the spatial derivatives. The centred difference approximation, which is second-order accurate, combined with sufficiently small spatial step-sizes, provides an accurate approximation of the spatial derivatives.

6.3 Forward Euler method

The Euler method (also called the forward Euler method) is a numerical procedure for solving ordinary differential equations with a given initial value. The Euler method is a first-order method, which means that the local error (error per step) is proportional to the square of the step-size, and the global error (error at a given time) is proportional to the step-size. The Euler method often serves as the basis to construct more complex methods like the predictor-corrector method, as we shall see in Section 6.4.

Consider an initial value problem as described by Equation (6.1). The forward Euler method is used to find a numerical solution to the problem as follows. First, set $\mathbf{y}_{(0)} = \mathbf{y}(t_0) = \mathbf{y}_0$. Next, choose a suitable step-size δt so that $t_k = t_0 + k\delta t$. Then, one step of the forward Euler method from t_k to t_{k+1} is given by

$$\mathbf{y}_{(k+1)} = \mathbf{y}_{(k)} + \delta t \mathbf{f}(t_k, \mathbf{y}_{(k)}). \quad (6.13)$$

The value of $\mathbf{y}_{(k)}$ is an approximation of the solution to the ordinary differential equation at time t_k i.e. $\mathbf{y}_{(k)} \approx \mathbf{y}(t_k)$. From Equation (6.13), it is clear that the state of the system at any given timestep can be calculated if the state of the system at the previous timestep is known. In other words, the Euler method is *explicit*.

Since the forward Euler method seems to be the most frequently used numerical scheme for vertex models [55, 68, 196], it was the first numerical scheme to be

Parameter	Value
Cells	271
K_n^A	0.3
K_n^P	0.2
T_{0n}	0.1
μ	1
κ_A	1
κ_P	0.001
ω_A	0.6
ω_P	0.8
A_n^0 (initial)	1
P_n^0 (initial)	5
A_n^0 (minimum)	0.3
P_n^0 (minimum)	2

Table 6.1: Parameter values for Figures 6.1, 6.2, 6.3, and 6.4.

implemented in CelluLink. Given the fact that $x_{i(0)}$ and $y_{i(0)}$ are known for all i , the forward Euler method can be used to compute the positions of the vertices at all subsequent timesteps. The expressions for the vertex positions at the k^{th} timestep are obtained by rearranging the discrete equations (6.11) and (6.12) as follows,

$$x_{i(k+1)} = x_{i(k)} - \frac{\delta t U \left(x_{i(k)} + \frac{\delta x}{2} \right) - U \left(x_{i(k)} - \frac{\delta x}{2} \right)}{\mu \delta x}, \quad (6.14)$$

$$y_{i(k+1)} = y_{i(k)} - \frac{\delta t U \left(y_{i(k)} + \frac{\delta y}{2} \right) - U \left(y_{i(k)} - \frac{\delta y}{2} \right)}{\mu \delta y}. \quad (6.15)$$

Since $A_{n(0)}^0$ and $P_{n(0)}^0$ are known for all n , the natural area and natural perimeter of the cells are also updated using the forward Euler method. The expressions for the natural area and natural perimeter at the k^{th} timestep are obtained by rearranging the discrete equations (6.9) and (6.10) as follows,

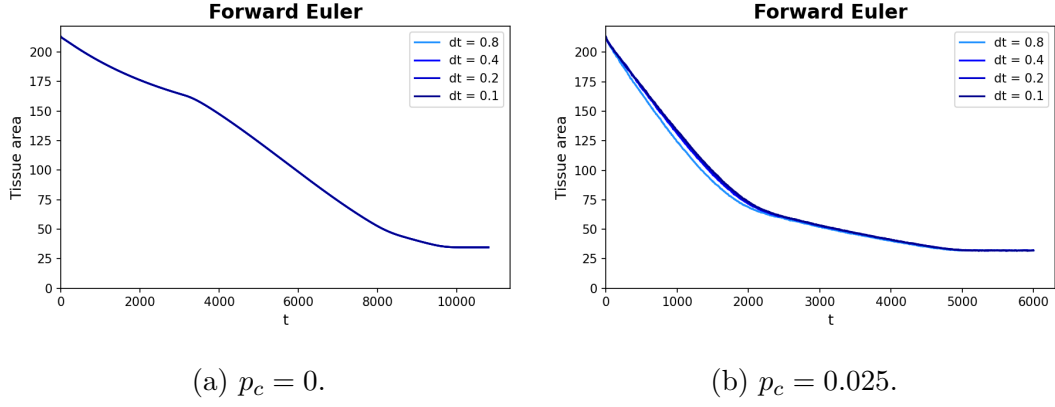


Figure 6.1: Time evolution of the tissue area for $\delta t = 0.8, 0.4, 0.2,$ and 0.1 for both $p_c = 0$ and $p_c = 0.025$. When the modified Suzuki model is solved using the forward Euler method for Equations (3.7), (3.9), and (3.10), the solution converges. Model parameters: Table 6.1.

$$A_{n(k+1)}^0 = \begin{cases} A_{n(k)}^0 + \delta t \kappa_A (A_{n(k)} - \omega_A A_{n(k)}^0), & \text{if } (A_{n(k)} - \omega_A A_{n(k)}^0) < 0, \\ A_{n(k)}^0, & \text{if } (A_{n(k)} - \omega_A A_{n(k)}^0) \geq 0, \end{cases} \quad (6.16)$$

$$P_{n(k+1)}^0 = \begin{cases} P_{n(k)}^0 + \delta t \kappa_P (P_{n(k)} - \omega_P P_{n(k)}^0), & \text{if } (P_{n(k)} - \omega_P P_{n(k)}^0) < 0, \\ P_{n(k)}^0, & \text{if } (P_{n(k)} - \omega_P P_{n(k)}^0) \geq 0. \end{cases} \quad (6.17)$$

Using the forward Euler method, we simulated the modified Suzuki model for $\delta t = 0.8, 0.4, 0.2,$ and 0.1 both, in the absence of Ca^{2+} flashes (Figure 6.1a) and, in the presence of Ca^{2+} flashes (Figure 6.1b). Apart from p_c and δt , all other parameters were set to the values listed in Table 6.1. From a visual inspection of Figures 6.1a and 6.1b, it can be seen that the numerical scheme converges. The convergent error for $\delta t = 0.8$ is prominently visible between $t = 0$ and $t \approx 2000$ in Figure 6.1b.

To calculate the rate of convergence of this method, we simulated the modified Suzuki model for $\delta t = 0.1, 0.2, \dots, 1$ (Figure 6.2) for $p_c = 0$ since the stochastic effects introduced by the Ca^{2+} flashes would make it difficult to measure the error for $p_c \neq 0$. We define the *convergent error* corresponding to

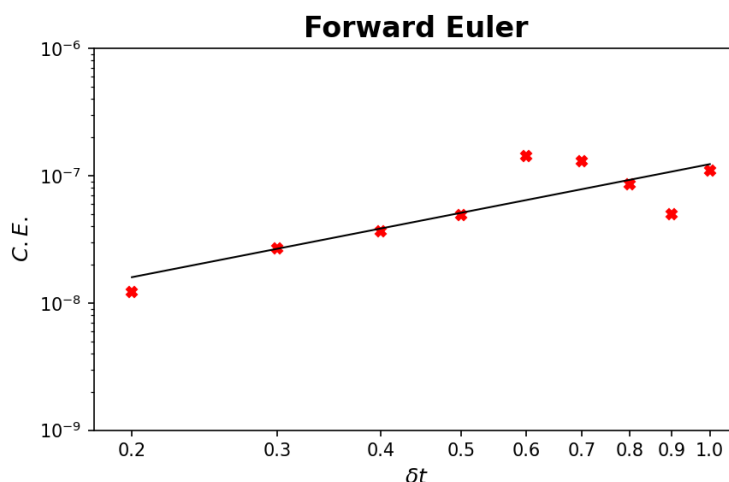


Figure 6.2: Convergence error ($C.E.$) versus the size of the timestep (δt). The red crosses mark the error values obtained for the different time step-sizes when the modified Suzuki model is solved using the forward Euler method for Equations (3.7), (3.9), and (3.10). Both the axes use a logarithmic scale. Model parameters: Table 6.1.

each value of δt using the L^2 norm such that $C.E. = \|\mathbf{r}(t_k) - \mathbf{r}_{(k), \delta t}\|_2$ where $\mathbf{r} = (x_1, y_1, x_2, y_2, \dots, x_{N_V}, y_{N_V})$. Recalling Equation (6.8), if $C.E. = C\delta t^P$, then taking the log of both sides of the equation, we get

$$\log(C.E.) = \log C + P \log \delta t. \quad (6.18)$$

We use the solution corresponding to the smallest timestep ($\delta t = 0.1$) as the best estimate of the true solution $\mathbf{r}(t_k)$ at timestep $k = 10800$. We chose to measure the positions of the vertices at $t = 10800$ because we estimated that the tissue would reach a steady size by then. Using the `numpy.polyfit()` function in Python, we fit a straight line to the data points in Figure 6.2 and obtained an estimate for its slope. The function uses the least squares method to fit a polynomial to the given set of data points. Since the slope corresponds to the order of accuracy P in Equation (6.18), we find that $P = 1.27$ for this method.

6.4 Predictor-corrector method

While the forward Euler method is undoubtedly effective in simulating vertex models, it is only a first-order explicit scheme. Because we were interested in examining the performance of a higher-order implicit scheme when applied to the vertex model, we decided to implement a simple predictor-corrector scheme in CelluLink. The predictor-corrector algorithm proceeds in two steps:

1. The initial, *predictor* step, uses an explicit method to estimate the value of the unknown function \mathbf{y} at the $k + 1^{\text{th}}$ timestep. We treat this as the ‘zeroth’ stage of the method and the estimate is denoted by $\mathbf{y}_{(k+1,r)}$ where $r = 0$.
2. The next, *corrector* step refines the initial estimate by using the *predicted* value of the function and an implicit method to interpolate the unknown function value at the same timestep. This *corrected* value is denoted by $\mathbf{y}_{(k+1,r)}$. The correction step can be applied repeatedly until the approximation $\mathbf{y}_{(k+1,r)}$ satisfies some criteria, for instance, the error lies within the desired tolerance level. In this sense, the predictor-corrector scheme becomes a good approximation to an implicit scheme.

The predictor-corrector scheme in CelluLink uses the forward Euler method in the predictor step and the trapezoidal rule in the corrector step. In contrast to the Euler method which is first-order accurate, the trapezoidal rule is a second-order method. For an initial value problem as described by Equation (6.1), the trapezoidal rule is given by the formula

$$\mathbf{y}_{(k+1)} = \mathbf{y}_{(k)} + \frac{1}{2}\delta t \left(\mathbf{f}(t_k, \mathbf{y}_{(k)}) + \mathbf{f}(t_{k+1}, \mathbf{y}_{(k+1)}) \right), \quad (6.19)$$

where δt is the size of the timestep. From Equation (6.19), it is clear that the state of the system at the k^{th} timestep cannot be expressed explicitly in terms of the state of the system at the previous timesteps. Therefore, the trapezoidal rule is an *implicit* method.

Using the predictor-corrector scheme, the force balance equation for the vertex model can be solved in the following manner. In the prediction step, the forward

Euler method is used to obtain initial estimates for the positions of the vertices at the $k + 1^{\text{th}}$ timestep. The initial estimates are given by

$$x_{i(k+1,0)} = x_{i(k)} - \frac{\delta t}{\mu} \frac{U(x_{i(k)} + \frac{\delta x}{2}) - U(x_{i(k)} - \frac{\delta x}{2})}{\delta x}, \quad (6.20)$$

$$y_{i(k+1,0)} = y_{i(k)} - \frac{\delta t}{\mu} \frac{U(y_{i(k)} + \frac{\delta y}{2}) - U(y_{i(k)} - \frac{\delta y}{2})}{\delta y}. \quad (6.21)$$

In the corrector step, the trapezoidal rule is used to refine the initial estimates $x_{i(k+1,0)}$ and $y_{i(k+1,0)}$ from the predictor step. From Equations (3.7), (6.11), and (6.12), we recall the discrete approximations of the first spatial derivative terms and denote them by D_x and D_y such that,

$$\frac{\partial U(x_i, y_i)}{\partial x_i} \approx D_x(x_i, y_i) = \frac{U(x_i + \frac{\delta x}{2}, y_i) - U(x_i - \frac{\delta x}{2}, y_i)}{\delta x}, \quad (6.22)$$

$$\frac{\partial U(x_i, y_i)}{\partial y_i} \approx D_y(x_i, y_i) = \frac{U(x_i, y_i + \frac{\delta y}{2}) - U(x_i, y_i - \frac{\delta y}{2})}{\delta y}. \quad (6.23)$$

The corrected values of the initial estimates from the predictor step can be found using the expressions

$$x_{i(k+1,r)} = x_{i(k)} - \frac{\delta t}{2\mu} (D_x(x_{i(k)}, y_{i(k)}) + D_x(x_{i(k+1,r-1)}, y_{i(k+1,r-1)})), \quad (6.24)$$

$$y_{i(k+1,r)} = y_{i(k)} - \frac{\delta t}{2\mu} (D_y(x_{i(k)}, y_{i(k)}) + D_y(x_{i(k+1,r-1)}, y_{i(k+1,r-1)})), \quad (6.25)$$

where $x_{i(k+1,r)}$ and $y_{i(k+1,r)}$ are the discrete approximations of the vertex position after r correction stages. We implement a tolerance condition wherein we rerun the correction step until both of the following inequalities are satisfied: $|x_{i(k+1,r)} - x_{i(k+1,r-1)}| < 10^{-8}$ and $|y_{i(k+1,r)} - y_{i(k+1,r-1)}| < 10^{-8}$. We implement an additional condition and restrict the method to a maximum of 10 correction steps to prevent large computational times per timestep.

To ensure robustness throughout the implementation of the vertex model, the differential equations for the ratchet-like mechanism are also solved using an implicit method, the *backward Euler method*. Like the forward Euler method, the backward Euler method is also first-order accurate. For an initial value problem described by Equation (6.1), the backward Euler method is given by

$$\mathbf{y}^{(k+1)} = \mathbf{y}^{(k)} + \delta t \mathbf{f}(t_{k+1}, \mathbf{y}^{(k+1)}). \quad (6.26)$$

Applying the backward Euler method, the natural area and natural perimeter of a cell are calculated using the expressions

$$A_{n(k+1)}^0 = \begin{cases} \frac{A_{n(k)}^0 + \delta t \kappa_A A_{n(k+1)}}{1 + \delta t \kappa_A \omega_A}, & \text{if } (A_{n(k)} - \omega_A A_{n(k)}^0) < 0, \\ A_{n(k)}^0, & \text{if } (A_{n(k)} - \omega_A A_{n(k)}^0) \geq 0, \end{cases} \quad (6.27)$$

$$P_{n(k+1)}^0 = \begin{cases} \frac{P_{n(k)}^0 + \delta t \kappa_P P_{n(k+1)}}{1 + \delta t \kappa_P \omega_P}, & \text{if } (P_{n(k)} - \omega_P P_{n(k)}^0) < 0, \\ P_{n(k)}^0, & \text{if } (P_{n(k)} - \omega_P P_{n(k)}^0) \geq 0. \end{cases} \quad (6.28)$$

Using the implicit methods, we simulated the modified Suzuki model for $\delta t = 0.8, 0.4, 0.2$, and 0.1 both, in the absence of Ca^{2+} flashes (Figure 6.3a) and, in the presence of Ca^{2+} flashes (Figure 6.3b). Apart from p_c and δt , all other parameters were set to the values listed in Table 6.1. From a visual inspection of Figures 6.3a and 6.3b, it can be seen that the numerical scheme converges. On comparing Figures 6.1b and 6.3b, the lack of a noticeable separation between the plot lines in the case of the latter indicates that the predictor-corrector method is more accurate than the forward Euler method.

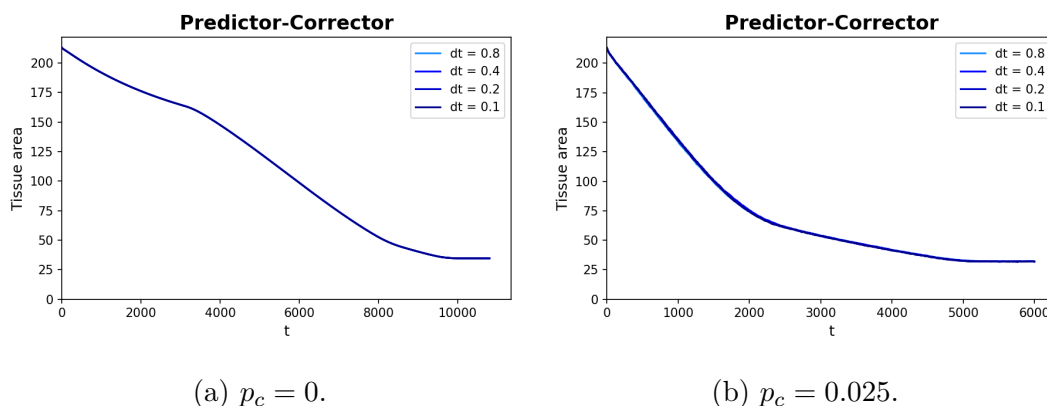


Figure 6.3: Time evolution of the tissue area for $\delta t = 0.8, 0.4, 0.2$, and 0.1 for both $p_c = 0$ and $p_c = 0.025$. When the modified Suzuki model is solved using the predictor-corrector method for Equation (3.7) and using the backward Euler method for Equations (3.9) and (3.10), the solution converges. Model parameters: Table 6.1.

Naturally, the predictor-corrector method is more computationally expensive than the forward Euler method. Near the start of the simulation, each computational step of the predictor-corrector method takes ≈ 7 times longer to execute than a step of the forward Euler method since the predictor-corrector method requires ≈ 6 iterations of the corrector until it converges. As the simulation progresses, each step of the predictor-corrector method becomes progressively less computationally expensive. Near the end of the simulation, ≈ 2 iterations of the corrector are sufficient for the scheme to converge.

To calculate the rate of convergence of this method, we follow the same procedure that we used for the forward Euler method in Section 6.3 and obtain order of accuracy $P = 1.69$. Comparing this to the order of accuracy obtained for the forward Euler method ($P = 1.27$), we can see that the predictor-corrector method has a higher order of accuracy than the forward Euler method, as expected.

The higher accuracy of the predictor-corrector method is also evident when we compare the magnitude of the errors of both methods for $\delta t = 0.1$ i.e. $C.E. \approx 10^{-8}$ for the forward Euler method and $C.E. \approx 10^{-5}$ for the predictor-corrector method. This implies that, with respect to $\mathbf{r}_{(k), \delta t}$ for $k = 10800$ and $\delta t = 0.1$, the $C.E.$ values are far larger in the case of the predictor-corrector method.

Although the $C.E.$ values are larger in the case of the predictor-corrector

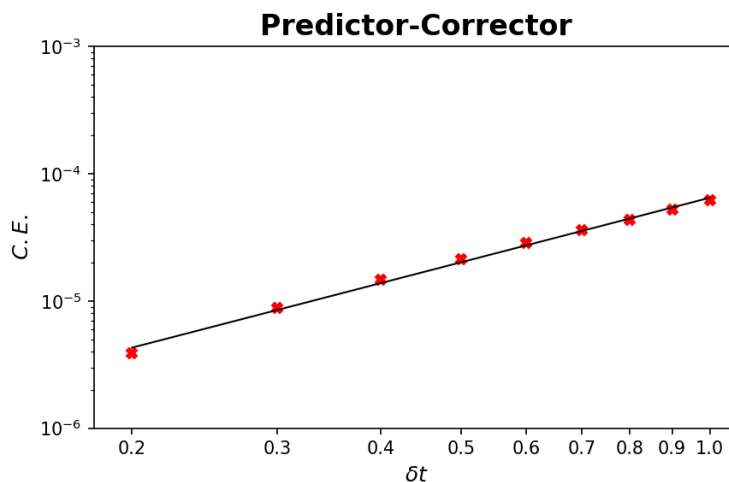


Figure 6.4: Convergence error ($C.E.$) versus the size of the timestep (δt). The red crosses mark the error values obtained for the different time step-sizes when the modified Suzuki model is solved using the predictor-corrector method for Equation (3.7) and using the backward Euler method for Equations (3.9) and (3.10). Both the axes use a logarithmic scale. Model parameters: Table 6.1.

method when the tissue has reached steady state, interestingly, when the tissue size is changing rapidly (from $t = 0$ to $t = 2000$ in Figures 6.1b and 6.3b), the differences between the numerically approximated solutions of the predictor-corrector method are far less prominent than those of the forward Euler method.

For the purposes of our modelling challenge, we are only interested in the final area of the tissue and the time taken to attain it. In Figures 6.1 and 6.3, it can be seen that each solution takes roughly the same amount of time to arrive at a steady tissue size. It can also be seen that the final value of the tissue area is roughly the same for all the solutions. For the forward Euler method, the final areas converge to ≈ 31.907 , and for the predictor-corrector method, the final areas converge to ≈ 31.806 . The values provided correspond to $\delta t = 0.1$ for each method and are the best estimates of the true solution in each case.

Since the final tissue area can, at minimum, be 2% of its initial value (Section 1.3.3) i.e. $0.02 \times 212.98 \approx 4.26$ and the difference between the best estimates of the final area is ≈ 0.1 , we can say that both the numerical schemes provide similar results, with regards to our modelling problem. Additionally, on further testing, it was observed that both numerical schemes failed for $\delta t > 1.5$. This

instability, arising as a result of large vertex displacements that grow unbounded, is inherent to the vertex model itself.

Based on the factors mentioned above, we chose to perform the simulations in the following chapters using the forward Euler method owing to its higher speed and lower computational cost. Additionally, we elected to use a time step-size of $\delta t = 1$ for the simulations since the corresponding *C.E.* is in the order of 10^{-7} . In making these choices, we prioritised the reduction of computation time per simulation since the development of the new models in chapters 7 and 8 necessitated many parameter sweeps.

Chapter 7

The one-way model

In our review of the Suzuki model (Chapter 3), we observed that despite its successes, the model had certain limitations. Many of these limitations were inherited by the modified Suzuki model (Chapter 5). To address these shortcomings and capture the range of behaviours observed *in vivo* (listed in Section 2.3), we require a new mechanochemical model of apical constriction (AC) during neural tube closure (NTC).

Following discussions with our experimental collaborators, Neophytos Christodoulou and Paris Skourides (authors of [33, 34]), we decided to model AC over 60 minutes. Consequently, the models presented in Chapters 7 and 8 were designed to illustrate that the simulated anterior neural plate contracts to within 2% to 8% of its initial area by $t = 6000$.

The AC phase of NTC takes approximately 40 to 60 minutes [34]. Since the vertex model employs non-dimensional units, we opted to use the simulation results of the modified Suzuki model as a reference to establish a relationship between non-dimensional time units and minutes. In Figure 4.9, it can be seen that the simulated neural plate in the modified Suzuki model completes AC around $t = 5000$. So, we equate $t = 5000$ to 50 minutes for the sake of convenience. Therefore, $t = 100$ corresponds to 1 minute.

In this chapter, we develop a new mechanochemical vertex model for the constriction of the anterior neural plate during AC. The model incorporates the surface ectoderm, actomyosin accumulation in the cell cortices, a damping function for the vertices, and an adhesion force for the cell edges, successfully demonstrating the desired tissue contraction along with most of the experimentally observed behaviours. Since this model captures only the effect of Ca^{2+} on cellular mechan-

ics and not vice versa, we refer to it as the one-way coupling model or the one-way model.

Starting from the modified Suzuki model, we build complexity by progressively incorporating features to reflect several experimental observations. After each addition, we demonstrate its effect on the model, highlight its limitations and discrepancy with experiments, and justify the need for adding the next feature.

For instance, after adding the surface ectoderm to the modified Suzuki model, we observe that AC stalls in the simulated neural plate. We conclude that this stalling occurs because the neural plate cannot generate enough force to resist the increasing elastic forces from the deforming surface ectoderm. To address this, we introduce the Ca^{2+} -induced increase in the cells' elastic constants and line tension. This modification is supported by experimental evidence that the neural plate is stiffer than the surrounding surface ectoderm and that its stiffness increases with the accumulation of actomyosin during AC [34, 196].

In a similar fashion, we derive and implement two other additions: a damping function for the motion of the vertices, and an adhesion term for the energy function. For the first time, we model the damping coefficient as a function of actomyosin concentration, which increases as actomyosin accumulates in the cell cortex [121, 196], and the adhesion force as a contribution from the cell's internal pressure and adherens junctions [21, 114, 116], which increases as cell edge length decreases.

We then incorporate experimental Ca^{2+} frequency and amplitude profiles [33, 95] and model the Ca^{2+} -induced elevation in line tension as a function of the Ca^{2+} flash amplitude. Finally, we discuss our results and propose new hypotheses for experimental testing, highlighting potential avenues for future research.

7.1 Adding the surface ectoderm

The first step towards developing a new model is the incorporation of the surface ectoderm. This layer of cells plays a key role in the development of the skin and certain parts of the nervous system in the early embryo. During AC, the contraction of the apical surface of the neural plate exerts a force on the cells of the surface ectoderm, deforming and displacing them. Consequently, the cells of the surface ectoderm exert a resistive force on the neural plate, influencing morphogenesis during NTC [34].

While the surface ectoderm comprises multiple cell layers, we model it as a single layer surrounding the neural plate for simplicity and to reduce computational costs. During the simulation, the outer edge of the surface ectoderm layer remains fixed, while the inner edge is pulled inwards by the contraction of the neural plate. The increasing elastic forces, resulting from the deformation of the surface ectoderm cells, exert a resistive force on the neural plate. Also, the surface ectoderm cells do not experience Ca^{2+} flashes, and the ratchet-like mechanism does not apply to them.

In Section 5.5, we establish a connection between experimentally measurable quantities and analogous parameters in the vertex model since no methodology equates them directly, as per our knowledge. For example, we consider Young's modulus as analogous to the elastic constants K_n^A and K_n^P because they determine how the material deforms in response to stress. Similarly, we equate traction stress with the line tension T_{0n} as both are associated with the deforming force.

Wiebe and Brodland [221] measured the Young's modulus of the surface ectoderm to be 0.55 times that of the neural plate, so we set $K_{n(SE)}^A = 0.55K_n^A$ and $K_{n(SE)}^P = 0.55K_n^P$, where $K_{n(SE)}^A$ and $K_{n(SE)}^P$ are the coefficients of elasticity for the area and perimeter of the surface ectoderm cells (SE cells), and K_n^A and K_n^P are the coefficients of elasticity for the area and perimeter of the neural plate cells (NP cells). Since we found no evidence to suggest a significant difference in traction stress between the surface ectoderm and neural plate, we set $T_{0n(SE)} = T_{0n}$, where $T_{0n(SE)}$ and T_{0n} are the baseline values of line tension for the surface ectoderm cells and neural plate cells, respectively.

To examine the impact of the surface ectoderm on neural plate morphogenesis, we integrate it into the modified Suzuki model and simulate the model using the same mechanical parameters as Suzuki et al [196]. We make adjustments to some parameters to ensure the neural plate contracts to 2% of its initial area. Additionally, we establish a relationship between the natural area A_n^0 and the natural perimeter P_n^0 of the cells to simplify the model. Since we model the cells as regular hexagons, the relationship between A_n^0 and P_n^0 is

$$P_n^0 = 6 \left(3^{-\frac{3}{4}} (2A_n^0)^{\frac{1}{2}} \right), \quad (7.1)$$

where the expression $3^{-\frac{3}{4}} (2A_n^0)^{\frac{1}{2}}$ represents the edge length of a regular hexagon with area A_n^0 .

Parameter	Value
SE Cells	60
NP Cells	271
p_c	0.025
δt	1
$K_n^A (SE)$	0.17
$K_n^P (SE)$	0.11
$T_{0n(SE)}$	0.1
K_n^A	0.3
K_n^P	0.2
T_{0n}	0.1
μ	1
κ_A	1
κ_P	0.001
ω_A	0.6
ω_P	0.8
A_n^0 (initial)	0.785
P_n^0 (initial)	3.3
A_n^0 (final)	0.015
P_n^0 (final)	0.456
ξ	0.05
τ	5

Table 7.1: Parameter values for Figure 7.1.

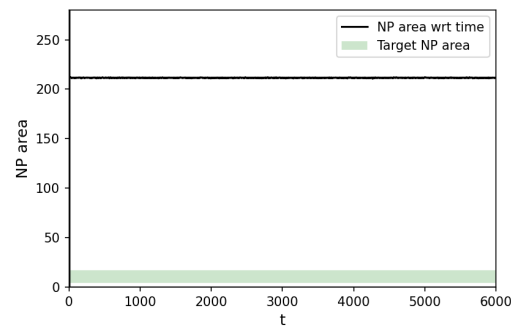
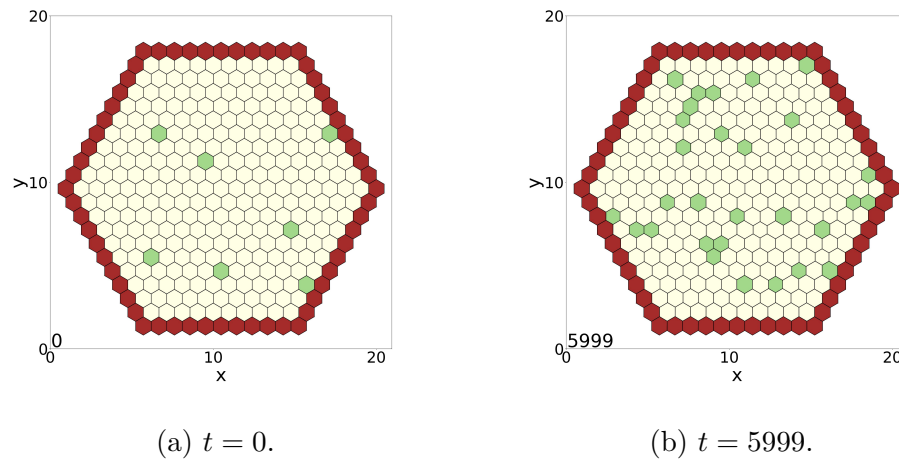


Figure 7.1: The effect of the surface ectoderm on AC in the modified Suzuki model. Depicted above are the snapshots of the apical surface of the anterior neural plate and surface ectoderm layer at the beginning and the end of the simulation along with a graph showing the time evolution of the apical surface area of the anterior neural plate. The shaded green region on the graph corresponds to 2-8% of the initial area of the anterior neural plate. Model parameters: Table 7.1.

Instead of arbitrarily selecting the initial values of A_n^0 and P_n^0 , as done by Suzuki et al, we assign them the values of area and perimeter corresponding to the cell edge length L_n at $t = 0$ i.e. $A_n^0 = \frac{3\sqrt{3}}{2}L_n^2$ and $P_n^0 = 6L_n$. Since $L_n = 0.55$ at $t = 0$ (determined in Section 5.1), the initial values of A_n^0 and P_n^0 are 0.785 and 3.3, respectively. Based on our desired final size for the neural plate, the final value of A_n^0 is $0.02 \times 0.785 = 0.015$, and therefore, according to Equation (7.1), the final value of P_n^0 is 0.456.

From Figure 7.1, it is evident that the addition of the surface ectoderm cells (red-brown) completely arrests AC in the modified Suzuki model. Although the neural plate cells (yellow) are individually contracting due to the effect of the Ca^{2+} flashes (green), this contraction does not lead to an irreversible reduction in the cells' apical surface area. We suspect two probable causes for the cessation of AC. First, the neural plate is unable to generate sufficient force to counteract the growing force resulting from the deformation of the surface ectoderm cells. And, second, the ratchet-like mechanism is unable to reduce A_n^0 and P_n^0 to a sufficient degree.

To counteract the growing force from the surface ectoderm, the model must account for the increasing contractile forces within the neural plate. The experiments of Christodoulou and Skourides [34] have demonstrated that the contractility of, and tension in, neural plate cells increases over the course of AC. This indicates that the parameters K_n^A , K_n^P , and T_{0n} should increase during the simulation runtime.

The increasing values of K_n^A , K_n^P , and T_{0n} correspond to the accumulation of actomyosin bundles in the apical cortex of neural plate cells following their activation by a Ca^{2+} flash [33, 196]. K_n^A and K_n^P relate to elastic forces, representing the medioapical and junctional actin networks, respectively. Meanwhile, T_{0n} denotes the contractile force aiming to reduce cell edge length, characterizing the contractile action of myosin motors attached to the junctional actin network.

Based on the simulation results of Suzuki et al [196], which utilize $K_n^A = 0.3$, $K_n^P = 0.2$, and $T_{0n} = 0.1$, we opt for a ratio of 3:2:1 for both the initial and final values of K_n^A , K_n^P , and T_{0n} . Our initial attempts to increase K_n^A , K_n^P , and T_{0n} from their initial values of 0.3, 0.2, and 0.1, respectively, resulted in poor outcomes. Even slight increments from these initial values generated strong forces, leading to large vertex displacements that rapidly destabilized the model. So, we set the final values of K_n^A , K_n^P , and T_{0n} to 0.3, 0.2, and 0.1, and commenced

testing suitable initial values for the model.

Based on our tests, we chose initial values of 0.03, 0.02, and 0.01 for K_n^A , K_n^P , and T_{0n} . As before, we set $K_{n(SE)}^A = 0.55K_n^A$, $K_{n(SE)}^P = 0.55K_n^P$, and $T_{0n(SE)} = T_{0n}$. The values of $K_{n(SE)}^A$, $K_{n(SE)}^P$, and $T_{0n(SE)}$ remain constant throughout the simulation. We chose these initial values because using higher initial values for K_n^A , K_n^P , and T_{0n} led to significant stretching of cells at the corners and edges of the neural plate after the completion of AC, contrary to experimental observations.

A quick check confirms that our parameter choices for the initial and final values of K_n^A , K_n^P , and T_{0n} are appropriate for modelling a realistic tissue since they result in a stable hexagonal network, as indicated by the bifurcation diagram derived in Section 5.3.

Region II of the bifurcation diagram (Figure 5.3) corresponds to a stable hexagonal network. The pair of aggregate parameters (\bar{K}, \bar{T}) lies within Region II when $1 - 3.722\frac{\sqrt{A^0}}{P^0} < \bar{T} < 1$, regardless of the value of \bar{K} , where \bar{K} and \bar{T} are defined as

$$\bar{K} = \frac{K_n^A A_n^0}{K_n^P P_n^0}, \quad (7.2)$$

$$\bar{T} = \frac{T_{0n}}{K_n^P}. \quad (7.3)$$

Since we have established a relationship between A_n^0 and P_n^0 (Equation (7.1)), (\bar{K}, \bar{T}) will lie in Region II if the following condition is satisfied: $1.13 \times 10^{-4} < \bar{T} < 1$. The initial values $K_n^A = 0.03$, $K_n^P = 0.02$, $T_{0n} = 0.01$, $A_n^0 = 0.785$, and $P_n^0 = 3.3$ yield $\bar{K} = 0.357$ and $\bar{T} = 0.5$. The final values $K_n^A = 0.3$, $K_n^P = 0.2$, $T_{0n} = 0.1$, $A_n^0 = 0.015$, and $P_n^0 = 0.456$ yield $\bar{K} = 0.049$ and $\bar{T} = 0.5$. In both cases, (\bar{K}, \bar{T}) will lie in Region II, as the ratio of T_{0n} to K_n^P is 1:2.

We define the increments of K_n^A , K_n^P , and T_{0n} with the following equations:

$$\frac{dK_n^A}{dt} = \begin{cases} R_A, & \text{if cell is activated,} \\ 0, & \text{if cell is not activated,} \end{cases} \quad (7.4)$$

$$\frac{dK_n^P}{dt} = \begin{cases} R_P, & \text{if cell is activated,} \\ 0, & \text{if cell is not activated,} \end{cases} \quad (7.5)$$

$$\frac{dT_{0n}}{dt} = \begin{cases} R_T, & \text{if cell is activated,} \\ 0, & \text{if cell is not activated,} \end{cases} \quad (7.6)$$

where R_A , R_P , and R_T are constants.

To determine the values of these constants, we use the data from Figures 2.6 and 2.7. Based on discussions with the experimentalists who provided the data for the figures [32], we learnt that each neural plate cell experiences a minimum of 15 Ca^{2+} flashes during the 60-minute period of AC, and that each Ca^{2+} flash lasts, on average, 40 seconds (Section 2.1).

Since 1 minute corresponds to a time interval $\Delta t = 100$ in the simulation, a Ca^{2+} flash should last for $\Delta t = 67$. Therefore, we set the activation period $\tau = 67$. This implies that a cell would be activated for a total time duration of $\Delta t \approx 1000$ over the simulation runtime. So, we determine R_A as follows:

$$\begin{aligned} R_A &= \frac{K_n^A(\text{final}) - K_n^A(\text{initial})}{\text{total activation time}} \\ &= \frac{0.3 - 0.03}{1000} \\ &= 2.7 \times 10^{-4}. \end{aligned} \quad (7.7)$$

We attempted to calculate R_P and R_T using the same approach. However, we found that if R_T changed at the same timescale as R_A , the resulting T_{0n} would not be sufficient to preserve cell integrity, leading to overlapping cell edges and destabilizing the model. Moreover, if the timescales over which R_P and R_T changed were too disparate, cells would contract sharply and assume erratic shapes during contraction, deviating from experimentally observed behaviour. So, we set $R_P = R_T$ since both parameters are linked to the junctional actomyosin, and calculate R_P as follows:

$$\begin{aligned} R_P &= \frac{K_n^P(\text{final}) - K_n^P(\text{initial})}{0.1 \times \text{total activation time}} \\ &= \frac{0.2 - 0.02}{100} \\ &= 1.8 \times 10^{-3}. \end{aligned} \quad (7.8)$$

Following this, we must derive a relationship between the flashes per minute per cell, denoted by the parameter fpm , and the probability of cell activation p_c . If we consider the simulation runtime $\Delta t = 6000$ to be divided into smaller

Parameter	Value
SE Cells	60
NP Cells	271
p_c	0.17
δt	1
$K_n^A (SE)$	0.02
$K_n^P (SE)$	0.01
$T_{0n}(SE)$	0.01
R_A	0.0003
R_P	0.002
R_T	0.002
K_n^A (initial)	0.03
K_n^P (initial)	0.02
T_{0n} (initial)	0.01
K_n^A (final)	0.3
K_n^P (final)	0.2
T_{0n} (final)	0.1
μ	1
κ_A	1
κ_P	0.001
ω_A	0.6
ω_P	0.8
A_n^0 (initial)	0.785
P_n^0 (initial)	3.3
A_n^0 (final)	0.015
P_n^0 (final)	0.456
k_ξ	0.5
τ	67

Table 7.2: Parameter values for Figure 7.2.

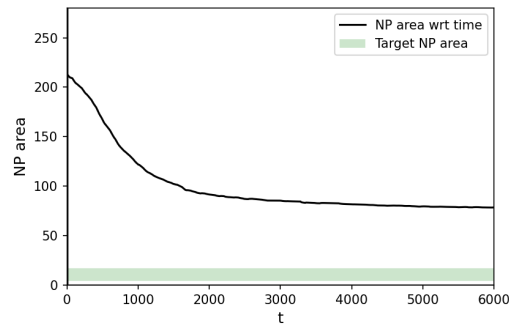
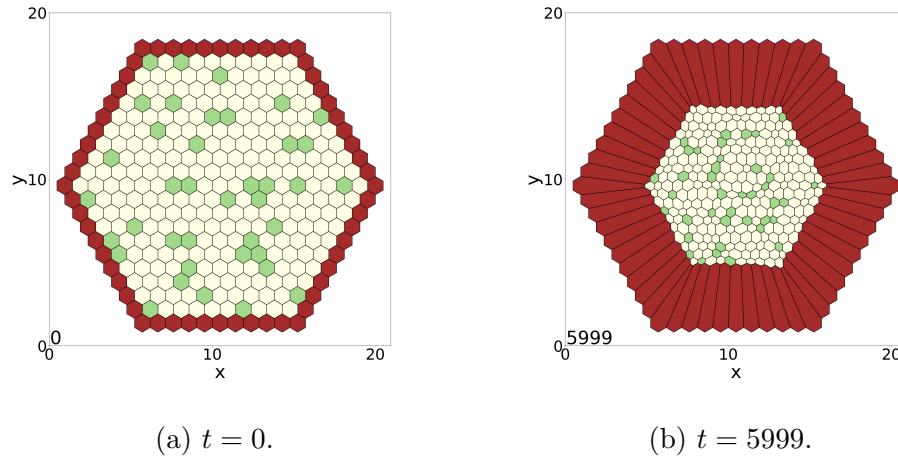


Figure 7.2: The effect of the introduction of growth laws for K_n^A , K_n^P , and T_{0n} on AC. Depicted above are the snapshots of the apical surface of the anterior neural plate and surface ectoderm layer at the beginning and the end of the simulation along with a graph showing the time evolution of the apical surface area of the anterior neural plate. The shaded green region on the graph corresponds to 2-8% of the initial area of the anterior neural plate. Model parameters: Table 7.2.

intervals of duration $\Delta t = \tau$, then p_c can be defined as

$$p_c = \begin{cases} \frac{60 \times fpm}{T_{60}/\tau}, & \text{if } \frac{60 \times fpm}{T_{60}/\tau} \leq 1, \\ 1, & \text{if } \frac{60 \times fpm}{T_{60}/\tau} > 1, \end{cases} \quad (7.9)$$

where T_{60} is the simulation time interval corresponding to 60 minutes. We take $T_{60} = 6000$, $\tau = 67$, and $fpm = 0.25$, because a cell experiences 15 flashes in 60 minutes, therefore, $p_c \approx 0.17$. The value of p_c is evaluated for each cell at the start of every τ -sized interval.

Finally, because T_{0n} increases over the course of the simulation, the Ca^{2+} -induced elevation in line tension ξ must also increase accordingly, to produce enough cell contraction to activate the ratchet-like mechanism. So, we redefine ξ in Equation (3.8) as follows:

$$\xi = k_\xi T_{0n}, \quad (7.10)$$

where k_ξ is a positive constant. Since Suzuki et al set $\xi = 0.5T_{0n}$, we adopt the same parameterization and set $k_\xi = 0.5$.

Figure 7.2 illustrates that implementing the growth laws for K_n^A , K_n^P , and T_{0n} enables the neural plate to partially overcome the resistive force exerted by the surface ectoderm, resulting in some contraction. However, this contraction is insufficient to achieve the required reduction of the apical surface of the anterior neural plate to within 2% to 8% of its initial area (visualised by the shaded green region in Figure 7.2c).

It should be noted that individual cells in the surface ectoderm do not deform to the extent shown in Figure 7.2b. The deformation of the single layer of surface ectoderm cells in Figure 7.2b represents the total deformation of all cells in the surface ectoderm due to the contraction of the neural plate [34].

Although the Ca^{2+} flashes elevate the values of K_n^A , K_n^P , and T_{0n} in neural plate cells, the cell contractions induced by Ca^{2+} fail to activate the ratchet-like mechanism for the reduction of A_n^0 and P_n^0 . To address this, we not only reselect suitable parameters for the ratchet-like mechanism but also simplify its structure.

As we have already established a relationship between A_n^0 and P_n^0 (Equation (7.1)), we can omit the equation governing the reduction in P_n^0 (Equation (3.10)) and concentrate solely on the equation governing the reduction in A_n^0 , as our focus is on the reduction in the apical surface area of the cells.

While the exact process underlying the equations of the ratchet-like mechanism remains unknown, the equations proposed by Suzuki et al (Equations (3.9) and (3.10)) show good agreement with experimental observations [223]. Therefore, we adopt their equation for the reduction in A_n^0 (Equation (3.9)) and modify it to reduce complexity. Due to the lack of experimental data, we model the reduction in A_n^0 as a linear decay, for simplicity. This ensures that the rate of reduction of A_n^0 remains constant regardless of the cell area. The revised equation governing the reduction of A_n^0 is

$$\frac{dA_n^0}{dt} = \begin{cases} -\kappa_A & , \text{ if } (A_n - \omega_A A_n^0) < 0, \\ 0 & , \text{ if } (A_n - \omega_A A_n^0) \geq 0, \end{cases} \quad (7.11)$$

where, similar to Equation (3.9), κ_A is a positive constant and ω_A is a threshold parameter that determines whether or not A_n^0 should be decreased. Since the smallest area that a cell can attain over the course of AC is 2% of its initial area, we limit the minimum value of A_n^0 to 0.015 ($A_{n(final)}^0$). The value of P_n^0 is updated using Equation (7.1) whenever A_n^0 changes according to Equation (7.11). The activation of the ratchet-like mechanism captures the reconfiguration of the actomyosin network, leading to a decrease in the natural area A_n^0 and natural perimeter P_n^0 .

For simplicity, we set $\omega_A = 1$ and determine the rate constant κ_A employing an approach similar to the one used to determine R_A :

$$\begin{aligned} \kappa_A &= \frac{A_{n(initial)}^0 - A_{n(final)}^0}{\text{total activation time}} \\ &= \frac{0.785 - 0.015}{1000} \\ &= 7.7 \times 10^{-4}. \end{aligned} \quad (7.12)$$

Upon trying to simulate the vertex model with these modifications in place, we discovered that the model quickly became unstable when cell sizes became too small. After analyzing the data from the failed simulations, we deduced that the instability arose from the increasing strength of the forces on the vertices, accompanied by the simultaneous decrease in cell edge lengths. This dual effect eventually led to vertex displacements exceeding the lengths of connected edges, causing cell edges to overlap, and ultimately rendering the model unstable.

For brevity, we will refer to this instability as the *small-edge instability*. Since it stems from the introduction of dynamics into the vertex model, the bifurcation diagram in Chapter 5 does not provide insights into the parameter choices leading to this instability. Given this limitation, our only recourse was to explore the model numerically through parameter sweeps. From the results, it became evident that cell integrity was compromised when both K_n^A and K_n^P were considerably higher than T_{0n} . However, setting a high value for T_{0n} resulted in small-edge instabilities.

Other studies employing vertex models have incorporated topology-changing events, such as the T1 transition (neighbour exchange), T2 transition (cell death), mitosis (cell division), and Node switch, to reconfigure vertex connections before cell edges reach a critically small size. These works have applied vertex models to simulate wound healing in cat corneal endothelium and regulation of tissue size in the *Drosophila* wing disc [2, 68, 101, 138, 163]. These biological processes involve cell-cell intercalation, mitosis, and apoptosis, all of which are effectively captured by the aforementioned topological transitions. However, the process of AC during NTC does not entail such topological events [32, 33, 34]. Consequently, the application of topological transitions to prevent the occurrence of small cell edges is not applicable in our study.

Therefore, we reasoned that other mechanisms must be at play to preserve cell integrity for small cell sizes. Since the instability arises from cell edges contracting too rapidly relative to the experimental timescale, we hypothesize that either the damping coefficient μ increases as cells contract, an additional force term counteracts the line tension when cell edges become very small, or a combination of both.

After consulting with our experimental collaborators [32], we learnt that the accumulation of actomyosin in the apical cortex inhibits vertex movement [121]. This justifies implementing μ as a function of cell size. Likewise, the force opposing the line tension could stem from the cell's internal pressure. As the apical surface area decreases, compression of the cytosol raises internal pressure, exerting a force that tends to increase cell edge length. Moreover, adherens junctions may also generate an adhesion force that counteracts the line tension.

The absence of strong adhesion, especially in the presence of tension, can result in the loss of mechanical integrity during tissue morphogenesis. Apical adherens junctions play a pivotal role in mediating mechanical coupling between epithelial

cells. These junctions contain adhesion receptors (e.g., E-Cadherin) that facilitate homophilic adhesion between the cells of the epithelial layer [24]. The application of tension triggers the formation of adhesion complexes¹, increasing the size of adherens junctions and strengthening cell-cell adhesion [21, 114, 116]. Additionally, elevated Ca^{2+} activity can enhance the function of adhesion receptors like E-Cadherin, further contributing to the elevation of adhesion strength within adherens junctions [77].

In Sections 7.1.1 and 7.1.2, we will derive expressions for the damping coefficient μ and adhesion as functions of the cell size. Due to the current lack of knowledge about the precise mechanisms underlying these processes and the dearth of associated experimental data, these expressions will be derived using available information on cell sizes.

7.1.1 Deriving the damping function

As discussed previously, small-edge instabilities occur when vertex displacements become significantly larger than the lengths of connected edges. As the simulation progresses, cells contract, while K_n^A , K_n^P , and T_{0n} progressively increase from 0.03 to 0.3, 0.02 to 0.2, and 0.01 to 0.1, respectively, due to actomyosin accumulation. The higher values of these parameters lead to stronger forces on vertices, causing larger displacements that eventually exceed the lengths of connected edges. This compromises cell integrity and destabilizes the model.

It is easy to understand that edge overlaps can occur only when the displacement of a vertex exceeds half the length of the smallest edge connected to it (Figure 7.3). As long as μ can produce sufficient damping to limit vertex displacement to less than half the length of the smallest connected edge, the model integrity should remain uncompromised.

From previous simulations (Figures 4.8 and 7.1), we know that the model is stable for $K_n^A = 0.3$, $K_n^P = 0.2$, $T_{0n} = 0.1$, and $\mu = 1$, when cell edge lengths are set to 0.55, at the start of the simulation. Therefore, as the cells contract, the value of μ should be increased to effectively dampen vertex motion and maintain stability. Since these models are stable at the start of the simulation, clearly $\mu = 1$ results in vertex displacements less than or equal to $\frac{0.55}{2} = 0.275$ for $K_n^A = 0.3$,

¹**Adhesion complexes** Multi-protein structures at cell junctions that facilitate and regulate cell-cell adhesion.

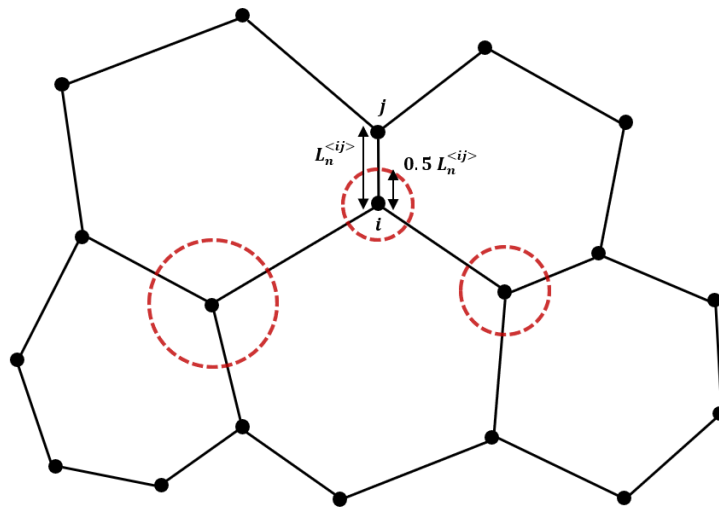


Figure 7.3: Schematic depicting the maximum allowable range for vertex displacement. The red dashed circles have a radius equal to half the length of the smallest edge connected to the vertex at the center of the circle. If the displacement of the vertex is confined to the area enclosed by the circle, edge overlaps cannot occur.

$K_n^P = 0.2$, $T_{0n} = 0.1$.

After introducing the growth laws for K_n^A , K_n^P , and T_{0n} , their initial values are set to 0.03, 0.02, and 0.01, respectively. This adjustment results in one-tenth of the force and, consequently, vertex displacement at the start of the simulation compared to the previous case. Naturally, this implies that the model would be stable for $\mu = 1$. As the simulation progresses and cell edge lengths decrease, an equation is needed to govern a proportional increase in μ .

At the start of the simulation, cell edge lengths are set to 0.55. Therefore, vertex displacements should be less than or equal to $\frac{0.55}{2} = 0.275$ to maintain stability. Towards the end of the simulation, the mechanical parameters of a cell are $K_n^A = 0.3$, $K_n^P = 0.2$, $T_{0n} = 0.1$, $A_n^0 = 0.015$, and $P_n^0 = 0.456$. Setting $K^A = 0.3$, $K^P = 0.2$, $T = 0.15$, $A^0 = 0.015$, and $P^0 = 0.456$ in Equation (5.32) gives the minimum edge length of a cell, which is $l = 0.02$. It is important to note that T should be set to 0.15 to account for the Ca^{2+} -induced elevation in line tension.²

$$\left(\frac{9}{4} \frac{K^A}{A^0}\right) l^3 + \left(6 \frac{K^P}{P^0} - \frac{\sqrt{3}}{2} K^A\right) l + (T - K^P) = 0. \quad (5.32 \text{ revisited})$$

Since the minimum edge length is 0.02, the vertex displacement should be $\leq \frac{0.02}{2} = 0.01$. This implies that μ should increase by a factor of $\frac{0.275}{0.01} \approx 30$ over the course of cell contraction.

To derive the equation for μ , we begin by defining a new quantity - the natural length of the cell L_n^0 . We set $L_n^0 = \frac{P_n^0}{6}$ since the cells are hexagons. At the start of the simulation, $L_n^0 = 0.55$ and $\mu = 1$. After a cell has contracted to its minimum size, $P_n^0 = 0.456 \implies L_n^0 = 0.076$, and $\mu = 30$.

We use L_n^0 as a measure of the accumulation of actomyosin in the apical cortex of a cell; the smaller the value of L_n^0 , the greater the amount of actomyosin. Assuming that the damping effect of actomyosin varies inversely with L_n^0 , we employ the method for deriving the equation of a straight line to establish a relationship between the damping coefficient μ and the natural length L_n^0 .

Consider the equation of a straight line,

²Since the surface ectoderm resists the contraction of the neural plate, the actual value of minimum edge length will be slightly greater than 0.02.

$$\frac{y - y_1}{y_2 - y_1} = \frac{x - x_1}{x_2 - x_1}, \quad (7.13)$$

where (x_1, y_1) and (x_2, y_2) are the x and y coordinates of two known points. Replacing x , y , (x_1, y_1) , and (x_2, y_2) with $\frac{1}{L_n^0}$, μ , $(\frac{1}{0.55}, 1)$, and $(\frac{1}{0.076}, 30)$, respectively, we get

$$\begin{aligned} \frac{\mu - 1}{30 - 1} &= \left(\frac{1}{L_n^0} - \frac{1}{0.55} \right) \div \left(\frac{1}{0.076} - \frac{1}{0.55} \right) \\ \mu &= 1 + 2.56 \left(\frac{1}{L_n^0} - 1.81 \right) \\ &= \frac{2.56}{L_n^0} - 3.65. \end{aligned} \quad (7.14)$$

It should be noted that, according to Equation (7.14), μ can drop to 0 or even take on negative values (for $L_n^0 \geq 0.7$). A negative damping coefficient would cause the vertex to move in the opposite direction to the applied force, which is unrealistic. However, since AC only involves the reduction of L_n^0 , this does not affect the robustness of our model.

Equation (7.14) provides the damping effect of a single cell on a vertex. As a vertex is associated with multiple cells, its damping coefficient results from the contributions of all associated cells. Treating the damping effects of cells as dampers in parallel, we sum their contributions to calculate the vertex's damping coefficient as follows:

$$\mu_i = \sum_n^{C_i} \frac{2.56}{L_n^0} - 3.65, \quad (7.15)$$

where μ_i is the damping coefficient for the i^{th} vertex, and C_i represents the set of cells that share the i^{th} vertex. n represents the cell index, denoting that the sum is over all cells that meet at the i^{th} vertex.

7.1.2 Deriving the adhesion term

In Section 7.1.1, we derived the damping coefficient for a vertex, which varies inversely with the length of the edges connected to the vertex. However, there is

still no mechanism in place to prevent cell edges from contracting to a point for high values of tension. This could happen when the Ca^{2+} -induced elevation in line tension is high enough to temporarily force a high degree of contraction in the edge or if a cell is forced to contract due to the high interfacial tension from an adjacent cell, but the actomyosin accumulation within the cell is not sufficient to dampen the motion of the vertices by the required amount.

In the absence of topology-altering processes, there must be a force that opposes the excessive contraction of a cell edge when it becomes too small. This force should be negligible compared to the line tension for larger edge lengths but needs to dominate the line tension as the edge length decreases.

Note that this force could originate from either the cell's internal pressure, adherens junctions, or a combination of both. However, since this force opposes tension, promoting an increase in edge lengths and interfacial contact between cells, we simply refer to it as *adhesion* for convenience.

Based on the profile described above, it is reasonable to model adhesion using a sigmoidal curve, commonly used to describe stress profiles in epithelial morphogenesis [95, 96, 136]. So, we assume that the adhesion force has the form

$$\sigma(l) = \frac{a}{b + (cl)^n}, \quad (7.16)$$

where l is the edge length, and a , b , c , and n are positive constants.

The parameter n controls the steepness of the sigmoid. A larger value of n results in a steeper increase in adhesion as l decreases. Additionally, since we need to incorporate adhesion into the line energy U_L (Equation (3.3)), it would be prudent to select a value of n that yields a straightforward antiderivative of $\sigma(l)$. The highest integer value of n for which a simple antiderivative of $\sigma(l)$ exists is 2, so we set $n = 2$.

Since we limit the minimum value of P_n^0 to 0.456, the minimum value of L_n^0 is 0.076. To penalize the contraction of edge length beyond this limit, the adhesion at $L_{n(final)}^0 = 0.076$ should match the maximum value of line tension $T_{n(final)}$:

$$\begin{aligned}
\sigma(L_{n(\text{final})}^0) &= T_{n(\text{final})} \\
&= T_{0n(\text{final})} + \xi && \text{(substituting 3.8)} \\
&= (1 + k_\xi) T_{0n(\text{final})} && \text{(substituting 7.10)} \\
&= 0.15. && (7.17)
\end{aligned}$$

Since we want the adhesion force to be significantly stronger than line tension for small l , we assume the asymptotic limit of the sigmoid to be slightly greater than 1, i.e., $\sigma(0) = \frac{a}{b} = 1$. Based on this assumption, we set a and b to 1 for the sake of simplicity. Rearranging the terms of Equation (7.16), c can be determined as follows:

$$\begin{aligned}
c &= \left(\frac{a}{\sigma(l)} - b \right)^{\frac{1}{n}} \left(\frac{1}{l} \right) \\
&= \left(\frac{1}{\sigma(L_{n(\text{final})}^0)} - 1 \right)^{\frac{1}{2}} \left(\frac{1}{L_{n(\text{final})}^0} \right) \\
&= \left(\frac{1}{0.15} - 1 \right)^{\frac{1}{2}} \left(\frac{1}{0.076} \right) \\
&= 31.32. && (7.18)
\end{aligned}$$

The method outlined above provides an expression for the adhesion force, tailored for a maximum line tension $T_{n(\text{final})} = 0.15$. However, studies indicate that adherens junctions grow and reinforce adhesion in response to tension [21, 114, 116]. Consequently, we scale the adhesion force σ as follows to obtain the expression for the scaled adhesion force at a cell-cell junction:

$$\begin{aligned}
S_n^{\langle ij \rangle} (T_n^{\langle ij \rangle}, L_n^{\langle ij \rangle}) &= \frac{T_n^{\langle ij \rangle}}{0.15} \cdot \sigma(L_n^{\langle ij \rangle}) \\
&= \frac{T_n^{\langle ij \rangle}}{0.15} \cdot \frac{1}{1 + (31.32 L_n^{\langle ij \rangle})^2}, && (7.19)
\end{aligned}$$

where n denotes the cell index, and $\langle ij \rangle$ denotes the edge connecting vertices i and j . The scaling has been performed so that the adhesion $S_n^{\langle ij \rangle}$ is equal to the line tension $T_n^{\langle ij \rangle}$ at the cell-cell junction for junction length $L_n^{\langle ij \rangle} = 0.076$ (Figure 7.4).

We then subtract $S_n^{\langle ij \rangle}$ from $T_n^{\langle ij \rangle}$ and integrate the result with respect to $L_n^{\langle ij \rangle}$ to find its antiderivative. This yields the updated expression for the potential energy of a cell-cell junction U_L , replacing Equation (3.3).

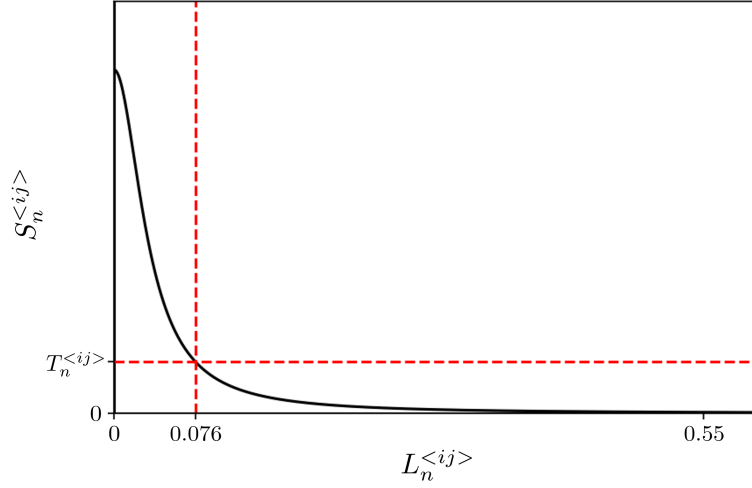


Figure 7.4: Scaled adhesion force at a cell-cell junction $S_n^{<ij>}$ versus the junction length $L_n^{<ij>}$. At $L_n^{<ij>} = L_n^{0(final)} = 0.076$, adhesion is equal to the line tension $T_n^{<ij>}$.

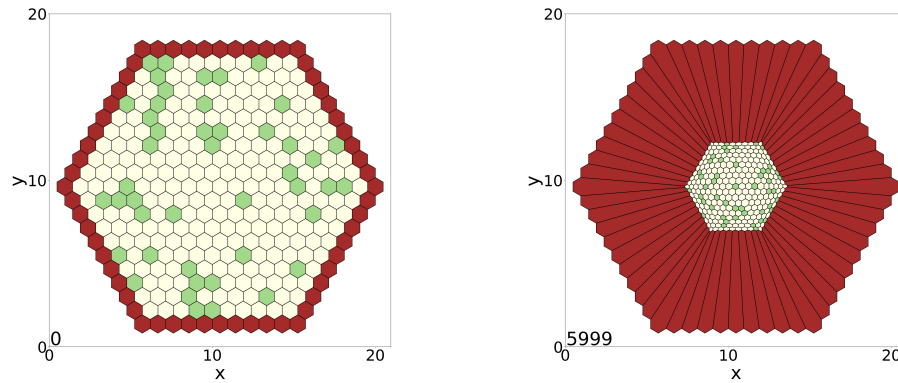
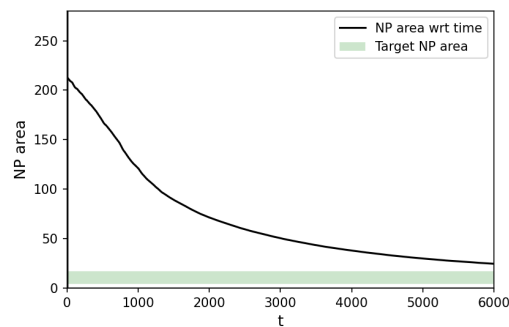
$$\begin{aligned}
 U_L &= \sum_n \sum_{<ij>}^{N_{cells} \text{ edge}} \left(\int_0^{L_n^{<ij>}} (T_n^{<ij>} - S_n^{<ij>}) dL_n^{<ij>} \right) \\
 &= \sum_n \sum_{<ij>}^{N_{cells} \text{ edge}} \left(T_n^{<ij>} L_n^{<ij>} - \frac{T_n^{<ij>}}{4.69} \cdot \arctan(31.32 L_n^{<ij>}) \right) \quad (7.20)
 \end{aligned}$$

It is important to note that with the inclusion of the adhesion term in the update of U_L , Equation (5.32) is no longer applicable for determining a cell's edge length at equilibrium (in the absence of the surface ectoderm). Instead, the equilibrium edge length is now L_n^0 since $U_A = U_P = U_L = U = 0$ in Equation (3.4) when all edge lengths are equal to L_n^0 .

After incorporating the damping and adhesion mechanisms (Equations (7.15) and (7.20)), along with the revised ratchet-like mechanism (Equation (7.11)), into the vertex model, we observe that the small-edge instability has been eliminated and the neural plate contracts to a much greater degree (Figure 7.5) than before (Figure 7.2).

Parameter	Value
SE Cells	60
NP Cells	271
p_c	0.17
δt	1
$K_n^A (SE)$	0.02
$K_n^P (SE)$	0.01
$T_{0n}(SE)$	0.01
R_A	0.0003
R_P	0.002
R_T	0.002
K_n^A (initial)	0.03
K_n^P (initial)	0.02
T_{0n} (initial)	0.01
K_n^A (final)	0.3
K_n^P (final)	0.2
T_{0n} (final)	0.1
κ_A	0.0008
ω_A	1
A_n^0 (initial)	0.785
A_n^0 (final)	0.015
k_ξ	0.5
τ	67

Table 7.3: Parameter values for Figure 7.5.

(a) $t = 0$.(b) $t = 5999$.

(c) NP area versus time.

Figure 7.5: The impact of the revised ratchet-like mechanism on AC. The revision of the ratchet-like mechanism necessitates the introduction of the damping and adhesion mechanisms. Depicted above are the snapshots of the apical surface of the anterior neural plate and surface ectoderm layer at the beginning and the end of the simulation along with a graph showing the time evolution of the apical surface area of the anterior neural plate. The shaded green region on the graph corresponds to 2-8% of the initial area of the anterior neural plate. Model parameters: Table 7.3.

However, although the apical surface area of the anterior neural plate comes very close, reaching 12% of the initial area, it still falls short of the required range (visualised by the shaded green region in Figure 7.5c) upon the completion of AC. This shortcoming likely arises from our simplified implementation of Ca^{2+} signalling, where we use a constant frequency of Ca^{2+} flashes per minute per cell (fpm), although in reality, the frequency of Ca^{2+} flashes increases as AC progresses. We will address this in the following section by introducing an experimentally observed Ca^{2+} frequency profile into the model.

To test the effectiveness of the damping and adhesion mechanisms, we ran simulations with each component removed in turn. The small-edge instability returned when either component was removed, demonstrating the necessity of both for the model's stability.

These mechanisms could also be applied to model other phenomena where implementing topological transitions is not feasible, similar to AC during NTC. For instance, lens pit invagination during the development of the eye [158, 159] and tissue folding during the development of the gut [32, 36].

In this section, we concentrated on enhancing the mechanical aspects of the vertex model to facilitate the contraction of the neural plate despite the resistive force exerted by the surface ectoderm. In the following sections (Sections 7.2 and 7.3), we will address the chemical aspect by incorporating frequency and amplitude profiles for Ca^{2+} signalling, derived from experimental data.

7.2 Modelling the Ca^{2+} frequency

To incorporate the Ca^{2+} frequency profile into the model, we refer to the experimental data from Christodoulou and Skourides (Figure 2.7) [33, 95]. It should be noted that the data in Figure 2.7 represents the behaviour of a small number of cells contracting over 40 minutes, whereas the entire process of AC can take up to 60 minutes. So, following discussions with the authors of [33], we extrapolated the data to establish the following Ca^{2+} frequency profile for the flashes:

$$fpm(t) = \begin{cases} 0.25 & , \text{ if } 0 \leq t < 4000, \\ 5 \times 10^{-5}(t - 4000) + 0.25, & \text{ if } 4000 \leq t \leq 6000, \end{cases} \quad (7.21)$$

where, as before, fpm denotes the number of flashes per minute per cell. From $t = 0$ to $t = 4000$, $fpm = 0.25$. From $t = 4000$ to $t = 6000$, the value of fpm increases linearly from 0.25 to 0.35.

Additionally, we acknowledge that the model developed thus far does not accurately depict the behaviour where Ca^{2+} flashes precede cellular contractions. Instead, a cell contracts as soon as it transitions from a low to a high Ca^{2+} state. However, experimental observations clearly show that cellular contraction follows the occurrence of a Ca^{2+} flash; in other words, there is a latency between the two events.

In non-muscle cells, such as neuroepithelial cells, contraction is mediated by calmodulin [40]. When Ca^{2+} binds to calmodulin, it induces a structural change in calmodulin. This activated form of calmodulin then interacts with and regulates the activity of MLCK, which in turn activates myosin [173] (Section 1.2.3). This activation enables myosin to interact with actin filaments, ultimately leading to the contraction of actomyosin complexes.

The process involves *positive cooperativity*, where the binding of Ca^{2+} to one calmodulin molecule facilitates the binding of Ca^{2+} to adjacent calmodulin molecules, enhancing the overall response [43, 112]. Moreover, myosin pulses have been shown to correlate with transient fluctuations of cell shape and area in epithelial cells [24]. This suggests that Ca^{2+} flashes directly lead to actomyosin contractions by facilitating myosin activity.

The ‘motor-like’ activity of myosin temporarily elevates the line tension. Therefore, we revise the mechanism governing the Ca^{2+} -induced elevation of line tension in the model (Equation (7.10)) as follows:

$$\xi(t_c) = \begin{cases} k_\xi T_{0n} \frac{(t_c/\tau)^n}{0.01 + (t_c/\tau)^n} & , \quad \text{if } 0 \leq t_c \leq \tau , \\ k_\xi T_{0n} 0.99 & , \quad \text{if } \tau < t_c \leq 2\tau , \\ 0 & , \quad \text{if } 2\tau < t_c \leq 3\tau , \end{cases} \quad (7.22)$$

where $\xi(t_c)$ is the Ca^{2+} -induced elevation in line tension as a function of time, n is a positive integer, k_ξ , T_{0n} , τ retain their usual meanings, and $t_c = 0$ denotes the instant when the cell transitions from a low to a high Ca^{2+} state. The sigmoidal function is defined with an asymptotic limit of 1, and it reaches 99% of that value at $t_c = \tau$, i.e., when the cell transitions from a high to a low Ca^{2+} state. After the cell reverts to a low Ca^{2+} state, ξ maintains its value for a duration of $\Delta t = \tau$

before dropping to 0, indicating the exhaustion of the myosin motors. Following this, the value of ξ is maintained at 0, again, for $\Delta t = \tau$. We estimate these time durations visually from Figure 2.6 since no studies provide precise measurements for these events.

The entire sequence of events described above constitutes a Ca^{2+} oscillation, having a time period $T_{osc} = 3\tau$, where a Ca^{2+} flash lasts for $\Delta t = \tau$, followed by a refractory period that lasts for $\Delta t = 2\tau$, during which no Ca^{2+} flash occurs. Since the duty ratio of the Ca^{2+} oscillation can be found using the expression

$$duty = \frac{\tau}{T_{osc}}, \quad (7.23)$$

we calculate the duty ratio to be 0.33.

The sigmoidal function in Equation (7.22) is commonly used in the Hill equation, which is employed to study the kinetics of many enzyme-catalyzed reactions and transporter-mediated processes. For brevity, we shall refer to it as an n -th degree Hill function. The Hill coefficient n provides a measure of the cooperativity of substrate binding to the protein, $n > 1$ suggests that two or more binding sites exist in the protein and that there is *positive cooperativity* with respect to substrate binding. Based on observations from our simulation results, we determined that $n = 10$ provided the closest match to the Ca^{2+} profile depicted in Figure 2.6.

Based on our new definition for a Ca^{2+} oscillation, we must revise the previously defined relationship between fpm and p_c (Equation (7.9)). If we consider the simulation runtime $\Delta t = 6000$ to be divided into smaller intervals of duration $\Delta t = T_{osc}$, then p_c can be defined as

$$p_c = \begin{cases} \frac{60 \times fpm}{T_{60}/T_{osc}}, & \text{if } \frac{60 \times fpm}{T_{60}/T_{osc}} \leq 1, \\ 1, & \text{if } \frac{60 \times fpm}{T_{60}/T_{osc}} > 1, \end{cases} \quad (7.24)$$

where T_{60} is the simulation time interval corresponding to 60 minutes, as before. The value of p_c is evaluated for each cell at the start of every T_{osc} -sized interval.

Upon updating our definition of the Ca^{2+} -induced elevation of line tension, we can now address an experimentally observed behaviour that the modified Suzuki model and, by extension, the model we have developed so far (Section 7.1) have been unable to capture.

It has been observed that the pharmacological elevation of cytosolic Ca^{2+} levels leads to synchronous and continuous cellular contractions, resulting in the failure of NTC. This suggests that asynchronous and cell-autonomous pulsed contractions are essential for the correct morphogenesis of the neural tube [33] (Chapter 2).

Contrary to this observation, the Suzuki model and the modified Suzuki model demonstrate maximal contraction of the apical surface area of the neural plate when $p_c = 1$, which corresponds to the scenario where all cells experience an elevated level of Ca^{2+} (Figures 3.7 and 5.9). This is because synchronous Ca^{2+} flashes across the neural plate induce a simultaneous increase in the line tension of all cells. Consequently, cell edges contract to minimize the total potential energy of the neural plate (Equation (3.4)).

To reproduce this behaviour *in silico*, we need to revise some of our modelling assumptions based on experimental evidence. We base our revisions on the following observations:

- (i) Actomyosin bundles can be rearranged by the application of a mechanical force [64, 212].
- (ii) Ca^{2+} flashes occur just before a cell contraction pulse but never during the stabilization step [33].

Therefore, we hypothesize that the Ca^{2+} -induced elevation in line tension (ξ) causes the rearrangement of actomyosin bundles, and this rearrangement - indicated by permanent changes in K_n^A , K_n^P , T_{0n} , A_n^0 , and P_n^0 - can only occur when the Ca^{2+} level in the cell is not elevated. So, we modify the growth laws for K_n^A , K_n^P , and T_{0n} (Equations (7.4)-(7.6)) and the ratchet-like mechanism (Equations (7.11)), as follows:

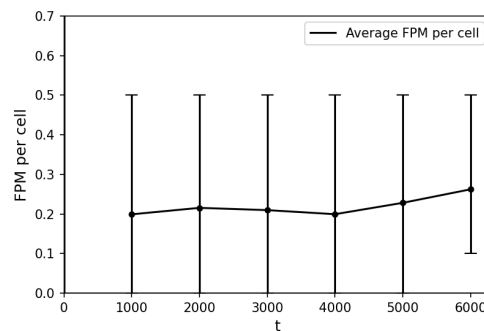
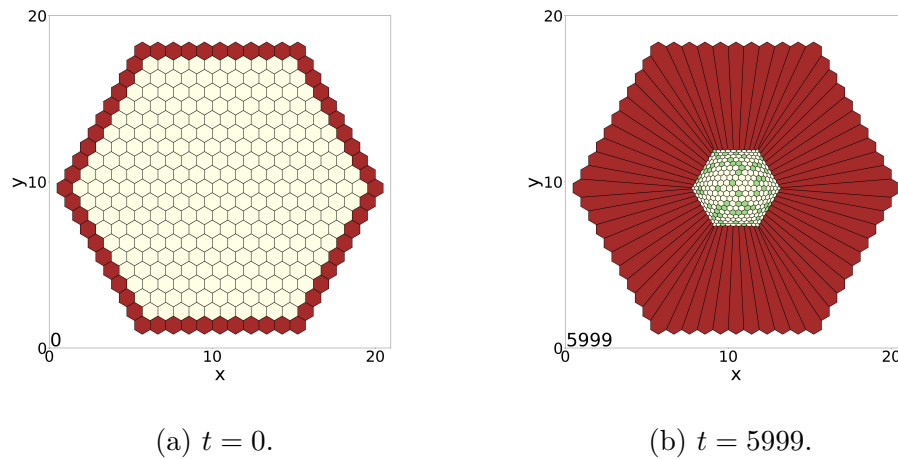
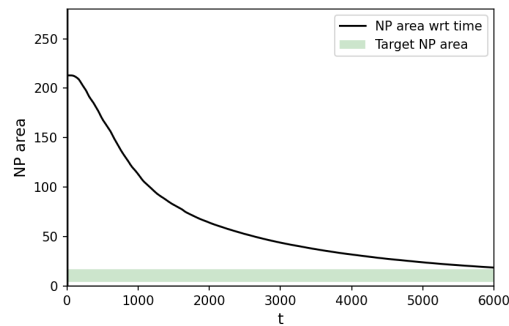
$$\frac{dK_n^A}{dt} = \begin{cases} R_A, & \text{if } \xi(t_c) \neq 0 \wedge \text{cell is not activated,} \\ 0, & \text{otherwise,} \end{cases} \quad (7.25)$$

$$\frac{dK_n^P}{dt} = \begin{cases} R_P, & \text{if } \xi(t_c) \neq 0 \wedge \text{cell is not activated,} \\ 0, & \text{otherwise,} \end{cases} \quad (7.26)$$

$$\frac{dT_{0n}}{dt} = \begin{cases} R_T, & \text{if } \xi(t_c) \neq 0 \wedge \text{cell is not activated,} \\ 0, & \text{otherwise,} \end{cases} \quad (7.27)$$

Parameter	Value
SE Cells	60
NP Cells	271
$duty$	0.33
δt	1
$K_n^A (SE)$	0.02
$K_n^P (SE)$	0.01
$T_{0n}(SE)$	0.01
R_A	0.0003
R_P	0.002
R_T	0.002
K_n^A (initial)	0.03
K_n^P (initial)	0.02
T_{0n} (initial)	0.01
K_n^A (final)	0.3
K_n^P (final)	0.2
T_{0n} (final)	0.1
κ_A	0.0008
ω_A	1
A_n^0 (initial)	0.785
A_n^0 (final)	0.015
k_ξ	0.5
τ	67

Table 7.4: Parameter values for Figures 7.6 and 7.7.

(c) Ca^{2+} flash frequency versus time.

(d) NP area versus time.

Figure 7.6: The effect of introducing the Ca^{2+} frequency profile into the vertex model. Depicted above are the snapshots of the apical surface of the anterior neural plate and surface ectoderm layer at the beginning and the end of the simulation along with graphs showing the time evolution of the number of flashes per minute per cell (averaged over the 271 neural plate cells) and the time evolution of the apical surface area of the anterior neural plate. The shaded green region on the latter corresponds to 2-8% of the initial area of the anterior neural plate. Model parameters: Table 7.4.

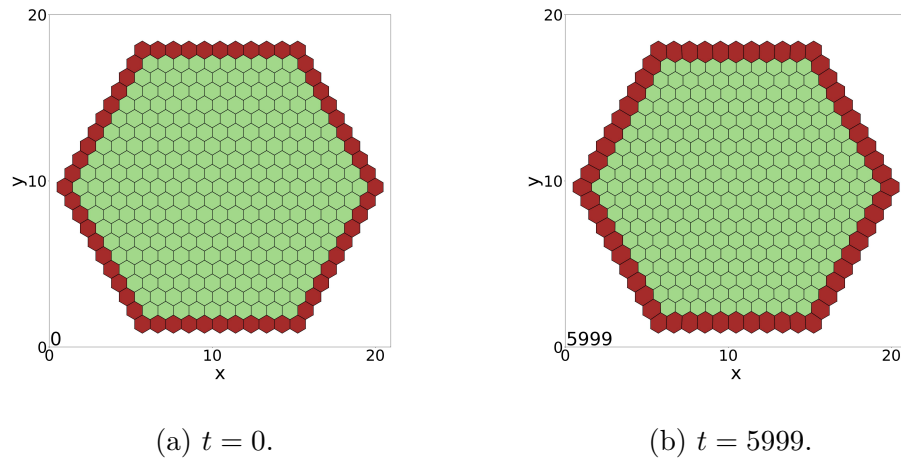


Figure 7.7: The effect of the continuous elevation of cytosolic Ca^{2+} on AC. The continuous elevation of cytosolic Ca^{2+} inhibits the contraction of the apical surface of the anterior neural plate, resulting in the failure of NTC. Depicted above are the snapshots of the apical surface of the anterior neural plate and surface ectoderm layer at the beginning and the end of the simulation. Except for *duty*, all model parameters have the same values as listed in Table 7.4. For a sustained elevation in Ca^{2+} levels ($p_c = 1$), we set $fpm = 1.5$ and $duty = 1$ (Equation (7.24)).

$$\frac{dA_n^0}{dt} = \begin{cases} -\kappa_A, & \text{if } (A_n - \omega_A A_n^0) < 0 \wedge \text{cell is not activated,} \\ 0, & \text{otherwise,} \end{cases} \quad (7.28)$$

where R_A , R_P , R_T , and κ_A are the corresponding rate constants and retain their values from Equations (7.7), (7.8), and (7.12), respectively. As before, we limit the minimum value of A_n^0 to $A_{n(\text{final})}^0 = 0.015$. The value of P_n^0 is updated using Equation (7.1) whenever A_n^0 changes according to Equation (7.28).

We then simulate the vertex model with these modifications in place (Figure 7.6). Figure 7.6c depicts the number of flashes per minute per cell (averaged over all the cells of the neural plate), measured over time windows of size $\Delta t = 1000$. The error bars indicate the range of variation in the number of flashes per minute per cell. The average frequency of Ca^{2+} flashes remains nearly constant from $t = 0$ to $t = 4000$, then linearly increases from $t = 4000$ to $t = 6000$, resembling the prescribed frequency profile (Equation (7.21)). Although the average number of flashes per minute per cell is slightly less than the prescribed frequency profile. In Figure 7.6d, we see that the apical surface area of the anterior neural plate contracts even more than in Figure 7.5, reaching 9% of the initial area upon the completion of AC, though still falling slightly short of the required range.

Figure 7.7 illustrates the effects of incorporating Equations (7.25)-(7.28) into the vertex model. The continuous elevation of cytosolic Ca^{2+} inhibits the contraction of the apical surface of the anterior neural plate, leading to the failure of NTC. This underscores the crucial role of the Ca^{2+} refractory period and asynchronous Ca^{2+} flashes in the proper morphogenesis of the neural tube, consistent with experimental observations [33].

7.3 Modelling the Ca^{2+} amplitude

To incorporate the Ca^{2+} amplitude profile into the model, we again refer to the experimental data from Christodoulou and Skourides (Figure 2.8) [33, 95]. As was the case for the Ca^{2+} frequency profile (Figure 2.7), the data in Figure 2.8 represents the behaviour of a small number of cells contracting over 40 minutes. So, we extrapolate the data to 60 minutes to establish the following Ca^{2+} amplitude profile for the flashes:

$$\text{amp}(t) = \begin{cases} 2.5 \times 10^{-5}(t) + 0.6 & , \quad \text{if } 0 \leq t < 4000, \\ 1 \times 10^{-4}(t - 4000) + 0.7, & \text{if } 4000 \leq t \leq 6000, \end{cases} \quad (7.29)$$

where amp denotes the amplitude of a Ca^{2+} flash. In [95], all Ca^{2+} flash amplitudes were normalized by dividing them by the highest amplitude measured during AC. From $t = 0$ to $t = 4000$, the value of amp increases linearly from 0.6 to 0.7. From $t = 4000$ to $t = 6000$, the value of amp increases linearly from 0.7 to 0.9.

In Section 7.2, we highlighted the role of Ca^{2+} in inducing actomyosin contractions by binding to calmodulin, which leads to the activation of myosin. As actomyosin accumulates in the apical cortex of neural plate cells during AC, the amount of Ca^{2+} required to activate it increases concomitantly. If an insufficient amount of actomyosin is activated, the resulting elevation in line tension is unable to overcome the elastic forces from the accumulated actomyosin. Hence, the amplitude of Ca^{2+} flashes must increase to trigger sufficient contraction in the cell's apical surface area.

Therefore, we update the mechanism governing the Ca^{2+} -induced elevation of line tension (Equation (7.22)) as follows:

$$\xi(t_c) = \begin{cases} k_\xi f(\text{amp}) \frac{(t_c/\tau)^{10}}{0.01 + (t_c/\tau)^{10}} & , \quad \text{if } 0 \leq t_c \leq \tau, \\ k_\xi f(\text{amp}) 0.99 & , \quad \text{if } \tau < t_c \leq 2\tau, \\ 0 & , \quad \text{if } 2\tau < t_c \leq 3\tau, \end{cases} \quad (7.30)$$

where $\xi(t_c)$ is the Ca^{2+} -induced elevation in line tension as a function of time, and $t_c = 0$ denotes the instant when the cell transitions from a low to a high Ca^{2+} state. The constants k_ξ and τ retain their usual meanings, and $f(\text{amp})$ represents the actomyosin activation as a function of Ca^{2+} flash amplitude.

As AC commences, the actomyosin level in the apical cortex is at its lowest (corresponding to $T_{0n} = 0.01$). At this stage, a Ca^{2+} flash with an amplitude of $\text{amp} = 0.6$ is sufficient to activate the existing actomyosin. Towards the end of AC, the actomyosin level in the apical cortex reaches its peak ($T_{0n} = 0.1$). At this stage, a Ca^{2+} flash with an amplitude of $\text{amp} = 0.6$ activates only a fraction of the total actomyosin. To fully activate the increased amount of actomyosin

Parameter	Value
SE Cells	60
NP Cells	271
$duty$	0.33
δt	1
$K_n^A (SE)$	0.02
$K_n^P (SE)$	0.01
$T_{0n}(SE)$	0.01
R_A	0.0003
R_P	0.002
R_T	0.002
K_n^A (initial)	0.03
K_n^P (initial)	0.02
T_{0n} (initial)	0.01
K_n^A (final)	0.3
K_n^P (final)	0.2
T_{0n} (final)	0.1
κ_A	0.0008
ω_A	1
A_n^0 (initial)	0.785
A_n^0 (final)	0.015
k_ξ	4
τ	67

Table 7.5: Parameter values for Figures 7.8, 7.9, 7.10, 7.11, 7.12, 7.13, and 7.14.

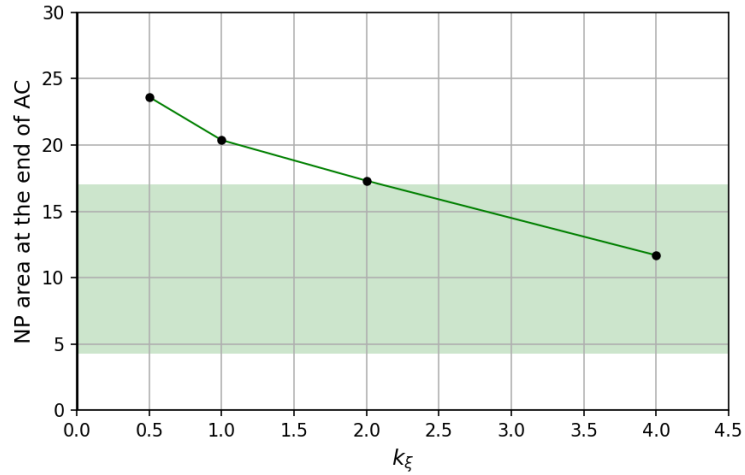


Figure 7.8: The effect of varying k_ξ on the final area attained by the apical surface of the anterior neural plate upon the completion of AC, i.e., at $t = 6000$. The shaded green region on the graph corresponds to 2-8% of the initial apical surface area of the anterior neural plate. Except for k_ξ , all model parameters have the same values as listed in Table 7.5.

accumulated in the apical cortex, a Ca^{2+} flash with an amplitude of $amp = 0.9$ is required.

Since the precise mechanism governing the relationship between Ca^{2+} flash amplitude and actomyosin activation is unknown, we use an exponential function that fits the known data points $f(0.6) = 0.01$ and $f(0.9) = 0.1$. This approach uses T_{0n} as a measure of the actomyosin level. So, we define $f(amp)$ as follows:

$$f(amp) = 1 \times 10^{-4} \exp(7.68 amp). \quad (7.31)$$

Taken together, Equations (7.30) and (7.31) imply that a sufficiently high Ca^{2+} amplitude can fully activate the actomyosin accumulated in the apical cortex (represented by T_{0n}). Subsequently, the Ca^{2+} -induced activity of the myosin motors elevates the line tension to $k_\xi T_{0n}$ within the time interval $\Delta t = \tau$. It is reasonable to assume that the maximum tension generated depends on the actomyosin level so we set the upper limit of $\xi(t_c)$ to $k_\xi T_{0n}$, i.e.,

$$\xi(t_c) = \begin{cases} \xi(t_c) & , \text{ if } 0 \leq \xi(t_c) \leq k_\xi T_{0n} , \\ k_\xi T_{0n} & , \text{ if } k_\xi T_{0n} < \xi(t_c) , \end{cases} \quad (7.32)$$

After incorporating these modifications into the vertex model, we conducted a parameter sweep for k_ξ . Starting at $k_\xi = 0.5$, we doubled its value successively until identifying the smallest value of k_ξ that achieved the desired degree of contraction. In Figure 7.8, it can be seen that the apical surface area of the anterior neural plate contracts to 5.5% of its initial value for $k_\xi = 4$. Since this area is within the desired range of 2% to 8%, we set k_ξ to 4.

With this final modification, we conclude the development of a mechanochemical vertex model that captures the impact of Ca^{2+} on the constriction of the apical surface area of the anterior neural plate, incorporating experimentally valid Ca^{2+} frequency and amplitude profiles, during the AC phase of NTC. Since this model only captures the unilateral effect of Ca^{2+} signalling on cellular mechanics and, consequently, tissue contraction, we call it the one-way coupling model or **the one-way model**.

Figure 7.9 visualises the time evolution of the apical surface of the anterior neural plate and surface ectoderm layer in the one-way model. The cell at the centre of the neural plate is marked with a red border. We demonstrate the effect of Ca^{2+} flashes on the apical surface area of cells by monitoring the area of the ‘marked’ cell along with the Ca^{2+} flashes it experiences.

Figure 7.10c depicts the cell undergoing pulsed contractions due to the influence of Ca^{2+} flashes. Although individual cells contract in a pulsed manner, the anterior neural plate contracts monotonically without recovery phases (Figure 7.10d), in line with experimental findings [33, 121]. The apical surface of the anterior neural plate contracts to 5.5% of its initial area, ultimately achieving the desired contraction and resulting in successful NTC.

Due to the folding of the anterior neural plate during NTC, it becomes challenging to track its apical surface area through live-cell imaging. Therefore, Christodoulou and Skourides [33] evaluated the rate of NTC by measuring the speed at which the periphery of the neural plate moved toward its centre (Figure 2.2). Similarly, we track the distance between the centroids of the cell at the centre of the neural plate and a cell at the edge of the neural plate (represented by the red line in Figures 7.9a-7.9f). The velocity of NTC is indicated by the rate at which this distance changes, visualised in Figure 7.10e.

In Figure 7.10e, the NTC velocity is initially depicted as negative. This is because the cells at the centre and edge initially move away from each other due to the spontaneous contraction of surrounding cells. However, as AC progresses,

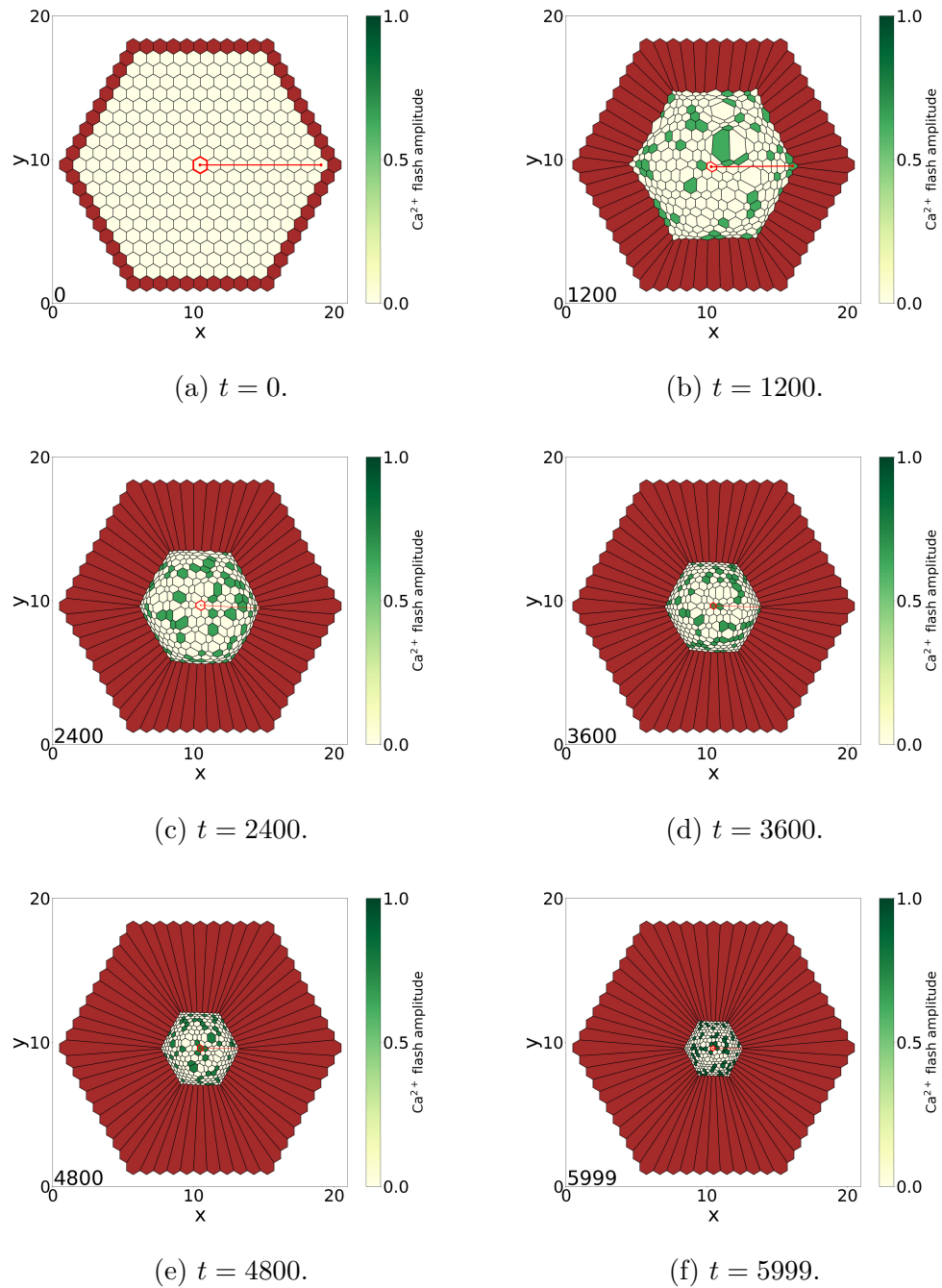
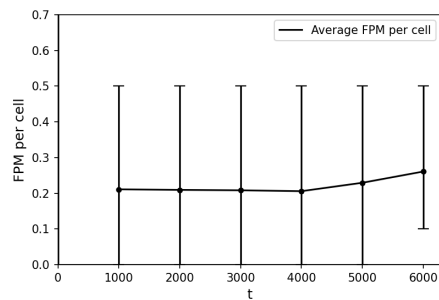
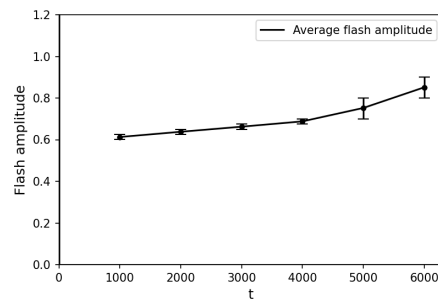
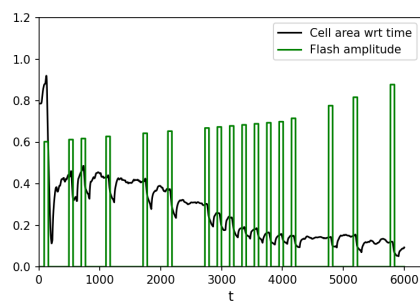
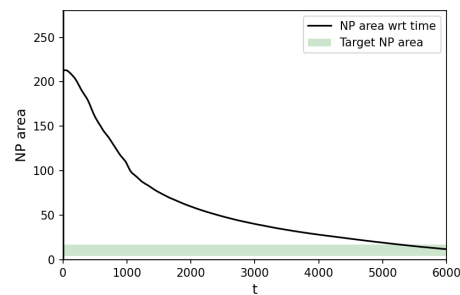
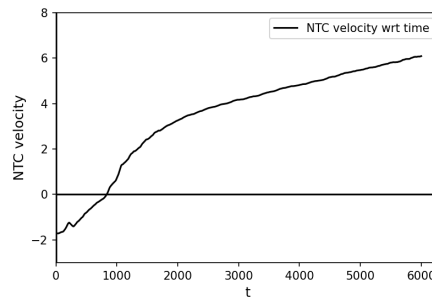


Figure 7.9: Depicted above are the snapshots of the apical surface of the anterior neural plate and surface ectoderm layer in the one-way model. The time evolution of the cells are visualised through images captured at the end of five equally-spaced time intervals. The cell at the centre of the neural plate is marked with a red border. Figure 7.10c illustrates the impact of Ca^{2+} flashes on the area of the ‘marked’ cell. The red line represents the distance between the centroids of the cell at the centre of the neural plate and a cell at the edge of the neural plate. The rate of change of this distance indicates the velocity of NTC (Figure 7.10e). Model parameters: Table 7.5.

(a) Ca^{2+} flash frequency versus time.(b) Ca^{2+} flash amplitude versus time.(c) Effect of Ca^{2+} flashes on the area of the 'marked' cell in Figure 7.9.

(d) NP area versus time.



(e) NTC velocity versus time.

Figure 7.10: Time series data for the anterior neural plate visualised in Figure 7.9. Figures 7.10a and 7.10b visualise the Ca^{2+} frequency and amplitude profiles, respectively. The number of flashes per minute per cell and the amplitude of the flashes were averaged over the 271 cells of the neural plate. The shaded green region in Figure 7.10d corresponds to 2-8% of the initial apical surface area of the anterior neural plate. Model parameters: Table 7.5.

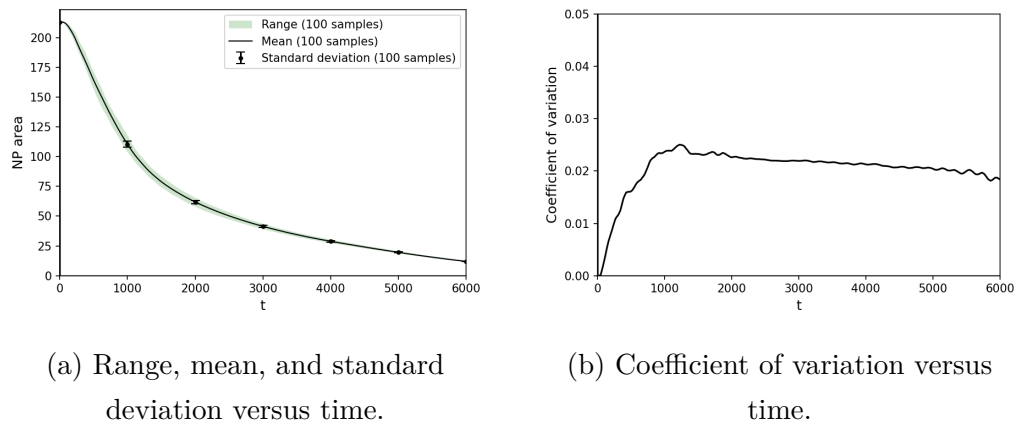


Figure 7.11: Descriptive statistics for the one-way model. The plots above visualise the range, mean, standard deviation, and coefficient of variation for 100 samples of the time evolution data of the apical surface area of the anterior neural plate. Model parameters: Table 7.5.

the cells move towards each other at an increasing rate, indicating an acceleration of NTC, which aligns with the observation in [33].

Figures 7.10a and 7.10b showcase the successful integration of Ca^{2+} frequency (Equation (7.21)) and amplitude (Equation (7.29)) profiles into the model. As AC progresses, both the frequency and amplitude of Ca^{2+} flashes increase as intended, consistent with experimental findings [33]. The measurements of flashes per minute per cell and flash amplitude (averaged over all cells in the anterior neural plate) were taken over time windows of size $\Delta t = 1000$. The error bars indicate the range of variation in the number of flashes per minute per cell and the amplitude of the flashes.

Owing to the randomness of the Ca^{2+} flashes, the one-way model is a stochastic model. Therefore, to gain an accurate understanding of the model's behaviour, it is necessary to run many stochastic iterations. So, we performed 100 simulations of the one-way model for the parameters listed in Table 7.5. We then calculated the range, mean, and standard deviation for the samples of the neural plate area at every timestep (Figure 7.11a). From Figure 7.11a, it is evident that there is very little variation in the neural plate area across iterations. As the neural plate area decreases over time and the slope becomes gentler, the variation in the neural plate area also decreases. Accordingly, the coefficient of variation also decreases

slowly over time (Figure 7.11b).

Given that there is very little variation in the neural plate area across stochastic iterations, all of which are performed using the same parameter values, data from a single iteration of the model offers a sufficiently accurate representation of the model's behaviour.

7.4 Discussion

In this chapter, we developed a new mechanochemical vertex model for the apical constriction (AC) of the anterior neural plate during NTC. Beginning with the modified Suzuki model, we made progressive modifications to allow for contraction despite the resistive force from the surface ectoderm. Furthermore, we incorporated experimentally validated frequency and amplitude profiles for Ca^{2+} flashes into the model. Given that Ca^{2+} signals influence a cell's mechanical properties but not vice versa, we refer to it as the one-way model. The parameters of the model are listed in Table 7.5 and the equations of the model are as follows:

Ca^{2+} frequency profile

$$fpm(t) = \begin{cases} 0.25 & , \text{ if } 0 \leq t < 4000, \\ 5 \times 10^{-5}(t - 4000) + 0.25, & \text{ if } 4000 \leq t \leq 6000, \end{cases} \quad (7.21 \text{ revisited})$$

where fpm : number of flashes per minute per cell.

Duty ratio of Ca^{2+} oscillation

$$duty = \frac{\tau}{T_{osc}}, \quad (7.23 \text{ revisited})$$

where $duty$: duty ratio of a Ca^{2+} oscillation, τ : cell activation period, and T_{osc} : time period of a Ca^{2+} oscillation.

Probability of cell activation

$$p_c = \begin{cases} \frac{60 \times fpm}{T_{60}/T_{osc}}, & \text{if } \frac{60 \times fpm}{T_{60}/T_{osc}} \leq 1, \\ 1, & \text{if } \frac{60 \times fpm}{T_{60}/T_{osc}} > 1, \end{cases} \quad (7.24 \text{ revisited})$$

where p_c : probability of cell activation, and T_{60} : simulation time interval corresponding to 60 minutes.

Ca²⁺ amplitude profile

$$amp(t) = \begin{cases} 2.5 \times 10^{-5}(t) + 0.6, & \text{if } 0 \leq t < 4000, \\ 1 \times 10^{-4}(t - 4000) + 0.7, & \text{if } 4000 \leq t \leq 6000, \end{cases} \quad (7.29 \text{ revisited})$$

where amp : Ca²⁺ flash amplitude.

Ca²⁺-induced elevation in line tension

$$\xi(t_c) = \begin{cases} k_\xi f(amp) \frac{(t_c/\tau)^{10}}{0.01 + (t_c/\tau)^{10}}, & \text{if } 0 \leq t_c \leq \tau, \\ k_\xi f(amp) 0.99, & \text{if } \tau < t_c \leq 2\tau, \\ 0, & \text{if } 2\tau < t_c \leq 3\tau, \end{cases} \quad (7.30 \text{ revisited})$$

and

$$\xi(t_c) = \begin{cases} \xi(t_c), & \text{if } 0 \leq \xi(t_c) \leq k_\xi T_{0n}, \\ k_\xi T_{0n}, & \text{if } k_\xi T_{0n} < \xi(t_c), \end{cases} \quad (7.32 \text{ revisited})$$

where ξ : Ca²⁺-induced elevation in line tension, T_{0n} : baseline value of line tension, k_ξ : scaling factor for T_{0n} , and

$$f(amp) = 1 \times 10^{-4} \exp(7.68 amp). \quad (7.31 \text{ revisited})$$

Energy function

$$U = U_A + U_P + U_L, \quad (3.4 \text{ revisited})$$

where U : total potential energy, U_A : potential energy of the cell areas, U_P : potential energy of the cell perimeters, U_L : potential energy of the cell-cell junctions, and

$$U_A = \sum_n^{N_{\text{cells}}} \frac{K_n^A}{2} \left(\frac{A_n}{A_n^0} - 1 \right)^2 A_n^0, \quad (3.1 \text{ revisited})$$

$$U_P = \sum_n^{N_{\text{cells}}} \frac{K_n^P}{2} \left(\frac{P_n}{P_n^0} - 1 \right)^2 P_n^0, \quad (3.2 \text{ revisited})$$

$$U_L = \sum_n^{N_{\text{cells}}} \sum_{\langle ij \rangle}^{\text{edge}} \left(T_n^{\langle ij \rangle} L_n^{\langle ij \rangle} - \frac{T_n^{\langle ij \rangle}}{4.69} \cdot \arctan(31.32 L_n^{\langle ij \rangle}) \right), \quad (7.20 \text{ revisited})$$

where K_n^A : area elasticity coefficient, A_n : area of the cell, A_n^0 : natural area of the cell, K_n^P : perimeter elasticity coefficient, P_n : perimeter of the cell, P_n^0 : natural perimeter of the cell, $T_n^{\langle ij \rangle}$: line tension at the cell edge, and $L_n^{\langle ij \rangle}$: length of the cell edge.

Damping function

$$\mu_i = \sum_n^{C_i} \frac{2.56}{L_n^0} - 3.65, \quad (7.15 \text{ revisited})$$

where μ_i : damping coefficient for the i^{th} vertex, C_i : set of cells sharing the i^{th} vertex, and L_n^0 : natural length of the cell.

Force on the i^{th} vertex

$$\begin{aligned}\mathbf{F}_i &= -\frac{\partial U}{\partial \mathbf{r}_i} \\ &= \mu_i \frac{d\mathbf{r}_i}{dt},\end{aligned}\tag{3.7 revisited}$$

where \mathbf{F}_i : force on the i^{th} vertex, and \mathbf{r}_i : position of the i^{th} vertex.

Growth laws for K_n^A , K_n^P , and T_{0n}

$$\frac{dK_n^A}{dt} = \begin{cases} R_A, & \text{if } \xi(t_c) \neq 0 \wedge \text{cell is not activated,} \\ 0, & \text{otherwise,} \end{cases}\tag{7.25 revisited}$$

$$\frac{dK_n^P}{dt} = \begin{cases} R_P, & \text{if } \xi(t_c) \neq 0 \wedge \text{cell is not activated,} \\ 0, & \text{otherwise,} \end{cases}\tag{7.26 revisited}$$

$$\frac{dT_{0n}}{dt} = \begin{cases} R_T, & \text{if } \xi(t_c) \neq 0 \wedge \text{cell is not activated,} \\ 0, & \text{otherwise,} \end{cases}\tag{7.27 revisited}$$

where R_A : growth rate of K_n^A , R_P : growth rate of K_n^P , and R_T : growth rate of T_{0n} .

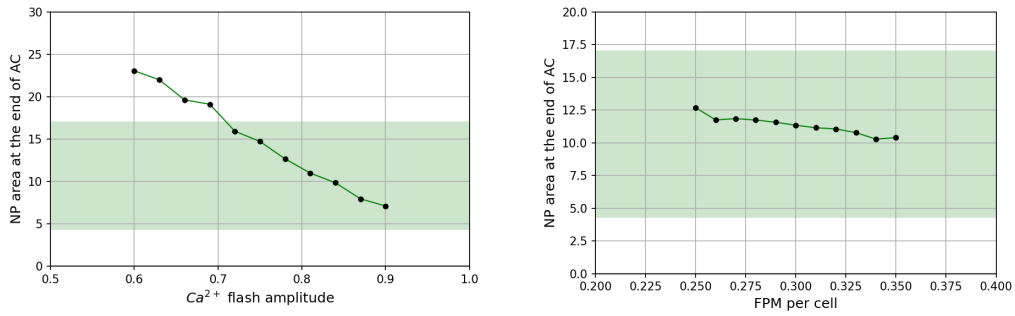
Ratchet-like mechanism

$$\frac{dA_n^0}{dt} = \begin{cases} -\kappa_A, & \text{if } (A_n - \omega_A A_n^0) < 0 \wedge \text{cell is not activated,} \\ 0, & \text{otherwise,} \end{cases}\tag{7.28 revisited}$$

and

$$P_n^0 = 6 \left(3^{-\frac{3}{4}} (2A_n^0)^{\frac{1}{2}} \right).\tag{7.1 revisited}$$

where κ_A : contraction rate of A_n^0 , and ω_A : threshold parameter for the activation of the ratchet-like mechanism.



(a) Final NP area versus Ca^{2+} flash amplitude.

(b) Final NP area versus FPM per cell.

Figure 7.12: The effect of varying the Ca^{2+} flash amplitude (amp) and the number of flashes per minute per cell (fpm) on the final area attained by the apical surface of the anterior neural plate upon the completion of AC, i.e., at $t = 6000$. The shaded green region corresponds to 2-8% of the initial apical surface area of the anterior neural plate. Model parameters: Table 7.5.

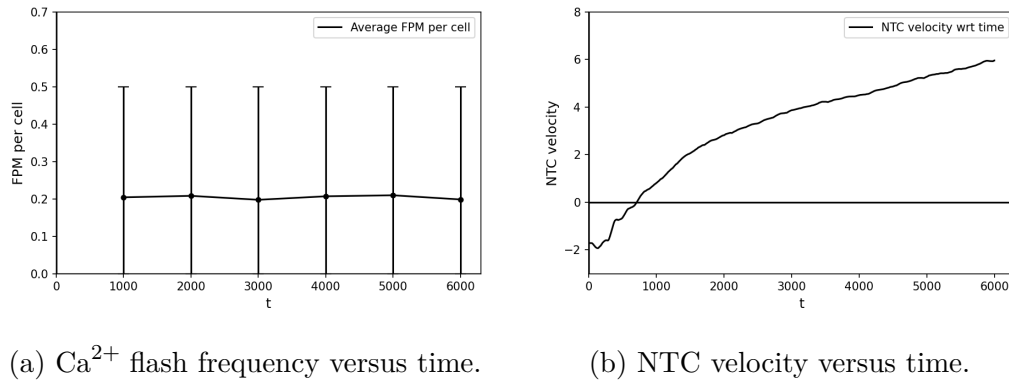
Having completed the development of the one-way model, we use it to investigate the impact of the amplitude and frequency of Ca^{2+} flashes on neural plate morphogenesis. To study the effect of Ca^{2+} flash amplitude on AC, we disable the Ca^{2+} amplitude profile (Equation (7.29)) and, instead, set a constant value for amp . We then perform a parameter sweep for amp , taking 11 equally spaced values between $amp = 0.6$ and $amp = 0.9$.

From Figure 7.12a, it is evident that the anterior neural plate fails to contract adequately at the end of AC when $amp < 0.7$. This underscores the necessity of increasing the amplitude of Ca^{2+} flashes throughout AC to achieve successful NTC.

Similarly, to study the effect of Ca^{2+} flash frequency on AC, we disable the Ca^{2+} frequency profile (Equation (7.21)) and, instead, set a constant value for fpm . We then perform a parameter sweep for fpm , taking 11 equally spaced values between $fpm = 0.25$ and $fpm = 0.35$.

From Figure 7.12b, it can be seen that the anterior neural plate contracts sufficiently for all fpm values in this range, suggesting that the increasing Ca^{2+} flash frequency might be a feature of AC but not necessary for successful NTC.

However, as NTC progresses, Christodoulou and Skourides [33] observe a grad-

(a) Ca^{2+} flash frequency versus time.

(b) NTC velocity versus time.

Figure 7.13: The time evolution of the number of flashes per minute per cell (averaged over the 271 neural plate cells) and the NTC velocity, for $fpm = 0.25$.

Model parameters: Table 7.5.

ual increase in the frequency of Ca^{2+} flashes along with the rate of NTC (Figure 2.2).

To investigate the relationship between Ca^{2+} flash frequency and the rate of NTC, we examined NTC velocity while maintaining a constant value of $fpm = 0.25$ throughout the duration of AC (Figure 7.13). The results showed an increase in NTC velocity, despite there being no change in the average number of flashes per minute per cell. Thus, the one-way model suggests that an increase in Ca^{2+} flash frequency is not the driving factor behind the increase in NTC velocity.

This aligns with the findings of Suzuki et al [196], where they suggest that the effect of Ca^{2+} fluctuations on tissue morphogenesis is independent of fluctuation frequency (Figure 3.7). Furthermore, the parameter sweeps in Section 5.5 also demonstrate that p_c is a low-sensitivity parameter (Figure 5.9a), i.e., small changes in p_c and, therefore, Ca^{2+} flash frequency have minimal impact on the final area attained by the neural plate.

However, in Figures 3.7 and 5.9a, we observe that the model is highly sensitive to changes in p_c for very small values of p_c . Additionally, Figure 7.7 suggests that changes in p_c sharply impact the final area attained by the neural plate as p_c approaches 1.

As p_c is no longer a free parameter in the one-way model, we cannot conduct a parameter sweep for p_c to study the effects of low and high cell activation times on AC. Instead, we adopt a different approach: performing a parameter sweep for the

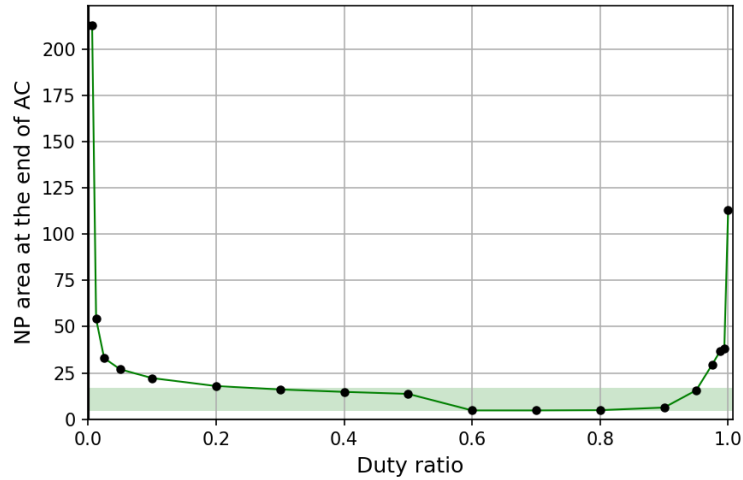


Figure 7.14: The effect of varying the duty ratio of the Ca^{2+} flashes ($duty$), for constant T_{osc} , on the final area attained by the apical surface of the anterior neural plate upon the completion of AC, i.e., at $t = 6000$. The shaded green region corresponds to 2-8% of the initial apical surface area of the anterior neural plate. Except for $duty$ and τ , all model parameters have the same values as listed in Table 7.5.

duty ratio ($duty$) while keeping the time period of the Ca^{2+} oscillation constant ($T_{osc} = 201$, corresponding to 120 seconds, as estimated from Figure 2.6). Since $duty$ and T_{osc} are related by Equation (7.23), changing $duty$ also implies a change in the value of the activation time (τ). Finally, we set $fpm = 0.5$ to achieve $p_c = 1$ (Equation (7.24)).

The results of our parameter sweep (Figure 7.14) demonstrate that the anterior neural plate contracts sufficiently for $0.2 < duty < 0.95$. Within this range, changing the value of $duty$ does not significantly impact the final area attained by the neural plate. However, for $duty < 0.025$ and $0.95 < duty$, the model exhibits high sensitivity to changes in $duty$, effectively demonstrating that NTC fails for sustained depletion or elevation in Ca^{2+} levels.

On the basis of established facts regarding the behaviour of sub-cellular machinery (Section 1.2), we developed a model that replicates a wide range of behaviours exhibited by the anterior neural plate during the AC phase of NTC (Chapter 2). Table 7.6 compares the one-way model with the Suzuki model in terms of their ability to reproduce experimentally observed behaviours *in silico*.

Behaviours captured	Suzuki model	One-way model
Pulsed contractions at the cell-level	Yes	Yes
Monotonic contraction at the tissue-level	Yes	Yes
NTC velocity increases with time	Yes	Yes
NP contracts to 2-8% of initial area when SE absent	Yes	Yes
NP contracts to 2-8% of initial area when SE present	No	Yes
Latency between Ca^{2+} flash and cell contraction	No	Yes
Frequency of Ca^{2+} flashes increases with time	No	Yes
Amplitude of Ca^{2+} flashes increases with time	No	Yes
NTC fails for sustained elevation of Ca^{2+}	No	Yes

Table 7.6: Comparing the one-way model and the Suzuki model in terms of their ability to capture experimentally observed behaviours.

The table highlights that the one-way model significantly outperforms the Suzuki model, capturing a broader range of behaviours.

Based on our simulation results and consultation with our experimental collaborators, we propose the following hypotheses for experimental testing, providing new directions for future research:

- Actomyosin exhibits persistent enrichment at cell-cell junctions, in contrast to the transient enrichment cycles followed by dissipation observed in medioapical actomyosin. This is essential for preserving cell and tissue integrity during AC.
- As cell-cell junctions decrease in size, apical adherens junctions exert a force, counteracting line tension, to prevent the cell surface from collapsing.
- The amplitude of a Ca^{2+} flash determines the extent of myosin activity and, thereby, cell contraction.
- A refractory period, characterized by a low Ca^{2+} level, is essential to alter the cell's mechanical properties and activate the ratchet-like mechanism.

In spite of the successes of the one-way model, we acknowledge that NTC is a phenomenon that entails the folding of the neural plate in three dimensions. As such, a 2D vertex model is inadequate for fully capturing neural plate morphogenesis. For instance, the one-way model is unable to capture the spatial distribution of constriction in the anterior neural plate.

Some regions of the anterior neural plate display increased constriction under normal conditions during AC. These regions, known as constriction foci, are located along the periphery (neural folds) and in the medial region of the anterior neural plate. Elevating Ca^{2+} levels pharmacologically disrupts the normal constriction patterning, causing the distribution of foci to become random. This disruption leads to NTC failure and severe defects in the embryo. These results suggest that asynchronous and cell-autonomous contraction pulses are necessary for the correct temporal and spatial distribution of constriction and, as a result, correct morphogenesis of the neural plate [33].

To capture the spatial distribution of constriction, we considered modelling the constriction foci as regions of elevated cellular constriction. However, experimental data reveals that upon the completion of AC, all cells will have constricted uniformly [32, 34]. In a 2D vertex model, this would result in the same final tissue shape regardless of the initial spatial patterning of constriction. This is because the neural plate undergoes three-dimensional folding along the constriction foci, rendering it impractical to capture this morphogenetic behaviour with a 2D model.

Moreover, the one-way model only captures the one-sided impact of Ca^{2+} signalling on cellular mechanics. However, the ‘stretch activation’ of Ca^{2+} is a well-documented phenomenon [11, 54, 78, 131], i.e., straining the cytogel induces a Ca^{2+} flash within a cell. There is also ample evidence to suggest that the mechanical stimulation of cells results in elevated Ca^{2+} levels [16, 139, 209, 225].

Additionally, during AC, regions of the anterior neural plate exhibiting the highest reduction in apical cell surface area also displayed the highest Ca^{2+} flash frequency. Hence, it is reasonable to hypothesize the existence of a mechanochemical feedback loop regulating Ca^{2+} signalling during AC. In this loop, Ca^{2+} -induced contraction in one cell mechanically stimulates adjacent cells, inducing Ca^{2+} flashes in them, leading to their contraction, and so forth.

Therefore, an ideal model of AC during NTC would involve a 3D vertex model incorporating bilateral feedback or two-way coupling between Ca^{2+} signalling and

cellular mechanics. While a complete 3D model is beyond the scope of this work, we take a step in this direction by incorporating a simple mechanism to simulate the behaviour of stretch sensitive Ca^{2+} channels, creating a two-way coupling model in the following chapter.

Chapter 8

The two-way model

In Chapter 7, we developed a novel mechanochemical vertex model of apical constriction (AC) during neural tube closure (NTC). In this model, Ca^{2+} signalling impacts cellular mechanics but not vice versa, so we refer to it as the one-way model.

In the one-way model, the Ca^{2+} frequency and amplitude profiles were imposed upon the model. However, there is ample evidence to suggest that there exists a bilateral feedback or two-way coupling between Ca^{2+} signalling and cellular mechanics [54, 78, 131, 139], i.e., the Ca^{2+} frequency and amplitude profiles should emerge as a natural consequence of the model's behaviour.

In this chapter, we extend the one-way model to create a new model that captures the two-way coupling between Ca^{2+} signals and cellular mechanics.

8.1 Modelling the SSCCs

We incorporate the feedback from cellular mechanics on Ca^{2+} signalling by introducing the action of the 'stretch activation' mechanism into the model. Stretch sensitive Ca^{2+} channels (SSCCs) on the cell membrane trigger the Ca^{2+} -induced Ca^{2+} release (CICR) mechanism by allowing an influx of Ca^{2+} from the extracellular space [136].

From studies on human retinal pigment epithelial cells [211] and on epithelial cells in the *Xenopus* neural plate [95], it is known that SSCCs on the cell membrane open as a response to the dilatation, or stretching, of the cytosol. Thus, the 'stretch activation' serves to oppose the stretching of the cytosol by inducing a Ca^{2+} flash within the cell, to trigger cell contraction.

The cited studies [95, 136, 211] utilize continuum models that characterize the Ca^{2+} influx through SSCCs as being directly proportional to the dilatation of the cytosol. To our knowledge, there are currently no vertex models that consider the effect of SSCC activation on cytosolic Ca^{2+} levels.

So, we propose a simple mechanism for SSCC-driven cell activation as follows: when the strain of a cell edge is greater than a predefined limit, the SSCCs on the edge are opened, and the edge is *activated*. If an edge is activated, the cell has a non-zero probability of experiencing a Ca^{2+} flash at every timestep. The greater the number of activated edges in a cell, the higher this probability. Conversely, if no edges are activated, the probability of a Ca^{2+} flash occurring in the cell is zero. Therefore, we define the stretch indices for an edge and a cell as

$$SI_{\langle ij \rangle} = \begin{cases} 1, & \text{if } \frac{L_n^{\langle ij \rangle} - L_n^0}{L_n^0} > 0.1, \\ 0, & \text{if } \frac{L_n^{\langle ij \rangle} - L_n^0}{L_n^0} \leq 0.1, \end{cases} \quad (8.1)$$

$$SI_n = \sum_{\langle ij \rangle}^{edge} SI_{\langle ij \rangle}, \quad (8.2)$$

where $SI_{\langle ij \rangle}$ is the stretch index of the cell edge connecting vertices i and j , $L_n^{\langle ij \rangle}$ is the length of the cell edge connecting vertices i and j , L_n^0 is the natural length of the cell (as defined in Section 7.1.1), and SI_n is the stretch index of the cell. Since we model the cells as hexagons, SI_n can range from 0 to 6. Given the absence of experimental data, we estimated the strain limit to be 0.1 based on insights from our simulation results.

To determine the probability of SSCC-driven cell activation $p_n(SI_n)$, we must derive a new relationship between the flashes per minute per cell fpm and the probability of cell activation p_c . If the time period of a Ca^{2+} oscillation is T_{osc} , then p_c is given by

$$p_c = \begin{cases} \left(\frac{60fpm}{T_{60} - 60fpm T_{osc}} \right) \delta t & , \text{ if } 60fpm \leq T_{60} - 60fpm T_{osc}, \\ 1 & , \text{ otherwise,} \end{cases} \quad (8.3)$$

where δt is the size of the timestep, and T_{60} is the simulation time interval corresponding to 60 minutes. The value of p_c is evaluated for each cell at every timestep.

From the Ca^{2+} frequency profile (Equation (7.21)), we know that the minimum value of fpm is 0.25. By substituting this value into Equation (8.3), we obtain $p_c = 0.005$. We consider this to be the smallest non-zero value of p_n , which represents the probability of cell activation when only one edge is activated. Therefore, the probability of SSCC-driven cell activation is

$$p_n(SI_n) = 0.005 SI_n. \quad (8.4)$$

The amount of actomyosin in the cell cortex plays a pivotal role in determining the sensitivity of the SSCCs [35]. The increasing cortical tension due to the accumulation of actomyosin in the apical cortex during AC heightens the sensitivity of the SSCCs [113, 177].

Owing to the absence of experimental data, we estimate the increase in SSCC sensitivity using the Ca^{2+} frequency profile. From the frequency profile, we know that the maximum value of fpm is 0.35. Substituting this value into Equation (8.3), we find $p_c = 0.015 \implies 3 \times 0.005$. So, it can be asserted that the SSCC sensitivity scales by a factor of 3 near the end of AC, when the amount of cortical actomyosin (represented by K_n^A) is at its highest.

According to the frequency profile, the frequency of Ca^{2+} flashes begins to increase at $t = 4000$. By this time, each cell will have experienced approximately 10 Ca^{2+} flashes. Using Equation (7.25) and parameter values from Table 7.5, we can approximate the value of K_n^A in a cell as follows: $K_n^A(\text{initial}) + R_A(10\tau) = 0.21$. Therefore, we assert that the sensitivity of the SSCCs in a cell increases significantly when $K_n^A = 0.21$ and modify Equation (8.4) as follows:

$$p_n(SI_n, K_n^A) = (1 + 2H(K_n^A - 0.21)) 0.005 SI_n, \quad (8.5)$$

where H is the Heaviside step function. The term $(1 + 2H(K_n^A - 0.21))$ transitions from 1 to 3 at $K_n^A = 0.21$ and represents the sensitivity of the SSCCs as a function of cortical actomyosin (Figure 8.1).

The sensitivity of the SSCCs is likely best represented by a sigmoidal curve, commonly used in biological models. However, for simplicity, we model SSCC sensitivity as a transition from a low to a high value at a specific actomyosin concentration (represented by K_n^A). Since we are not interested in the steepness of

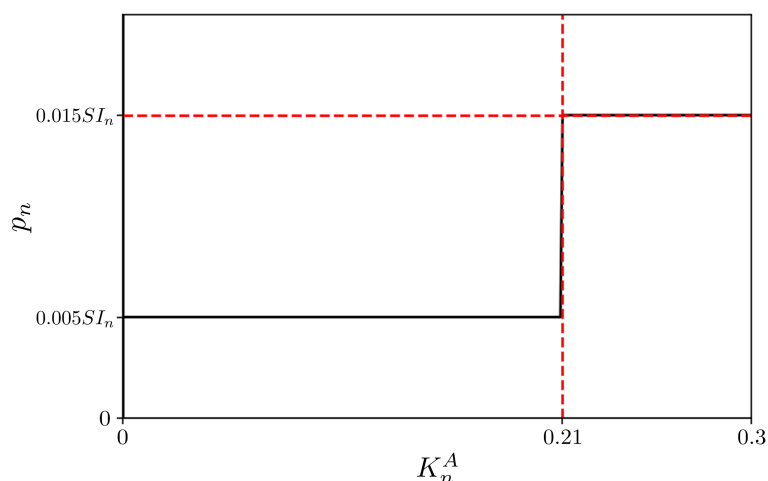


Figure 8.1: Probability of SSCC-driven cell activation p_n versus the area elasticity coefficient K_n^A , which represents the concentration of cortical actomyosin in the cell. SI_n is the stretch index of the cell.

the curve, we approximate SSCC sensitivity using the Heaviside function instead of a sigmoid to avoid introducing an additional parameter for steepness.

To our knowledge, there are no studies examining the influence of cortical actomyosin enrichment on the opening of the SSCCs, the CICR mechanism and, consequently, on the amplitude of Ca^{2+} flashes. However, it is understood that the amplitude of Ca^{2+} flashes needs to increase to counteract the elastic forces from the accumulating cortical actomyosin and facilitate cell contraction (Section 7.3). Through discussions with our experimental collaborators, we hypothesize that the accumulation of cortical actomyosin signals, even if indirectly, the increase in Ca^{2+} flash amplitude.

Since the precise relationship between cortical actomyosin level and Ca^{2+} flash amplitude is unknown, we assume a linear relationship between them for simplicity. The Ca^{2+} amplitude profile indicates that $amp = 0.6$ at the start of AC when cortical actomyosin levels are at their lowest (corresponding to $K_n^A = 0.03$), and $amp = 0.9$ towards the end of AC when cortical actomyosin levels are at their highest (corresponding to $K_n^A = 0.3$). So, we fit a linear function to the known data points $amp(0.03) = 0.6$ and $amp(0.3) = 0.9$, which gives us the Ca^{2+} flash

amplitude as a function of the cortical actomyosin level:

$$\text{amp}(K_n^A) = 1.11 K_n^A + 0.57. \quad (8.6)$$

With this final modification, we conclude the development of a mechanochemical vertex model that captures the two-way coupling between Ca^{2+} signals and cellular mechanics in the anterior neural plate during the AC phase of NTC. In this model, Ca^{2+} flashes signal the onset of cell contraction. Contraction in one cell strains the cytosol of neighbouring cells, inducing a Ca^{2+} flash in them, triggering their contraction to counteract cytosol straining. Since this model captures the bilateral feedback or two-way mechanochemical coupling between Ca^{2+} signals and cellular mechanics, we call it **the two-way model**.

Figure 8.2 visualises the time evolution of the apical surface of the anterior neural plate and surface ectoderm layer in the two-way model. At $t = 0$, 10% of the neural plate cells are activated in the two-way model. We considered this to be a reasonable estimate based on our observations of the Ca^{2+} frequency profile in the one-way model. The absence of this initial activation prevents the apical surface of the neural plate from contracting (Figure 8.4). So, we introduce a new parameter, α , to represent the fraction of neural plate cells activated at $t = 0$, and we set $\alpha = 0.1$.

This initial activation might stem from the mechanical forces generated during the convergent extension phase preceding AC [33, 34], or it could result from chemical signals such as the Sonic Hedgehog, which plays a crucial role in regulating Ca^{2+} activity during neurulation [178].

In Figure 8.2, the cell at the centre of the neural plate is marked with a red border. Figure 8.3c depicts the ‘marked’ cell undergoing pulsed contractions due to the influence of Ca^{2+} flashes. Although individual cells contract in a pulsed manner, the anterior neural plate contracts monotonically without recovery phases (Figure 8.3d), similar to the one-way model. The apical surface of the anterior neural plate contracts to 3% of its initial area, achieving the desired contraction and resulting in successful NTC.

As evidenced in Figures 8.3a and 8.3b, the Ca^{2+} frequency and amplitude profiles arise naturally in the two-way model as a consequence of the interactions between the cells. The measurements of flashes per minute per cell and flash amplitude (averaged over all cells in the anterior neural plate) were taken over time windows of size $\Delta t = 1000$. The error bars indicate the range of variation

Parameter	Value
SE Cells	60
NP Cells	271
α	0.1
$duty$	0.33
δt	1
$K_n^A (SE)$	0.02
$K_n^P (SE)$	0.01
$T_{0n}(SE)$	0.01
R_A	0.0003
R_P	0.002
R_T	0.002
K_n^A (initial)	0.03
K_n^P (initial)	0.02
T_{0n} (initial)	0.01
K_n^A (final)	0.3
K_n^P (final)	0.2
T_{0n} (final)	0.1
κ_A	0.0008
ω_A	1
A_n^0 (initial)	0.785
A_n^0 (final)	0.015
k_ξ	4
τ	67

Table 8.1: Parameter values for Figures 8.2, 8.3, 8.4, 8.5, 8.6, 8.7, and 8.8.

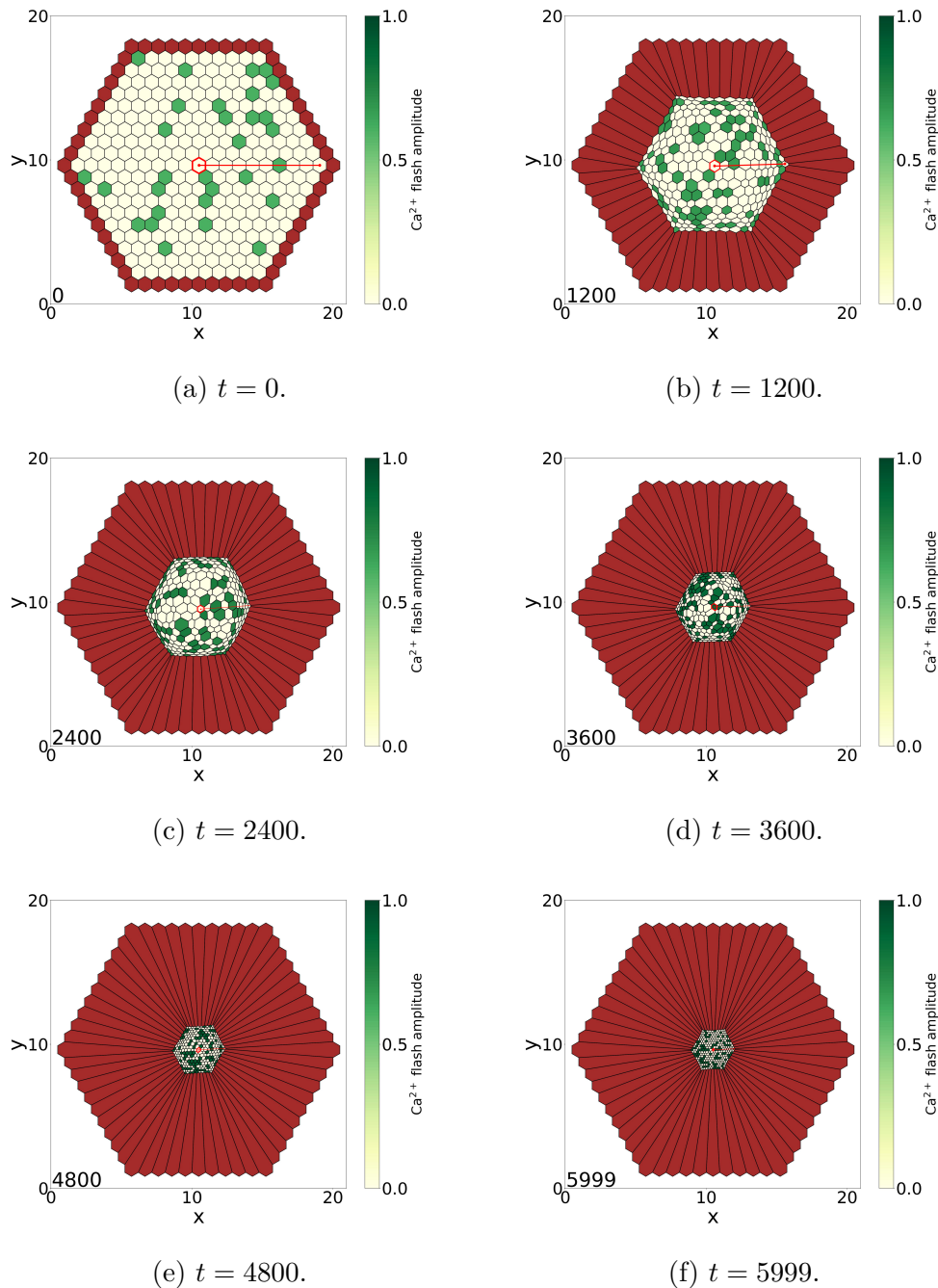
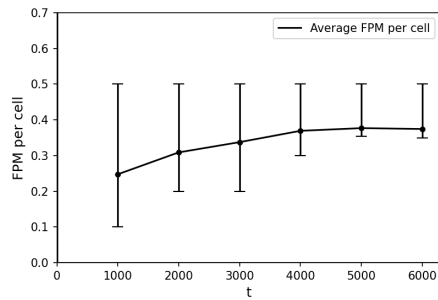
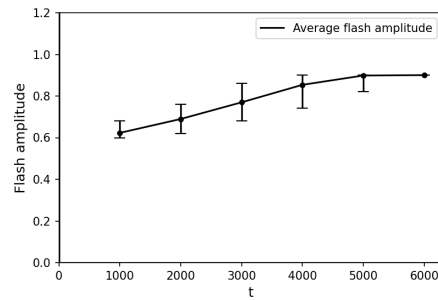
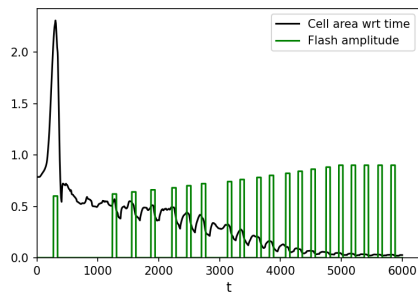
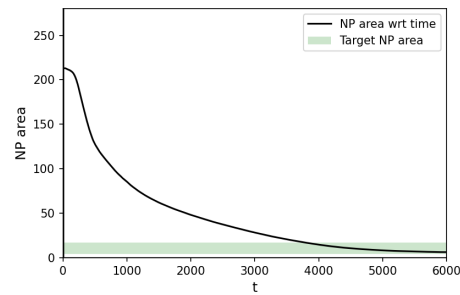
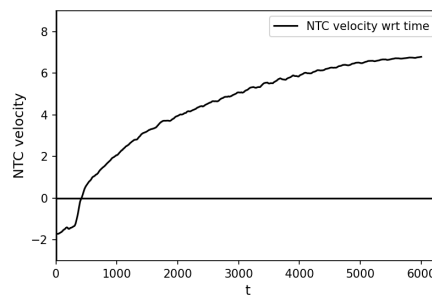


Figure 8.2: Depicted above are the snapshots of the apical surface of the anterior neural plate and surface ectoderm layer in the two-way model. The time evolution of the cells are visualised through images captured at the end of five equally-spaced time intervals. The cell at the centre of the neural plate is marked with a red border. Figure 8.3c illustrates the impact of Ca^{2+} flashes on the area of the ‘marked’ cell. The red line represents the distance between the centroids of the cell at the centre of the neural plate and a cell at the edge of the neural plate. The rate of change of this distance indicates the velocity of NTC (Figure 8.3e). Model parameters: Table 8.1.

(a) Ca^{2+} flash frequency versus time.(b) Ca^{2+} flash amplitude versus time.(c) Effect of Ca^{2+} flashes on the area of the 'marked' cell in Figure 8.2.

(d) NP area versus time.



(e) NTC velocity versus time.

Figure 8.3: Time series data for the anterior neural plate visualised in Figure 8.2. Figures 8.3a and 8.3b visualise the Ca^{2+} frequency and amplitude profiles, respectively. The number of flashes per minute per cell and the amplitude of the flashes were averaged over the 271 cells of the neural plate. The shaded green region in Figure 8.3d corresponds to 2-8% of the initial apical surface area of the anterior neural plate. Model parameters: Table 8.1.

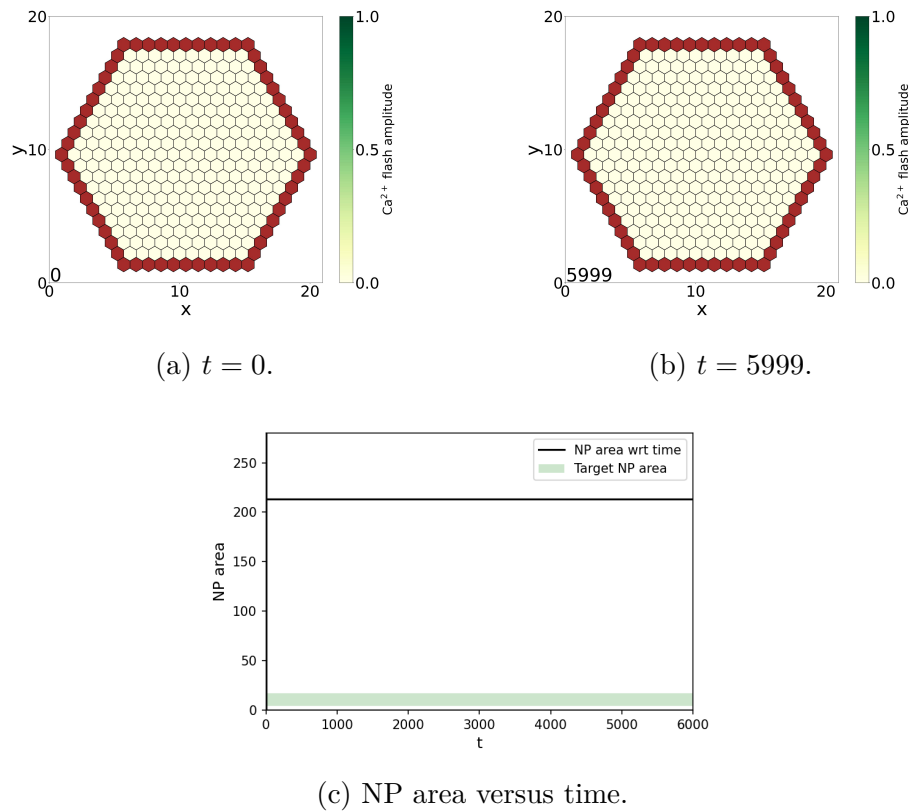
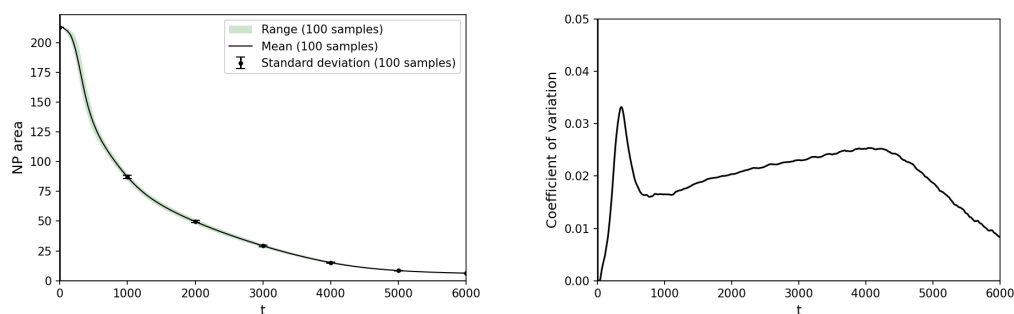


Figure 8.4: Without the initial activation of cells in the anterior neural plate, i.e., for $\alpha = 0$, AC does not occur in the two-way model. Depicted above are the snapshots of the apical surface of the anterior neural plate and surface ectoderm layer at the beginning and the end of the simulation along with a graph showing the time evolution of the apical surface area of the anterior neural plate. The shaded green region on the graph corresponds to 2-8% of the initial area of the anterior neural plate. Except for α , all model parameters have the same values as listed in Table 8.1.



(a) Range, mean, and standard deviation versus time.

(b) Coefficient of variation versus time.

Figure 8.5: Descriptive statistics for the two-way model. The plots above visualise the range, mean, standard deviation, and coefficient of variation for 100 samples of the time evolution data of the apical surface area of the anterior neural plate. Model parameters: Table 8.1.

in the number of flashes per minute per cell and the amplitude of the flashes.

In the two-way model, similar to the one-way model, NTC velocity increases over the course of AC. Figure 8.3e shows an initial negative NTC velocity as cells at the center and edge move apart due to the spontaneous contraction of the surrounding cells. Subsequently, the cells move towards each other at an increasing rate, indicating an acceleration of NTC as AC progresses.

Owing to the randomness of the Ca^{2+} flashes, the two-way model is a stochastic model. Similar to the one-way model, we conducted 100 simulations of the two-way model for the parameters listed in Table 8.1. We then calculated the range, mean, and standard deviation for the samples of the neural plate area at every timestep (Figure 8.5a). From Figure 8.5a, it is evident that there is very little variation in the neural plate area across iterations. Accordingly, the coefficient of variation is small (Figure 8.5b). Notably, it does not exhibit a distinct increasing or decreasing trend, unlike the one-way model.

Given that there is very little variation in the neural plate area across stochastic iterations, all of which are performed using the same parameter values, data from a single iteration of the model offers a sufficiently accurate representation of the model's behaviour.

8.2 Discussion

In this chapter, we developed a new vertex model that captures the two-way mechanochemical coupling between Ca^{2+} signals and cellular mechanics in the anterior neural plate during the AC phase of NTC. To our knowledge, this is currently **the only vertex model that captures this two-way feedback**.

We extended the one-way model developed in Chapter 7 by incorporating ‘stretch activation’ as a characteristic of the neural plate cells. The ‘stretch activation’ mechanism is driven by the action of the SSCs located on the cell membrane. This modification led to the natural emergence of Ca^{2+} frequency and amplitude profiles within the model, arising from the interactions between cells. The parameters of the two-way model are listed in Table 8.1 and the equations of the model are as follows:

Probability of cell activation

$$p_n(SI_n, K_n^A) = (1 + 2H(K_n^A - 0.21)) 0.005 SI_n, \quad (8.5 \text{ revisited})$$

where p_n : probability of cell activation, H : Heaviside step function, K_n^A : area elasticity coefficient, and

$$SI_n = \sum_{\langle ij \rangle}^{edge} SI_{\langle ij \rangle}, \quad (8.2 \text{ revisited})$$

where SI_n : stretch index of the cell, and

$$SI_{\langle ij \rangle} = \begin{cases} 1, & \text{if } \frac{L_n^{\langle ij \rangle} - L_n^0}{L_n^0} > 0.1, \\ 0, & \text{if } \frac{L_n^{\langle ij \rangle} - L_n^0}{L_n^0} \leq 0.1, \end{cases} \quad (8.1 \text{ revisited})$$

where $SI_{\langle ij \rangle}$: stretch index of the cell edge, $L_n^{\langle ij \rangle}$: length of the cell edge, and L_n^0 : natural length of the cell.

Ca^{2+} flash amplitude

$$amp(K_n^A) = 1.11 K_n^A + 0.57. \quad (8.6 \text{ revisited})$$

where amp : Ca^{2+} flash amplitude.

Ca^{2+} -induced elevation in line tension

$$\xi(t_c) = \begin{cases} k_\xi f(amp) \frac{(t_c/\tau)^{10}}{0.01 + (t_c/\tau)^{10}} & , \text{ if } 0 \leq t_c \leq \tau , \\ k_\xi f(amp) 0.99 & , \text{ if } \tau < t_c \leq 2\tau , \\ 0 & , \text{ if } 2\tau < t_c \leq 3\tau , \end{cases} \quad (7.30 \text{ revisited})$$

and

$$\xi(t_c) = \begin{cases} \xi(t_c) & , \text{ if } 0 \leq \xi(t_c) \leq k_\xi T_{0n} , \\ k_\xi T_{0n} & , \text{ if } k_\xi T_{0n} < \xi(t_c) , \end{cases} \quad (7.32 \text{ revisited})$$

where ξ : Ca^{2+} -induced elevation in line tension, τ : cell activation period, T_{0n} : baseline value of line tension, k_ξ : scaling factor for T_{0n} , and

$$f(amp) = 1 \times 10^{-4} \exp(7.68 amp) . \quad (7.31 \text{ revisited})$$

Energy function

$$U = U_A + U_P + U_L, \quad (3.4 \text{ revisited})$$

where U : total potential energy, U_A : potential energy of the cell areas, U_P : potential energy of the cell perimeters, U_L : potential energy of the cell-cell junctions, and

$$U_A = \sum_n^{N_{cells}} \frac{K_n^A}{2} \left(\frac{A_n}{A_n^0} - 1 \right)^2 A_n^0, \quad (3.1 \text{ revisited})$$

$$U_P = \sum_n^{N_{cells}} \frac{K_n^P}{2} \left(\frac{P_n}{P_n^0} - 1 \right)^2 P_n^0, \quad (3.2 \text{ revisited})$$

$$U_L = \sum_n^{N_{cells}} \sum_{\langle ij \rangle}^{edge} \left(T_n^{\langle ij \rangle} L_n^{\langle ij \rangle} - \frac{T_n^{\langle ij \rangle}}{4.69} \cdot \arctan(31.32 L_n^{\langle ij \rangle}) \right), \quad (7.20 \text{ revisited})$$

where A_n : area of the cell, A_n^0 : natural area of the cell, K_n^P : perimeter elasticity coefficient, P_n : perimeter of the cell, P_n^0 : natural perimeter of the cell, and $T_n^{<ij>}$: line tension at the cell edge.

Damping function

$$\mu_i = \sum_n^{C_i} \frac{2.56}{L_n^0} - 3.65, \quad (7.15 \text{ revisited})$$

where μ_i : damping coefficient for the i^{th} vertex, and C_i : set of cells sharing the i^{th} vertex.

Force on the i^{th} vertex

$$\begin{aligned} \mathbf{F}_i &= -\frac{\partial U}{\partial \mathbf{r}_i} \\ &= \mu_i \frac{d\mathbf{r}_i}{dt}, \end{aligned} \quad (3.7 \text{ revisited})$$

where \mathbf{F}_i : force on the i^{th} vertex, and \mathbf{r}_i : position of the i^{th} vertex.

Growth laws for K_n^A , K_n^P , and T_{0n}

$$\frac{dK_n^A}{dt} = \begin{cases} R_A, & \text{if } \xi(t_c) \neq 0 \wedge \text{cell is not activated,} \\ 0, & \text{otherwise,} \end{cases} \quad (7.25 \text{ revisited})$$

$$\frac{dK_n^P}{dt} = \begin{cases} R_P, & \text{if } \xi(t_c) \neq 0 \wedge \text{cell is not activated,} \\ 0, & \text{otherwise,} \end{cases} \quad (7.26 \text{ revisited})$$

$$\frac{dT_{0n}}{dt} = \begin{cases} R_T, & \text{if } \xi(t_c) \neq 0 \wedge \text{cell is not activated,} \\ 0, & \text{otherwise,} \end{cases} \quad (7.27 \text{ revisited})$$

where R_A : growth rate of K_n^A , R_P : growth rate of K_n^P , and R_T : growth rate of T_{0n} .

Ratchet-like mechanism

$$\frac{dA_n^0}{dt} = \begin{cases} -\kappa_A, & \text{if } (A_n - \omega_A A_n^0) < 0 \wedge \text{cell is not activated,} \\ 0, & \text{otherwise,} \end{cases} \quad (7.28 \text{ revisited})$$

and

$$P_n^0 = 6 \left(3^{-\frac{3}{4}} (2A_n^0)^{\frac{1}{2}} \right). \quad (7.1 \text{ revisited})$$

where κ_A : contraction rate of A_n^0 , and ω_A : threshold parameter for the activation of the ratchet-like mechanism.

To test the effectiveness of the two-way coupling, we disable the ‘stretch activation’ mechanism by setting $p_n = 0$ in the two-way model. From Figure 8.6, it is clear that disabling the ‘stretch activation’ mechanism completely arrests AC. Therefore, the two-way coupling between Ca^{2+} signals and cellular mechanics is vital for successful NTC.

Table 8.2 compares the two-way model with the one-way model in terms of their ability to reproduce experimentally observed behaviours *in silico*. The table highlights that the two-way model not only replicates all the behaviours of the one-way model but also exhibits additional behaviours.

In particular, the two-way mechanochemical coupling makes it possible to capture the experimentally observed *multicellular Ca^{2+} transients* [33, 196], discussed in Chapter 2, that the Suzuki model was unable to reproduce (Section 3.2). In the case of a single-cell Ca^{2+} transient, a single cell is activated spontaneously. In contrast, a multicellular Ca^{2+} transient involves the coordinated activation of a group of cells through mechanochemical transduction.

Figure 8.7 demonstrates an instance of a multicellular Ca^{2+} transient. At $t = 2400$, a single cell within the red circle is activated. By $t = 2420$, the originally activated cell triggers the activation of three nearby cells through mechanochemical transduction. In this manner, a Ca^{2+} wave has propagated from one cell to its neighbours. Subsequently, at $t = 2460$, these newly activated cells, in turn, activate their neighbours. Finally, at $t = 2480$, the initially activated cells start to deactivate as they enter their refractory periods.

Based on our simulation results and consultation with our experimental collaborators, we propose the following hypotheses for experimental testing, providing

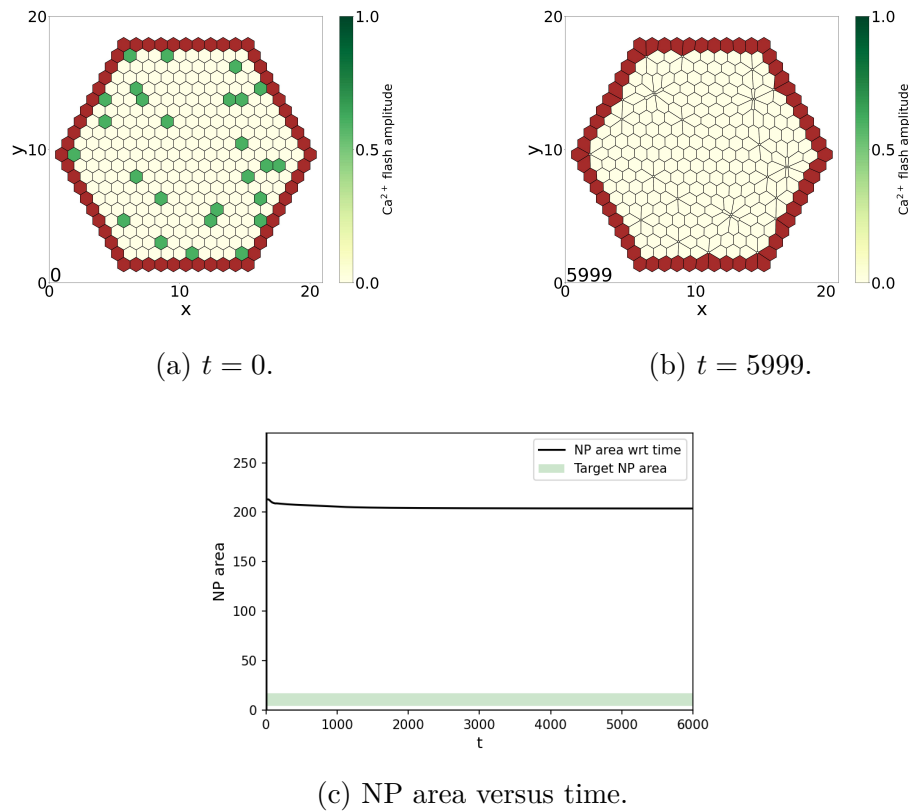


Figure 8.6: The effect of disabling the ‘stretch activation’ mechanism on AC. Without the two-way coupling, contracting cells are unable to induce Ca^{2+} flashes in their neighbours. Depicted above are the snapshots of the apical surface of the anterior neural plate and surface ectoderm layer at the beginning and the end of the simulation along with a graph showing the time evolution of the apical surface area of the anterior neural plate. The shaded green region on the graph corresponds to 2-8% of the initial area of the anterior neural plate.

Model parameters: Table 8.1.

Behaviours captured	One-way model	Two-way model
Pulsed contractions at the cell-level	Yes	Yes
Monotonic contraction at the tissue-level	Yes	Yes
NTC velocity increases with time	Yes	Yes
NP contracts to 2-8% of initial area when SE absent	Yes	Yes
NP contracts to 2-8% of initial area when SE present	Yes	Yes
Latency between Ca^{2+} flash and cell contraction	Yes	Yes
NTC fails for sustained elevation of Ca^{2+}	Yes	Yes
Frequency of Ca^{2+} flashes increases with time	Yes*	Yes
Amplitude of Ca^{2+} flashes increases with time	Yes*	Yes
Two-way coupling between Ca^{2+} and mechanics	No	Yes
Ca^{2+} wave propagation	No	Yes
Multicellular Ca^{2+} transients	No	Yes

* Ca^{2+} frequency and amplitude profiles imposed

Table 8.2: Comparing the two-way model and the one-way model in terms of their ability to capture experimentally observed behaviours.

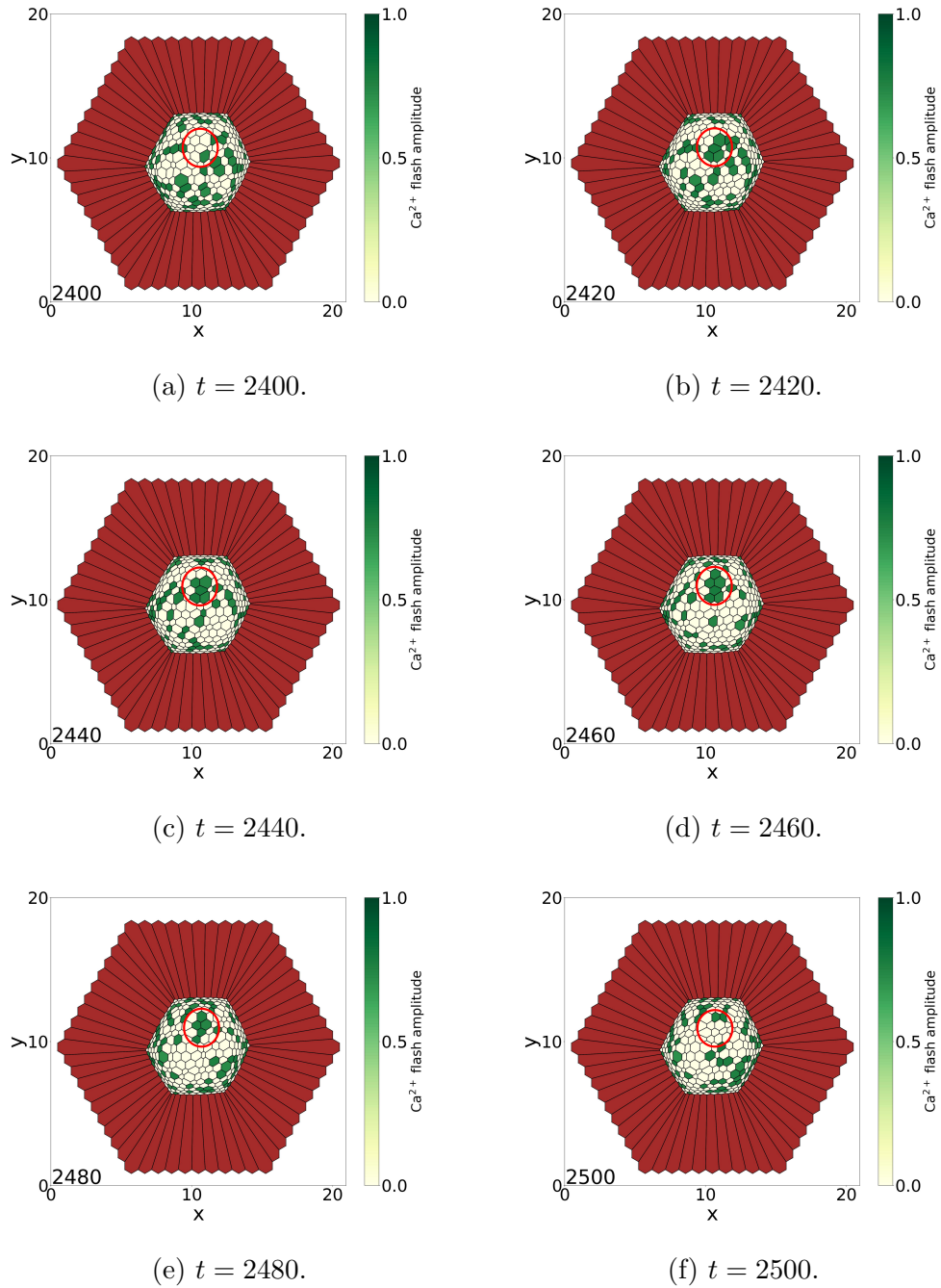


Figure 8.7: Visualising a multicellular Ca^{2+} transient and Ca^{2+} wave propagation in the two-way model. Depicted above are the snapshots of the apical surface of the anterior neural plate and surface ectoderm layer. The region of interest is demarcated by the red circle. A multicellular Ca^{2+} transient is facilitated by the propagation of a Ca^{2+} wave among the cells inside the circle. Model parameters: Table 8.1.

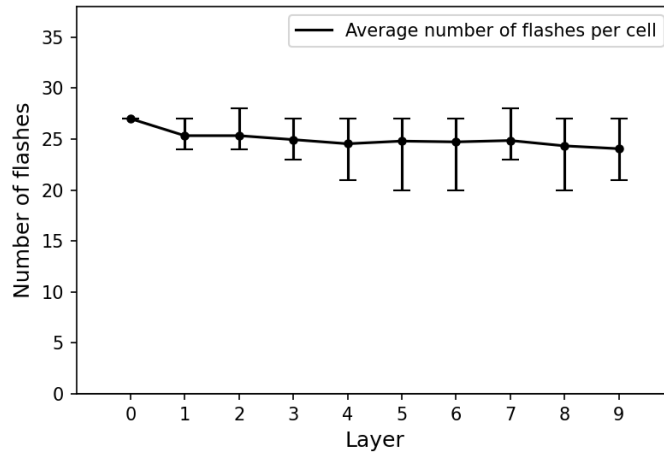


Figure 8.8: The average number of Ca^{2+} flashes per cell in each layer of the anterior neural plate. The average number of flashes was determined by calculating the total number of flashes experienced (over the entire duration of AC) by all the cells in a layer and then dividing it by the total number of cells in that layer. The error bars indicate the range of variation in the number of flashes experienced by the cells in that layer. Model parameters: Table 8.1.

new directions for future research:

- The level of cortical actomyosin in a cell influences the amplitude of induced Ca^{2+} flashes, either by modulating the opening of the SSCCs or by impacting the Ca^{2+} -induced Ca^{2+} release (CICR) mechanism.
- At low levels of cortical actomyosin, SSCC sensitivity remains fairly constant, but beyond a certain threshold of cortical actomyosin, SSCC sensitivity increases sharply.
- During AC, intercellular Ca^{2+} signalling between anterior neural plate cells occurs via mechanochemical transduction.
- A fraction of anterior neural plate cells must be activated to initiate AC. This initial activation could be caused by mechanical forces generated during convergent extension or chemical signals.

In spite of the successes of the two-way model, it has its limitations. For instance, it has been observed that the frequency of Ca^{2+} flashes is higher in

areas of increased constriction, like the neural folds and the medial region [33]. These regions correspond to the edges (layer 9) and centre (layer 0)¹ of the neural plate in our model. Therefore, layers 9 and 0 should demonstrate a significantly higher number of Ca^{2+} flashes on average than the other layers.

However, Figure 8.8 reveals that the average number of flashes per cell is fairly consistent across all layers, i.e., no layer exhibits a significantly higher Ca^{2+} flash frequency than the others. This is because the two-way model cannot capture the spatial distribution of constriction in the neural plate. Like the one-way model, the two-way model cannot model the constriction foci of the neural plate for the reasons given in Section 7.4.

As discussed in Section 7.4, an ideal model of AC during NTC would be a 3D vertex model that incorporates the two-way coupling between Ca^{2+} signalling and cellular mechanics. In this chapter, we progressed towards that model by developing a 2D vertex model that captures the two-way coupling between Ca^{2+} signalling and cellular mechanics.

¹The layers of the modelled neural plate are visualised in Figure 4.3.

Chapter 9

Summary, conclusions, and future work

In this doctoral work, we investigated the crucial role played by the coupling between Ca^{2+} signalling and cellular mechanics in the apical constriction (AC) of anterior neural plate cells during neural tube closure (NTC).

This work builds on the efforts of experimental biologists who explored the relationship between Ca^{2+} and cell mechanics in neural plate cells undergoing AC during NTC. Their findings present evidence that cell-autonomous Ca^{2+} flashes trigger cell contraction events, and emphasize the critical role of cell autonomy and asynchrony in the success of NTC [33, 196].

During the AC phase of NTC, the constricting anterior neural plate exhibits a variety of characteristic behaviours [33, 196]. This doctoral thesis introduces two new mathematical models capable of replicating most of the behaviours documented in [33] and [196] *in silico*.

This concluding chapter reemphasizes the outcomes of this doctoral work, comments on limitations, and proposes directions for future work.

Summary and conclusions

In Chapter 1, we start by introducing the biological challenge that motivates the work undertaken in this doctoral thesis. Then, we examine some seminal works to understand the landscape of the field and explore state-of-the-art developments as reflected in the existing literature. This review encompasses discussions on both experimental and mathematical modelling studies. In the process of

surveying the literature, we review the biological mechanisms underpinning intracellular Ca^{2+} dynamics and the sub-cellular structures responsible for generating the forces driving cellular deformation.

In Chapter 2, we provide a summary of the observations made by Christodoulou and Skourides [33] and Suzuki et al [196]. These studies detail the distinctive behaviours displayed by the constricting anterior neural plate during the AC phase of NTC, and are of particular importance since the central objective of this doctoral work is to develop mathematical models capable of reproducing these behaviours *in silico*.

In Chapter 3, we provide a detailed description of the 2D mechanochemical vertex model developed by Suzuki et al [196], followed by a critical analysis of their simulation results. We conclude that, despite its successes, the Suzuki model has several limitations, with a notable one being its omission of the surface ectoderm layer bounding the neural plate. This underscores the necessity of developing a new mechanochemical vertex model of AC during NTC.

In Chapter 4, we justify the development of a novel software package for vertex models—CelluLink—substantiated through a comprehensive comparison of existing computational tools. CelluLink is a newly designed Python package for vertex models that prioritizes user-friendly modifications and facilitates the implementation of new features by its use of the procedural programming paradigm. A standout attribute of CelluLink lies in its utilization of parallel processing, enabling the execution of large parameter sweeps for vertex models on desktop machines or computational clusters. This chapter provides a detailed exposition of CelluLink’s features and algorithm.

In Chapter 5, we revise the modelling assumptions of the Suzuki model to better reflect the biology and simplify its structure, creating the modified Suzuki model. We then simulate the modified Suzuki model in CelluLink and compare its behaviour to the Suzuki model. Since the simplified structure of the modified Suzuki model enables analytical study, we derive a bifurcation diagram to explore its behaviour at equilibrium. Utilizing the results obtained from this analytical work, we then explore the conditions required to activate the ratchet-like mechanism and visualize its impact on the rate of contraction of the apical surface of the anterior neural plate. Finally, we conduct a systematic parameter sweep of the modified Suzuki model to numerically investigate the effects of varying model parameters on both the final area achieved by the apical surface of the anterior

neural plate and the time taken to reach that final area.

These studies inform our understanding of the parameter sensitivity of the modified Suzuki model, enabling us to identify the parameter ranges for which the model is stable and yields the desired contraction. The insights gained from Chapter 5 guide the parameter estimation for the new mathematical models in subsequent chapters.

In Chapter 6, we review key concepts related to the convergence of one-step numerical methods. We then compare the performance of two numerical schemes used to simulate the modified Suzuki model - the forward Euler method and a predictor-corrector method based on an Euler/trapezoidal pair. Based on the results of this comparison, we adopt the forward Euler method for the simulations in subsequent chapters due to its higher speed and lower computational cost.

In Chapter 7, we develop a new 2D mechanochemical vertex model for the constriction of the apical surface of the anterior neural plate during the AC phase of NTC. Starting with the modified Suzuki model as a foundation, we incorporate the surface ectoderm and make progressive modifications to facilitate the contraction of the neural plate despite the resistive force exerted by the surface ectoderm.

To maintain cell integrity when large forces are generated within cells with small surface areas, we develop and implement: (i) a damping function for the motion of the vertices, and (ii) an adhesion term for the energy function. For the first time, we derive the damping coefficient of the vertices as a function of the accumulating actomyosin, and the adhesion term as a contribution from the cell's internal pressure and adherens junctions.

Additionally, we incorporate frequency and amplitude profiles for Ca^{2+} flashes into the model, based on the experimental data provided in Chapter 2. Since this model only captures the effect of Ca^{2+} on cellular mechanics and not vice versa, we refer to it as the one-way model.

In Chapter 8, we extend the one-way model by incorporating the experimentally-validated 'stretch activation' mechanism into the behaviour of the neural plate cells, creating a new model. Since this model captures the bilateral feedback or two-way mechanochemical coupling between Ca^{2+} signals and cellular mechanics, we refer to it as the two-way model. In contrast to the one-way model, where the Ca^{2+} frequency and amplitude profiles are imposed upon the model, the Ca^{2+} frequency and amplitude profiles in the two-way model emerge as a natural con-

sequence of the interactions between cells.

To our knowledge, our two-way model is currently the only vertex model that captures the two-way feedback between Ca^{2+} signals and cellular mechanics in the anterior neural plate during the AC phase of NTC.

In summary, the key achievements of this doctoral work include the creation of a novel computational tool for vertex models called CelluLink, and the development of two new mathematical models for AC during NTC – the one-way model and the two-way model.

Both models are capable of reproducing a large number of experimentally observed behaviours, described in Chapter 2, *in silico*. The full range of behaviours captured by the one-way and two-way models are listed in Tables 7.6 and 8.2, respectively.

In mathematical biology, experiments shape the development of mathematical models, and these models, in turn, suggest hypotheses for experimental testing or provide new insights with regards to phenomena that cannot be investigated through experimental means, fostering a dynamic interplay that drives both theoretical understanding and experimental investigation.

Accordingly, the one-way model proposes the following hypotheses for experimental testing, providing new directions for future research:

- Actomyosin exhibits persistent enrichment at cell-cell junctions, in contrast to the transient enrichment cycles followed by dissipation observed in medioapical actomyosin. This is essential for preserving cell and tissue integrity during AC.
- As cell-cell junctions decrease in size, apical adherens junctions exert a force, counteracting line tension, to prevent the cell surface from collapsing.
- The amplitude of a Ca^{2+} flash determines the extent of myosin activity and, thereby, cell contraction.
- A refractory period, characterized by a low Ca^{2+} level, is essential to alter the cell's mechanical properties and activate the ratchet-like mechanism.

Similarly, the two-way model proposes the following hypotheses for experimental testing:

- The level of cortical actomyosin in a cell influences the amplitude of induced Ca^{2+} flashes, either by modulating the opening of the SSCCs or by impacting the Ca^{2+} -induced Ca^{2+} release (CICR) mechanism.
- At low levels of cortical actomyosin, SSCC sensitivity remains fairly constant, but beyond a certain threshold of cortical actomyosin, SSCC sensitivity increases sharply.
- During AC, intercellular Ca^{2+} signalling between anterior neural plate cells occurs via mechanochemical transduction.
- A fraction of anterior neural plate cells must be activated to initiate AC. This initial activation could be caused by mechanical forces generated during convergent extension or chemical signals.

Future work

In spite of the successes of the one-way and two-way models, they have some limitations. Given that NTC involves the three-dimensional folding of the neural plate, 2D vertex models prove inadequate in fully capturing neural plate morphogenesis.

Notably, the models are unable to capture the spatial distribution of constriction foci on the anterior neural plate. However, the neural plate folds along the constriction foci during AC. Therefore, it is essential for a biologically accurate model to generate constriction foci through the two-way coupling between Ca^{2+} signals and cellular mechanics.

It has been observed that the frequency of Ca^{2+} flashes is higher in regions of increased constriction, such as the constriction foci [33]. However, since the one-way and two-way models are unable to generate constriction foci, they cannot reproduce this behaviour.

Therefore, we posit that either a 3D apical vertex model or a full 3D vertex model, incorporating the two-way coupling between Ca^{2+} signalling and cellular mechanics, would be required to capture the spatial distribution of constriction foci on the anterior neural plate.

In the one-way and two-way models, cells are modelled as hexagons, resulting in the anterior neural plate having a hexagonal shape. However, in reality, the anterior neural plate is circular, and its cells can take on various polygonal shapes.

Although the hexagonal approximation serves the purpose of this doctoral work, for a more accurate representation of the shape of the anterior neural plate, cells should be modelled as polygons with different numbers of sides. This could be achieved by generating initial cell configurations using Voronoi diagrams and placing the cells in a circular region [196].

The Suzuki model and, by extension, the models developed in this doctoral work, operate with simplified bistable Ca^{2+} dynamics, where a cell is either in a low Ca^{2+} (inactivated) state or a high Ca^{2+} (activated) state. While this simplification suffices for the current doctoral work, it should be noted that more recent models of Ca^{2+} signalling incorporate more sophisticated Ca^{2+} dynamics, such as IP_3 -mediated CICR which has been validated by experiments [12, 95, 96]. Moreover, when a cell undergoes activation in our models, the Ca^{2+} concentration remains elevated for a fixed duration, τ , before returning to baseline. In reality, the duration of cell activation is governed by the CICR mechanism. Therefore, a biologically accurate model should incorporate IP_3 -mediated Ca^{2+} dynamics.

This would be an important step in developing a model to assess the effects of potential treatments, such as clinical interventions. These interventions could involve pharmacologically increasing Ca^{2+} levels to induce cell contractions in regions of the neural plate that do not contract sufficiently or suppressing elevated Ca^{2+} levels in regions contracting too rapidly.

During NTC, two types of multicellular Ca^{2+} transients have been observed in the anterior neural plate: short-range Ca^{2+} waves that propagate over two to five cells and long-range Ca^{2+} waves that propagate over tens of cells [33]. While the two-way model successfully demonstrates short-range Ca^{2+} waves, it fails to reproduce long-range Ca^{2+} waves. A model with more sophisticated Ca^{2+} dynamics, such as IP_3 -mediated CICR, may address this limitation.

The Suzuki model and the models developed in this doctoral work assume that the ratchet-like mechanism is area-dependent. However, the transcription factors Snail and Twist play crucial roles in the contraction and stabilization phases of apical constriction (AC), respectively. Their activities are temporally coordinated to drive productive AC [121], indicating that gene regulatory networks play a vital role in the functioning of the ratchet-like mechanism.

Intracellular signalling pathways, such as the ones that govern IP_3 -mediated CICR and gene expression, are typically modelled using differential equations and can be easily integrated into continuum models. It is more challenging to inte-

grate them into cell-based models, however, the approaches taken in the following studies could potentially be used to introduce these signalling pathways into the two-way model.

Smith et al [183] propose a method to incorporate morphogen diffusion into the vertex model framework to study the role of morphogen dynamics in the development of the *Drosophila* imaginal wing disc. In their study, they treat the nodes and edges of the vertex model as a mesh over which the morphogen reaction-diffusion equations are solved using the finite element method.

Moore et al [130] investigate the effect of juxtacrine signalling¹ on bilayer patterning in developing mammary organoids. In their study, they incorporate an ODE model for Notch-Delta signalling into the overlapping spheres framework. The bilayer is represented by a graph, where each node corresponds to a cell, and a spatially-discrete ODE system is solved for each cell.

While their study investigates intercellular signalling over a cell-centre model, their approach can also be applied to model intracellular signalling in vertex models. In the one-way and two-way models, each cell corresponds to a node in the cell graph (Section 4.3). Since constricting cells are isolated from their neighbours due to the closure of gap junctions [151], a spatially-discrete system of ODEs for IP₃-mediated CICR [12] could be solved for each cell to compute the cytosolic Ca²⁺ concentration at every timestep.

In spite of the utility offered by vertex models, experimental validation of the model's parameter choices remains a significant challenge in this field. Currently, there is no straightforward methodology that directly relates experimentally measurable tissue properties (continuum-level parameters), such as Young's modulus and traction stress, to the mechanical parameters of the vertex model (cell-level parameters).

Prior studies have analytically derived expressions for the shear and bulk moduli of the tissue in their vertex models [81, 124, 194] and parametrised their model simulations to match experimental results [81]. The two-way model could be parametrised using a similar approach.

Alternatively, conducting *in silico* stress tests could elucidate the relationship between cell-level and continuum-level parameters in the vertex model. For example, Honda and Nagai [87] explored the viscoelastic properties of a cell aggregate

¹**Juxtacrine signalling** A mechanism of cell communication where cells interact by direct contact, transmitting signals through membrane-bound molecules.

through a stress test on their 3D vertex model. By analysing the deformation curves obtained from the stress test, they were able to determine the viscosity and elastic constants of the cell aggregate. A similar method could be employed to establish a connection between the properties of the anterior neural plate and the cell-level parameters in the two-way model.

To conclude, we envision that the ideal model of AC during NTC will be a 3D vertex model that incorporates the two-way coupling between Ca^{2+} signalling and cellular mechanics. In this doctoral thesis, we take a significant step in this direction by developing a 2D vertex model with two-way coupling between Ca^{2+} signalling and cellular mechanics, laying the foundation for future work.

Bibliography

- [1] T. Aegerter-Wilmsen, C. M. Aegerter, E. Hafen, and K. Basler. Model for the regulation of size in the wing imaginal disc of drosophila. *Mechanisms of development*, 124(4):318–326, 2007.
- [2] T. Aegerter-Wilmsen, A. C. Smith, A. J. Christen, C. M. Aegerter, E. Hafen, and K. Basler. Exploring the effects of mechanical feedback on epithelial topology. *Development*, 137(3):499–506, 2010.
- [3] T. Aegerter-Wilmsen, M. B. Heimlicher, A. C. Smith, P. B. de Reuille, R. S. Smith, C. M. Aegerter, and K. Basler. Integrating force-sensing and signaling pathways in a model for the regulation of wing imaginal disc size. *Development*, 139(17):3221–3231, 2012.
- [4] A. Ajduk, T. Ilozue, S. Windsor, Y. Yu, K. B. Seres, R. J. Bompfrey, B. D. Tom, K. Swann, A. Thomas, C. Graham, et al. Rhythmic actomyosin-driven contractions induced by sperm entry predict mammalian embryo viability. *Nature communications*, 2(1):417, 2011.
- [5] B. Alberts, D. Bray, K. Hopkin, A. D. Johnson, J. Lewis, M. Raff, K. Roberts, and P. Walter. *Essential cell biology*. Garland Science, 2013.
- [6] M. P. Allen and D. J. Tildesley. Computer simulation of liquids. *Clarendon-0.12*, 1987.
- [7] A. A. Almet, B. D. Hughes, K. A. Landman, I. S. Näthke, and J. M. Osborne. A multicellular model of intestinal crypt buckling and fission. *Bulletin of Mathematical Biology*, 80:335–359, 2018.
- [8] S. Alt, P. Ganguly, and G. Salbreux. Vertex models: from cell mechanics to tissue morphogenesis. *Philosophical Transactions of the Royal Society B: Biological Sciences*, 372(1720):20150520, 2017.

- [9] R. Ananthakrishnan and A. Ehrlicher. The forces behind cell movement. *International journal of biological sciences*, 3(5):303, 2007.
- [10] A. Anderson and K. Rejniak. *Single-cell-based models in biology and medicine*. Springer Science & Business Media, 2007.
- [11] J. Árnadóttir and M. Chalfie. Eukaryotic mechanosensitive channels. *Annual review of biophysics*, 39:111–137, 2010.
- [12] A. Atri, J. Amundson, D. Clapham, and J. Sneyd. A single-pool model for intracellular calcium oscillations and waves in the xenopus laevis oocyte. *Biophysical Journal*, 65(4):1727–1739, 1993.
- [13] K. Atwell. *Investigating the interplay between cellular mechanics and decision-making in the C. elegans germ line*. University of Oxford, 2016.
- [14] R. Balaji, C. Bielmeier, H. Harz, J. Bates, C. Stadler, A. Hildebrand, and A.-K. Classen. Calcium spikes, waves and oscillations in a large, patterned epithelial tissue. *Scientific reports*, 7(1):42786, 2017.
- [15] D. L. Barton, S. Henkes, C. J. Weijer, and R. Sknepnek. Active vertex model for cell-resolution description of epithelial tissue mechanics. *PLoS computational biology*, 13(6):e1005569, 2017.
- [16] J. Bereiter-Hahn. Mechanics of crawling cells. *Medical engineering & physics*, 27(9):743–753, 2005.
- [17] M. J. Berridge, P. Lipp, and M. D. Bootman. The versatility and universality of calcium signalling. *Nature reviews Molecular cell biology*, 1(1):11–21, 2000.
- [18] J. T. Blankenship, S. T. Backovic, J. S. Sanny, O. Weitz, and J. A. Zallen. Multicellular rosette formation links planar cell polarity to tissue morphogenesis. *Developmental cell*, 11(4):459–470, 2006.
- [19] G. W. Brodland and J. H. Veldhuis. Computer simulations of mitosis and interdependencies between mitosis orientation, cell shape and epithelia reshaping. *Journal of Biomechanics*, 35(5):673–681, 2002.
- [20] F. L. Bygrave and A. Benedetti. What is the concentration of calcium ions in the endoplasmic reticulum? *Cell calcium*, 19(6):547–551, 1996.

- [21] M. Cavey, M. Rauzi, P.-F. Lenne, and T. Lecuit. A two-tiered mechanism for stabilization and immobilization of e-cadherin. *Nature*, 453(7196):751–756, 2008.
- [22] CDC. Spina bifida. <https://www.cdc.gov/ncbddd/birthdefects/surveillancemanual/quick-reference-handbook/spinaBifida.html>, 2012. Public domain.
- [23] E. L. Chambers, B. C. Pressman, and B. Rose. The activation of sea urchin eggs by the divalent ionophores a23187 and x-537a. *Biochemical and biophysical research communications*, 60(1):126–132, 1974.
- [24] S. Chanet and A. C. Martin. Mechanical force sensing in tissues. *Progress in molecular biology and translational science*, 126:317–352, 2014.
- [25] A. C. Charles, J. E. Merrill, E. R. Dirksen, and M. J. Sanderson. Intercellular signaling in glial cells: calcium waves and oscillations in response to mechanical stimulation and glutamate. *Neuron*, 6(6):983–992, 1991.
- [26] A. C. Charles, C. Naus, D. Zhu, G. M. Kidder, E. R. Dirksen, and M. J. Sanderson. Intercellular calcium signaling via gap junctions in glioma cells. *The Journal of cell biology*, 118(1):195–201, 1992.
- [27] A. C. Charles, E. R. Dirksen, J. E. Merrill, and M. J. Sanderson. Mechanisms of intercellular calcium signaling in glial cells studied with dantrolene and thapsigargin. *Glia*, 7(2):134–145, 1993.
- [28] X. Chen. *Multiscale modeling of Amphibian neurulation*. University of Waterloo, 2007.
- [29] X. Chen and G. W. Brodland. Multi-scale finite element modeling allows the mechanics of amphibian neurulation to be elucidated. *Physical biology*, 5(1):015003, 2008.
- [30] J. C. Cheng, A. L. Miller, and S. E. Webb. Organization and function of microfilaments during late epiboly in zebrafish embryos. *Developmental dynamics: an official publication of the American Association of Anatomists*, 231(2):313–323, 2004.

- [31] E. A. Chernoff and S. R. Hilfer. Calcium dependence and contraction in somite formation. *Tissue and Cell*, 14(3):435–449, 1982.
- [32] N. Christodoulou. Personal communication, 2022, 2023, 2024.
- [33] N. Christodoulou and P. A. Skourides. Cell-autonomous Ca^{2+} flashes elicit pulsed contractions of an apical actin network to drive apical constriction during neural tube closure. *Cell Reports*, 13(10):2189–2202, 2015.
- [34] N. Christodoulou and P. A. Skourides. Distinct spatiotemporal contribution of morphogenetic events and mechanical tissue coupling during xenopus neural tube closure. *Development*, 149(13):dev200358, 2022.
- [35] Y. C. Chuang and C. C. Chen. Force from filaments: The role of the cytoskeleton and extracellular matrix in the gating of mechanosensitive channels. *Frontiers in Cell and Developmental Biology*, 10:886048, 2022.
- [36] M. I. Chung, N. M. Nascone-Yoder, S. A. Grover, T. A. Drysdale, and J. B. Wallingford. Direct activation of *shroom3* transcription by *pitx* proteins drives epithelial morphogenesis in the developing gut. *Development*, 137(8):1339–1349, 2010.
- [37] D. E. Clapham. Calcium signaling. *Cell*, 131(6):1047–1058, 2007.
- [38] D. N. Clarke and A. C. Martin. Actin-based force generation and cell adhesion in tissue morphogenesis. *Current Biology*, 31(10):R667–R680, 2021.
- [39] F. R. Cooper, R. E. Baker, M. O. Bernabeu, R. Bordas, L. Bowler, A. Bueno-Orovio, H. M. Byrne, V. Carapella, L. Cardone-Noott, J. Cooper, et al. Chaste: Cancer, heart and soft tissue environment. *Journal of Open Source Software*, 2020.
- [40] G. M. Cooper and R. E. Hausman. *The Cell: A Molecular Approach*, volume 10. ASM Press, Washington, DC, 2000.
- [41] A. Cordero, J. Mulinare, R. Berry, C. Boyle, W. Dietz, R. Johnston Jr, J. Leighton, T. Popovic, et al. Cdc grand rounds: additional opportunities to prevent neural tube defects with folic acid fortification. *Morbidity and mortality weekly report*, 59(31):980–984, 2010.

- [42] M. Costa. Gastrulation in drosophila: cellular mechanisms of morphogenetic movements. *The development of Drosophila melanogaster*, 1:425–465, 1993.
- [43] T. H. Crouch and C. B. Klee. Positive cooperative binding of calcium to bovine brain calmodulin. *Biochemistry*, 19(16):3692–3698, 1980.
- [44] S. Curran, C. Strandkvist, J. Bathmann, M. de Gennes, A. Kabla, G. Salbreux, and B. Baum. Myosin ii controls junction fluctuations to guide epithelial tissue ordering. *Developmental cell*, 43(4):480–492, 2017.
- [45] J. T. Daub and R. M. Merks. A cell-based model of extracellular-matrix-guided endothelial cell migration during angiogenesis. *Bulletin of mathematical biology*, 75:1377–1399, 2013.
- [46] D. J. David, A. Tishkina, and T. J. Harris. The par complex regulates pulsed actomyosin contractions during amnioserosa apical constriction in drosophila. *Development*, 137(10):1645–1655, 2010.
- [47] L. A. Davidson, A. M. Ezin, and R. Keller. Embryonic wound healing by apical contraction and ingression in xenopus laevis. *Cell motility and the cytoskeleton*, 53(3):163–176, 2002.
- [48] G. W. De Young and J. Keizer. A single-pool inositol 1, 4, 5-trisphosphate-receptor-based model for agonist-stimulated oscillations in ca^{2+} concentration. *Proceedings of the National Academy of Sciences*, 89(20):9895–9899, 1992.
- [49] R. Deguchi, H. Shirakawa, S. Oda, T. Mohri, and S. Miyazaki. Spatiotemporal analysis of ca^{2+} waves in relation to the sperm entry site and animal–vegetal axis during ca^{2+} oscillations in fertilized mouse eggs. *Developmental biology*, 218(2):299–313, 2000.
- [50] D. Drasdo and S. Höhme. A single-cell-based model of tumor growth in vitro: monolayers and spheroids. *Physical biology*, 2(3):133, 2005.
- [51] D. Drasdo, R. Kree, and J. McCaskill. Monte carlo approach to tissue-cell populations. *Physical review E*, 52(6):6635, 1995.

- [52] G. Dupont, M. Berridge, and A. Goldbeter. Signal-induced ca^{2+} oscillations: properties of a model based on ca^{2+} -induced ca^{2+} release. *Cell calcium*, 12(2-3):73–85, 1991.
- [53] G. Dupont, L. Combettes, G. S. Bird, and J. W. Putney. Calcium oscillations. *Cold Spring Harbor perspectives in biology*, 3(3):a004226, 2011.
- [54] G. Dupont, M. Falcke, V. Kirk, and J. Sneyd. *Models of calcium signalling*, volume 43. Springer, 2016.
- [55] C. H. Durney. *Applications of vertex modelling to epithelial morphogenesis*. University of British Columbia, 2020.
- [56] C. H. Durney and J. J. Feng. A three-dimensional vertex model for drosophila salivary gland invagination. *Physical Biology*, 18(4):046005, 2021.
- [57] C. H. Durney, T. J. Harris, and J. J. Feng. Dynamics of par proteins explain the oscillation and ratcheting mechanisms in dorsal closure. *Biophysical journal*, 115(11):2230–2241, 2018.
- [58] G. Eguchi. Cell shape changes and establishment of tissue structure. *Saiensu (Japanese edition of Scientific American)*, 7(5):66–77, 1977.
- [59] M. Eiraku, N. Takata, H. Ishibashi, M. Kawada, E. Sakakura, S. Okuda, K. Sekiguchi, T. Adachi, and Y. Sasai. Self-organizing optic-cup morphogenesis in three-dimensional culture. *Nature*, 472(7341):51–56, 2011.
- [60] M. Falcke. On the role of stochastic channel behavior in intracellular ca^{2+} dynamics. *Biophysical journal*, 84(1):42–56, 2003.
- [61] A. C. Falick. *Vertex Modeling of Confluent Cellular Networks Within a Molecular Dynamics Framework in LAMMPS*. University of Colorado at Boulder, 2023.
- [62] R. Farhadifar, J. Röper, B. Aigouy, S. Eaton, and F. Jülicher. The influence of cell mechanics, cell-cell interactions, and proliferation on epithelial packing. *Current Biology*, 17(24):2095–2104, 2007.
- [63] S. Federico and W. Herzog. Towards an analytical model of soft biological tissues. *Journal of biomechanics*, 41(16):3309–3313, 2008.

- [64] R. Fernandez-Gonzalez, S. de Matos Simoes, J. Röper, S. Eaton, and J. A. Zallen. Myosin ii dynamics are regulated by tension in intercalating cells. *Developmental cell*, 17(5):736–743, 2009.
- [65] M. C. Ferreira and S. R. Hilfer. Calcium regulation of neural fold formation: visualization of the actin cytoskeleton in living chick embryos. *Developmental biology*, 159(2):427–440, 1993.
- [66] E. A. Finch, T. J. Turner, and S. M. Goldin. Calcium as a coagonist of inositol 1, 4, 5-trisphosphate-induced calcium release. *Science*, 252(5004):443–446, 1991.
- [67] T. M. Finegan, N. Hervieux, A. Nestor-Bergmann, A. G. Fletcher, G. B. Blanchard, and B. Sanson. The tricellular vertex-specific adhesion molecule sidekick facilitates polarised cell intercalation during drosophila axis extension. *PLoS biology*, 17(12):e3000522, 2019.
- [68] A. G. Fletcher, J. M. Osborne, P. K. Maini, and D. J. Gavaghan. Implementing vertex dynamics models of cell populations in biology within a consistent computational framework. *Progress in biophysics and molecular biology*, 113(2):299–326, 2013.
- [69] A. G. Fletcher, M. Osterfield, R. E. Baker, and S. Y. Shvartsman. Vertex models of epithelial morphogenesis. *Biophysical journal*, 106(11):2291–2304, 2014.
- [70] T. Furuichi, K. Kohda, A. Miyawaki, and K. Mikoshiba. Intracellular channels. *Current opinion in neurobiology*, 4(3):294–303, 1994.
- [71] A. Ghaffarizadeh, R. Heiland, S. H. Friedman, S. M. Mumenthaler, and P. Macklin. Physicell: an open source physics-based cell simulator for 3-d multicellular systems. *PLoS computational biology*, 14(2):e1005991, 2018.
- [72] S. Girard and D. Clapham. Acceleration of intracellular calcium waves in xenopus oocytes by calcium influx. *Science*, 260(5105):229–232, 1993.
- [73] J. A. Glazier and F. Graner. Simulation of the differential adhesion driven rearrangement of biological cells. *Physical Review E*, 47(3):2128, 1993.

- [74] A. Goldbeter. Cell to cell signalling: From experiments to theoretical models, 2014.
- [75] A. Goldbeter, G. Dupont, and M. J. Berridge. Minimal model for signal-induced ca^{2+} oscillations and for their frequency encoding through protein phosphorylation. *Proceedings of the National Academy of Sciences*, 87(4):1461–1465, 1990.
- [76] M. Gracia, S. Theis, A. Proag, G. Gay, C. Benassayag, and M. Suzanne. Mechanical impact of epithelial- mesenchymal transition on epithelial morphogenesis in drosophila. *Nature communications*, 10(1):2951, 2019.
- [77] B. M. Gumbiner. Regulation of cadherin-mediated adhesion in morphogenesis. *Nature reviews Molecular cell biology*, 6(8):622–634, 2005.
- [78] O. Hamill. Twenty odd years of stretch-sensitive channels. *Pflügers Archiv*, 453:333–351, 2006.
- [79] K. Hayashi, T. S. Yamamoto, and N. Ueno. Intracellular calcium signal at the leading edge regulates mesodermal sheet migration during xenopus gastrulation. *Scientific Reports*, 8(1):1–12, 2018.
- [80] L. He, X. Wang, H. L. Tang, and D. J. Montell. Tissue elongation requires oscillating contractions of a basal actomyosin network. *Nature cell biology*, 12(12):1133–1142, 2010.
- [81] S. Henkes, K. Kostanjevec, J. M. Collinson, R. Sknepnek, and E. Bertin. Dense active matter model of motion patterns in confluent cell monolayers. *Nature communications*, 11(1):1405, 2020.
- [82] L. Herrgen, O. P. Voss, and C. J. Akerman. Calcium-dependent neuroepithelial contractions expel damaged cells from the developing brain. *Developmental cell*, 31(5):599–613, 2014.
- [83] S. D. Hester, J. M. Belmonte, J. S. Gens, S. G. Clendenon, and J. A. Glazier. A multi-cell, multi-scale model of vertebrate segmentation and somite formation. *PLoS Computational Biology*, 7(10):e1002155, 2011.

- [84] A. L. Hodgkin and A. F. Huxley. A quantitative description of membrane current and its application to conduction and excitation in nerve. *The Journal of physiology*, 117(4):500–544, 1952.
- [85] S. Hoehme and D. Drasdo. A cell-based simulation software for multicellular systems. *Bioinformatics*, 26(20):2641–2642, 2010.
- [86] H. Honda and G. Eguchi. How much does the cell boundary contract in a monolayered cell sheet? *Journal of theoretical biology*, 84(3):575–588, 1980.
- [87] H. Honda, M. Tanemura, and T. Nagai. A three-dimensional vertex dynamics cell model of space-filling polyhedra simulating cell behavior in a cell aggregate. *Journal of theoretical biology*, 226(4):439–453, 2004.
- [88] H. Honda, T. Nagai, and M. Tanemura. Two different mechanisms of planar cell intercalation leading to tissue elongation. *Developmental dynamics: an official publication of the American Association of Anatomists*, 237(7):1826–1836, 2008.
- [89] G. L. Hunter, J. M. Crawford, J. Z. Genkins, and D. P. Kiehart. Ion channels contribute to the regulation of cell sheet forces during drosophila dorsal closure. *Development*, 141(2):325–334, 2014.
- [90] M. Iino and M. Endo. Calcium-dependent immediate feedback control of inositol 1, 4, 5-trisphosphate-induced ca^{2+} release. *Nature*, 360(6399):76, 1992.
- [91] Y. Inoue, T. Watanabe, S. Okuda, and T. Adachi. Mechanical role of the spatial patterns of contractile cells in invagination of growing epithelial tissue. *Development, Growth & Differentiation*, 59(5):444–454, 2017.
- [92] Y. Ishimoto and Y. Morishita. Bubbly vertex dynamics: a dynamical and geometrical model for epithelial tissues with curved cell shapes. *Physical Review E*, 90(5):052711, 2014.
- [93] J. A. Izaguirre, R. Chaturvedi, C. Huang, T. Cickovski, J. Coffland, G. Thomas, G. Forgacs, M. Alber, G. Hentschel, S. A. Newman, et al. CompuCell, a multi-model framework for simulation of morphogenesis. *Bioinformatics*, 20(7):1129–1137, 2004.

- [94] S. Kang, S. Kahan, J. McDermott, N. Flann, and I. Shmulevich. Biocellion: accelerating computer simulation of multicellular biological system models. *Bioinformatics*, 30(21):3101–3108, 2014.
- [95] K. Kaouri, P. K. Maini, P. A. Skourides, N. Christodoulou, and S. J. Chapman. A simple mechanochemical model for calcium signalling in embryonic epithelial cells. *Journal of mathematical biology*, 78(7):2059–2092, 2019.
- [96] K. Kaouri, N. Christodoulou, A. Chakraborty, P. E. Méndez, P. Skourides, and R. Ruiz-Baier. A new mechanochemical model for apical constriction: Coupling calcium signalling and viscoelasticity. *Frontiers in Systems Biology*, 2:962790, 2022.
- [97] J. Kashir, B. Heindryckx, C. Jones, P. De Sutter, J. Parrington, and K. Coward. Oocyte activation, phospholipase c zeta and human infertility. *Human reproduction update*, 16(6):690–703, 2010.
- [98] J. Keener and J. Sneyd. *Mathematical physiology 1: Cellular physiology*, 2009.
- [99] N. Kleinstreuer, D. Dix, M. Rountree, N. Baker, N. Sipes, D. Reif, R. Spencer, and T. Knudsen. A computational model predicting disruption of blood vessel development. *PLoS computational biology*, 9(4):e1002996, 2013.
- [100] A. L. Krause, D. Beliaev, R. A. Van Gorder, and S. L. Waters. Lattice and continuum modelling of a bioactive porous tissue scaffold. *Mathematical medicine and biology: a journal of the IMA*, 36(3):325–360, 2019.
- [101] J. Kursawe, P. A. Brodskiy, J. J. Zartman, R. E. Baker, and A. G. Fletcher. Capabilities and limitations of tissue size control through passive mechanical forces. *PLoS computational biology*, 11(12):e1004679, 2015.
- [102] P. Y. Lam, S. E. Webb, C. Leclerc, M. Moreau, and A. L. Miller. Inhibition of stored ca^{2+} release disrupts convergence-related cell movements in the lateral intermediate mesoderm resulting in abnormal positioning and morphology of the pronephric anlagen in intact zebrafish embryos. *Development, growth & differentiation*, 51(4):429–442, 2009.

- [103] M. C. Lane, M. Koehl, F. Wilt, and R. Keller. A role for regulated secretion of apical extracellular matrix during epithelial invagination in the sea urchin. *Development*, 117(3):1049–1060, 1993.
- [104] J. D. Lechleiter and D. E. Clapham. Molecular mechanisms of intracellular calcium excitability in *x. laevis* oocytes. *Cell*, 69(2):283–294, 1992.
- [105] C. Leclerc, S. E. Webb, C. Daguzan, M. Moreau, and A. L. Miller. Imaging patterns of calcium transients during neural induction in *xenopus laevis* embryos. *Journal of cell science*, 113(19):3519–3529, 2000.
- [106] H. Lee and R. Nagele. Toxic and teratologic effects of verapamil on early chick embryos: evidence for the involvement of calcium in neural tube closure. *Teratology*, 33(2):203–211, 1986.
- [107] Y. Lee, S. Kouvroukoglou, L. V. McIntire, and K. Zygourakis. A cellular automaton model for the proliferation of migrating contact-inhibited cells. *Biophysical journal*, 69(4):1284–1298, 1995.
- [108] R. Lemlich. *Journal of Colloid and Interface Science*, 64:107, 1977.
- [109] C. F. Leung, A. L. Miller, V. Korzh, S. W. Chong, I. Sleptsova-Freidrich, and S. E. Webb. Visualization of stochastic ca^{2+} signals in the formed somites during the early segmentation period in intact, normally developing zebrafish embryos. *Development, growth & differentiation*, 51(7):617–637, 2009.
- [110] L. Leybaert and M. J. Sanderson. Intercellular ca^{2+} waves: mechanisms and function. *Physiological reviews*, 92(3):1359–1392, 2012.
- [111] Y. X. Li and J. Rinzel. Equations for $insp3$ receptor-mediated $[ca^{2+}]_i$ oscillations derived from a detailed kinetic model: a hodgkin-huxley like formalism. *Journal of theoretical Biology*, 166(4):461–473, 1994.
- [112] S. Linse, A. Helmersson, and S. Forsen. Calcium binding to calmodulin and its globular domains. *Journal of Biological Chemistry*, 266(13):8050–8054, 1991.

- [113] C. Liu and C. Montell. Forcing open trp channels: Mechanical gating as a unifying activation mechanism. *Biochemical and biophysical research communications*, 460(1):22–25, 2015.
- [114] Z. Liu, J. L. Tan, D. M. Cohen, M. T. Yang, N. J. Sniadecki, S. A. Ruiz, C. M. Nelson, and C. S. Chen. Mechanical tugging force regulates the size of cell–cell junctions. *Proceedings of the National Academy of Sciences*, 107(22):9944–9949, 2010.
- [115] R. Magno, V. A. Grieneisen, and A. F. Marée. The biophysical nature of cells: potential cell behaviours revealed by analytical and computational studies of cell surface mechanics. *BMC biophysics*, 8:1–37, 2015.
- [116] J. L. Maître and C. P. Heisenberg. Three functions of cadherins in cell adhesion. *Current Biology*, 23(14):R626–R633, 2013.
- [117] M. Marin-Riera, M. Brun-Usan, R. Zimm, T. Välikangas, and I. Salazar-Ciudad. Computational modeling of development by epithelia, mesenchyme and their interactions: a unified model. *Bioinformatics*, 32(2):219–225, 2016.
- [118] O. Markova and P. F. Lenne. Calcium signaling in developing embryos: focus on the regulation of cell shape changes and collective movements. In *Seminars in cell & developmental biology*, volume 23, pages 298–307. Elsevier, 2012.
- [119] A. C. Martin. Pulsation and stabilization: contractile forces that underlie morphogenesis. *Developmental biology*, 341(1):114–125, 2010.
- [120] A. C. Martin and B. Goldstein. Apical constriction: themes and variations on a cellular mechanism driving morphogenesis. *Development*, 141(10):1987–1998, 2014.
- [121] A. C. Martin, M. Kaschube, and E. F. Wieschaus. Pulsed contractions of an actin–myosin network drive apical constriction. *Nature*, 457(7228):495–499, 2009.
- [122] E. Martin, S. Theis, G. Gay, B. Monier, C. Rouvière, and M. Suzanne. Arp2/3-dependent mechanical control of morphogenetic robustness in an

- inherently challenging environment. *Developmental Cell*, 56(5):687–701, 2021.
- [123] F. M. Mason, M. Tworoger, and A. C. Martin. Apical domain polarization localizes actin–myosin activity to drive ratchet-like apical constriction. *Nature cell biology*, 15(8):926–936, 2013.
- [124] M. Merkel and M. L. Manning. A geometrically controlled rigidity transition in a model for confluent 3d tissues. *New Journal of Physics*, 20(2):022002, 2018.
- [125] R. M. Merks and J. A. Glazier. A cell-centered approach to developmental biology. *Physica A: Statistical Mechanics and its Applications*, 352(1):113–130, 2005.
- [126] R. M. Merks, E. D. Perryn, A. Shirinifard, and J. A. Glazier. Contact-inhibited chemotaxis in de novo and sprouting blood-vessel growth. *PLoS computational biology*, 4(9):e1000163, 2008.
- [127] R. M. Merks, M. Guravage, D. Inzé, and G. T. Beemster. Virtualleaf: an open-source framework for cell-based modeling of plant tissue growth and development. *Plant physiology*, 155(2):656–666, 2011.
- [128] M. Misra, B. Audoly, I. G. Kevrekidis, and S. Y. Shvartsman. Shape transformations of epithelial shells. *Biophysical journal*, 110(7):1670–1678, 2016.
- [129] B. Monier, M. Gettings, G. Gay, T. Mangeat, S. Schott, A. Guarner, and M. Suzanne. Apico-basal forces exerted by apoptotic cells drive epithelium folding. *Nature*, 518(7538):245–248, 2015.
- [130] J. W. Moore, T. C. Dale, and T. E. Woolley. Algebraic framework for determining laminar pattern bifurcations by lateral-inhibition in 2d and 3d bilayer geometries. *arXiv:2104.12142*, 2021.
- [131] S. W. Moore, P. Roca-Cusachs, and M. P. Sheetz. Stretchy proteins on stretchy substrates: the important elements of integrin-mediated rigidity sensing. *Developmental cell*, 19(2):194–206, 2010.
- [132] D. Moran and R. W. Rice. Action of papaverine and ionophore a23187 on neurulation. *Nature*, 261(5560):497–499, 1976.

- [133] B. Mouillac, M. N. Balestre, and G. Guillon. Positive feedback regulation of phospholipase c by vasopressin-induced calcium mobilization in wrk1 cells. *Cellular signalling*, 2(5):497–507, 1990.
- [134] N. Murisic, V. Hakim, I. G. Kevrekidis, S. Y. Shvartsman, and B. Audoly. From discrete to continuum models of three-dimensional deformations in epithelial sheets. *Biophysical Journal*, 109(1):154–163, 2015.
- [135] J. Murray. *Mathematical biology II: spatial models and biomedical applications*. Springer-Verlag, 2001.
- [136] J. Murray and G. Oster. Generation of biological pattern and form. *Mathematical Medicine and Biology: A Journal of the IMA*, 1(1):51–75, 1984.
- [137] J. D. Murray, P. K. Maini, and R. T. Tranquillo. Mechanochemical models for generating biological pattern and form in development. *Physics Reports*, 171(2):59–84, 1988.
- [138] T. Nagai and H. Honda. A dynamic cell model for the formation of epithelial tissues. *Philosophical Magazine B*, 81(7):699–719, 2001.
- [139] Narciso, N. M. Contento, T. J. Storey, D. J. Hoelzle, and J. J. Zartman. Release of applied mechanical loading stimulates intercellular calcium waves in drosophila wing discs. *Biophysical journal*, 113(2):491–501, 2017.
- [140] C. Narciso, Q. Wu, P. Brodskiy, G. Garston, R. Baker, A. Fletcher, and J. Zartman. Patterning of wound-induced intercellular ca^{2+} flashes in a developing epithelium. *Physical biology*, 12(5):056005, 2015.
- [141] E. Nikolopoulou, G. L. Galea, A. Rolo, N. D. Greene, and A. J. Copp. Neural tube closure: cellular, molecular and biomechanical mechanisms. *Development*, 144(4):552–566, 2017.
- [142] NLM. Neural crest. <https://www.ncbi.nlm.nih.gov/books/NBK547700/figure/article-25761.image.f1/>, 2014. Public domain.
- [143] D. R. Nolan, A. L. Gower, M. Destrade, R. W. Ogden, and J. McGarry. A robust anisotropic hyperelastic formulation for the modelling of soft tissue. *Journal of the mechanical behavior of biomedical materials*, 39:48–60, 2014.

- [144] P. W. Oakes, S. Banerjee, M. C. Marchetti, and M. L. Gardel. Geometry regulates traction stresses in adherent cells. *Biophysical journal*, 107(4): 825–833, 2014.
- [145] G. M. Odell, G. Oster, P. Alberch, and B. Burnside. The mechanical basis of morphogenesis: I. Epithelial folding and invagination. *Developmental Biology*, 85(2):446–462, 1981.
- [146] S. Okuda, Y. Inoue, M. Eiraku, Y. Sasai, and T. Adachi. Apical contractility in growing epithelium supports robust maintenance of smooth curvatures against cell-division-induced mechanical disturbance. *Journal of biomechanics*, 46(10):1705–1713, 2013.
- [147] S. Okuda, Y. Inoue, M. Eiraku, T. Adachi, and Y. Sasai. Vertex dynamics simulations of viscosity-dependent deformation during tissue morphogenesis. *Biomechanics and modeling in mechanobiology*, 14:413–425, 2015.
- [148] S. Okuda, Y. Inoue, T. Watanabe, and T. Adachi. Coupling intercellular molecular signalling with multicellular deformation for simulating three-dimensional tissue morphogenesis. *Interface Focus*, 5(2):20140095, 2015.
- [149] S. Okuda, Y. Inoue, M. Eiraku, T. Adachi, and Y. Sasai. Modeling cell apoptosis for simulating three-dimensional multicellular morphogenesis based on a reversible network reconnection framework. *Biomechanics and modeling in mechanobiology*, 15:805–816, 2016.
- [150] J. M. Osborne, A. G. Fletcher, J. M. Pitt-Francis, P. K. Maini, and D. J. Gavaghan. Comparing individual-based approaches to modelling the self-organization of multicellular tissues. *PLoS computational biology*, 13(2): e1005387, 2017.
- [151] A. Oshima. Structure and closure of connexin gap junction channels. *FEBS letters*, 588(8):1230–1237, 2014.
- [152] G. Oster and G. Odell. The mechanochemistry of cytogels. *Physica D: Nonlinear Phenomena*, 12(1-3):333–350, 1984.
- [153] M. Osterfield, X. Du, T. Schüpbach, E. Wieschaus, and S. Y. Shvartsman. Three-dimensional epithelial morphogenesis in the developing drosophila egg. *Developmental Cell*, 24(4):400–410, 2013.

- [154] K. Owaribe, R. Kodama, and G. Eguchi. Demonstration of contractility of circumferential actin bundles and its morphogenetic significance in pigmented epithelium in vitro and in vivo. *The Journal of cell biology*, 90(2): 507–514, 1981.
- [155] R. S. Palais and R. A. Palais. *Differential equations, mechanics, and computation*, volume 51. American Mathematical Soc., 2009.
- [156] I. Parker and I. Ivorra. Inhibition by ca^{2+} of inositol trisphosphate-mediated ca^{2+} liberation: a possible mechanism for oscillatory release of ca^{2+} . *Proceedings of the National Academy of Sciences*, 87(1):260–264, 1990.
- [157] M. C. Perrone, J. H. Veldhuis, and G. W. Brodland. Non-straight cell edges are important to invasion and engulfment as demonstrated by cell mechanics model. *Biomechanics and modeling in mechanobiology*, 15(2): 405–418, 2016.
- [158] T. F. Plageman Jr, M. I. Chung, M. Lou, A. N. Smith, J. D. Hildebrand, J. B. Wallingford, and R. A. Lang. Pax6-dependent shroom3 expression regulates apical constriction during lens placode invagination. *Development*, 137(3):405–415, 2010.
- [159] T. F. Plageman Jr, B. K. Chauhan, C. Yang, F. Jaudon, X. Shang, Y. Zheng, M. Lou, A. Debant, J. D. Hildebrand, and R. A. Lang. A trio-rhoa-shroom3 pathway is required for apical constriction and epithelial invagination. *Development*, 138(23):5177–5188, 2011.
- [160] O. Polyakov, B. He, M. Swan, J. W. Shaevitz, M. Kaschube, and E. Wieschaus. Passive mechanical forces control cell-shape change during drosophila ventral furrow formation. *Biophysical journal*, 107(4):998–1010, 2014.
- [161] N. Popgeorgiev, B. Bonneau, K. F. Ferri, J. Prudent, J. Thibaut, and G. Gillet. The apoptotic regulator nrz controls cytoskeletal dynamics via the regulation of ca^{2+} trafficking in the zebrafish blastula. *Developmental cell*, 20(5):663–676, 2011.

- [162] E. M. Purcell. Life at low reynolds number. *American journal of physics*, 45(1):3–11, 1977.
- [163] M. Rauzi, P. Verant, T. Lecuit, and P. F. Lenne. Nature and anisotropy of cortical forces orienting drosophila tissue morphogenesis. *Nature cell biology*, 10(12):1401–1410, 2008.
- [164] M. Rauzi, U. Krzic, T. E. Saunders, M. Krajnc, P. Zihlerl, L. Hufnagel, and M. Leptin. Embryo-scale tissue mechanics during drosophila gastrulation movements. *Nature communications*, 6(1):8677, 2015.
- [165] M. R. Rohrschneider and J. Nance. Polarity and cell fate specification in the control of caenorhabditis elegans gastrulation. *Developmental Dynamics*, 238(4):789–796, 2009.
- [166] S. U. Sahu, M. R. Visetsouk, R. J. Garde, L. Hennes, C. Kwas, and J. H. Gutzman. Calcium signals drive cell shape changes during zebrafish midbrain–hindbrain boundary formation. *Molecular biology of the cell*, 28(7):875–882, 2017.
- [167] G. Salbreux, L. K. Barthel, P. A. Raymond, and D. K. Lubensky. Coupling mechanical deformations and planar cell polarity to create regular patterns in the zebrafish retina. *PLoS Computational Biology*, 8(8):e1002618, 2012.
- [168] M. Sanderson and M. Sleight. Ciliary activity of cultured rabbit tracheal epithelium: beat pattern and metachrony. *Journal of Cell Science*, 47(1):331–347, 1981.
- [169] M. J. Sanderson, A. Charles, and E. R. Dirksen. Mechanical stimulation and intercellular communication increases intracellular ca²⁺ in epithelial cells. *Cell regulation*, 1(8):585–596, 1990.
- [170] J. M. Sawyer, J. R. Harrell, G. Shemer, J. Sullivan-Brown, M. Roh-Johnson, and B. Goldstein. Apical constriction: a cell shape change that can drive morphogenesis. *Developmental biology*, 341(1):5–19, 2010.
- [171] S. Schilling, M. Willecke, T. Aegerter-Wilmsen, O. A. Cirpka, K. Basler, and C. von Mering. Cell-sorting at the A/P boundary in the drosophila wing primordium: a computational model to consolidate observed non-local effects of Hh signaling. *PLoS Computational Biology*, 7(4):e1002025, 2011.

- [172] K. Schlichting and C. Dahmann. Hedgehog and dpp signaling induce cadherin cad86c expression in the morphogenetic furrow during drosophila eye development. *Mechanisms of development*, 125(8):712–728, 2008.
- [173] J. Scholey, K. Taylor, and J. Kendrick-Jones. Regulation of non-muscle myosin assembly by calmodulin-dependent light chain kinase. *Nature*, 287(5779):233–235, 1980.
- [174] M. Scianna, L. Munaron, and L. Preziosi. A multiscale hybrid approach for vasculogenesis and related potential blocking therapies. *Progress in biophysics and molecular biology*, 106(2):450–462, 2011.
- [175] T. Sego, J. Sluka, H. Sauro, and J. Glazier. Tissue forge: Interactive biological and biophysics simulation environment. *bioRxiv*, pages 2022–11, 2022.
- [176] T. Sego, T. Comlekoglu, S. M. Peirce, D. W. Desimone, and J. A. Glazier. General, open-source vertex modeling in biological applications using tissue forge. *Scientific Reports*, 13(1):17886, 2023.
- [177] Z. Shi, Z. T. Graber, T. Baumgart, H. A. Stone, and A. E. Cohen. Cell membranes resist flow. *Cell*, 175(7):1769–1779, 2018.
- [178] S. Shim, R. Goyal, A. A. Panoutsopoulos, O. A. Balashova, D. Lee, and L. N. Borodinsky. Calcium dynamics at the neural cell primary cilium regulate hedgehog signaling-dependent neurogenesis in the embryonic neural tube. *Proceedings of the National Academy of Sciences*, 120(23):e2220037120, 2023.
- [179] A. Shindo, Y. Hara, T. S. Yamamoto, M. Ohkura, J. Nakai, and N. Ueno. Tissue-tissue interaction-triggered calcium elevation is required for cell polarization during xenopus gastrulation. *PLoS One*, 5(2):e8897, 2010.
- [180] A. Shirinifard, J. S. Gens, B. L. Zaitlen, N. J. Popławski, M. Swat, and J. A. Glazier. 3d multi-cell simulation of tumor growth and angiogenesis. *PloS one*, 4(10):e7190, 2009.
- [181] B. R. Simon. Multiphase poroelastic finite element models for soft tissue structures. *Applied Mechanics Reviews*, 45(6):191–218, June 1992.

- [182] M. J. Smedley and M. Stanisstreet. *Calcium and neurulation in mammalian embryos: II. Effects of cytoskeletal inhibitors and calcium antagonists on the neural folds of rat embryos*. The Company of Biologists Limited, 1986.
- [183] A. M. Smith, R. E. Baker, D. Kay, and P. K. Maini. Incorporating chemical signalling factors into cell-based models of growing epithelial tissues. *Journal of mathematical biology*, 65:441–463, 2012.
- [184] A. V. Smrcka, K. Brown, and P. Sternweis. Regulation of polyphosphoinositide-specific phospholipase c activity by purified gq. *Science*, 251(4995):804–807, 1991.
- [185] J. Sneyd. Models of calcium dynamics. *Scholarpedia*, 2(3):1576, 2007.
- [186] P. Spahn and R. Reuter. A vertex model of drosophila ventral furrow formation. *PloS one*, 8(9):e75051, 2013.
- [187] M. A. Spencer, Z. Jabeen, and D. K. Lubensky. Vertex stability and topological transitions in vertex models of foams and epithelia. *The European Physical Journal E*, 40(1):1–17, 2017.
- [188] D. Staple. *Understanding mechanics and polarity in two-dimensional tissues*. Technische Universitat at Dresden, 2012.
- [189] D. B. Staple, R. Farhadifar, J. C. Röper, B. Aigouy, S. Eaton, and F. Jülicher. Mechanics and remodelling of cell packings in epithelia. *The European Physical Journal E*, 33:117–127, 2010.
- [190] J. Starruß, W. De Back, L. Brusch, and A. Deutsch. Morpheus: a user-friendly modeling environment for multiscale and multicellular systems biology. *Bioinformatics*, 30(9):1331–1332, 2014.
- [191] R. A. Steinhardt and D. Epel. Activation of sea-urchin eggs by a calcium ionophore. *Proceedings of the National Academy of Sciences*, 71(5):1915–1919, 1974.
- [192] R. A. Steinhardt, D. Epel, E. J. Carroll, and R. Yanagimachi. Is calcium ionophore a universal activator for unfertilised eggs? *Nature*, 252(5478):41–43, 1974.

- [193] D. M. Sussman. cellgpu: Massively parallel simulations of dynamic vertex models. *Computer Physics Communications*, 219:400–406, 2017.
- [194] D. M. Sussman and M. Merkel. No unjamming transition in a voronoi model of biological tissue. *Soft matter*, 14(17):3397–3403, 2018.
- [195] T. Sütterlin, C. Kolb, H. Dickhaus, D. Jäger, and N. Grabe. Bridging the scales: semantic integration of quantitative sbml in graphical multi-cellular models and simulations with episim and copasi. *Bioinformatics*, 29(2):223–229, 2013.
- [196] M. Suzuki, M. Sato, H. Koyama, Y. Hara, K. Hayashi, N. Yasue, H. Imamura, T. Fujimori, T. Nagai, R. E. Campbell, et al. Distinct intracellular Ca^{2+} dynamics regulate apical constriction and differentially contribute to neural tube closure. *Development*, 144(7):1307–1316, 2017.
- [197] M. Suzuki, N. Ueno, and H. Koyama. Personal communication, 2022.
- [198] T. M. Svitkina. Actin cell cortex: structure and molecular organization. *Trends in cell biology*, 30(7):556–565, 2020.
- [199] K. Swann and J. P. Ozil. Dynamics of the calcium signal that triggers mammalian egg activation. *International review of cytology*, 152:183–222, 1994.
- [200] M. H. Swat, G. L. Thomas, J. M. Belmonte, A. Shirinifard, D. Hmeljak, and J. A. Glazier. Multi-scale modeling of tissues using compucell3d. In *Methods in cell biology*, volume 110, pages 325–366. Elsevier, 2012.
- [201] K. Takano, S. Obata, S. Komazaki, M. Masumoto, T. Oinuma, Y. Ito, T. Ariizumi, H. Nakamura, and M. Asashima. Development of ca^{2+} signaling mechanisms and cell motility in presumptive ectodermal cells during amphibian gastrulation. *Development, growth & differentiation*, 53(1):37–47, 2011.
- [202] D. Tartarini and E. Mele. Adult stem cell therapies for wound healing: biomaterials and computational models. *Frontiers in bioengineering and biotechnology*, 3:206, 2016.

- [203] J. E. Taylor. The structure of singularities in soap-bubble-like and soap-film-like minimal surfaces. *Annals of Mathematics*, 103(3):489–539, 1976.
- [204] S. J. Taylor and J. H. Exton. Guanine-nucleotide and hormone regulation of polyphosphoinositide phospholipase c activity of rat liver plasma membranes. bivalent-cation and phospholipid requirements. *Biochemical Journal*, 248(3):791–799, 1987.
- [205] S. Theis, M. Suzanne, and G. Gay. Tyssue: an epithelium simulation library. *Journal of Open Source Software*, 6(62):2973, 2021.
- [206] A. P. Thompson, H. M. Aktulga, R. Berger, D. S. Bolintineanu, W. M. Brown, P. S. Crozier, P. J. in’t Veld, A. Kohlmeyer, S. G. Moore, T. D. Nguyen, et al. Lammmps-a flexible simulation tool for particle-based materials modeling at the atomic, meso, and continuum scales. *Computer Physics Communications*, 271:108171, 2022.
- [207] L. Tranqui and P. Tracqui. Mechanical signalling and angiogenesis. the integration of cell–extracellular matrix couplings. *Comptes Rendus de l’Académie des Sciences-Series III-Sciences de la Vie*, 323(1):31–47, 2000.
- [208] G. Trichas, A. M. Smith, N. White, V. Wilkins, T. Watanabe, A. Moore, B. Joyce, J. Sugnaseelan, T. A. Rodriguez, D. Kay, et al. Multi-cellular rosettes in the mouse visceral endoderm facilitate the ordered migration of anterior visceral endoderm cells. *PLoS biology*, 10(2):e1001256, 2012.
- [209] M. Tsutsumi, K. Inoue, S. Denda, K. Ikeyama, M. Goto, and M. Denda. Mechanical-stimulation-evoked calcium waves in proliferating and differentiated human keratinocytes. *Cell and tissue research*, 338(1):99, 2009.
- [210] E. Uthman. Anencephaly. <https://www.medlink.com/media/D1fo3>, 2002. Public domain.
- [211] I. Vainio, A. Abu Khamidakh, M. Paci, H. Skottman, K. Juuti-Uusitalo, J. Hyttinen, and S. Nymark. Computational model of ca²⁺ wave propagation in human retinal pigment epithelial arpe-19 cells. *PLoS One*, 10(6):e0128434, 2015.

- [212] S. Varadarajan, R. E. Stephenson, E. R. Misterovich, J. L. Wu, I. S. Erofeev, A. B. Goryachev, and A. L. Miller. Mechanosensitive calcium signaling in response to cell shape changes promotes epithelial tight junction remodeling by activating rhoa. *bioRxiv*, pages 2021–05, 2021.
- [213] D. S. Vijayraghavan and L. A. Davidson. Mechanics of neurulation: From classical to current perspectives on the physical mechanics that shape, fold, and form the neural tube. *Birth defects research*, 109(2):153–168, 2017.
- [214] D. C. Walker and J. Southgate. The virtual cell — a candidate co-ordinator for ‘middle-out’ modelling of biological systems. *Briefings in Bioinformatics*, 10(4):450–461, 2009.
- [215] J. B. Wallingford, A. J. Ewald, R. M. Harland, and S. E. Fraser. Calcium signaling during convergent extension in xenopus. *Current Biology*, 11(9):652–661, 2001.
- [216] D. Weaire and R. Phelan. *Journal of Physics: Condensed Matter*, 8:L37, 1996.
- [217] D. L. Weaire and S. Hutzler. *The physics of foams*. Oxford University Press, 2001.
- [218] S. E. Webb and A. L. Miller. Ca²⁺ signalling and early embryonic patterning during zebrafish development. *Clinical and experimental pharmacology and physiology*, 34(9):897–904, 2007.
- [219] M. Weliky and G. Oster. The mechanical basis of cell rearrangement. i. epithelial morphogenesis during fundulus epiboly. *Development*, 109(2):373–386, 1990.
- [220] M. Weliky, S. Minsuk, R. Keller, and G. Oster. Notochord morphogenesis in xenopus laevis: simulation of cell behavior underlying tissue convergence and extension. *Development*, 113(4):1231–1244, 1991.
- [221] C. Wiebe and G. W. Brodland. Tensile properties of embryonic epithelia measured using a novel instrument. *Journal of biomechanics*, 38(10):2087–2094, 2005.

- [222] M. Wilkins and J. Sneyd. Intercellular spiral waves of calcium. *Journal of theoretical biology*, 191(3):299–308, 1998.
- [223] S. Xie and A. C. Martin. Intracellular signalling and intercellular coupling coordinate heterogeneous contractile events to facilitate tissue folding. *Nature communications*, 6(1):7161, 2015.
- [224] N. Yamaguchi, Z. Zhang, T. Schneider, B. Wang, D. Panozzo, and H. Knaut. Rear traction forces drive adherent tissue migration in vivo. *Nature cell biology*, 24(2):194–204, 2022.
- [225] W. Yang, J. Y. Chen, and L. Zhou. Effects of shear stress on intracellular calcium change and histamine release in rat basophilic leukemia (rbl-2h3) cells. *Journal of Environmental Pathology, Toxicology and Oncology*, 28(3), 2009.
- [226] S. Young, H. Ennes, J. McRoberts, V. Chaban, S. Dea, and E. Mayer. Calcium waves in colonic myocytes produced by mechanical and receptor-mediated stimulation. *American Journal of Physiology-Gastrointestinal and Liver Physiology*, 276(5):G1204–G1212, 1999.
- [227] S. M. Zehnder, F. M. Zegers, and T. E. Angelini. A langevin model of physical forces in cell volume fluctuations. *Journal of biomechanics*, 49(8):1286–1289, 2016.
- [228] J. Zhang, S. E. Webb, L. H. Ma, C. M. Chan, and A. L. Miller. Necessary role for intracellular ca^{2+} transients in initiating the apical-basolateral thinning of enveloping layer cells during the early blastula period of zebrafish development. *Development, growth & differentiation*, 53(5):679–696, 2011.
- [229] J. Zhou, H. Y. Kim, and L. A. Davidson. Actomyosin stiffens the vertebrate embryo during crucial stages of elongation and neural tube closure. *Development*, 136(4):677–688, 2009.